
CHARACTERIZATION OF SINGLE QUANTUM DOT BLINKING

Dwell Time Statistics and
Electrochemical Control

Von der Fakultät für Physik- und Geowissenschaften
der Universität Leipzig
genehmigte

DISSERTATION

zur Erlangung des akademischen Grades

doctor rerum naturalium

(Dr. rer. nat.)

vorgelegt

von Dipl.-Phys. Nicole Amecke-Mönnighoff

geboren am 16.04.1982 in Köln

Gutachter: Prof. Dr. Alf Mews, Universität Hamburg
Prof. Dr. Frank Cichos, Universität Leipzig

Tag der Verleihung: 22.06.2015

Bibliographic Description

Amecke-Mönnighoff, Nicole

Characterization of Single Quantum Dot Blinking: Dwell Time Statistics and Electrochemical Control

Universität Leipzig, Dissertation

201 pages, 249 references, 91 figures, 4 tables, 3 appendices

Abstract:

This thesis addresses the observed fluorescence intermittency of single semiconductor nanocrystals, also referred to as blinking. Despite continuous excitation their fluorescence is randomly interrupted by dark periods that can last over several minutes. Especially the extraction of power law dwell time statistics in bright and dark states indicates very complex underlying processes that are not fully understood to date. Here two approaches are followed to reveal the nature of the blinking mechanism.

One addresses the common threshold method for extraction of power law dwell times. Its performance is tested with simulations to a broad range of experimentally determined parameters. Strong deviations are found between input and extracted statistics dependent on input parameters themselves. A comparison with experimental data does not support the assignment of power law statistics for the bright state and indicates the existence of distinct blinking mechanisms.

The second approach directly aims at the nature of the dark state, which is mostly attributed to charges in the QD or trap states in its vicinity. A method is developed to detect charging processes on single QDs with their fluorescence. Electrochemistry is combined with confocal microscopy also allowing evaluations of excited state lifetimes and emission spectra. Reduction and oxidation of the QD bands are successfully observed as a quenching of QD fluorescence. Single QD observations identify two independent blinking mechanisms, that are assigned to positive and negative charging. Positive charging is not only observed after hole injection but also the extraction of excited electrons. Three additional quenching mechanisms are identified, two of which are assigned to trap relaxation. Differences between two substrate electrodes demonstrate the importance of the substrate material.

Contents

Bibliographic Description	III
Contents	V
List of Figures	IX
List of Tables	XI
Abbreviations and Symbols	XIII
1 Introduction	1
2 Semiconductor Quantum Dots	7
2.1 Basic Properties of Quantum Dots	8
2.1.1 Confinement	8
2.1.2 Band Structure of CdSe	11
2.1.3 Synthesis and Structural Properties	13
2.2 Optical Properties of Colloidal Quantum Dots	16
2.2.1 Radiative and Non-Radiative Decay Pathways	16
2.2.2 Fluorescence Intermittency	20
2.2.3 Lifetime and Spectral Fluctuations	28
3 Electrochemistry on Semiconductor Electrodes	31
3.1 Electrochemical Analysis	31
3.2 Semiconductors	32
3.2.1 Semiconductor Junctions	33
3.2.2 Semiconductor-Electrolyte Interface	34
3.3 Electron Transfer Rates	34
3.3.1 Bias Potentials for Ideal Surfaces	36
3.3.2 Bias Potentials with Surfaces States	37
4 Experimental and Analysis Techniques	39
4.1 CdSe/ZnS Quantum Dots	39
4.2 Fluorescence Microscopy	40
4.2.1 Resolution	40
4.2.2 Confocal Microscopy	41
4.2.3 Time Correlated Single Photon Counting (TCSPC)	42

4.3	Voltammetry	43
4.3.1	Cyclic Voltammetry in Solution	44
4.3.2	Cyclic Voltammetry on an Adsorbed Analyte	45
4.4	Experimental Setup	46
4.4.1	Fluorescence Detection	46
4.4.2	Voltage Application and Current Detection	50
4.5	Sample Preparation	50
4.5.1	Single Quantum Dots on Glass	50
4.5.2	Electrochemical Cell	51
4.6	Data Analysis	52
4.6.1	Excited State Lifetime	52
4.6.2	Simulation of Two-State Blinking	52
4.6.3	Probability Distributions via Thresholding	53
5	Power Law Blinking of Single Quantum Dots	55
5.1	Artifacts of Thresholding Due to Unresolved Blinking	56
5.1.1	Threshold Placement	56
5.1.2	Bin Time	57
5.1.3	Different Power Law Exponents	59
5.1.4	Distinct On- and Off-State Exponents	59
5.1.5	Discussion	60
5.2	Additional Influences in Experiments	64
5.2.1	On-Time Cut-Off	65
5.2.2	Poisson Noise	66
5.2.3	Intermediate Intensity Levels	67
5.2.4	Discussion	68
5.3	Comparison to Experiments	71
5.3.1	Influence of Bin Time and Threshold	71
5.3.2	Excitation Dependence	74
5.3.3	Continuous Distribution of Intermediate Intensity Levels	76
5.3.4	Dim-State Above the Background Intensity	77
5.3.5	Discussion	78
6	Electrochemical Charging of Quantum Dots	83
6.1	Characterization of Sample and Cell	84
6.1.1	Film Morphology	84
6.1.2	Quenching Close to a Conducting Interface	85
6.1.3	Determination of the Reference Potential	87
6.1.4	Band Alignment at the Electrode Surface	88
6.2	Cyclic Voltammetry on a Quantum Dot Film	89
6.2.1	ZnO/ITO Electrode	90
6.2.2	ITO Electrode	90
6.2.3	Discussion	91
6.3	Dependence on Scan Parameters	94
6.3.1	ZnO/ITO Electrode	95
6.3.2	ITO Electrode	97

6.3.3	Discussion	98
6.4	Potential Dependence of the Excited State Lifetime	101
6.4.1	ZnO/ITO Electrode	101
6.4.2	ITO Electrode	103
6.4.3	Discussion	105
6.5	Cyclic Voltammetry on Single Quantum Dots	107
6.5.1	ZnO/ITO Electrode	108
6.5.2	ITO Electrode	110
6.5.3	Discussion	111
6.6	Distribution of Negative Turn-Off Characteristics	115
6.6.1	Transition Width of the Ensemble	115
6.6.2	Distribution of Negative Turn-Off Characteristics	116
6.6.3	Discussion	116
6.7	Illumination Dependence of Fluorescence Quenching and Recovery	123
6.7.1	Photoinduced Quenching and Recovery	124
6.7.2	Recovery Acceleration with Selected Potential Steps	126
6.7.3	Discussion	127
7	Summary and Outlook	131
7.1	Summary	131
7.1.1	Identification of Power Laws with Thresholding	131
7.1.2	Controlling Quantum Dot Fluorescence with Charges	133
7.2	Outlook	136
7.2.1	Investigating Quenching Dynamics with Electrochemistry	136
7.2.2	Adjusting Fluorescence Electrochemistry to Other Systems	137
7.2.3	Unbiased Extraction of Dwell Time Statistics	137
A	Mathematical Auxiliaries	139
A.1	Relative Time Spent in Unresolved Blinking Events	139
A.2	Distribution of Injection Edges	139
A.3	Rate Equations for Charge Injection and Ejection	140
B	Instrument and References of the Electrochemical Setup	143
B.1	Electric Circuit of the Home-Built Potentiostat	143
B.2	Thickness of Spin Cast PVA Spacer Layers	143
B.3	Transmission of ITO and ZnO/ITO Electrodes	144
B.4	Fluorescence in Propylene Carbonate	144
B.5	Background Fluorescence of ZnO/ITO Electrodes	145
C	Electrochemical Investigations	147
C.1	Shift Due to Quantum Dot Concentration	147
C.2	Influences of Solvent Drying with Molecular Sieves	148
C.3	Shift of the Negative Turn-Off Edge over Time	151
C.4	Dependence on the Excitation Intensity	152
C.5	Single Quantum Dots	153
C.6	Ensemble Fluorescence Spectra	154

CONTENTS

Bibliography	159
Publications	179
Acknowledgements	181
Declaration	183

List of Figures

1.1	Size Dependence of Absorption and Emission Spectra	2
1.2	Fluorescence Intermittency of a Single Quantum Dot	4
2.1	Electronic Confinement in a Semiconductor Quantum Dot	7
2.2	CdSe Bulk Band Structure and Quantum Dot Optical Transitions	12
2.3	Fine Structure of the Lowest Exciton Transition	13
2.4	Lattice and Surface Structure of Core(-Shell) CdSe Quantum Dots . . .	14
2.5	Types of Quantum Dot Heterojunctions	15
2.6	Radiative and Non-Radiative Decay Channels	16
2.7	Auger Relaxation in Bulk CdSe	17
2.8	Auger Relaxation in a Quantum Dot	18
2.9	Antibunching at Continuous and Pulsed Excitation	19
2.10	Scheme of the Static Trap Model	23
2.11	Scheme of Diffusion Controlled Electron Transfer	25
2.12	Lifetime Fluctuations of a Single Quantum Dot	28
2.13	Spectral Diffusion of a Single Quantum Dot	29
3.1	Semiconductor Heterojunctions	32
3.2	Metal/Electrolyte-Semiconductor Junctions	33
3.3	The Gerischer Model	35
3.4	Bias Potentials in the Gerischer Model	37
4.1	Properties of Fort Orange Quantum Dots	40
4.2	Principles of Widefield and Confocal Microscopy	41
4.3	Principle of Time-Tagged Time Correlated Single Photon Counting . . .	42
4.4	Principle of Cyclic Voltammetry	45
4.5	Experimental Setup	47
4.6	Excitation Foci	48
4.7	Time-Resolved Instrument Response and Fluorescence Spectra	49
4.8	Sample Preparation	50
4.9	Simulation of a Binned Time-Traces	52
4.10	Logarithmic Binning	54
5.1	Threshold Dependence of Dwell Time Histograms	57
5.2	Bin Time Dependence of Intensity and Dwell Time Histograms	58
5.3	Dependence on Different Power Law Exponents	58
5.4	Distinct Exponents for On- and Off-State	59

LIST OF FIGURES

5.5	Fraction of Time Spent in Unresolved Events	62
5.6	Lamperti Function and Unresolved Events for Distinct Exponents	63
5.7	Influence of an On-State Cut-Off	65
5.8	Influence of Poisson Noise	67
5.9	Influence of Intermediate Intensity Levels	68
5.10	Estimated Noise-Induced Cut-Offs	70
5.11	Analysis of a Single Quantum Dot at Different Bin Times	72
5.12	Fit Results for an On-State Power Law with Exponential Cut-Off	73
5.13	Comparison of Fitted and Noise-Induced Cut-Offs	74
5.14	Excitation Dependence of a Single Quantum Dot	75
5.15	Lifetime Fluctuations at Different Excitation Intensities	76
5.16	Estimation of the Influence of Intermediate Intensities	76
5.17	Distinct Intermediate Intensity Level	77
6.1	Confocal Scans of Quantum Dot Films on ZnO/ITO	85
6.2	Intensity and Lifetime Quenching on Different Substrates	86
6.3	Cyclic Voltammograms of a Cobaltocene-Ferrocene Reference	87
6.4	Fluorescence Voltammogram on ZnO/ITO	90
6.5	Fluorescence Voltammogram on ITO	91
6.6	Absolute Potentials of Electrodes and Quantum Dots	92
6.7	Scan Rate Dependence of the Fluorescence Voltammogram	95
6.8	Different Negative Reversal Potentials on ZnO/ITO	96
6.9	Dependence of Peak Height and Position on Reversal Potentials	97
6.10	Different Positive Reversal Potentials on ZnO/ITO	98
6.11	Different Reversal Potentials on ITO	99
6.12	Quenching Mechanisms Deduced from Scan Parameter Variations	100
6.13	Lifetime Voltammograms on ZnO/ITO	102
6.14	Voltage Dependent Fluorescence Decays on ZnO/ITO	103
6.15	Voltage Dependent Fluorescence Decays on ITO	104
6.16	Trap Relaxation, Negative and Positive Charging	106
6.17	Time Averages of Single Quantum Dots on Ga:ZnO/ITO	108
6.18	Individual Cycles of Single Quantum Dots on Ga:ZnO/ITO	109
6.19	Confocal Measurement of a Single Quantum Dot	110
6.20	Single Quantum Dots on ITO	111
6.21	Dependence of Quantum Yield and Lifetime on the Radiative Rate	114
6.22	Ensemble Edge for Electron Injection into the Conduction Band	115
6.23	Distribution of Quenching Potentials for Single Quantum Dots	117
6.24	Transition Width of Single QDs	119
6.25	Relative Probability of Direct and Auger Electron Ejection	122
6.26	Illumination Dependence of the Fluorescence Voltammogram	124
6.27	Illumination Dependence of Fluorescence Quenching and Recovery	125
6.28	Acceleration of Fluorescence Recovery	126
6.29	Fluorescence Recovery in the Dark	127
6.30	Hole Trap Creation in Negatively Charged Quantum Dots	129
7.1	Fluorescence Recovery Dynamics of QD Ensembles	136

B.1	Electric Circuit of the Home-Built Potentiostat	143
B.2	Thickness of Spin Cast PVA Spacer Layers	144
B.3	Electrode Transmission and Background Fluorescence	145
C.1	Influence of Quantum Dot Concentration	147
C.2	Fluorescence of a TBAP/PC Solution Dried with Molecular Sieves . .	148
C.3	Dependence of the Current Reduction Peak on Scan Rate	149
C.4	Potential Shift in Undried Solution	150
C.5	Potential Shift over Time	151
C.6	Dependence on Excitation Rate	152
C.7	Single Quantum Dots on ZnO/ITO in Undried Solution	154
C.8	Single Quantum Dots on ITO in Undried Solution	155
C.9	Voltage Dependent Fluorescence Spectra on ITO	156
C.10	Voltage Dependent Fluorescence Spectra on ZnO/ITO	157
C.11	Time Development of Spectra and Lifetime on ZnO/ITO	157

List of Tables

2.1	Lattice and Band Gap Parameters of Different Semiconductors	14
4.1	Properties of Fort Orange Quantum Dots	40
6.1	Fitted Widths and Positions of the Negative Turn-Off Edge	116
7.1	Summary of the Different Observed Quenching Mechanisms	135

Abbreviations and Symbols

Abbreviations

3D	three dimensional
AFM	atomic force microscope
Ag	silver
APD	avalanche photodiode
ca.	circa
CB	conduction band
Cc	cobaltocene
CCD	charge-coupled device
Cd	cadmium
CdS	cadmium sulfide
CdSe	cadmium selenide
CdTe	cadmium telluride
CE	counter electrode
Chap.	chapter
CPA	change point analysis
cpb (kcpb)	counts per bin (kilocounts per bin)
cps (kcps)	counts per second (kilocounts per second)
cts (kcts)	counts (kilocounts)
DCET	diffusion controlled electron transfer
e.g.	exempli gratia – for example
Eq.	equation
et al.	et alii – and others
Fc	ferrocene
Fig.	figure
FRET	Förster resonance energy transfer
FTO	fluorine doped tin oxide

ABBREVIATIONS AND SYMBOLS

FWHM	full width at half maximum
Ga	gallium
Ga:ZnO	gallium doped zinc oxide
Ga:ZnO/ITO	20 nm Ga:ZnO coated ITO substrate
HDA	hexadecylamine
i.e.	id est – that is
IRF	instrument response function
ITO	indium tin oxide
LED	light emitting diode
NA	numerical aperture
PC	propylene carbonate
psf	point spread function
Pt	platinum
PVA	polyvinyl alcohol
QD	quantum dot
QY	quantum yield
RE	reference electrode
rpm	rounds per minute
S	sulfur
Se	selenium
Sec.	section
SHE	standard hydrogen electrode
SNR	signal to noise ratio
TBAP	tetrabutylammonium perchlorate
TBAP/PC	solution of TBAP in PC
TCSPC	time correlated single photon counting
TiO₂	titanium dioxide
TOPO	trioctylphosphine oxide
VB	valence band
WE	working electrode
Zn	zinc
ZnO	zinc oxide
ZnO/ITO	20 nm ZnO coated ITO substrate
ZnS	zinc sulfide
ZnSe	zinc selenide

Symbols

$\alpha_{\text{on/off}}$	on-/off-state power law exponent
$c_{\text{red/ox}}$	concentration of reduced/oxidized species
e_{CB}	energy of QD conduction band
E_{g}	band gap
E_{F}	Fermi-level energy
E_{redox}	energy corresponding to the redox potential U_{redox}
FWHM	average/ensemble electron injection transition width (cathodic sweep)
FWHM'	average/ensemble electron ejection transition width (anodic sweep)
fwhm	single QD electron injection transition width (cathodic sweep)
fwhm'	single QD electron ejection transition width (anodic sweep)
fwhm _{1 cycle}	single cycle single QD electron injection transition width
FWHM _{1st cycle}	ensemble average electron injection width of the 1 st cycle
FWHM _{edges}	distribution width of single QD electron injection potentials
FWHM _{mean}	mean of single QD electron injection transition widths
FWHM _{sum}	ensemble time average electron injection transition width
$\Gamma_{\text{r/nr}}$	radiative/non-radiative decay rate
I	fluorescence intensity or current
I_{on}	on-state intensity
I_{p}	current peak amplitude in voltammograms
k_{B}	Boltzmann constant
$k_{\text{in/out}}$	charging/neutralization rate
$k_{\text{in}}^{-/+}$	negative/positive charging rate
k_{in}^{*+}	photoinduced positive charging rate (electron extraction from the CB)
$k'_{\text{in/out}}{}^{-}$	negative charging/neutralization rate from/to electrode states at the QD conduction band energy
$k_{\text{in}}^{D/P-}$	electron injection rate into the conduction band 1D/1P levels
$k_{\text{out}}^{-/+}$	neutralization rate of the negative/positive trion
k_{out}^{A-}	Auger ejection rate of an electron from the negative trion
λ_{em}	emission wavelength
λ_{a}	wavelength of first absorption peak
$m_{e/h}^*$	effective mass of electron/hole
v	scan rate in voltammograms
p_{avg}	average QD intensity relative to the on-state intensity

ABBREVIATIONS AND SYMBOLS

p_N	fraction of neutral QDs
$QY^{-/+}$	quantum yield of negative/positive trion
R_{exc}	excitation rate
$\rho_{red/ox}$	area density of reduced/oxidized species
T	threshold intensity or temperature
τ_{avg}	calculated average lifetime with Eq. (4.16)
t_{bin}	bin time
t_c	shortest blink time (onset of the power law)
$\tau_{cut-off}$	on-time cut-off
τ_{eff}	effective excited state lifetime given in Eq. (2.21)
t_{max}	maximum dwell time
$t_{on/off}$	length of an on-/off-time
$\tau_{on/off}$	noise-induced on-/off-state cut-off according to Eq. (5.6)
$\tau'_{on/off}$	noise-induced on-/off-state additional short time exponential distribution according to Eq. (5.6)
τ_{tot}	total measurement time
U	applied potential between WE and RE
U_0	average/ensemble electron injection potential (Eq. (6.1) cathodic sweep)
u_0	single QD electron injection potential (Eq. (6.1) cathodic sweep)
U'_0	average/ensemble electron ejection potential (Eq. (6.1) anodic sweep)
u'_0	single QD electron ejection potential (Eq. (6.1) anodic sweep)
u_{CB}	redox potential of QD conduction band
U_F	electrode potential of the Fermi-level
$U_{min/max}$	negative/positive reversal potential in voltammograms
U_{redox}	redox potential
U_p	current peak potential in voltammograms

1 Introduction

The decreasing dimensions of today's technologies are starting to reach down to length-scales where material properties are determined by the actual size of the objects. This size is at the scale of a few nanometers, not much bigger than a single molecule. Nanometer sized semiconductors gained special attention among these nanomaterials. Semiconductor nanocrystals or quantum dots (QDs) show electronic properties between those of bulk crystals and molecules. A quantum mechanical effect, called the quantum confinement effect, is macroscopically observable as a shift in absorption and emission spectra with their size. This leads to an easy tunability of energy levels with object size, which is very interesting for a broad range of applications. Especially materials with band gaps in the visible range are studied and used for QD-LEDs [1–4], solar cells [5–7], lasers [8–10] or biological labels [11–13]. Even an employment as single photon sources for quantum cryptography or computing is discussed [14–16]. One drawback of QD fluorescence in most applications, however, was discovered with single particle spectroscopy. Like other nanoemitters, they exhibit random intensity fluctuations between a bright and a dark state. No scientific consensus has been reached so far on an explanation of this behavior. In contrast to single molecules, QDs still allow multiple excitations like bulk crystals. Dark states thus cannot be connected to forbidden transitions like a triplet state. Despite an appreciation of the so-called “blinking” in the growing field of super resolution microscopy [17–19], intensity fluctuations especially compromise the use of QDs as fluorescent markers or single photon sources. An understanding is thus desired for a controlled blinking suppression. Maybe more importantly, it also promises the discovery of new fundamental physics on the nanoscale. Uncovering the underlying blinking mechanisms has been the primary aim of this thesis.

The first changes of optical properties with particle size were reported by Faraday in the 1850s [20]. He recognized that different colors of gold dispersions result from variations in particle size. For semiconductor particles a size-dependence of optical spectra was not discovered before the 1980s. In 1985 Ekimov et al. [21] reported on shifts in absorption and emission spectra of semiconductor doped glasses with the size of the included semiconductor nanocrystals. This shift of electronic levels was assigned to confinement of the excited charge carriers to the QD core. In contrast to bulk semiconductors, excited electrons and holes in nanocrystals “feel” the boundaries defined by the particle radius. The particle size is then smaller than the exciton Bohr radius a_B , which describes the size of an exciton. When the confinement applies to all three dimensions ($R_{x,y,z} < a_B$), like in semiconductor nanocrystals, only discrete energy levels remain allowed as in atoms or molecules. These levels separate for electrons and

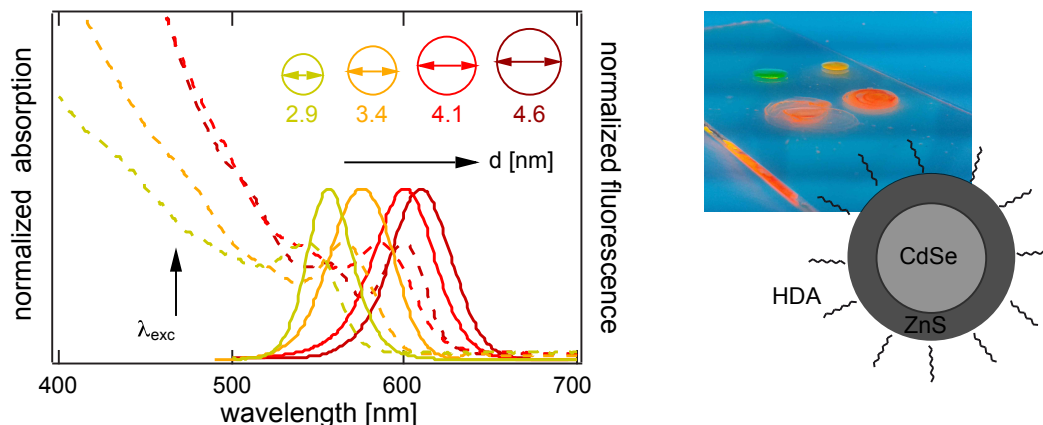


Figure 1.1: Left: Absorption (dashed lines) and emission spectra (solid lines) for CdSe/ZnS nanocrystals of four different core diameters d (Evidots). Relative diameters are indicated in the graph. Emission spectra are collected at the excitation wavelength $\lambda_{exc} = 470$ nm. Right: Picture of the corresponding QD solutions under UV illumination and a sketch of the investigated core-shell QDs in this thesis.

holes with decreasing particle size. This leads to increasing transition energies, thus, a shift of the spectrum. For CdSe with a bulk band gap of 1.75 eV emission can be tuned over the complete visible range with QD diameters of 2 – 8 nm (see Fig. 1.1). This range is extremely valuable in optical applications.

Semiconductor quantum dots can for instance be grown with molecular beam epitaxy [22, 23]. Here, islands are formed via self-assembly on a lattice-mismatched substrate. 3D confinement can also be achieved with lithographic methods [23]. A cheap and easy way to synthesize quantum dots is found in wet chemical methods [24, 25]. Here QDs are grown from precursors in solution. The growth process can directly be monitored with absorption or emission spectra and interrupted at the desired particle size. Such colloidal QDs are typically round or slightly prolate. Colloidal QDs with a CdSe core and ZnS shell have also been investigated in this thesis.

The sensing of the particle boundaries by confined excitons, is intimately connected to a strong influence of the surface on fluorescence properties. Due to their small size, this surface comprises a considerable part of the crystals. For 3 nm colloidal particles half of all atoms are at the surface. Potential barriers at the edges are not infinite. A corresponding leakage of the exciton wave function to the surface leads to non-radiative decay pathways, reducing quantum yield and photostability. Uncapped colloidal CdSe QDs even show a red emission band, that is associated with the emission from surface defects. The growth of a shell of particular types and capping with ligands (see right of Fig. 1.1) decrease these effects without diminishing emission tunability [26]. Influences of the specific surface characteristics [27], shell thickness [28, 29], ligand capping [30, 31] and the surrounding environment [32, 33] are, however, still observed. For applications a complete elimination or control of non-radiative recombination is desired to increase device or detection efficiencies. Such a control demands an identification of the specific decay pathways.

The discovery of fluorescence fluctuations of single particles unambiguously showed that for such an identification ensemble measurements are not sufficient. The implementation of single particle spectroscopy allows the detection of single particle fluorescence in the absence of ensemble averaging. First investigations of single molecules [34] and colloidal semiconductor nanocrystals [35] showed strong intensity fluctuations that have neither been observed nor expected from ensemble techniques. Similar fluctuations have also been found in some self-assembled QDs [36]. They effectively quench ensemble fluorescence. Fluctuations were characterized by jumps between a defined high intensity level and the background (see Fig. 1.2). For a first description, dwell times at high (bright) and low (dark) intensity were examined. For molecules relatively short dark events of micro- and milliseconds showed exponential statistics and were assigned to the triplet state. In QDs such forbidden transitions like the triplet state could not quench fluorescence, as multiple excitations are possible. Dark states further neither exhibit exponential dwell time statistics nor are they limited to milliseconds. Instead, power law statistics were observed with dark periods t_{off} that could also last over several minutes [37, 38]. Later, power law statistics were also observed in the probability of bright periods t_{on} , albeit with an exponential cut-off at long times $\tau_{\text{cut-off}}$

$$p(t_{\text{off}}) \propto t_{\text{off}}^{-\alpha_{\text{off}}} \quad p(t_{\text{on}}) \propto t_{\text{on}}^{-\alpha_{\text{on}}} e^{-t_{\text{on}}/\tau_{\text{cut-off}}} \quad (1.1)$$

Similar long dark periods with the same statistics were even observed for proteins [39] and molecules [40–42] indicating a very fundamental single particle process. Power law characteristics of QD fluorescence were also detected on the microsecond and nanosecond scale [43–45]. Power law blinking is thus expected to extend over more than ten decades. These statistics with essentially unlimited dwell times in the dark state are highly extraordinary for a two-state transition. For QDs, the dark state was soon accepted as a charged QD, with all excitation energy being transferred to the extra charge instead of a photon [46]. Blinking is then the result of charging and neutralization due to electron or hole ejection and return. Long transition times result from the corresponding tunneling process. Power law statistics, however, could not easily be explained and brought about new models for possible underlying processes [47–49]. Those are mostly based on charging and neutralization via tunneling. They range from a distribution of traps over fluctuating tunneling distances and barriers to diffusing energy levels. Even great advances in blinking suppression [50] and the successful synthesis of non-blinking QDs [51, 52] did not solve the questions to the underlying mechanisms. Recently even the assignment of the off-state to a charged QD was challenged [53, 54].

The typical procedure to obtain dwell time statistics of bright (on) and dark (off) states is the application of a threshold to a recorded intensity time-trace as in Fig. 1.2. Intensities above the threshold are defined as on and below as off. The lengths of periods between threshold crossings are then analyzed in dwell time histograms showing linear slopes in log-log plots (see Fig. 1.2 b)). Problems with this method are the limited time resolution, the arbitrary choice of threshold and noise-induced threshold crossing. Several resulting artifacts like noise-induced cut-offs have already been identified [55, 56]. Also an apparently detected dynamic disorder for the enzyme α -chymotrypsin could be revealed as a thresholding artifact [57]. Especially for the extraction of such extraordinary statistics as the observed power laws, any influence of method deficiencies

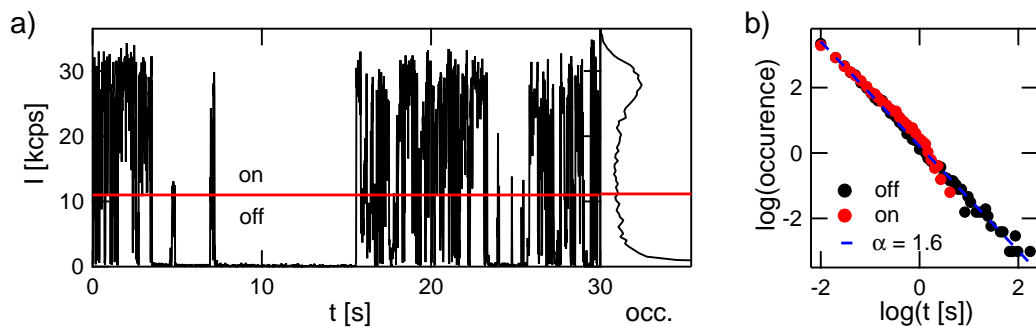


Figure 1.2: a) Intensity time-trace of a single CdSe/ZnS QD with the corresponding intensity histogram on the right. Switching between bright and dark periods is observed. A threshold (red line) separates on- from off-events. b) Histogram of durations of the corresponding on- and off-events. Both appear to follow an inverse power law with a cut-off in the on-events.

needs to be excluded. As all blinking models are based on power law dwell times, these statistics are crucial to the models' validity. Problems with the method performance on power law data have not been identified so far. A great part of experimentally extracted statistics has, however, not yet been tested, like differences between power law exponents or a time resolution far from shortest blink events. A verification of the method performance or an identification of its deficiencies for corresponding power law distributions is the first objective of this thesis. For its attainment intensity time-traces are simulated based on power law blinking and evaluated like in experiments. With a comparison of extracted and input dwell time distributions arising artifacts are identified.

Most blinking models are based on the fluctuation of charges in the QD environment. Those are suggested to lead to energy transfer, trap relaxation or influences of electric fields. Direct information on specifically charged QDs is thus required to relate it to the observed blinking phenomenon. The charged state of an object can be controlled with the application of a defined potential. The direct investigation of QD fluorescence at different potentials is thus a key step towards understanding fluorescence intermittency. Such an investigation is the second objective of this thesis. It is approached with the combination of electrochemistry and confocal microscopy to optically investigate specifically charged fluorophores on the single particle level.

Electrochemistry could already be successfully used to identify the conduction and valence band edge via electron injection and extraction, respectively [58–65]. Even defect states in the band gap could be accessed [60, 63]. During the course of this thesis, the idea of combining fluorescence spectroscopy and electrochemistry has also been followed by other groups [51, 66–78]. This allowed the determination of the negative trion lifetime [51, 71, 74–77] as well as the detection of quenching and enhancement at potentials in the QD band gap [66–68, 72, 78], typically assigned to the activation and passivation of electron traps. Two groups, those of Philippe Guyot-Sionnest [73–75, 77] and Victor Klimov [51, 76], also investigated the single particle level. They identified multiple charges also in single QDs [51, 75, 76] and different kinds of potential induced blinking mechanisms [76]. In addition to their observations also the influence of the electrode material and illumination itself are addressed here.

The manuscript is structured as follows: Chapter two describes the basic properties of QDs, their electronic structure and especially the observed fluorescence fluctuations and developed models to explain them. The third chapter is dedicated to the principles of electrochemical investigations especially at transparent semiconductor electrodes which are needed for the investigation of single particle fluorescence. In the fourth chapter the applied different methods for single particle fluorescence observation, charge injection and data analysis are described in more detail. Finally, chapters five and six comprise the results for the two approaches to the mechanisms of blinking. In chapter five results are presented to the analysis of simulated power law blinking with the threshold method. Here, the limited time resolution, differences between power law exponents and effects of noise are addressed in particular. Observations are further compared to experimental intensity traces of single QDs. Chapter six summarizes the results to the fluorescence of electrochemically charged QDs. Observations include voltage dependent intensity and excited state lifetime of thin ensembles as well as intensities of single particles. Ensemble emission spectra are included in the appendix. Investigations are compared on two different electrodes in the presence and absence of illumination. In chapter seven results and conclusions are summarized followed by an outlook to future perspectives.

2 Semiconductor Quantum Dots

The fundamental interest in the physics of nanoscale objects, like semiconductor quantum dots (QDs), is significantly fueled by the rapidly decreasing size of today's electronics. Once the size of a semiconductor enters the typical dimension of excited or injected charge carriers, those carriers will "feel" the boundaries, thus no longer move freely through the crystal. In bulk semiconductors continuous bands (dashed lines in Fig. 2.1 a)) describe the typically occupied (valence band, VB) and unoccupied (conduction band, CB) energy states of electrons. Their confinement to nanocrystals leads to a quantization of allowed kinetic energies (vertical lines), also known as *the quantum size effect*. This quantization also leads to discrete lines in the absorption and emission spectrum, which is one of the reasons why quantum dots are sometimes referred to as artificial atoms.

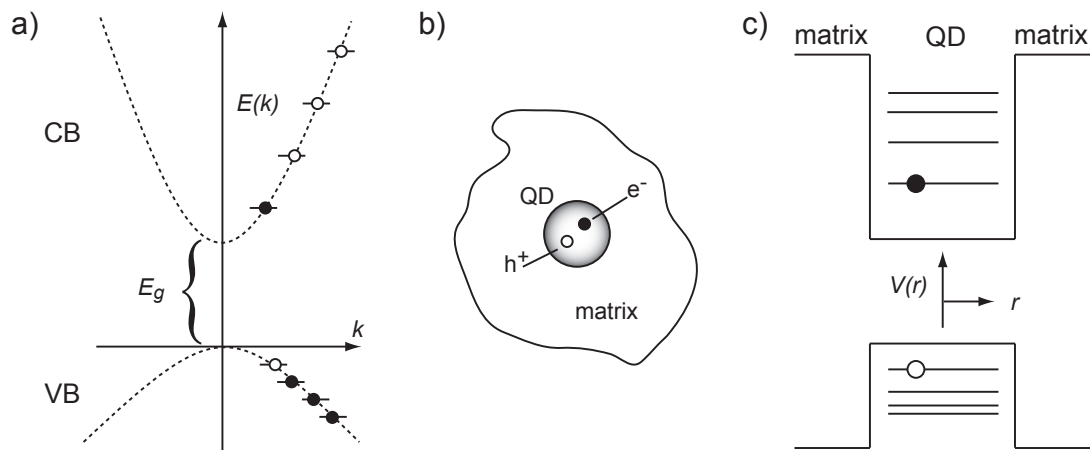


Figure 2.1: a) Schematic band diagram of a direct gap semiconductor with parabolic bands (dashed lines) close to conduction and valence band edges. The right side indicates the quantization of these bands once the semiconductor's dimensions confine electron and hole states. b) Simple model of a quantum dot as a small semiconductor sphere embedded in an insulating matrix. c) Typical energy diagram representation for quantum dots. Electron and hole states are quantized and confined to the QD radius.

2.1 Basic Properties of Quantum Dots

2.1.1 Confinement

The typical dimension of a quasiparticle (electron, hole or exciton) in a semiconductor is given by its Bohr radius

$$a_B = \varepsilon \frac{m_e}{m^*} a_0 \quad (2.1)$$

which differs from the Bohr radius of the hydrogen atom a_0 due to the non-zero dielectric constant of the crystal ε and the different effective mass m^* of the particle compared to the free electron mass m_e . The effective mass of the hole m_h^* is greater than that of the electron m_e^* . The exciton has the reduced mass $m_{\text{exc}}^* = \frac{m_e^* m_h^*}{m_e^* + m_h^*}$, thus $a_B^h < a_B^e < a_B^{\text{exc}}$. Depending on the size of the crystal R in relation to these Bohr radii three regimes are distinguished, where different approximations hold. In the regime of *strong confinement* electron and hole are each independently confined ($R < a_B^h, a_B^e, a_B^{\text{exc}}$). At *weak confinement* only the exciton as a whole is confined ($a_B^h, a_B^e < R < a_B^{\text{exc}}$) and at *intermediate confinement* the electron is confined but the hole is not ($a_B^h < R < a_B^e, a_B^{\text{exc}}$). When the confinement is *strong*, electron and hole are treated separately and their Coulomb attraction as a perturbation. If it is *weak*, the confinement itself can be treated as a perturbation to the Coulomb bound exciton. For the intermediate regime no such approximations hold, rendering calculations more complicated. The CdSe QDs examined in this thesis lie in the strong to intermediate confinement regime with an exciton Bohr radius of CdSe of ≈ 5 nm.

2.1.1.1 Particle-in-a-Box

In a colloidal quantum dot excited electrons and holes are confined to a semiconductor sphere, typically embedded in an insulating matrix (Fig. 2.1 b)). The effects of such spherical confinement on the wave function of a particle are best described in the particle-in-a-sphere model. This model considers a particle of mass m trapped in a spherical box of radius R with infinitely high barriers, thus a potential

$$V(r) = \begin{cases} 0 & r < R \\ \infty & r \geq R \end{cases} \quad (2.2)$$

Solutions to the Schrödinger equation of this problem

$$H\psi(\mathbf{r}) = \left[-\frac{\hbar^2}{2m} \nabla^2 + V(r) \right] \psi(\mathbf{r}) = E\psi(\mathbf{r}) \quad (2.3)$$

are found in textbooks of quantum mechanics [79] as wave functions of the form

$$\psi(r, \theta, \phi) = A_l j_l(kr) Y_{l,m}(\theta, \phi) \quad \text{with} \quad k = \sqrt{\frac{2mE}{\hbar^2}} \quad (2.4)$$

where A_l is a normalization constant, j_l the l^{th} order spherical Bessel function, and $Y_{l,m}$ a spherical harmonic. Infinite barriers at $r = R$ furthermore demand

$$j_l(kR) = 0 \quad \text{thus} \quad k = \frac{\chi_{n,l}}{R} \quad (2.5)$$

with $\chi_{n,l}$ the n^{th} zero of j_l . Eq. (2.4) describes ordinary atomic orbitals with eigenvalues

$$E_{n,l} = \frac{\hbar^2 k_{n,l}^2}{2m} = \frac{\hbar^2 \chi_{n,l}^2}{2mR^2} \quad (2.6)$$

These particle energies are quantized (see Fig. 2.1) and their orbitals characterized by the typical quantum numbers $n = 1, 2, 3 \dots$ (energy), $l = s, p, d \dots$ (angular momentum) and $|m_l| = 0, \dots, l$ (magnetic moment). The orbital of lowest energy, the 1S-state, is found at $n = 1, l = 0$ and $\chi_{1,0} = \pi$. A typical representation for a QD energy diagram is depicted in Fig. 2.1 c). Due to a higher effective mass the separation of energy states for the hole is smaller. Energies are strongly dependent on the confining radius ($E \propto R^{-2}$).

2.1.1.2 Confinement of Quasiparticles in a Semiconductor

The confinement of quasiparticles to a semiconductor nanocrystal is a more complicated problem. Even if barriers are assumed to be infinite, the potential inside the semiconductor is not zero, but determined by the lattice atoms. However, as long as the crystal radius R remains much larger than the lattice constant d , it can still be approximated as a bulk crystal. In bulk, Bloch's theorem states, that the Schrödinger equation (2.3) for a periodically varying potential $V(\mathbf{r}) = V(\mathbf{r} + \mathbf{d})$ can be solved by Bloch-wave functions

$$\Psi_{j,\mathbf{k}}(\mathbf{r}) = e^{i\mathbf{k}\mathbf{r}} u_{j,\mathbf{k}}(\mathbf{r}). \quad (2.7)$$

These are composed of a plane wave $e^{i\mathbf{k}\mathbf{r}}$ and a periodically varying function $u_{j,\mathbf{k}}(\mathbf{r}) = u_{j,\mathbf{k}}(\mathbf{r} + \mathbf{d})$ with the same periodicity as the potential $V(\mathbf{r})$. The wave vector \mathbf{k} is reduced to the first Brillouin zone and j is the index of different bands. These bands compose the band structure of the crystal. They are each characterized by a dispersion relation $E_j(\mathbf{k})$. Close to band minima or maxima the dispersion relation is approximated by parabolas (effective mass approximation). Thus, the band bending is constant and an effective mass

$$m^* = \hbar^2 \left(\frac{\partial^2}{\partial k^2} E_j(\mathbf{k}) \right)^{-1} \quad (2.8)$$

can be assigned to the particle. For a direct gap semiconductor, like CdSe, conduction band minimum and valence band maximum both lie at $k = 0$. Close to $k = 0$ their energies are then given by

$$E_{\text{CB}}(k) = \frac{\hbar^2 k^2}{2m_e^*} + E_g \quad E_{\text{VB}}(k) = -\frac{\hbar^2 k^2}{2m_h^*} \quad (2.9)$$

with respect to the valence band maximum. E_g is the energy gap between valence and conduction band. Thus, electrons in the conduction band and holes in the valence band behave like free particles with effective masses m_e^* and m_h^* , respectively.

For $R \gg d$ the volume of the nanocrystal is still approximated as bulk-like. Thus, wave functions of single particles confined to a spherical nanocrystal will be given by a superposition of these bulk solutions, the Bloch functions (2.7),

$$\Psi_p(\mathbf{r}) = \sum_k B_{jk} u_{jk}(\mathbf{r}) e^{i\mathbf{k}\mathbf{r}} \quad (2.10)$$

with coefficients B_{jk} chosen to satisfy the spherical boundary conditions. If a weak k -dependence of u_{jk} is assumed, it can be written

$$\Psi_p(\mathbf{r}) = u_{j0}(\mathbf{r}) \sum_k B_{jk} e^{i\mathbf{k}\mathbf{r}} = u_{j0}(\mathbf{r}) \psi_p(\mathbf{r}) \quad (2.11)$$

with the envelope function $\psi_p(\mathbf{r})$. The function u_{j0} can be approximated by a linear combination of atomic wave functions φ_a (linear combination of atomic orbitals, LCAO approximation)

$$u_{j0} = \sum_a C_{ja} \varphi_a(\mathbf{r} - \mathbf{r}_a). \quad (2.12)$$

Only the envelope $\psi_p(\mathbf{r})$ still needs to be determined. For spherically confined carriers, this envelope is exactly Eq. (2.4), the solution for particles in a spherical potential well.

2.1.1.3 Coulomb Interaction

The determined wave functions are valid for electrons and holes separately. When an exciton is examined, both carriers are involved and their Coulomb attraction affects their wave functions. The complete Hamiltonian for the envelope function is as follows

$$H = -\frac{\hbar^2 \nabla_e^2}{2m_e} - \frac{\hbar^2 \nabla_h^2}{2m_h} - \frac{e^2}{\varepsilon |\mathbf{r}_e - \mathbf{r}_h|} + V_e(\mathbf{r}_e) + V_h(\mathbf{r}_h) \quad (2.13)$$

with the dielectric constant of the semiconductor ε . The dependence on the distance between electron and hole $|\mathbf{r}_e - \mathbf{r}_h|$ breaks the symmetry of the problem and renders analytical solutions difficult. Good approximations can be made for the strong and the weak confinement regimes (see Sec. 2.1.1). The Coulomb interaction basically scales with $1/R$, while the confinement energy scales with $1/R^2$. In the strong confinement regime ($R \ll a_B$), thus for very small crystals, the quadratic confinement term dominates and electron and hole can be treated independently, while the Coulomb interaction is merely treated as perturbation. The energies in Eq. (2.6) are then corrected by the Coulomb binding energy E_C , so that the lowest excited state energy reads

$$E_{10} = \frac{\hbar^2 \pi^2}{2R^2} \left[\frac{1}{m_e} + \frac{1}{m_h} \right] - E_C. \quad (2.14)$$

E_C has been approximated with perturbation theory [80] and as a first order correction gives

$$E_C = \frac{1.8e^2}{4\pi\varepsilon_0\varepsilon R}. \quad (2.15)$$

For weak confinement ($R \gg a_B$) the exciton can be treated as a single particle-in-a-box while the confinement merely acts on its center-of-mass motion.

2.1.1.4 Optical Transitions

The probability P of an optical transition between the ground state $|0\rangle$ and an exciton state $|\Psi_{\text{exc}}\rangle$ is proportional to the square of the transition dipole moment

$$P \propto |\langle \Psi_{\text{exc}} | \hat{p} | 0 \rangle|^2 \quad (2.16)$$

with the dipole moment operator \hat{p} . For strong confinement, when electron and hole can be treated separately, this is described by the transition from a valence band (hole) state $|\Psi_h\rangle$ to a conduction band (electron) state $|\Psi_e\rangle$.

$$P \propto |\langle \Psi_e | \hat{p} | \Psi_h \rangle|^2 \quad (2.17)$$

The dipole moment operator \hat{p} only acts on the periodic functions $|u\rangle$ of the total wave function in Eq. (2.11) as the envelope functions $|\psi\rangle$ of electron and hole vary very slowly with \mathbf{r} . Eq. (2.17) can, thus, be simplified to

$$P \propto |\langle u_{\text{CB}} | \hat{p} | u_{\text{VB}} \rangle|^2 |\langle \Psi_e | \Psi_h \rangle|^2 \quad (2.18)$$

which for the orthonormal envelope functions given by the particle-in-a-sphere model (Eq. (2.4)) yields

$$P \propto |\langle u_{\text{CB}} | \hat{p} | u_{\text{VB}} \rangle|^2 \delta_{n_e, n_h} \delta_{l_e, l_h}. \quad (2.19)$$

This describes simple selection rules for allowed optical transitions, namely $\Delta n = 0$ and $\Delta l = 0$.

2.1.2 Band Structure of CdSe

When looking more closely, only the conduction band minimum is well-approximated by a parabola. It is composed of the Cd 5s orbitals with angular momentum $L = 0$, thus, simply 2-fold degenerate considering the electron spin $S = \pm \frac{1}{2}$. The valence band consists of the Se 4p orbitals with $L = 1$. Those are 6-fold degenerate due to spin and magnetic moment $m_L = 0, \pm 1$. The coupling of Spin \mathbf{S} and angular momentum \mathbf{L} (spin-orbit-coupling) leads to a band splitting dependent on the total angular momentum $\mathbf{J} = \mathbf{L} + \mathbf{S}$ ($J = \frac{1}{2}, \frac{3}{2}$). For zinc-blende and wurtzite type semiconductors, the band with $J = \frac{1}{2}$ ($m_J = \pm \frac{1}{2}$), called the split-off hole, is lowered in energy with respect to the band with $J = \frac{3}{2}$ ($m_J = \pm \frac{1}{2}, \pm \frac{3}{2}$), see Fig. 2.2 a). The top valence band ($J = \frac{3}{2}$) is further split for $k \neq 0$ depending on the projections of \mathbf{J} into heavy-hole ($m_J = \pm \frac{3}{2}$) and light-hole ($m_J = \pm \frac{1}{2}$). For diamond-like lattices, thus also for the zinc blende structure, this splitting of the 6-fold degenerate valence band into three subbands can be well-described by the Luttinger Hamiltonian [81, 82]. In wurtzite structures also the degeneracy at $k = 0$ is lifted due to the crystal field between Cd and Se ions (crystal field splitting).

2.1.2.1 Confinement in CdSe

Considering now the spherical confinement, one could expect three separate series of discrete hole states originating from each band according to the particle-in-a-box energies given in Eq. (2.6). However, the spherical confinement leads to a mixing of heavy and light hole bands as well as envelope confinement states of equal parity (L and $L+2$). The confinement angular momentum \mathbf{L} and the angular momentum of the lattice states \mathbf{J} are thus no longer conserved. Instead they couple to the total angular momentum $\mathbf{F} = \mathbf{L} + \mathbf{J}$. Only F ($m_F = 0, \dots, \pm F$) and parity remain as good quantum numbers. Resulting states can be denoted as

$$n(L, L+2)_F \quad \text{or} \quad nL_F \quad (2.20)$$

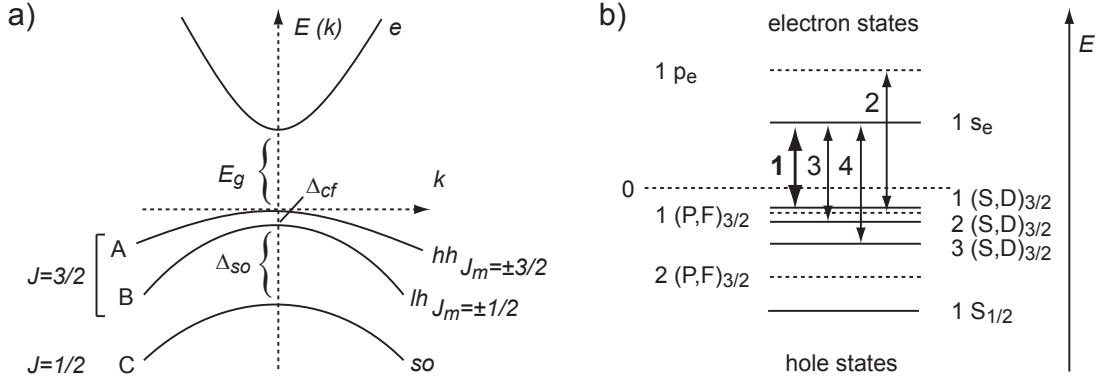


Figure 2.2: a) Schematic band structure of bulk CdSe. The valence band is split into three subbands according to their angular momentum J and its projections J_m on the crystal axis. Corresponding effective masses are $m_e^* = 0.11 m_e$, $m_{hh}^* = 1.14 m_e$, $m_{lh}^* = 0.31 m_e$, $m_{so}^* = 0.49 m_e$ [83]. Crystal field splitting and the separation of the split-off band amount to $\Delta_{cf} = 25 \text{ meV}$ and $\Delta_{so} = 0.42 \text{ eV}$ [24] with a CdSe band gap at room temperature of $E_g = 1.75 \text{ eV}$ [84]. b) Lowest allowed optical transitions in CdSe QDs according to [85]. States are labeled following Eq. (2.20).

where n is the counter of the confinement states of Eq. (2.6). The lowest hole state in energy, at the top of the valence band, is $1(S,D)_{3/2}$ or abbreviated $1S_{3/2}$. It contains three hole components leading to $F = \frac{3}{2}$: $(J = \frac{3}{2}, L = 0)$, $(J = \frac{3}{2}, L = 2)$, and $(J = \frac{1}{2}, L = 2)$ [83]. Allowed optical transitions between the mixed hole states and the lowest electron states nl_e are indicated in Fig. 2.2 b). Former selection rules, $\Delta n = 0$ and $\Delta L = 0$, no longer apply. Correspondingly, the lowest transition is $1S_{3/2}1s_e$. Absorption and emission spectra for CdSe/ZnS nanocrystal of four different core diameters are depicted in Fig. 1.1.

2.1.2.2 Fine Structure and the Dark Exciton

This lowest transition ($1S_{3/2}1s_e$) consisting predominantly of the $J = \frac{3}{2}$ valence subband and the $s = \frac{1}{2}$ conduction band is eightfold degenerate. Due to several effects the degeneracy will be lifted as depicted in Fig. 2.3 a). As already mentioned, in bulk the crystal field of the wurtzite structure lifts the degeneracy in two fourfold degenerate states corresponding to the projections of \mathbf{J} on the crystal axis, denoted as light hole ($J_m = \pm\frac{3}{2}$) and heavy hole ($J_m = \pm\frac{1}{2}$) (left of Fig. 2.3 a)). Also a non-spherical shape, typically slightly prolate for wurtzite quantum dots, induces a characteristic crystal axis and increases this splitting. For small quantum dots also the electron-hole exchange interaction can lead to a splitting of energy levels. While negligible in bulk, the spatial overlap of electron and hole wave functions is highly enhanced when the size is decreased. This leads to an additional coupling of the angular momenta of hole $F_h = \frac{3}{2}$ and electron $F_e = \frac{1}{2}$ to the total angular momentum $\mathbf{N} = \mathbf{F}_h + \mathbf{F}_e$. Only $N = 1, 2$ remains as good quantum number. As depicted on the right of Fig. 2.3 a), the fivefold degenerate state of $N = 2$ and the threefold degenerate state of $N = 1$ are further split dependent on their projections $|N_m|$ along the defined crystal axis of the wurtzite structure or prolate shape. They are labeled by $|N_m|$ with the subscript U (upper) or L

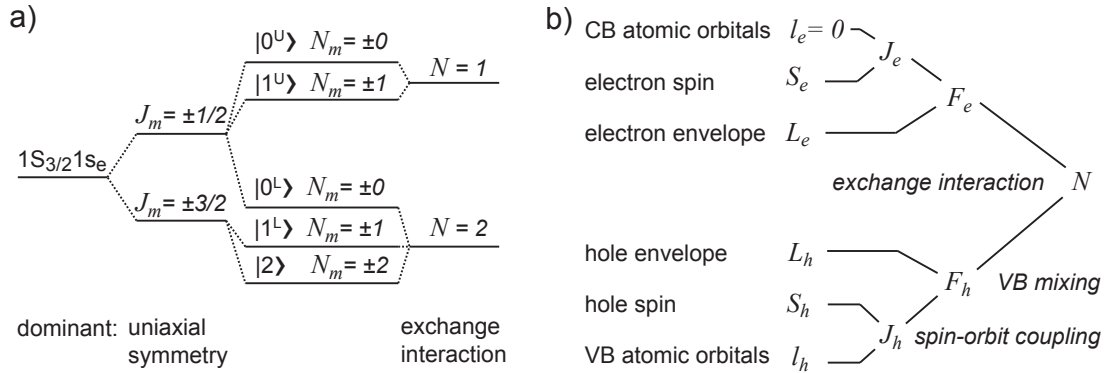


Figure 2.3: a) Lifting of the 8-fold degeneracy of the lowest exciton transition. In wurtzite bulk crystals (uniaxial symmetry) bands are split to heavy hole ($J = \frac{3}{2}$) and light hole ($J = \frac{1}{2}$). In QDs the degeneracy is further lifted depending on the projection of the total angular momentum N . The lowest transition $|2\rangle$ is optically forbidden. b) Summary of all introduced quantum numbers.

(lower) for equal $|N_m|$. A summary of all the discussed quantum numbers is given in Fig. 2.3 b).

Most interestingly, this fine structure reveals, that the transition from the lowest excited state $|2\rangle$ to the ground state is optically forbidden for a one-photon process. A single photon only supplies an angular momentum of $1\hbar$. The first allowed transition is $|1^L\rangle$. This fact explains the extraordinarily long lifetime close to a microsecond of the excited state at low temperatures. After excitation the exciton relaxes to its lowest energy level $|2\rangle$. From there no direct, but only slow phonon-assisted decay is possible. With increasing temperature a mixture with the $|1^L\rangle$ transition decreases the observed lifetime.

More details to theoretical descriptions of the basic properties of semiconductor quantum dots are summarized in Refs. [24] and [85].

2.1.3 Synthesis and Structural Properties

2.1.3.1 Synthesis

In comparison to epitaxially grown semiconductor nanocrystals, colloidal nanocrystals are easily and cheaply synthesized with hot-chemical methods. The procedure slightly varies from group to group and has been improved over the years. It is based on the method described by Murray et al. [25]. The basic routine is as follows: With a single injection a mixture of the precursors Me_2Cd (dimethyl cadmium) and TOPSe (trioctylphosphine selenide) in TOP (trioctylphosphine) is added to a TOPO (trioctylphosphine oxide) solution that was kept at 300°C . The temperature immediately drops to $\approx 180^\circ\text{C}$ and nucleation starts. Gradual heating to $230 - 260^\circ\text{C}$ initiates the growth-process. The changing size of the nanocrystals can be monitored with absorption spectra. This enables a growth control with adjustments in temperature. Temperature is lowered when sizes start to spread and increased when growth appears to stop. When the desired size is reached nanocrystals can be precipitated from the solution with methanol and redispersed in different desired unpolar solvents. Further

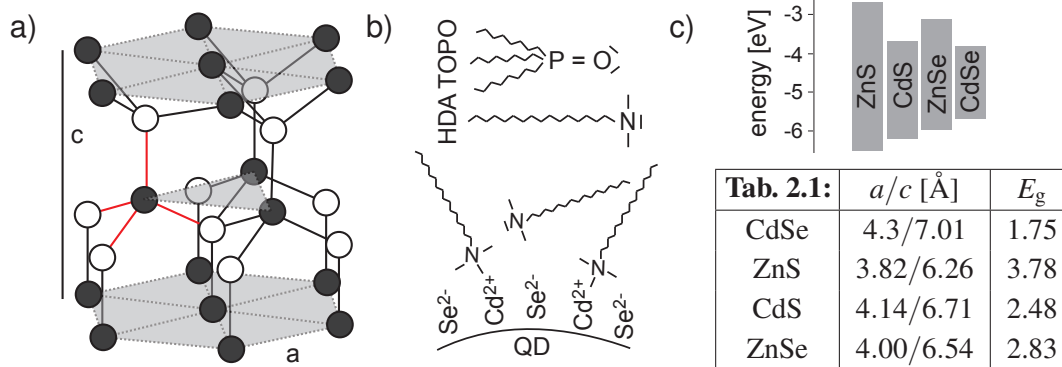


Figure 2.4: a) Wurtzite crystal structure as also observed for the CdSe QDs in the present work. Filled circles represent Cd and empty circles Se atoms. Lattice constants c and a are indicated. b) Chemical structure of TOPO and HDA ligands and their preferred binding to Cd^{2+} surface sites. c) Top: Bulk band alignments of different II-IV semiconductors taken from [86]. Tab.: Corresponding lattices parameters and band gap energies taken from [87].

centrifugation removes residual elemental Cd and Se. To avoid oxidation all solutions are constantly kept under Argon atmosphere. This procedure leads to a low size distribution with a standard deviation $< 5\%$ and a quantum yield of $\approx 10\%$. The obtained nanocrystals are slightly prolate with an aspect ratio of 1.1-1.3 and predominantly show a wurtzite lattice structure (see Fig. 2.4 a)).

With different types of ligands and depending on the initial monomer concentration also different shapes (rods, wires, tetrapods,...) can be synthesized [88–93]. This shape control is possible due to the differences in reactivity for the different facets of the crystal lattice and the ligand’s capability to passivate them [94–97]. Passivation of the surface also increases the quantum yield by eliminating surface traps and defects. The epitaxial growth of a shell around the CdSe nanocrystals with a material of wider band gap leads to even better chemical and electronic passivation. In the case of ZnS, as in the present thesis, the quantum yield increases to $\approx 50\%$, while both electron and hole are still confined to the CdSe core [26]. This type of core-shell QD is referred to as type I (see Fig. 2.5 a)). For shell growth a solution of dimethylzinc (Me_2Zn) and bis(trimethylsilyl)sulfide ($(TMS)_2S$) in TOP is injected in several portions to the freshly grown CdSe crystals at $\approx 300^\circ C$ before precipitation [26]. The growth of CdS or ZnSe shells instead of ZnS reduces strain-induced defects due to better matching lattice constants (see Tab. 2.1 in Fig. 2.4 c)). However, either electron (CdS) or hole (ZnSe) are only weakly confined by the shell, which is referred to as quasi-type II core-shell structure (see Fig. 2.5 c) and the bulk band gaps in Fig. 2.4 c)). Also multilayered nanocrystals [98–100] have been developed. In the last years alloyed QDs with a soft transition from core to shell material (see Fig. 2.5 d)) gained a lot of attention due to even higher, sometimes near-unity quantum yield [50, 101]. This has been argued to originate from reduced Auger efficiencies for soft potential changes (see Sec. 2.2.1.2).

2.1.3.2 Surface Passivation

Due to the high surface-to-volume ratio of semiconductor nanocrystals, defects and traps at the surface of the nanocrystals strongly influence their luminescence properties. Surface reconstruction and unpassivated dangling bonds lead to mid-gap energy

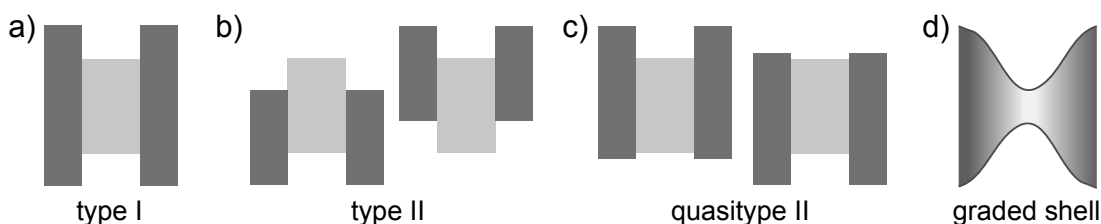


Figure 2.5: Different types of heterostructures for semiconductor nanocrystals depending on the confinement of electron and hole by the shell material. Type I structures indicate a confinement of electrons and holes in the QD core. For Type II heterostructures they are separated in core and shell. A quasi-type II structure indicates the presence of one carrier in both materials due to low potential barriers. Type I CdSe/ZnS QDs (see Fig. 2.4 c)) are used in this thesis. Commonly studied quasi-type II QDs are CdSe/CdS and CdSe/ZnSe.

states and non-radiative decay channels that quench QD fluorescence. For core-only crystals also a red-shifted emission band is observed [26] ascribed to emission from surface traps. The ligand TOPO (Fig. 2.4 b)) of the solution can partially passivate the surface, preferably binding to the Cd sites of CdSe [102] with a coordinate bond. Especially the oxidation of unpassivated selenium atoms leads to an increasing degradation when exposed to air. Se atoms are better passivated by TOP ligands [103], while HDA-ligands (see Fig. 2.4 b)) could be shown to further improve the passivation of Cd [104]. Long-chain primary amines like HDA are found to very efficiently passivate the QD surface as compared to other Lewis bases (electron pair donating species) and other ligands [105]. HDA ligands are also passivating the QDs used in this thesis. The passivation with a shell of wider band gap material not only increases the quantum yield but also eliminates the red-shifted trap emission band [26]. Due to a certain leakage of the wave function into the shell, a small red shift of the band edge emission is observed upon shell growth [26]. This leakage also enables luminescence quenching by surface defects and traps at the shell surface. The ZnS shell is equally passivated by ligands to reduce quenching. As for the CdSe core, it was found that a higher cation (thus Cd or Zn) concentration at the surfaces increases the quantum yield as compared to an anion excess of S [27]. This is rationalized with a better passivation of the cation by most ligands. Apart from certain examples (e. g. oleic acid) most ligands, like HDA and TOPO, are not tightly bound to the surface but randomly adsorb and desorb from the QD surface [106]. This can be very important for the synthesis process. It, however, also leads to an increasing desorption of ligands from the surface upon dilution [105, 107]. An equilibrium is obtained between free and adsorbed ligands. Accordingly, the passivation decreases and with it the quantum yield. Strong luminescence enhancement has been reported for β -mercaptoethanol [31, 108] or propyl gallate ligands [33]. It was observed to result from near complete suppression of blinking (see Sec. 2.2.2) and enhancements in the radiative decay rate.

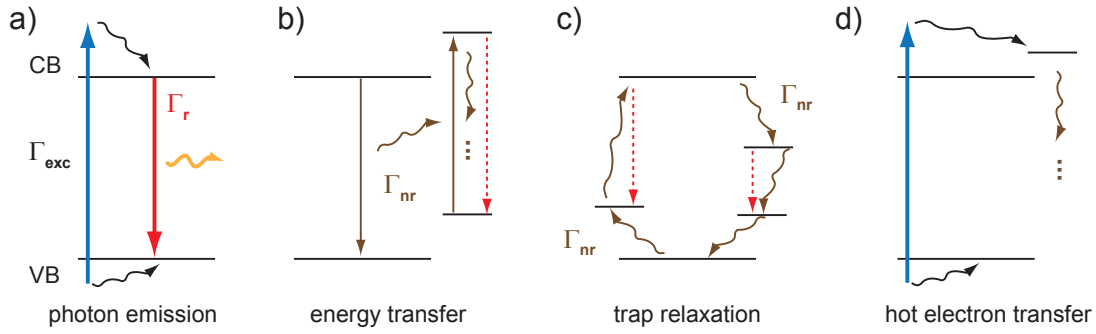


Figure 2.6: a) Excitation and radiative relaxation of an electron hole pair in a QD. b)-d) Different non-radiative decay pathways (brown and wavy lines) after excitation. Some decay paths can involve radiative relaxation (red dashed lines) of lower energy than the QD band edge transition. Hot-carrier relaxation in d) does not effect the excited state decay time.

2.2 Optical Properties of Colloidal Quantum Dots

2.2.1 Radiative and Non-Radiative Decay Pathways

In a semiconductor quantum dot, an electron can be excited by lifting it from the valence to the conduction band, as depicted in blue in Fig. 2.6 a). High above the band edge, a continuum of states allows the excitation with any energy above the band gap energy E_g . After excitation electron and hole quickly relax to the lowest excited state. From this lowest excited state, radiative decay of the exciton is possible as indicated in red. This radiative decay generally is not the only possible decay mechanism of the exciton. It can also decay non-radiatively (brown lines), either by a transfer of the band gap energy to a nearby acceptor (e. g. Förster resonance energy transfer [109]) b) or by a decay of electron or hole via accessible states in the band gap c). When radiative decay from the band edge is observed, the excited state decay time τ_{eff} is given by the radiative Γ_r and all non-radiative Γ_{nr} decay rates.

$$\tau_{\text{eff}} = \frac{1}{\Gamma_r + \Gamma_{\text{nr}}} \quad \Gamma_r = \frac{1}{\tau_r} \quad \Gamma_{\text{nr}} = \frac{1}{\tau_{\text{nr}}} \quad (2.21)$$

Thus, any changes of τ_{eff} result from changes in Γ_r or Γ_{nr} . For a given absorption rate, the emission intensity is proportional to the quantum yield QY, which is defined as the probability of radiative decay. Without a participation of hot carrier traps (see below), it is directly linked to τ_{eff} via

$$I \propto \text{QY} = \frac{\Gamma_r}{\Gamma_r + \Gamma_{\text{nr}}} = \Gamma_r \cdot \tau_{\text{eff}} = 1 - \Gamma_{\text{nr}} \cdot \tau_{\text{eff}} \quad (2.22)$$

Fluctuations of only non-radiative or only radiative decay rate thus lead to positive or negative proportionality between intensity I and excited state decay time τ_{eff} . In QDs both rates are observed to show fluctuations. Without the presence of non-radiative decay the quantum yield is 1. Thus, fluctuations in Γ_r will lead to different lifetimes without a change in intensity. With the excitation of states high above the band edge also the direct transfer of the excited electron or hole to a trap state can be possible, see

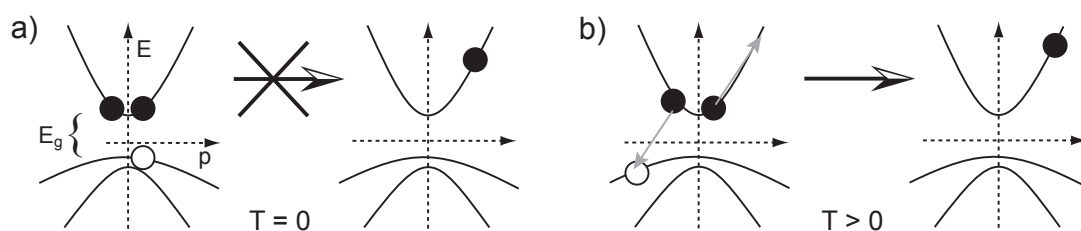


Figure 2.7: Auger relaxation in bulk CdSe. Due to momentum conservation Auger relaxation is not allowed from the ground state at low temperature a), but only from excited electron and hole at high temperature b).

Fig. 2.6 d). This can charge the QD if the electron remains in the trap. If it recombines with the hole before the next excitation, such a hot carrier transfer reduces fluorescence intensity without a corresponding decrease of τ_{eff} . Only the population of the excited state is reduced.

Energy transfer and trap relaxation can also lead to radiative decay from the excited acceptor or between different trap states and the band edges (red dashed lines) in b) and c). This is exploited when doping QDs e. g. with copper (Cu^{2+}) or manganese (Mn^{2+}) impurities [66, 67, 72]. Trap emission is also observed in core-only QDs as an emission band red-shifted from the band edge emission, as discussed before.

2.2.1.1 Trap Relaxation

States to trap electrons or holes from the conduction or valence band have to lie within the QD band gap. Localized trap states can result from imperfections in the crystal lattice such as lattice vacancies or impurities. They are, however, mostly expected at the CdSe/ZnS interface, the ZnS surface or in the surrounding matrix. They arise due to lattice mismatch induced strain, surface reconstruction and dangling bonds or self-trapping of carriers in the matrix. Several surface defects in the band gap have been assigned with electrochemistry for CdSe core-only QDs [60]. Unpassivated Zn^{2+} and S^{2-} sites at the surface are discussed to act as electron or hole traps, respectively. A loss of ligands, e. g. upon dilution [107], is observed to decrease the quantum yield. Due to its lower effective mass (see. Fig. 2.2), the electron's wave function shows a higher overlap with surface sites. This increases electron transfer probabilities. Thus, electron trapping is often assumed to be more likely than hole trapping. However, HDA ligands primarily passivate Zn^{2+} sites (see Sec. 2.1.3.2), leaving S^{2-} largely unpassivated. A higher hole trap density can thus be expected to increase hole trapping probabilities. Whether electron or hole ejection is more likely remains an ongoing discussion [32, 49, 66, 72, 75, 76, 110]. Also trap states in the surrounding matrix could be accessed. Here the polarization of the matrix due to the presence of a charge can stabilize and thus trap ejected charges, also referred to as self-trapping [32].

2.2.1.2 Auger Processes

An Auger process is a non-radiative relaxation of an excited charge carrier via energy transfer to another charge carrier due to Coulomb interaction. Like for any process, momentum and energy of the initial state need to be conserved in the final state. For an

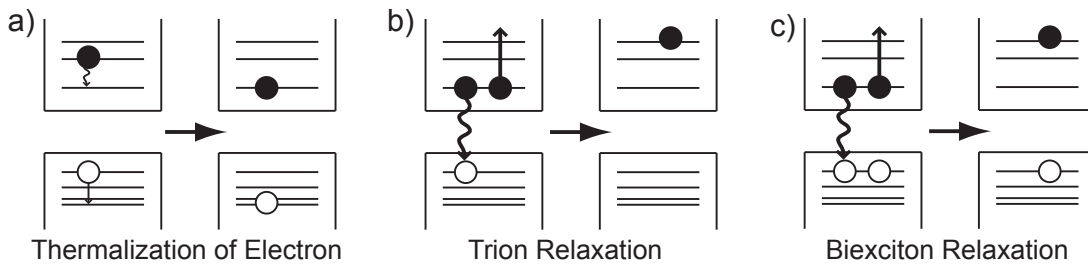


Figure 2.8: Three possible Auger relaxation processes in a semiconductor quantum dots.

exciton in a bulk semiconductor, this means that Auger relaxation (without additional participation of phonons) is not possible from the ground state [24]. This is illustrated in Fig. 2.7 a). In an Auger relaxation of the exciton, an additional charge carrier receives the band gap energy E_g , which corresponds to a high translational momentum. This process is only possible from excited carriers possessing this momentum, as illustrated in b). The Auger process is, thus, a thermally activated process. It is exponentially dependent on the energy gap $\propto e^{-E_g/k_B T}$ and highly unlikely for CdSe at room temperature. For 3D confinement with abrupt heteroboundaries these constraints for Auger recombination are expected to be relaxed [24, 111–113]. The discrete energy states are no longer described by translational but angular momentum (F or N , see Sec. 2.1.2). Angular momentum and energy are not directly related. Angular momentum conservation is, thus, a much lower and temperature independent restriction. Matching angular momenta to band gap energies can easily be found in the continuum of high energetic states. This and the strong interaction of particles in a small volume, renders Auger processes extremely efficient even at low temperatures. Several possible Auger recombination pathways in a QD are plotted in Fig. 2.8. Not only excitons can relax in an Auger process in the presence of an additional charge carrier, as shown in b). Also the relaxation of an excited electron to the ground state is facilitated by energy transfer to the hole. The separation of the lowest energy states of the electron is generally too high to fit the energy of phonons. This is referred to as phonon bottleneck. Energy level spacing of the hole is much closer due to its higher effective mass. Energy transfer to the hole, thus, leads to the observed fast relaxation to the ground state [114–117]. Evidence of the phonon bottleneck has been found in a slow decay component for QDs with unpassivated surface [116]. It is argued that hole trapping at the surface renders the hole unavailable for energy transfer from the electron. In quantum dots with abrupt heteroboundaries Auger relaxation of excitons is orders of magnitude faster (at the timescale of picoseconds [114, 117]) than radiative recombination (typically around 10 ns). Radiative relaxation of charged QDs or higher order excitons is thus strongly quenched. This is visible in decreased lifetime and quantum yield for multiexcitons [118]. Calculations to Auger rates show, that Auger processes can be highly suppressed, when the transition from core to bulk is not abrupt, but smooth, e. g. parabolic [119] (also see Fig. 2.5 d)). Recently the synthesis of QDs with alloyed shell was possible, which are expected to possess a smoother boundary between core and shell. Alloyed QDs indeed showed a strong suppression of Auger processes [50, 52, 101, 120] as detected in high quantum yields of charged and multiexcitons.

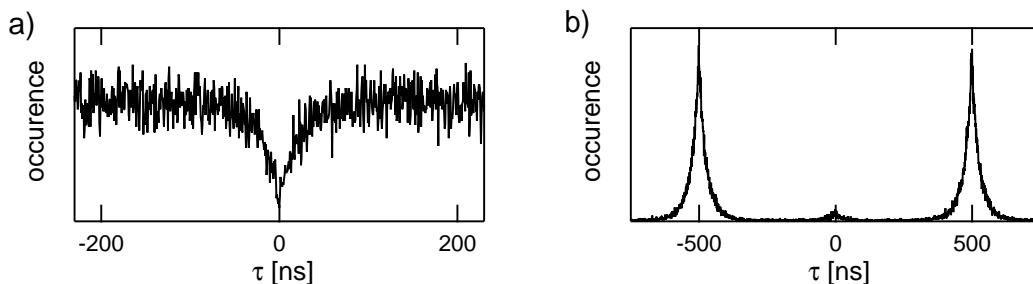


Figure 2.9: Histograms of time delays between consecutive photons emitted by a single CdSe/ZnS QD ($\lambda_{\text{em}} = 600\text{nm}$). Measurements are performed with a Hanbury-Brown-Twiss Setup [126] at a) continuous wave b) pulsed excitation. The dip in a) and the strongly reduced peak in b) at zero time delay indicate close to zero probability of simultaneous emission of two photons.

Photon Statistics The high efficiency of Auger processes in QDs leads to a strong quenching of radiative multiexcitonic relaxation. Thus, photons will only be observed from the last remaining exciton after non-radiative decay of all multiexcitons. This means that emission is only possible for one photon at a time. Before the emission of the next photon, the QD needs to be reexcited. This non-classical light emission, referred to as antibunching, has prior been observed for atoms [121], ions [122] and molecules [123, 124] and is characteristic for any two-level system. A method to quantify the single photon emission, or multi-photon suppression, of light is the second order intensity correlation function

$$G^{(2)}(\tau) = \frac{\langle I(t)I(t+\tau) \rangle}{\langle I(t) \rangle^2} \quad (2.23)$$

Considering single photons, it gives the probability to find a photon at time $t + \tau$ after detecting one at time t . Photons in coherent light (laser light) are Poisson distributed and show no correlation,. Photon antibunching will lead to a minimum at time $\tau = 0$. Classical light sources like thermal light, show intensity fluctuations and thus a maximum at $\tau = 0$. In measurements it is possible to measure the time delay between consecutive photons, which at low excitation is proportional to $G^{(2)}(\tau)$. An exemplary measurement on a single CdSe/ZnS QD ($\lambda_{\text{em}} = 606\text{nm}$) is displayed in Fig. 2.9 and was first measured for single QDs by Michler et al. [125]. The value at $\tau = 0$ can also be used as a confirmation of measuring a single emitter as two uncorrelated single emitters show $G^{(2)}(0) \geq 0.5$. Due to this intrinsic suppression of multiple photons and the possibility of pulsed excitation (see Fig. 2.9 b)), QDs are considered as potential single photon sources for quantum information [15, 16].

2.2.1.3 Quenching on Conducting Surfaces

Close to a metal surface the radiative rate of any emitter is observed to oscillate with the distance d , when d is comparable to the emission wavelength λ . At even closer distances $d < 50\text{nm}$ fluorescence is strongly quenched. These observations can well be described by the classical theory of an oscillating point dipole interacting with a medium of frequency-dependent dielectric constant $\epsilon(\omega)$ [127–130]. The oscillation

of the radiative rate results from an interference of the directly radiated emission with its reflection from the interface. Quenching at smaller distances results from energy transfer from the dipole to the metal. Energy can be transferred to surface plasmons or at even closer distances to electronic charge density oscillations, so-called “lossy surface waves”, that dissipate through scattering in the lattice (e. g. electron-hole excitations). The ratio of the energy transfer rate Γ_{ET} to the radiative rate Γ_r of such a dipole $b_{ET} = \Gamma_{ET}/\Gamma_r$ is given by [73, 127]

$$b_{ET} = \frac{\theta}{4\left(\frac{2\pi n_1}{\lambda}d\right)^3} \text{Im}\left(\frac{\varepsilon_2 - \varepsilon_1}{\varepsilon_2 + \varepsilon_1}\right) \quad (2.24)$$

with ε_1 and n_1 relative dielectric constant and refractive index of the surrounding medium, ε_2 the relative dielectric constant of the metal and λ the emission wavelength. The orientational factor θ is $\frac{3}{2}$, $\frac{3}{4}$ or 1 for perpendicular, parallel and isotropic dipole configurations, respectively.

At very small distances fluorescence close to a conducting interface can also be quenched due to electron transfer to or from the fluorophore. Such a transfer demands for a suitable alignment of energy levels. When charge transfer to and from the QD is strongly limited by the potential barriers of the ZnS shell and passivating ligands, electrons need to tunnel. The tunneling rate from an initial state i of energy E_i to a final state f at E_f is given by Fermi’s golden rule

$$k_T = \frac{2\pi}{\hbar} |T_{if}|^2 \delta(E_i - E_f) \quad (2.25)$$

with the transition matrix element T_{if} and the Dirac delta function δ . The transition matrix element T_{if} depends on the leakage of the wave function at energy $E_i = E_f$ through the tunnel barrier. As a first approximation of a simple one-dimensional rectangular potential barrier of height V_B and width d it shows a leakage of [79]

$$\psi \propto e^{-\kappa d} \quad \kappa = \sqrt{\frac{2m}{\hbar^2}(V_B - E)} \quad (2.26)$$

and a transmission probability of

$$p = \left[1 + \frac{V_B^2}{4E(V_B - E)} \sinh^2(\kappa d)\right]^{-1} \propto e^{-2\kappa d} \quad \text{for } p \ll 1 \quad (2.27)$$

It thus shows an exponential dependence on the separation between fluorophore and electrode and will only be observed within a few nanometers of the electrode surface.

2.2.2 Fluorescence Intermittency

The probably most intriguing fluorescence characteristic of all quantum emitters [47, 48], also molecules [40–42, 131, 132], proteins [133], quantum dots [35, 37, 38, 48, 134–137], nanorods [138] or nanowires [139], could be revealed with single particle microscopy. When monitoring the fluorescence of single emitters under continuous illumination, it was found, that they do not continuously emit. Instead, their fluorescence

randomly turns off and on (see Fig. 1.2), they blink between high and background intensity, with off-times up to many minutes. The statistics of the blinking process add another puzzling feature. When a threshold is placed in a time-trace to separate on-from off-events, the dwell times in either state are not exponentially distributed nor limited to timescales of μs or ms (see Fig. 1.2 b)). Both, however, would be expected for a switching between two well-defined quantum mechanical states. Instead they show inverse power law characteristics. Especially durations of off-events t_{off} have been extensively studied to follow a robust power law of

$$p_{\text{off}}(t_{\text{off}}) \propto t_{\text{off}}^{-\alpha_{\text{off}}} \quad (2.28)$$

with $1.1 < \alpha_{\text{off}} < 2.2$ [47, 48, 140] for at least six decades in time and dwell times lasting over more than one minute [37, 38]. The exponent α_{off} is found to be independent of temperature or excitation [38, 134, 135, 141–143], but decrease with the dielectric constant of the surrounding medium [32] and increase with size [144]. The on-events t_{on} turn out to be less robust. They also show a power law distribution but with an exponential cut-off $\tau_{\text{cut-off}}$ for long times

$$p_{\text{on}}(t_{\text{on}}) \propto t_{\text{on}}^{-\alpha_{\text{on}}} e^{-t_{\text{on}}/\tau_{\text{cut-off}}} \quad (2.29)$$

This cut-off shifts to shorter times with temperature and excitation [38, 135, 142, 143, 145] and without a capping shell [38, 43]. It often reduces the initial power law to less than two decades. Also α_{on} is determined to lie in the same range of exponents, often very close or equal to the value of α_{off} . An exponent between 1 and 2 implies, that no average dwell time can be found for the dwell time distribution. The average on/off-time will increase with the measurement time t_{max} and decrease with the bin time t_{bin} of an experiment.

$$t_{\text{avg}} = \frac{\int_{t_{\text{bin}}}^{t_{\text{max}}} t \cdot t^{-\alpha}}{\int_{t_{\text{bin}}}^{t_{\text{max}}} t^{-\alpha}} = \frac{1 - \alpha}{2 - \alpha} \cdot \frac{t_{\text{max}}^{2-\alpha} - t_{\text{bin}}^{2-\alpha}}{t_{\text{max}}^{1-\alpha} - t_{\text{bin}}^{1-\alpha}} \rightarrow \frac{\alpha - 1}{2 - \alpha} \cdot \frac{t_{\text{max}}^{2-\alpha}}{t_{\text{bin}}^{1-\alpha}} \quad (2.30)$$

for $t_{\text{bin}} \rightarrow 0$, $t_{\text{max}} \rightarrow \infty$ if $1 < \alpha < 2$. For long times, the on-state cut-off leads to a convergence of the average on-time for $t_{\text{max}} \rightarrow \infty$. At short times, power law statistics are observed to reach down to the microsecond or even nanosecond scale [43–45].

This blinking behavior is also responsible for a reversible fluorescence decrease of QD-ensembles under illumination. The decrease results from the on-state cut-off and thus the shorter average dwell time of the QD in the on-state. Especially due to this photoinduced cut-off,¹ the probability to find a QD in the off-state increases during illumination, which lowers the ensemble luminescence. In the dark, the on-state is recovered. A switch to the off-state appears to only proceed from the excited state under illumination. A switch to the bright state also proceeds in the dark. Bawendi et al. [136] found that the reversible decrease of ensemble luminescence saturates at $\approx 3900\text{s}$. This indicates the existence of an off-state cut-off as well, however, at much longer times than accessed in single QD experiments. In contrast to this reversible bleaching, irreversible bleaching is attributed to a partial photooxidation of the CdSe core. In single QDs this irreversible bleaching is often accompanied by a luminescence blue shift [146, 147], in agreement with a stronger confinement of the exciton.

¹Ensemble fluorescence would also decrease for a higher on-state exponent.

nature of the off-state It was soon postulated that the dark state of a QD could be a charged QD, with an additional electron or hole residing in the core [46]. Very efficient Auger processes (see 2.2.1.2) lead to a strong quenching of the charged QD's fluorescence. Blinking can then be interpreted as charging and neutralization of the QD, thus, the escape and return of an electron or hole from or to the QD core, respectively. Indeed, electrostatic force microscopy could show a single positive charge developing on a significant fraction of QDs under illumination [148, 149]. Even blinking of this charge was found on a small percentage of QDs. While most models are based on this assumption of QD charging, two years ago, two groups [53, 54] separately discovered off-states, that cannot result from Auger quenching of a single charge. Zhao et al. [53] investigated larger QDs with reduced Auger rates. They found that the quantum yield of the off-state can be 10 times lower than that of the biexciton. As the biexciton suffers from Auger quenching of electron and hole, its quantum yield should be significantly lower than that of a singly charged QD (see 2.2.1.2). Additionally, multiexcitonic (MX) fluorescence from the electronic 1P state could be spectrally and temporally separated. They observed on-off intensity ratios > 10 for the MX, which should be < 4 , when simply due to a single additional charge. Rosen et al. [54] investigated the excitonic decay rate of the off-state. They found an excitation dependence and a size-independence, both contradicting expectations from the one-charge-quenching scenario. Suggested alternatives for the off-state are a multiply charged state, with more efficient Auger quenching, or an efficient non-radiative decay involving trap states. Very recently Cohn et al. [150] found trap-assisted Auger decay in ZnO nanocrystals to be very efficient and surprisingly weakly dependent on QD-size. They argue that such an assisted Auger process of a trion should be efficient enough to completely quench QD luminescence and thus might be responsible for the off-state.

Based on blinking statistics and assumptions to the nature of the two states different models were developed. Due to early postulations, most of them treat the off-state as a charged state. However, with certain adjustments they can maintain their validity also for different quenching mechanisms, e. g. multiple charging or trap-assisted decay as described in Ref. [150]. In each of them, the focus is laid on the generation of power law statistics. The simple model of ionization and neutralization due to a defined trap state [46] only leads to exponential distributions of on- and off-states. The most popular models producing power law statistics are described in the following.

2.2.2.1 Blinking Models

The Static Trap Model The static trap model is an easy model to obtain power law statistics at least for one state, the off-state, which is expected to be a charged QD. A uniform and static distribution of traps around the spherical core of the QD is assumed to be present at energy V_T , where V_T lies in the band gap (see Fig. 2.10a)). The probability of an excited charge carrier to tunnel to one of those traps at distance r is proportional to the exponential leakage of the wave function into the environment and the number of available traps at r . The leakage decays as $|\Psi|^2 \propto e^{-\kappa_1 r}/r^2$ with the decay length $\kappa_1 = \sqrt{2m^*\Delta V_1}/\hbar$ given by the carrier mass m^* and the tunneling barrier ΔV_1 [79]. Due to the lower effective mass of the electron, its wave function extends

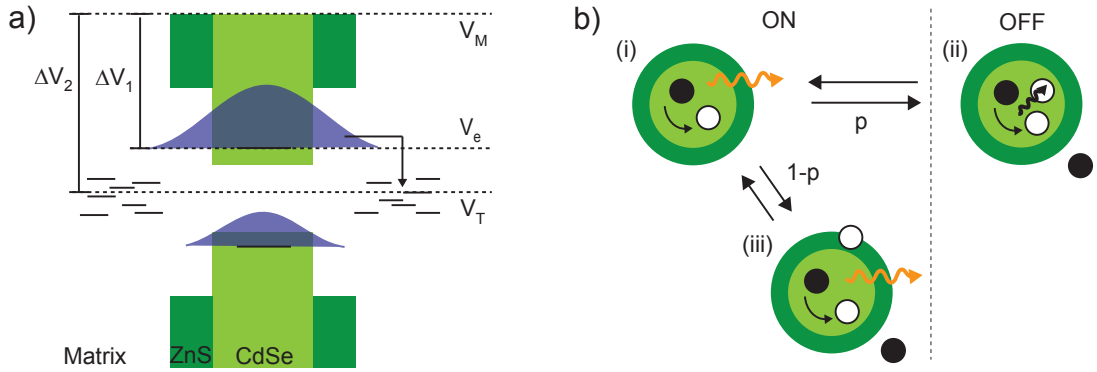


Figure 2.10: Illustration of the static trap model for electron tunneling. a) Potentials involved in electron trapping: potential of the excited electron V_e , the matrix V_M and traps V_T . b) Involved bright and dark states leading to power law distributions for on- and off-states: (i) neutral bright QD, (ii) charged dark QD, charge in the core leads to completely quenched luminescence, (iii) charged bright QD, charge trapped away from the core allows radiative decay. After electron ejection from (i) the hole remains in the core with probability p (ii) and is trapped with $1 - p$ (iii).

much deeper into the environment. At equal trap density, electron tunneling is thus more likely. For a uniform distribution of trap states, the number of available traps at distance r scales with the area r^2 . Thus, the probability of trapping a charge at radius r is given by

$$p_t(r) = \kappa_1 e^{-\kappa_1 r} \quad (2.31)$$

The back tunneling probability also decays exponentially but with a different tunneling barrier ΔV_2 , thus a different decay length $\kappa_2 = \sqrt{2m^* \Delta V_2} / \hbar$. The decay time from the charge separated state back to the core will thus be given by

$$t = t_0 e^{\kappa_2 r} \quad (2.32)$$

Performing a change of variables from r to t

$$r = \frac{1}{\kappa_2} \ln \frac{t}{t_0} \quad dr = \frac{1}{\kappa_2 t_0} \left(\frac{t}{t_0} \right)^{-1} dt \quad (2.33)$$

in Eq. (2.31), we obtain the probability distribution of off-state dwell times

$$p(t) = \frac{\kappa_1}{\kappa_2 t_0} \left(\frac{t}{t_0} \right)^{-(1 + \frac{\kappa_1}{\kappa_2})} \propto t^{-(1 + \mu)} \quad (2.34)$$

which follows a power law. The exponent naturally lies between 1 and 2 as

$$\mu = \frac{\kappa_1}{\kappa_2} = \sqrt{\frac{\Delta V_1}{\Delta V_2}} = \sqrt{\frac{V_M - V_e}{V_M - V_T}} < 1 \quad (2.35)$$

with V_M , V_e , and V_T the potential energies of matrix, QD excited state and trap, respectively. Thus, the experimentally observed off-state distribution is easily obtained. Also the independence from temperature is understood, due to the tunneling process.

A continuous distribution of traps can arise from carrier self-trapping in the surrounding matrix. Here V_T is expected to decrease with increasing dielectric constant of the environment ϵ , leading to a decreasing exponent. This could indeed be observed by Isaac et al [32], however, without quantitative agreement. In addition, the on-state dwell times would simply be exponentially distributed for static traps. The charge ejection rate Γ_{on} is simply given by the sum of all decay rates to all available trap states.

Verberk et al. [43] extended this model to explain also the on-state power law, outlined in Fig. 2.10 b). Next to the bright neutral state (i) and the dark charged state (ii) with one charge in the core, they included a third state (iii) in the model. This additional state is a long lived bright state, characterized by a charged but luminescent QD. This is possible if the remaining charge upon ionization is not located in the core, triggering highly efficient Auger processes, but in the close vicinity. In the vicinity, Auger processes can be strongly inhibited. The trapped charge is still assumed to prevent further charging by Coulomb blockade. Upon ionization, e. g. electron ejection, the hole will then either remain in the core with probability p and lead to an off-state. Or, it will immediately be trapped in the shell with probability $1 - p$, leaving the QD bright. The neutral state (i) of the QD is expected to be very short-lived and usually not resolved. Following these assumptions, the exponents for on- and off-states are predicted to be very similar. Certain differences are still explained by influences of the trapped charge on the potentials. This extended model can also explain spectral diffusion (see Sec. 2.2.3.2) and the continuous distribution of intensity states (see Sec. 2.2.3.1).

Diffusion Models In contrast to static traps, Shimizu et al. [38] introduced a dynamic model of a dark trap state, diffusing in energy. Each time it shifts into resonance with the QD excited state, the QD turns from bright to dark or dark to bright due to ejection or return of a charge carrier. This simple random-walk-first-passage-time model [151] directly yields the exponent 1.5 for diffusion in one dimension (energy). It can also explain the lack of temperature dependence. While the shortest time-scale for diffusion is expected to change with temperature, the statistics will not. The cut-off in the on-state is described by a separate process, e. g. Auger ionization. For this process temperature and excitation as well as the ionization energy start to play a role.

Tang and Marcus [152–154] developed a similar dynamic model referred to as **diffusion-controlled electron-transfer (DCET)**. It is based on Marcus theory² for electron transfer reactions [155], which takes into account the involved solvent relaxation processes for a changing charge configurations. When solvent relaxation is fast, it typically describes transfer reactions by a single transfer rate $\Gamma_T \propto e^{-E_A/k_B T}$. The activation energy E_A can then be determined. For electron transfer from a QD to a trap state reorganization of the environment (e.g. a polymer matrix) is much slower. The situation is thus described by the short time limit of Marcus theory.

Four states are defined, the ground $|G\rangle$ and the excited $|L^*\rangle$ light state and the ground $|D\rangle$ and the excited $|D^*\rangle$ dark state, see Fig. 2.11 a). The light state represents the neutral QD with only radiative decay γ_{em} . The dark state is described as the charge-separated QD which is governed by non-radiative Auger decay γ_A . With a certain

²In 1992 R. A. Marcus received the Nobel Prize in Chemistry for this theory.

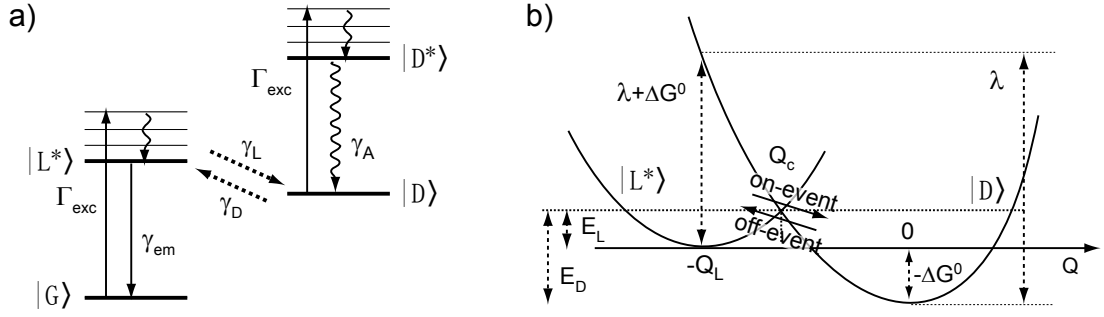


Figure 2.11: a) Schematic diagram of the four involved states in the DCET model: ground $|G\rangle$ and excited $|L^*\rangle$ light state and ground $|D\rangle$ and excited $|D^*\rangle$ dark state. Transfer between $|L^*\rangle$ and $|D\rangle$ proceeds with rates γ_L and γ_D , respectively. The QD is excited with Γ_{exc} and decays radiatively with γ_{em} in the light state and non-radiatively with γ_A in the dark state. b) Diffusion along the reaction coordinate Q in the parabolic potentials of excited and dark state. ΔG^0 is the free energy gap between $|L^*\rangle$ and $|D\rangle$ and λ the reorganization energy. Graphics are adapted from [152].

probability γ_L the system can transfer from the excited light state $|L^*\rangle$ to the ground dark state $|D\rangle$ and back with γ_D . The transfer is possible due to the diffusion of the system in energy space. This diffusion is mainly ascribed to local charge rearrangements in the environment and reduced to a single reaction coordinate Q . For harmonic oscillations all states are described as parabolic potentials along Q . The system diffuses along Q with a diffusion constant D related to the effective diffusion time constant τ ($D = \Delta^2/\tau$). It increases with thermal energy and excess energy of the absorption process. $|L^*\rangle$ and $|D\rangle$ are offset in energy by ΔG^0 , the free-energy gap for electron transfer, and by Q_L in reaction coordinate, see Fig. 2.11 b). Their potentials write $U_{L^*}(Q) = \kappa_E(Q + Q_L)^2/2$ and $U_D(Q) = \Delta G^0 + \kappa_E Q^2/2$. $\lambda = \kappa_E Q_L^2/2$ is the reorganization energy for electron transfer. When the system reaches the intersection of $|L^*\rangle$ and $|D\rangle$ at $Q_c = (\Delta G^0 - \lambda)/\sqrt{(2\kappa_E\lambda)}$ it can cross over from the light to the dark state or back, thus transfer an electron. The probability for a cross-over at the intersection is given by the electronic coupling V between $|L^*\rangle$ and $|D\rangle$. The time it remains in either state after the last and before the next crossing gives a distribution of dwell times, which is measured in experiments. It can be found solving rate equations for the populations of either state, starting at the intersection Q_c .

The dwell time distributions are found for three approximations for three different time regimes after the crossing. The first two are separated by a critical time t_c

$$t_c = 2\kappa_E\lambda \left(\frac{\hbar}{|V|^2\pi} \right)^2 D \quad (2.36)$$

and follow

$$P(t) \approx \frac{1}{\sqrt{\pi t_c}} t^{-1/2} \quad \text{for } t < t_c \quad (2.37)$$

$$P(t) \approx \frac{\sqrt{t_c}}{2\sqrt{\pi}} t^{-3/2} \quad \text{for } t_c < t < \tau \quad (2.38)$$

As the critical time t_c depends on V and D it can differ for on- (L) and off-state (D).

It decreases to zero for infinitely strong coupling ($|V|^2 \rightarrow \infty$) between the two states, thus, instantaneous absorption into the sink. The system then simply represents a first-passage problem [151] with $P(t) \propto t^{-3/2}$, thus, the experimentally observed power law distribution. When the interaction is weaker, short times are influenced by this finite crossing rate. t_c then represents the time, when the influence of a finite $|V|^2$ vanishes. It is longer, when the forces driving the system away from the crossing, as diffusion D and the parabola's slope $\kappa_E \lambda$, are strong compared to the interaction $|V|^2$. The DCET theory thus predicts a change in slope for on- and off-state distributions at short times. Some experiments claim to observe [156] such a change, while others do not [44, 45]. For even longer times the distribution follows

$$P(t) \approx \frac{\sqrt{t_c}}{2\sqrt{\pi}} t^{-3/2} \exp -\Gamma t \quad (2.39)$$

where

$$\Gamma_{\text{on}} = \frac{(\lambda + \Delta G^0)^2}{8\tau_L \kappa_E \lambda \Delta_L^2} = \frac{E_L}{2\tau_L k_B T} \quad \Gamma_{\text{off}} = \frac{(\lambda - \Delta G^0)^2}{8\tau_D \kappa_E \lambda \Delta_D^2} = \frac{E_D}{2\tau_D k_B T} \quad (2.40)$$

with $\kappa_E \Delta^2 = k_B T$ for the classical limit and

$$E_L = U(Q_c) = \frac{(\lambda + \Delta G^0)^2}{4\lambda} \quad E_D = U(Q_c) - \Delta G_0 = \frac{(\lambda - \Delta G^0)^2}{4\lambda} \quad (2.41)$$

the energies from the vertices of both parabolas at Q_L and $Q_D = 0$ to the intersection Q_c (see Fig. 2.11 b)). E_L and E_D represent the activation energies for the conventional electron transfer reaction with fast solvent relaxation or here at even longer times $t \gg \tau$, $\Gamma_T \propto e^{-E_{L,D}/k_B T}$ [154, 155]. The DCET model thus also predicts the observed cut-off for the on-state Γ_{on} . The power law cut-off rates Γ increase with E and decrease with the effective diffusion time constant τ . In experiments it is found $\Gamma_{\text{on}} > \Gamma_{\text{off}}$ [136] or even no off-state cut-off Γ_{off} at all. This could mean $E_L > E_D$, thus a lower parabola for the excited on-state $|L^*\rangle$ than for the ground off-state $|D\rangle$ ($\Delta G_0 > 0$), different from Fig. 2.11 b). Another possibility is $\tau_L < \tau_D$, implying a higher diffusion constant D_L for the excited on-state. It is argued that this could be linked to the faster excited state decay in the off-state (Auger decay) than in the on-state (radiative decay) [152]. Spectral diffusion (see Sec. 2.2.3.2), which is expected to increase according to $1/\tau$, is found to be driven by the excitation intensity and temperature [157]. Consequently, as predicted by Eq. (2.40), also the on-state cut-off $\Gamma_{\text{on}} \propto 1/\tau_L$ is observed to increase with excitation and temperature [38]. The DCET model thus describes several experimental observations. Exponents different from 1.5 can be obtained, when the diffusion constant is time dependent [153].

A similar but **non-Auger-based diffusion model** was developed by Frantsuzov and Marcus [158]. They assume the existence of hole traps, possibly due to Se dangling bonds. After relaxation to the band edge, the hole can relax to these deep surface traps with an Auger-assisted process, transferring its energy to the electron. The electron will be lifted from its $1S_e$ to its $1P_e$ state (see Sec. 2.1.1.1 and Fig. 2.2). Subsequently it relaxes to the band edge and recombines non-radiatively with the trapped hole. This

Auger-assisted hole trapping is argued to only be possible when the two transitions (valence band edge - hole trap and $1S_e - 1P_e$) are in resonance. The electron's $1S_e-1P_e$ transition is now assumed to energetically diffuse leading to fluctuations in the non-radiative decay rate. Diffusion on a parabolic potential along a reaction coordinate Q yields the same probability distributions as the DCET model (Eq. (2.37) to (2.39)). Differences in on- and off-state cut-offs are proposed to be due to different diffusion constants or influences of the $1S_e-1D_e$ transition. The model also naturally explains a continuous distribution of decay times and intensities (see Sec. 2.2.3.1).

Other Models Frantsuzov et al. [49] consider non-radiative decay via multiple recombination centers (MRC) randomly switching from active to passive. Those are expected to be hole traps with different trapping efficiency. Hole trapping is then followed by non-radiative decay with the electron. With approximately 10 recombination centers similar behavior as in experiments was found. Also the threshold dependence of dwell time statistics as well as the continuous distribution of intensity and lifetime could qualitatively be reproduced. Kuno et al. proposed fluctuating tunneling barriers for charge transfer to and from traps outside of the quantum dot to account for power law statistics [134, 159]. Changes in the barrier of only 25% in height or width can lead to changes of five to seven decades in time. Such changes were suggested to arise from conformational changes in the ligands or charge hopping in the QD vicinity [134].

2.2.2.2 Blinking Suppression

Some advances have been made concerning the suppression of blinking [50]. A ligand exchange to charge transferring ligands was found to strongly suppress blinking and enhance luminescence [31, 108, 160–163]. This was rationalized with a better passivation of surface traps. Especially the use of electron donors, like thiol groups, has been successful [31, 108, 160, 161], indicating the existence of electron traps. However, at high concentrations of thiols the quantum yield was found to decrease, which was explained by the simultaneous creation of hole traps [31]. Also TiO_2 nanoparticles could be shown to suppress blinking. On the basis of QD charging and neutralization, this was explained by the electron acceptance but fast back-transfer by the TiO_2 particle [164]. Other successes were achieved with the increase of the radiative rate close to metal [165–168] or in a different buffer solution [33]. It decreases the effect of fluctuating non-radiative decay channels. Recently, blinking suppression was observed in QDs with thick CdS shells [29, 51, 100, 169] or alloyed CdZnSe/ZnSe core-shell QDs [52]. Both additionally showed reduced Auger efficiency, indicating a connection of Auger suppression and blinking suppression. Blinking could also be reduced in QDs on an electrode at a potential close to the QD conduction band [74–76]. Either reduced blinking in negatively charged QDs [74, 75] or the filling of electron traps [76] was considered as the reason for suppression. Despite these advances, no consistent explanation of the blinking phenomenon could yet be given. A strong influence of the surface and close environment, as well as Auger processes is evident. The specific mechanism with its power law dwell time statistics, however, has not been identified.

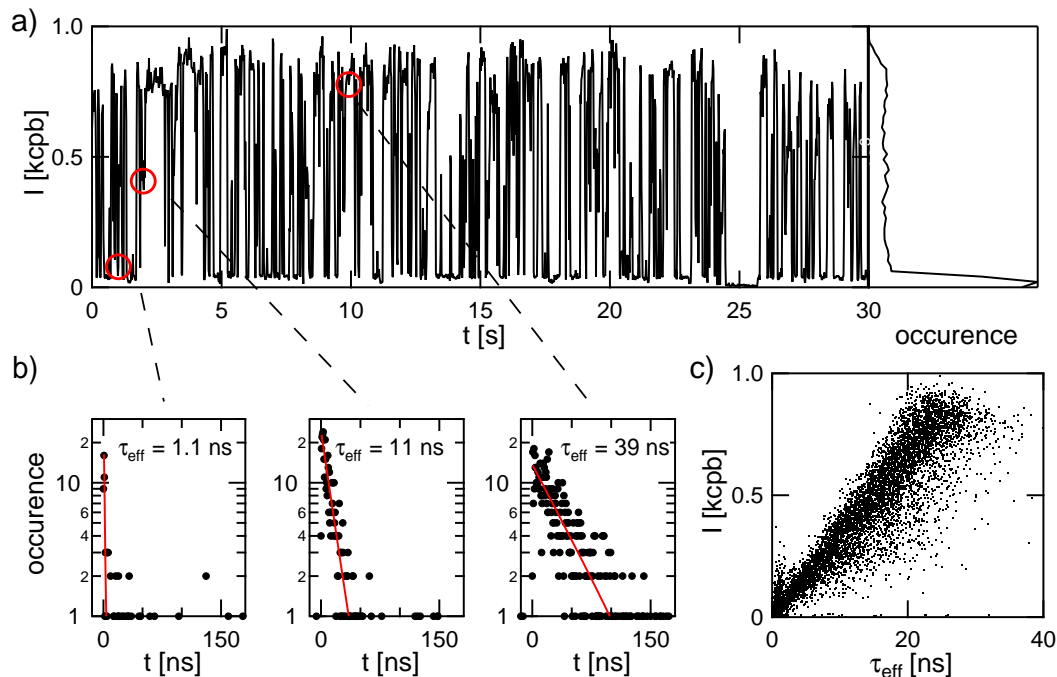


Figure 2.12: Lifetime fluctuations of a single QD. a) Time-trace and intensity histogram on the right. b) Delay time histograms for the indicated instants (red circles). c) Correlation between bin intensity and fitted lifetime τ_{eff} , which is obtained in a single exponential fit.

2.2.3 Lifetime and Spectral Fluctuations

2.2.3.1 Intermediate Intensity Levels

When examining an intensity time-trace like in Fig. 1.2 or 2.12 more closely, not only two distinct (on and off) intensity levels are observed. In-between those, there is a number of equally distributed intermediate intensity levels. Those could in principal result from blinking events that are faster than the chosen bin time, thus not resolved. However, they are often accompanied by a change, usually a decrease, in excited state lifetime τ_{eff} [170, 171]. Fig. 2.12 a) shows such a time-trace. Excited state decay histograms at three specific instants are shown in b). Each of these instants represents a different fluorescence intensity. The highest intensity shows the slowest, the lowest intensity the fastest decay. The correlation of intensity with the fitted decay time in c) yields a direct proportionality. Unresolved blinking would simply result in intensity fluctuations without a change in τ_{eff} . Then only photons from on-periods are detected. A change in the excited state lifetime thus demonstrates the existence of real intermediate intensity levels. The direct proportionality of lifetime and intensity further indicates quenching mostly due to fluctuations of the non-radiative rate Γ_{nr} , as seen from Eq. (2.22). Fluctuations in Γ_{nr} are generally argued to arise from Auger processes enabled due to fluctuating charges in the close vicinity. Also indications of a fluctuating radiative rate have been found [172, 173]. In correspondence to the quantum confined stark effect (QCSE) [173, 174] (see below) a spectral red shift was observed with decreasing radiative rate.

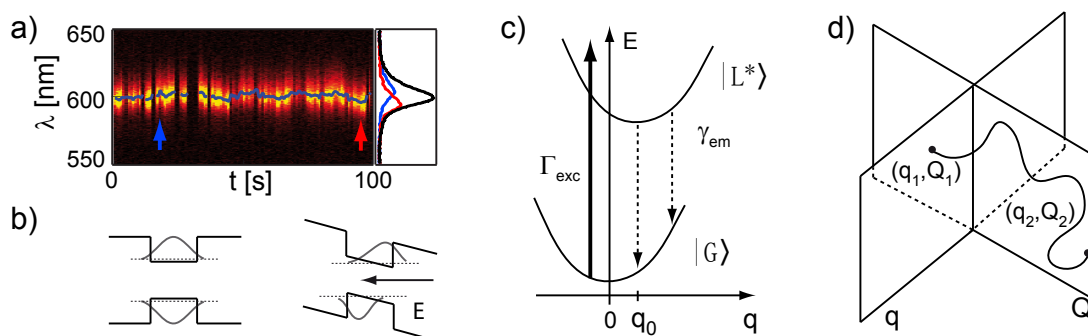


Figure 2.13: a) Spectral diffusion of a single QD at room temperature. Spectral intensities are given in the color scale. Accumulation time for each spectrum is 1 s. The blue line indicates the center of fitted Gaussians to each spectrum. Two single spectra (red and blue) at the instants of the corresponding arrows are shown on the right. The average spectrum of the displayed 100 s (black) is multiplied by 4 for clarity. It shows a FWHM of 85 meV. b) Scheme of the QCSE. Energy levels without electric field are shown on the left, the effect of an applied field on the right. c) Spectral diffusion in the DCET model. The system diffuses on parabolic potentials of ground $|G\rangle$ and excited state $|L^*\rangle$ along a reaction coordinate q . After excitation with Γ_{exc} the system decays with γ_{em} . The transition energy changes with q according to the differences in energy of $|G\rangle$ and $|L^*\rangle$. d) Hyperplanes corresponding to reaction coordinate q of spectral diffusion and Q of fluorescence intermittency (see Fig. 2.11) in the DCET model. Graphics are adapted from [152].

2.2.3.2 Spectral Diffusion

Consecutive spectra of single QDs reveal, that the spectral peak position shifts over time [175, 176]. Shifts as much as 20 meV or even 60 meV at timescales of minutes have been observed at low temperature. This so-called spectral diffusion accelerates with increasing temperature and excitation [157]. It also proceeds at much shorter time-scales and is the main reason for inhomogeneous broadening of a single QD's spectral line at low temperature. Line widths down to ≈ 0.12 meV (FWHM) at 10 K are observed but only expected as an upper bound for the intrinsic line width [176]. At room temperature (FWHM of ≈ 67 meV) thermal broadening due to coupling to phonons generally exceeds the effects of spectral diffusion [157]. Fig. 2.13 a) shows spectral diffusion of a single QD at room temperature. Its origin is also expected to be found in fluctuating charges in the QD environment. They can induce fluctuating electric fields and a shift of the emission line, see Fig. 2.13 b). An applied field lowers the energy levels of the electron and lifts those of the hole. This leads to a red shift of the transition energy. The separation of electron and hole by the field also reduces the wave function overlap and leads to a decrease of the radiative rate. This so-called quantum-confined Stark effect was directly measured in single CdSe QDs applying external electric fields [177]. A linear and a quadratic component were observed. The linear component was attributed to existing local electric fields. Fluctuations of these local electric fields were concluded to be the origin of spontaneous spectral diffusion. Stark shifts in the range of 10 meV per 100 kV/cm were detected. This order of magnitude corresponds well to local fields of charges at the QD surface.

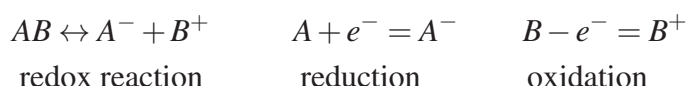
Interestingly, a direct correlation was found between fluorescence intermittency and spectral diffusion [178]. It was observed, that the largest spectral shifts occur after dark (off) periods. With the idea of charge ejection for an off-event, this correlation could be explained. An ejected charge itself changes the charge configuration at the surface simply due to its presence. After a return to the core, the local fields at the surface will still be different. The transition energy, thus has changed. Also the neutralization of the core with a different charge will equally yield another charge configuration.

Also the DCET model (see 2.2.2.1) explains spectral diffusion. Excited state $|L^*\rangle$ and ground state $|G\rangle$ are described by parabolic potentials along a reaction coordinate q , which are offset by a certain q_0 (see Fig. 2.13 b)). When the system diffuses along q , the transition from excited to ground state will change in energy, thus emission wavelength. This reaction coordinate q is not the same as the one describing fluorescence intermittency (Q in Fig. 2.11). It can rather be thought of two intersecting hyperplanes described by q and Q (see Fig. 2.13 c)). As diffusion along q continues during an off-event, also larger shifts are possible upon return to the fluorescent state.

3 Electrochemistry on Semiconductor Electrodes

3.1 Electrochemical Analysis

A chemical reaction, where an electron is transferred from one species to another is called a redox reaction. It consists of a reduction, the gain of an electron for one species (A), and an oxidation, the loss of an electron for the other species (B).



An electron can also be transferred at an electrode, thus separating both processes. The tendency of a species to acquire or release electrons is given by its reduction or oxidation potential, respectively. The probability of a redox process to occur is thus given by a combination of the corresponding reduction and oxidation potentials, referred to as redox potential. For an electrode reduction process A to A^- , the redox potential is identified as the reduction potential of A or the oxidation potential of A^- , respectively. Redox potentials are given relative to the redox potential of the standard hydrogen electrode (SHE [179]), which is arbitrarily set to 0V. The absolute electrode potential of the SHE is estimated to -4.44 V. At an electrode of potential U_F (with a Fermi level E_F)¹ a redox species is reduced or oxidized depending on its redox potential U_{redox} relative to U_F . At equilibrium the concentrations of reduced c_{red} and oxidized c_{ox} species at the electrode surface are given by the Nernst equation

$$U_F = U_{\text{redox}} + \frac{RT}{nF} \ln \frac{c_{\text{ox}}}{c_{\text{red}}} \quad \frac{R}{F} = \frac{k}{e} \quad (3.1)$$

were R , T , F and n are gas constant, temperature, Faraday constant and number of transferred electrons, respectively. The fraction R/F can also be expressed by the Boltzmann constant k and the electronic charge e . Redox potentials can be determined with cyclic voltammetry. Here the potential U_F of an electrode is scanned in the presence of the analyte. The corresponding current due to charge transfer between electrode and analyte, thus, oxidation or reduction to achieve the equilibrium of Eq. (3.1), is measured.

¹Electrode potentials (given in volt) are conventionally referred to with the symbol E . Here U is used for potentials, E for energies.

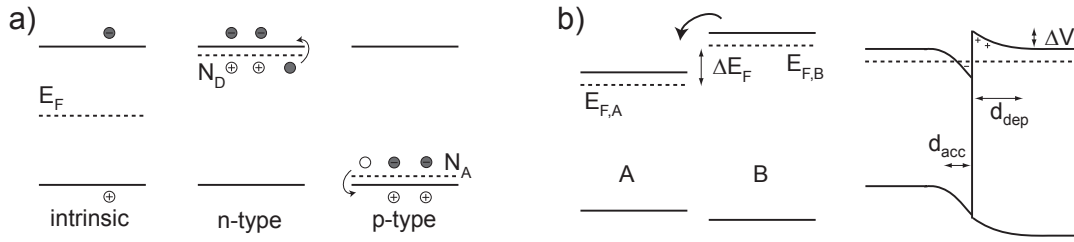


Figure 3.1: a) Different types of semiconductors depending on doping impurities with donor or acceptor densities N_D or N_A , respectively. b) Heterojunction of two n-type semiconductors A and B before contact (left) and in contact (right). Electron flow from B to A due to the Fermi level offset ΔE_F leads to band bending and an accumulation region of width d_{acc} in A and a depletion region of d_{dep} in B. Fermi levels are indicated as dashed lines.

3.2 Semiconductors

Semiconductors are materials that are characterized by an energy gap between bands of occupied (valence band, VB) and unoccupied (conduction band, CB) electron levels of $E_g < 4\text{eV}$. Conduction is only possible in partially filled levels, as electrons can only move from occupied to unoccupied states. Semiconductors are thus insulating at low temperature T . Conductivity increases with T as carriers from the valence band can be excited to the conduction band. Carrier densities n_i and p_i in CB and VB are given by $n_i = p_i = \sqrt{N_V N_C} e^{-\frac{E_C - E_V}{2k_B T}} = \sqrt{N_V N_C} e^{-\frac{E_g}{2k_B T}}$ with the Boltzmann constant k and N_V and N_C the effective densities of states at the top and bottom of VB and CB, respectively [180]. Doping of semiconductors with elements that possess additional valence electrons like Sn in In_2O_3 (ITO) or Ga in ZnO^2 introduces electron states just below the conduction band (within $k_B T$) that can be thermally excited into the conduction band, see Fig. 3.1 a). Semiconductors doped with such electron donating impurities are called n-type. For a donor density N_D , they show carrier densities $n \approx N_D \gg p = \frac{n_i^2}{N_D}$. P-type semiconductors possess electron accepting impurities of density N_A just above the valence band and $p \approx N_A \gg n = \frac{n_i^2}{N_A}$. Conductivities typically increase by several orders of magnitude due to n- or p-type doping, as $N_D, N_A \gg n_i$. In n-type semiconductors electrons are thus referred to as majority and holes as minority carriers, in p-type semiconductors vice versa.

By analogy, a Fermi level E_F is assigned like in metals. It characterizes the energy at which half of all available electron states are filled. For intrinsic semiconductors it lies mid-way between CB and VB, where no energy levels exist, see Fig. 3.1 a). For n-type semiconductors E_F lies just below the CB, for p-type semiconductors just above the VB (dashed lines). In electrochemistry the Fermi level can be identified as the electrochemical potential of an electrode.³

²Indium possesses three and tin four valence electrons, while zinc has two and gallium three.

³The electrochemical potential $\bar{\mu}$ typically carries the unit J/mol , while the Fermi level E_F is given in eV. It is thus $E_F = e\bar{\mu}/F$.

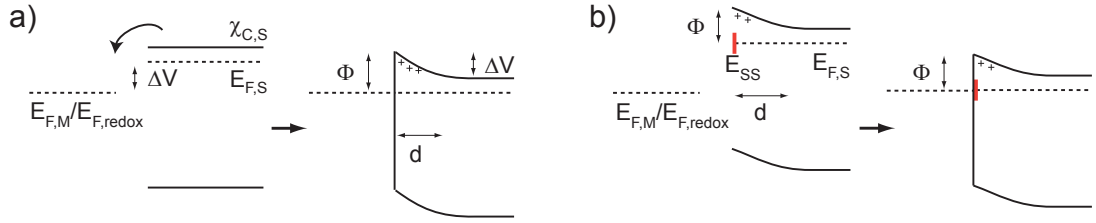


Figure 3.2: Metal-semiconductor or electrolyte-semiconductor junction before (left) and after (right) contact without a) and with b) surface states. Fermi levels of the metal $E_{F,M}$ or the electrolyte solution $E_{F,redox}$ and the n-type semiconductor $E_{F,S}$ are marked as dashed lines. Surface states in b) are marked in red at an energy E_{SS} . The Schottky barrier Φ inhibits electron injection to the semiconductor. It is $\Phi = \chi_{C,S} - E_{F,M}$ for the ideal junction and $\Phi = \chi_{C,S} - E_{SS}$ for Fermi level pinning due to surface states.

3.2.1 Semiconductor Junctions

3.2.1.1 Ideal Band Alignment

When two metals or semiconductors are in contact, their Fermi levels align. This means electrons will flow from the material with higher Fermi level to the one with lower Fermi level. This is demonstrated for two n-type semiconductors in Fig. 3.1 b). On the left, semiconductor bands are indicated without contact with a higher Fermi level in material B. On the right semiconductors are contacted. The induced electric field after a transfer of electrons from B to A is screened by a depletion of electrons close to the interface in B and an accumulation in A. The energy bands are bend upward in the depletion region and downward in the accumulation region. The depletion region is characterized by ionized donor molecules and its width d is given by [180]

$$d = \sqrt{\frac{2\epsilon\epsilon_0}{eN}\Delta V} \quad (3.2)$$

with the static dielectric constant ϵ , the carrier concentration N and the total band bending ΔV of semiconductor B, see Fig. 3.1 b). For high charge densities N like in metals, the space charge layer vanishes ($d \rightarrow 0$), as depicted in Fig. 3.2 a). Total band bending is then given by the Fermi level offset of metal and semiconductor before contact $e\Delta V = E_{F,S} - E_{F,M}$. The induced barrier Φ , referred to as Schottky barrier, inhibits electron flow from metal to semiconductor, thus leads to rectifying characteristics for $\Phi \gg k_B T$. Ideally it is given by the difference of metal work function $E_{F,M}$ and semiconductor electron affinity $\chi_{C,S}$.

$$\Phi = \chi_{C,S} - E_{F,M} \quad (3.3)$$

3.2.1.2 Surface States and Fermi Level Pinning

When surface states are present, the induced barrier Φ becomes independent of the metal work function. This is referred to as Fermi level pinning and shown in Fig. 3.2 b). A high density of surface states at energy E_{SS} (red) leads to an accumulation of electrons at the surface. Bands bend due to a depletion region in the semiconductor

even without a metal contact. At contact electrons flow into the metal from these surface states which changes the Fermi level position only very little. It is pinned to the energy of the surface states. The Schottky barrier is then simply given by the prior band bending of the semiconductor and independent of the metal work function.

3.2.2 Semiconductor-Electrolyte Interface

A semiconductor electrode in contact with a solution containing a redox couple O/R, can be regarded as a similar junction like the metal-semiconductor interface. It is equally well described by Fig. 3.2 a) for an n-type semiconductor electrode. A Fermi level $E_{F,\text{redox}}$ can also be assigned to the solution with the couple O/R with redox potential $U_{\text{redox}} = E_{F,\text{redox}}/e$. Fermi levels of electrode and solution also align via electron transfer. At the semiconductor surface, the couple O/R is reduced or oxidized depending on the relative positions of $E_{F,S}$ and $E_{F,\text{redox}}$. Reduction leads to a positive charge on the semiconductor and a negative charge in solution. The electric field is screened in the semiconductor as for a heterojunction by a depletion of electrons close to the surface, thus, an upward band bending. Its width is equally given by Eq. (3.2). The screening in solution is accomplished by an accumulation of electrolyte counter ions at the electrode. At high electrolyte concentrations, which are typically used, most of the voltage drops in a layer of adsorbed ions, the so-called Helmholtz layer, directly at the surface. As in a metal, the space charge region in the electrolyte is thus a lot smaller than in the semiconductor. Screening at lower electrolyte concentrations and a residual screening at high concentrations is established by a diffuse layer of solvated ions. Here the potential drops exponentially, which is characterized by the Debye length [181]

$$\lambda_D = \sqrt{\frac{\epsilon_0 \epsilon k_B T}{e^2 c_\infty}} \quad (3.4)$$

with the solution's dielectric constant ϵ , and the total concentration c_∞ of all ions in the bulk solution.⁴ Also in semiconductors the same Debye screening is observed for small band offset close to $k_B T$ [182].

Like the Schottky barrier in a metal-semiconductor contact, the voltage drop Φ over the depletion region is given by Eq. (3.3). It is thus proportional to the difference between semiconductor conduction band and the solution's Fermi level. Surface states at the semiconductor interface show the same influence of a pinning of the Fermi level at the surface and a band bending independent of $E_{F,\text{redox}}$.

3.3 Electron Transfer Rates

Electron Transfer between a redox couple and a semiconductor electrode can be described by the Gerischer model [179]. Like in Marcus Theory (see Sec. 2.2.2.1 and [155]) thermally fluctuating solvent molecules are considered to lead to fluctuations of electronic energy levels. According to their different charge and polarizability reduced and oxidized species carry a different shell of solvent molecules. This stabilizes the

⁴The latter is more precisely given by $c_\infty = \sum_i c_i z_i^2$ with concentrations of all ionic species c_i and number of charges z_i . For a symmetric monovalent electrolyte of concentration c_0 it is $c_\infty = 2c_0$.

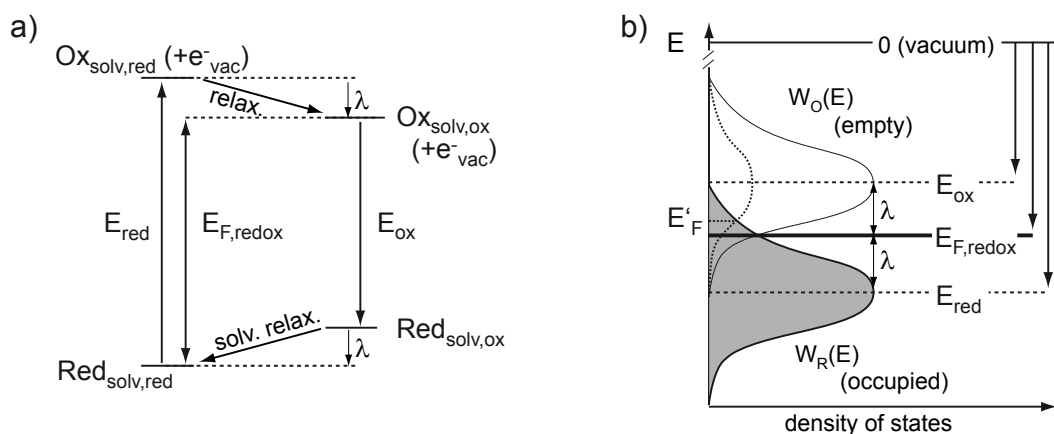


Figure 3.3: a) Cycle of reduction and oxidation processes including solvent relaxation by the reorganization energy λ . Energy differences are electronic energies as plotted in b). Subscripts indicate the solvent shell. b) Time averaged density of states for oxidized (W_O) and reduced (W_R) species of Eq. (3.5) described in the Gerischer model. Solid lines are for an electrode Fermi level $E_F = E_{F,\text{redox}}$. The dotted line indicates a higher E'_F with W_R normalized to the same value. Plots are adapted from [179].

species in the solvent. Upon a reduction or oxidation process, which usually is fast compared to solvent motion (Frank-Condon principle), solvent molecules thus have to reorganize. This is schematically depicted in Fig. 3.3 a). After solvent relaxation the reduced species (Red) is surrounded by a solvent shell adapted to its charge and polarizability ($\text{Red}_{\text{solv,red}}$). Electron ejection into the vacuum requires an energy E_{red} . The oxidized species (Ox) still carries the solvent shell adapted to the reduced species ($\text{Ox}_{\text{solv,red}}$). Solvent molecules thus reorganize and relax with the reorganization energy λ until the solvent shell is adapted to the oxidized species ($\text{Ox}_{\text{solv,ox}}$). Upon reduction of the oxidized species the energy E_{ox} is gained but the reduced species is still surrounded by the shell adapted to the oxidized species ($\text{Red}_{\text{solv,ox}}$). The solvent thus further reorients lowering the energy by λ ($\text{Red}_{\text{solv,red}}$). For simplicity the two reorganization energies are assumed equal. The energy difference between the two relaxed species then gives the redox energy $E_{F,\text{redox}}$. On an absolute scale, the energies for reduction and oxidation are thus separated by 2λ as shown in Fig. 3.3 b).

Solvent relaxation is not a one-step process but generated by thermal fluctuations, which continue also in the relaxed state. As in Marcus theory (see Sec. 2.2.2.1 and [155]) the system can be described as diffusing along a reaction coordinate representing this motion. For harmonic oscillations a parabolic potential is obtained. It effectively yields Gaussian probability distributions of electronic energy levels centering at the reduction E_{red} and oxidation E_{ox} energies (see Fig. 3.3 b)). Energy levels of the redox couple can thus be described by a time-averaged density of occupied (reduced, W_R) and unoccupied (oxidized, W_O) states according to

$$W_R(E) = \frac{1}{\sqrt{4\pi\lambda k_B T}} e^{-\frac{(E-E_{F,\text{redox}}+\lambda)^2}{4\lambda k_B T}} \quad W_O(E) = \frac{1}{\sqrt{4\pi\lambda k_B T}} e^{-\frac{(E-E_{F,\text{redox}}-\lambda)^2}{4\lambda k_B T}} \quad (3.5)$$

Distributions are each offset from the $E_{F,\text{redox}}$ by λ with a standard deviation $\sigma = \sqrt{2\lambda k_B T}$. The effective time-averaged density of states further scales with the

concentration of reduced and oxidized species. At an electrode they are equal when $E_F = E_{F,\text{redox}}$ is applied, leading to two Gaussians of equal amplitude. At a different Fermi level E'_F concentrations also differ and are given by the Nernst equation (3.1). For a higher E'_F this difference in concentrations is representatively indicated by the dotted curve for the oxidized species in Fig. 3.3 b). At equilibrium (Eq. (3.1)) the time-averaged density of states at any applied potential is equal for reduced and oxidized species ($W_R(E'_F) = W_O(E'_F)$).

Electron transfer rates $k_{O/R}$ then are given by [183, 184]

$$k_{O/R} = \frac{2\pi}{\hbar} \int_{-\infty}^{\infty} \rho_{\text{MO}}(E) f'_{\pm}(E) |T_{O/R}(E)|^2 W_{O/R}(E) dE \quad (3.6)$$

with $\rho_{\text{MO}}(E)$ the density of states in the metal oxide and $f'_{\pm}(E)$ its occupation level. $|T_{O/R}(E)|^2$ quantifies the physical overlap between the transferred electron in its initial and final states. For semiconductors of low doping level $\rho_{\text{MO}}(E)$ is given by

$$\rho_{\text{MO}}(E) = \frac{(2m_e^*)^{3/2}}{2\pi^2 \hbar^3} \sqrt{\Delta E_{C/V}} \quad (3.7)$$

with m_e^* the effective mass of the electrons and $\Delta E_C = E - E_C$ and $\Delta E_V = E_V - E$ for conduction and valence band, respectively. The functions $f'_-(E)$ and $f'_+(E)$ represent the fraction of unoccupied and occupied states at energy E in the metal oxide, respectively. For a Fermi level E_F of the metal oxide, they are given by the Fermi-Dirac distribution $f(E)$

$$f'_+(E) = f(E) = \frac{1}{1 + e^{\frac{E - E_F}{k_B T}}} \quad f'_-(E) = (1 - f(E)) \quad (3.8)$$

For a QD, the redox energies are determined by the discrete electronic energy levels in conduction and valence band $E_{C,V}(\text{QD})$ and the charging energy E_{ch} of the QD [183]. For transfer from the excited state, the Coulomb attraction E_C of the exciton is also included. For electron tunneling $|T_{O/R}(E)|^2$ is exponentially dependent on the distance d and the square root of the barrier height $\sqrt{V_B - E}$ between redox couple and electrode (see Eq. (2.27)). At Fermi levels high above the QD conduction or below the QD valence band, tunneling of electrons to and from the QD can proceed into several QD energy levels (see Fig. 2.2 b)). The tunnel rate correspondingly increases.

3.3.1 Bias Potentials for Ideal Surfaces

When a bias is applied to the semiconductor electrode, the Fermi level $E_{F,S}$ and bulk band edges shift (see Fig. 3.4). Band edges at the interface ($E_{C,S}$ and $E_{V,S}$), however, remain unchanged for an ideal semiconductor electrode. For redox couples with $E_{F,\text{redox}}$ in the semiconductor band gap, reduction and oxidation can only proceed from these surface band edges. For n-type semiconductors as depicted in Fig. 3.4 charge transfer primarily involves the conduction band, thus, also the surface band edge $E_{C,S}$. Transfer rates k_R and k_O then are proportional to the densities of occupied and unoccupied states at $E_{C,S}$ in the electrode and the redox couple [185].

$$k_R \propto n_S W_O(E_{C,S}) \quad k_O \propto N_C W_R(E_{C,S}) \quad (3.9)$$

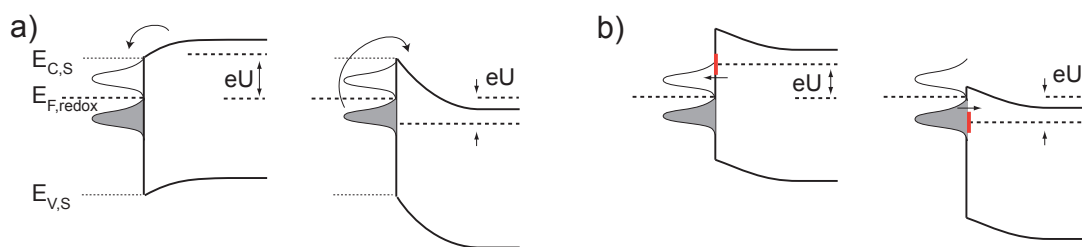


Figure 3.4: Negative (left) and positive (right) bias potentials U in the Gerischer model for a semiconductor without a) and with b) surface states (red). In the ideal case a) band edges ($E_{C,S}$ and $E_{V,S}$) are pinned to the surface. With surface states b) they are fixed relative to the semiconductor Fermi level. Time-averaged density of reduced (W_R , gray) and oxidized (W_O , white) states of the redox couple are indicated to the left.

with W_O and W_R given by Eq. (3.5), $N_C = \rho_{MO}(E_C)$ the density of states at the conduction band edge, and n_S the electron density at the surface, given by

$$n_S \approx N_C e^{-(E_{C,S} - E_F)/k_B T} \quad (3.10)$$

For redox energies deep in the band gap, reduction and oxidation are strongly limited or even inhibited by the vanishing density of states $W_R(E_{C,S})$ and $W_O(E_{C,S})$ with $W_R(E_{C,S}) < W_O(E_{C,S})$ (see Fig. 3.3 b) and 3.4). For $E_{F,redox} > E_{C,S}$ electron states at $E_{F,S}$ are available at the semiconductor and reduction and oxidation proceed as on a metal electrode.

3.3.2 Bias Potentials with Surface States

When surface states in the band gap are involved in the electron transfer, reduction and oxidation rates are given by [185]

$$k_R \propto s p W_O(E_S) \quad k_O \propto s (1 - p) W_R(E_S) \quad (3.11)$$

with density s occupancy p and energy E_S of the surface states. For redox energies deep in the band gap electron transfer to and from surface states can be very efficient. For a high density of surface states, an applied bias will not change the band bending at the surface. The relative position of conduction and valence band edges to the Fermi level then remain unchanged also at the surface. In reality reduction and oxidation occur via both, directly from the conduction band and surface states. Interesting effects can be observed when the semiconductor is illuminated with light of energy above the band gap. Oxidation then also involves valence band holes. A detailed description of electrochemical measurements on semiconductor electrodes can be found in Refs. [179, 185–187].

4 Experimental and Analysis Techniques

4.1 CdSe/ZnS Quantum Dots

The investigated quantum dots (QDs) in this thesis are colloidal CdSe/ZnS QDs from evident technology (Evidots) with an emission maximum of 600nm (Fort Orange). They are dispersed in toluene at 20 μM concentration with hexadecylamine (HDA) as ligand in excess. Absorption and emission spectra are displayed in Fig. 4.1 a). They are recorded with a Varian UV-Vis Spectrometer (Cary 1 Bio) and a PerkinElmer Fluorescence Spectrometer (LS55), respectively. The excitation wavelengths used in this thesis are indicated in the figure (black arrows). The measured emission peak λ_{em} is slightly blue-shifted from that specified by the manufacturer λ_{man} . The quantum yield QY is determined to $\text{QY} \approx 0.27$ by comparison with Rhodamine 6G with known quantum yield $\text{QY}_{\text{R6G}} = 0.95$ [188] via [189]

$$\text{QY} = \text{QY}_{\text{R}} \frac{I}{I_{\text{R}}} \frac{1 - 10^{-\text{OD}_{\text{R}}}}{1 - 10^{-\text{OD}}} \frac{n^2}{n_{\text{R}}^2} \quad (4.1)$$

where I , OD and n are the fluorescence integral, the optical density at the corresponding excitation wavelength and the refractive index of the solvent, respectively¹. The index R denotes the reference sample, here Rhodamine 6G. The CdSe core diameter d_{c} is approximated following the experimental formula for core-only crystals by Yu et al. [190]

$$d_{\text{c}}[\text{nm}] = 1.6122 \cdot 10^{-9} \cdot \lambda_{\text{a}}^4 - 2.6575 \cdot 10^{-6} \cdot \lambda_{\text{a}}^3 + 1.6242 \cdot 10^{-3} \cdot \lambda_{\text{a}}^2 - 0.4277 \cdot \lambda_{\text{a}} + 41.57 \quad (4.2)$$

with the wavelength of the first absorption peak λ_{a} . In this approximation the red-shift due to ZnS-capping [191] is neglected. Gaussian fits to the emission and first absorption peak ($1\text{S}_{3/2}1\text{S}_e$) yield a full width at half maximum (FWHM) of ≈ 150 meV, giving a size distribution of $\approx 10\%$. With the molar absorption coefficient $\varepsilon(\lambda_{\text{exc}})$ at the excitation wavelength λ_{exc} the absorption cross section σ can be estimated according to Leatherdale et al. [192] via

$$\sigma[\text{cm}^2] = \frac{2303\varepsilon(\lambda_{\text{exc}})}{N_{\text{A}}} \quad (4.3)$$

where N_{A} is the Avogadro constant. An approximate value for the molar absorption coefficient at the first absorption peak is given by the manufacturer ($\varepsilon_{1\text{abs}} = 260000$

¹ $1 - 10^{-\text{OD}}$ is the absorbed fraction of the absolute light intensity at the excitation wavelength.

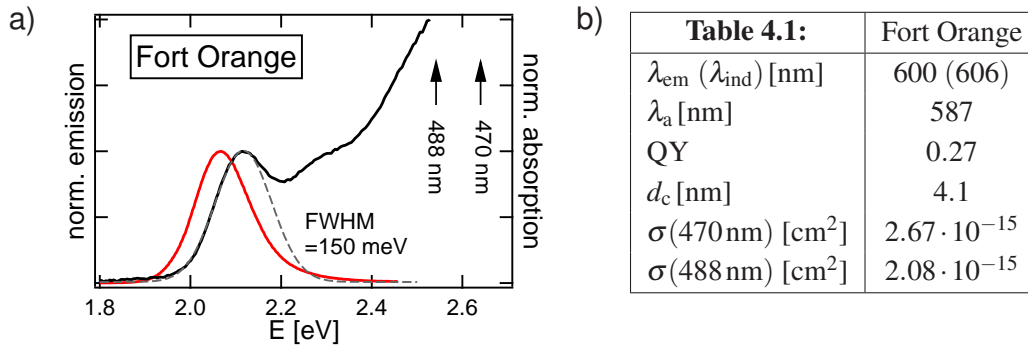


Figure 4.1: a) Normalized absorption (black) and emission (red) spectra of Fort Orange Evidots. The excitation wavelength of the pulsed laser diode (470 nm) and the Argon-ion laser (488 nm) are indicated with arrows. Emission spectra are recorded at 470 nm excitation. Emission and first absorption peak both show a FWHM of 150 meV. b) Properties of Fort Orange Evidots: wavelengths of emission λ_{em} , first absorption peak λ_a and manufacturer's indication λ_{man} , quantum yield QY, core diameter d_c and absorption cross section σ .

for Fort Orange). $\varepsilon(\lambda_{exc})$ is then found with the absorption spectrum of Fig. 4.1 a). Properties for Fort Orange are summarized in Tab. 4.1 of Fig. 4.1 b).

4.2 Fluorescence Microscopy

Fluorescence microscopy is based on the excitation of a sample with a light source, often a laser, and the subsequent collection of the photons that are emitted during radiative relaxation to the ground state. The emission is typically red-shifted from the absorption (for QDs see Fig. 4.1 a)), which makes separation of fluorescence and scattered excitation light possible. Even very small objects like molecules with low scattering cross section can thus easily be detected when they are strong emitters on a low-fluorescent background.

4.2.1 Resolution

For any lens or optical system, the image of a point source is never a point, but always results in a diffraction limited spot. This spot is referred to as the point spread function (psf) $p(z, r)$, with lateral and axial dimensions r and z . The intensity distribution in the focal volume is given by $I(z, r) = I_0 p(z, r)$. In the focal plane ($z = 0$) the psf is commonly approximated by

$$p(0, \rho) = 2 \frac{J_1^2(\rho)}{\rho^2} \quad \text{with} \quad \rho(r) = 2\pi \frac{\text{NA}}{\lambda} r \quad (4.4)$$

which is also known as the Airy pattern [193] and depends on the utilized wavelength λ . J_1 is the first order Bessel function of the first kind and $\text{NA} = n \sin \theta$ the numerical aperture of the objective with n the index of refraction and θ half of the angular

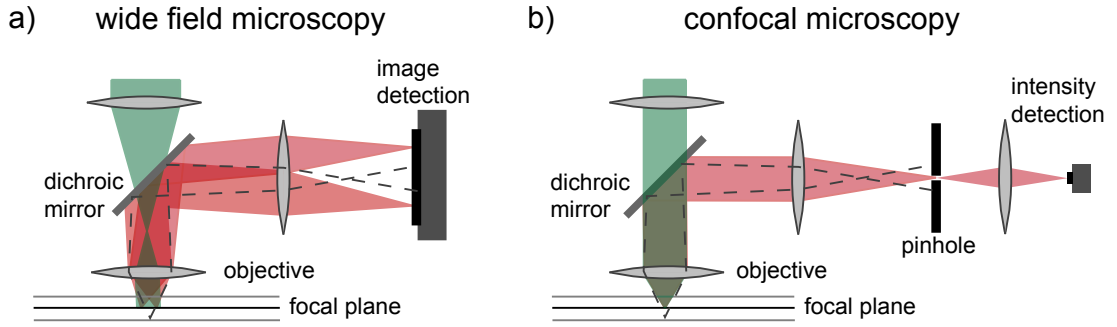


Figure 4.2: Principle schemes of a) widefield and b) confocal microscopy. Excitation light is shown in green, fluorescence in red. Dashed lines indicate light from planes out of the focus.

aperture. Even though this is an approximation for paraxial optics, thus small NA, deviations at high NA are minor [194]. Along the optical axis ($r = 0$) the psf is approximated by

$$p(\zeta, 0) = \left(\frac{\sin \frac{\zeta}{4}}{\frac{\zeta}{4}} \right)^2 \quad \text{with} \quad \zeta(z) = 2\pi \frac{\text{NA}^2}{n\lambda} z \quad (4.5)$$

The lateral resolution Δr_{wf} of such an optical system is usually defined by the Rayleigh criterion. It identifies two points as resolved when the intensity maximum of either image lies in the first minimum of the other, thus at

$$\Delta r_{\text{wf}} = 0.61 \frac{\lambda}{\text{NA}} \quad (4.6)$$

This leads to a dip in intensity of $\approx 26\%$ between the two central maxima for equally bright spots. However, this definition of resolution is somewhat arbitrary. Whether two objects are perceived as distinct from one another not only depends on the optics, but also on the signal to noise ratio (SNR). This ratio decides if a given intensity dip can be differentiated from noise. For given signal counts N_S the SNR is given as $\text{SNR} = \frac{N_S}{\sigma_N}$, where the standard deviation σ_N of the total number of counts $N = N_S + N_B$ also depends on fluctuations of background counts N_B . Background and signal counts show a standard deviation $\sigma_N = \sqrt{N}$, due to the Poisson distribution of independent single photons. This means, the SNR not only decreases with decreasing signal, but also with increasing background photons, thus decreasing contrast. The enhancement of contrast is the most important achievement of confocal microscopy.

4.2.2 Confocal Microscopy

In conventional microscopy (wide field microscopy) a wide area of the sample is illuminated by focusing light into the back focal plane of the objective. This results in a parallel excitation beam (see Fig. 4.2 a)). The image of this area is investigated by eye or captured on a camera chip. The beam paths of two different fluorescent spots in the focal plane are represented in red. Any fluorescent objects along the beam path will be excited and contribute background light to the image. Light of a fluorescent

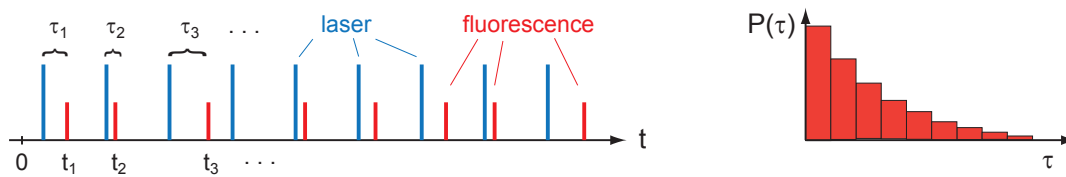


Figure 4.3: Principle of time-tagged TCSPC. Left: Schematic stream of excitation (blue) and resulting fluorescence (red) photons. Recorded microtimes τ_i and macrotimes t_i are labeled. Right: Schematic histogram of microtimes τ .

spot from an out-of-focus plane is indicated by dashed lines. In confocal microscopy only one point in the focus is excited and, more importantly, the fluorescence of only this point is collected. For excitation a parallel laser beam is focused onto the sample to a diffraction limited spot (see Sec. 4.2.1). To achieve the selective detection, the collected fluorescence is focused onto a pinhole and only light passing this pinhole reaches the detector (see Fig. 4.2 b)). Light from objects in planes out of the focus is blocked, as shown in the representative beam path (dashed line). To obtain an image of the sample, each point needs to be addressed separately, thus, the sample needs to be scanned.

Due to the two foci of excitation and detection, the total psf for confocal microscopy p_{conf} will be the product of two psfs, one for the excited and one for the observed volume. Those two are identical for identical optics [194]

$$p_{\text{conf}}(\zeta, \rho) = p(\zeta, \rho) \cdot p(\zeta, \rho) \quad (4.7)$$

For finite pinhole size the detection psf needs to be convolved with the actual pinhole dimensions. Eq. (4.7) features a steeper drop than the psf in conventional microscopy and, thus, leads to a slightly higher resolution in lateral direction when defined by the 26% dip in-between peaks

$$\Delta r_{\text{conf}} = 0.72 \Delta r_{\text{wf}} = 0.44 \frac{\bar{\lambda}}{\text{NA}} \quad (4.8)$$

where $\bar{\lambda}$ is the average of excitation and emission wavelength. More importantly, in contrast to conventional microscopy, also in axial direction a real resolution can be defined, again by the 26% dip.

$$\Delta z_{\text{conf}} = 1.5 \frac{n \bar{\lambda}}{\text{NA}^2} \quad (4.9)$$

As the pinhole prevents spoiling of the contrast by light from out-of-focus planes, this resolution is actually reached. A detailed derivation of the above summary can be found in Ref. [194].

4.2.3 Time Correlated Single Photon Counting (TCSPC)

With TCSPC the depopulation kinetics of a fluorophore's excited state can be monitored. The basic scheme is illustrated in Fig. 4.3. A pulsed light source excites the fluorophore with short pulses at constant pulse rate. When it radiatively decays to the

ground state, the fluorophore emits a photon which is detected by a photodiode. A single photon counting card records the time difference between this photon and the excitation pulse (either via a sync signal from the laser or another photodiode). A histogram of the delay times τ (microtimes) will then give the decay kinetics of the excited state (right of Fig. 4.3). It is exponential for the transition between two well-defined states.² When also the total time from the start of the experiment (macrotime) is recorded for each photon, it is referred to as time-tagged TCSPC.

TCSPC is also used to record photon antibunching of single emitters (see Fig. 2.9). Not only time delays between fluorescence and excitation photons, but also between subsequent fluorescence photons can be recorded. The detectable delay between two consecutive photons with the same detector is, however, limited by the detector dead time t_d (typically $t_d \approx 50$ ns). After the detection of one photon, no further detection is possible for a time span of t_d . Delays $\tau < t_d$ can be determined with a Hanbury-Brown-Twiss Setup [126] using two detectors. Here the photon stream is split into equal parts with each part sent to a different detector. Delays between consecutive photons going to different detectors (approximately half the intensity) can thus be detected with the time resolution of the counting cart.

4.3 Voltammetry

Voltammetry is a method to investigate redox potentials of different analytes by measuring the electric current resulting from the reduction or oxidation of the analyte at an electrode of varying electric potential. The analyte of redox potential U_{redox} in an electrolyte solution is reduced or oxidized at the electrode of defined potential U_F , depending on U_{redox} relative to U_F . As U_F is changed, the corresponding current due to reduction and oxidation is detected and U_{redox} can be determined. The electrode where the reaction of interest takes place is referred to as the working electrode (WE). To obtain a defined potential U_F at this working electrode ($U_{\text{WE}} = U_F$), a well-defined and stable reference potential is needed. This potential is found at a reference electrode (RE). When applying a voltage difference between working and reference electrode, only the working electrode potential changes while the reference electrode potential remains constant. Any polarization of the reference electrode would change its potential with respect to the bulk solution and needs to be avoided. This can be achieved with a potentiostat and the introduction of a third electrode, the auxiliary or counter electrode (CE), see Fig. 4.4 a). The potentiostat applies the desired potential between working and reference electrode, while suppressing any current through the reference electrode. This keeps the reference electrode at constant potential and varies only that of the working electrode. The current through the working electrode is instead compensated by the counter electrode, whose potential is adjusted accordingly by the potentiostat. Typical reference electrodes in aqueous solution, whose potentials against the standard hydrogen electrode (SHE) are well-known, are the reversible hydrogen, saturated calomel, copper-copper(II) sulfate or silver chloride electrodes [195]. These are either directly placed in the electrolyte solution (reversible hydrogen) or electrically

²For a continuously occurring process with constant average rate and independent events (a Poisson process) the time between events is exponentially distributed.

connected, e. g. via a semi-permeable membrane. For non-aqueous solutions often pseudo-references are used. Those are usually silver or platinum wires placed directly in the electrolyte solution close to the working electrode. As they show constant but unknown potential, the potential is determined by addition of an internal standard, i. e. a redox couple of known redox potential, often ferrocene/ferrocenium (see Fig. 4.4 c)) or cobaltocene/cobaltocenium.

For fast charge transfer at the electrode, the concentrations of reduced and oxidized species at the electrode surface are at all times given by the Nernst equation (3.1). The net current is then determined by the transport of reduced and oxidized species to the electrode. To avoid particle flux due to electrostatic forces (at least one species is charged) a supporting electrolyte is added. It quickly polarizes working and counter electrode, and leads to a bulk solution free of electric fields. The flux \mathbf{J} of analyte particles is then only determined by diffusion and given by Fick's Law.

$$\mathbf{J}_{\text{ox/red}} = -D\nabla c_{\text{ox/red}} \quad (4.10)$$

with the analyte's diffusion coefficient D and the concentration $c_{\text{ox/red}}$ for oxidized or reduced species. With an electrode area A and n transferred electrons of charge e this leads to a current

$$I = neAD \left(\frac{\partial}{\partial x} c_{\text{ox}} \right)_{x=0} = -neAD \left(\frac{\partial}{\partial x} c_{\text{red}} \right)_{x=0} \quad c_{\text{ox}} + c_{\text{red}} = \text{const.} \quad (4.11)$$

The current is thus directly proportional to the concentration gradient of oxidized or reduced species at the electrode surface ($x = 0$).

4.3.1 Cyclic Voltammetry in Solution

In cyclic voltammetry the applied voltage at the working electrode is of triangular shape (see Fig. 4.4 b)) with a certain scan rate v and lower and upper reversal potentials U_{min} and U_{max} . A schematic voltammogram of the reversible reaction ferrocene/ferrocenium with redox potential U_{redox} is depicted in Fig. 4.4 c). Starting from the lower reversal potential U_{min} , only reduced species (ferrocene) is present at the working electrode. When increasing the potential the current stays almost constant until approaching the redox potential. It steeply increases as ferrocene is oxidized at the electrode to ferrocenium according to Eq. (3.1). The current is given by the increasing concentration gradient in Eq. (4.11). As soon as the concentration of ferrocene at the electrode is zero, the gradient can only decrease. The current reaches a peak as observed in Fig. 4.4 c) at $U_{\text{p,ox}}$. When the potential is reversed at U_{max} , any freshly arriving ferrocene from the bulk is still oxidized until approaching U_{redox} again. Here the current increases steeply in negative direction due to the reduction of ferrocenium to ferrocene. It likewise reaches a maximum at $U_{\text{p,red}}$ and decreases with the concentration gradient when ferrocenium is depleted at the electrode. For equal diffusion coefficients for oxidized and reduced species the redox potential U_{redox} is given as the mean of the two peak potentials $U_{\text{p,ox}}$ and $U_{\text{p,red}}$. The peak current I_{p} is proportional to \sqrt{v} . For an ideal reversible process and fast charge transfer at the electrode it can be found, that $I_{\text{p,ox}} = I_{\text{p,red}}$ and the peak potentials U_{p} are independent of v with $\Delta U_{\text{p}} \approx 59 \text{ mV}$ (for $1e^-$ transfer). For hindered electron transfer at the electrode the

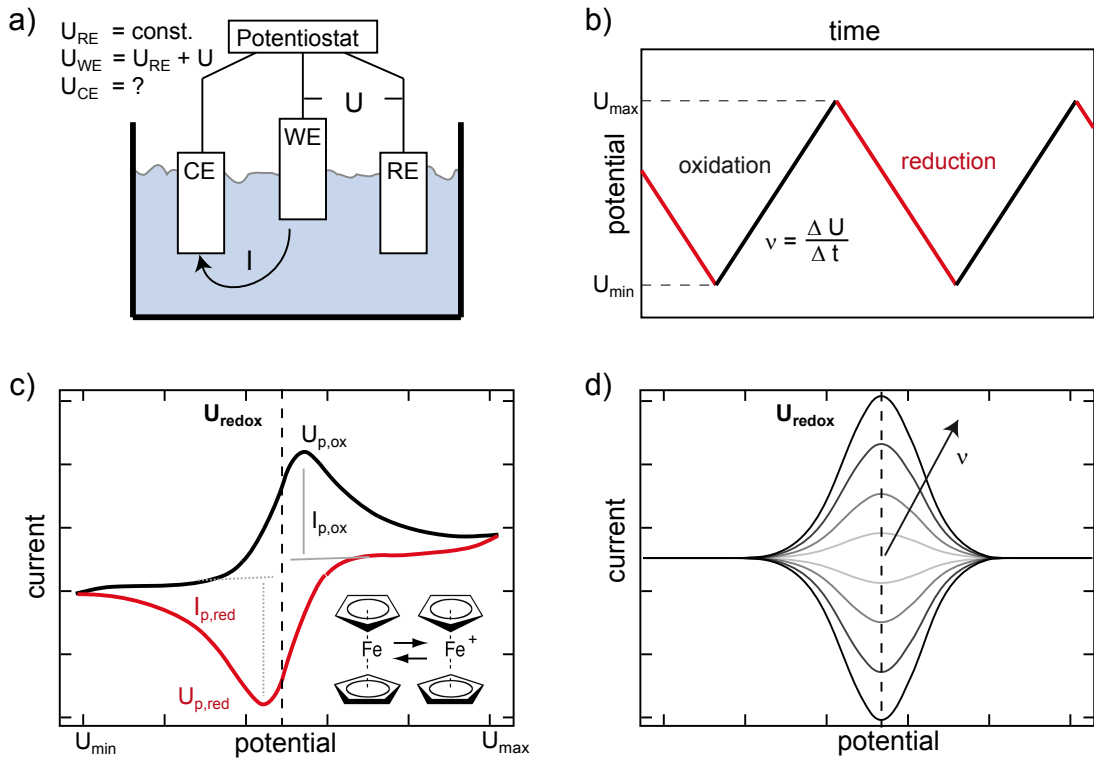


Figure 4.4: Principle of cyclic voltammetry. a) Three electrode setup controlled by a potentiostat. Voltage U is applied between working (WE) and reference electrode (RE). Current I is measured between working and counter electrode (CE). The reference electrode shows a constant potential U_{RE} . b) Triangular waveform applied in cyclic voltammetry, characterized by the reversal potentials U_{min} and U_{max} as well as the scan rate v . c) Illustration of a typical voltammogram of ferrocene in solution. Peak potentials U_p and peak currents I_p as well as the redox potential U_{redox} are labeled. Inset: Chemical structure of the ferrocene/ferrocenium couple. d) Illustration of a voltammogram of an adsorbed analyte with increasing scan rate v . A current peak is observed at the redox potential U_{redox} .

concentration gradient of Eq. (3.1) will be reached with a delay after the application of the electrode potential U_F . For low scan rates v , when the transfer rate is still fast compared to v , the voltammogram is not influenced. However, with increasing scan rate, the peak potentials U_p will separate. Irreversible reactions are marked by deviations from $I_{p,ox} = I_{p,red}$ or the complete absence of reduction or oxidation peak.

4.3.2 Cyclic Voltammetry on an Adsorbed Analyte

When the analyte is adsorbed to the working electrode, the voltammogram shows different characteristics (see Fig. 4.4 d)). The current is no longer determined by diffusion but simply gives the change from reduced to oxidized species and vice versa.

$$I = neA \frac{\partial}{\partial t} \rho_{ox} = -neA \frac{\partial}{\partial t} \rho_{red} \quad \rho_{ox} + \rho_{red} = \text{const.} \quad (4.12)$$

where ρ_{ox} and ρ_{red} are the area densities of oxidized and reduced species, respectively. Those are again given by the Nernst equation (3.1) as

$$\frac{\rho_{ox}}{\rho_{red}} = \exp \left[\frac{e}{k_B T} (U_F - U_{redox}) \right] \quad (4.13)$$

For fast charge transfer, the current reaches its peak in both scan directions at the redox potential with a FWHM ≈ 90 mV (see Fig. 4.4 d)). The peak current increases proportional to the scan rate v . Again, slow charge transfer rates lead to a delayed reaction and a separation of oxidation and reduction peak. For more details on the electrochemical methods see Refs. [196, 197].

4.4 Experimental Setup

4.4.1 Fluorescence Detection

Absorption and fluorescence measurements in solution are carried out with a Varian Cary 1 Bio UV-Vis and a PerkinElmer LS 55 fluorescence spectrometer, respectively. The experimental setup of the microscope is illustrated with its four different operating modes (A, B, C, D) in Fig. 4.5. The sample is excited with a pulsed blue laser diode (Hamamatsu, pulse width 88.67 ps, used pulse rates 1-10 MHz) at 470 nm (A, B, C) or with the 488 nm line of an Argon ion laser (coherent) (D) when higher excitation power is needed. To optimize the beam shape, especially for the laser diode, the excitation light is coupled into and guided through a single mode glass fiber (Thorlabs, 460HP, FC/APC connectors). The fiber also allows an easy exchange of the two lasers by connecting its entrance to either fiber coupler. The FC/APC connector reduces back-reflections in the fiber due to an 8° angle at the output. This eliminates reflection peaks in the time correlated measurements (see 4.2.3). After leaving the fiber, the beam is expanded by two lenses (focal lengths of 40 mm and 60 mm) to overfill the objective's aperture. It is then reflected by a dichroic mirror *DM* (Thorlabs, DMCP505) towards an oil immersion objective (Olympus, UPlanSapo, NA 1.4, $100\times$). The same objective directs the light onto and collects the fluorescence from the sample. The sample is mounted on a 3D piezo scanner (P-517.3CL, Physik Instrumente), which is controlled by a specifically designed Labview program. The fluorescence then passes the dichroic mirror and is cleaned by a 502 nm (Omega Optical, 502ALP) long pass filter *LP* of all residual laser light.³ With this basic setup (top left of Fig. 4.5) four different operating modes are used to obtain time-resolved, spectral and intensity information on ensembles and single quantum dots. They are as follows:

- A) **Confocal Detection:** For confocal detection (see Sec. 4.2.2) the collimated beam leaving the fiber is focused onto the sample to a diffraction limited spot. The fluorescence from this spot is collected, passes a dichroic mirror (*DM*) and a long-pass filter (*LP*) and is then focused ($L_{A_1} = 200$ mm) onto a $50\ \mu\text{m}$ pinhole (P). The light passing the pinhole is recollimated ($L_{A_2} = 100$ mm), split by a polarizing beam splitter *BS* (Thorlabs) and imaged onto two APDs (mpd, picoquant). A single photon counting card (DPC230, Becker & Hickl) records for each detected photon of both APDs the time elapsed from the beginning of the experiment and the time to the next laser reference pulse. Setup A is used for measurements in Chap. 5 and Fig. 6.19 of Chap. 6 as well as several examples in Chap. 2.

³It has only once (see Fig. C.11 of the appendix) been exchanged for a band pass filter (595AF60, Omega Optical), centered around 605 nm (despite the indicated center wavelength of 595 nm).

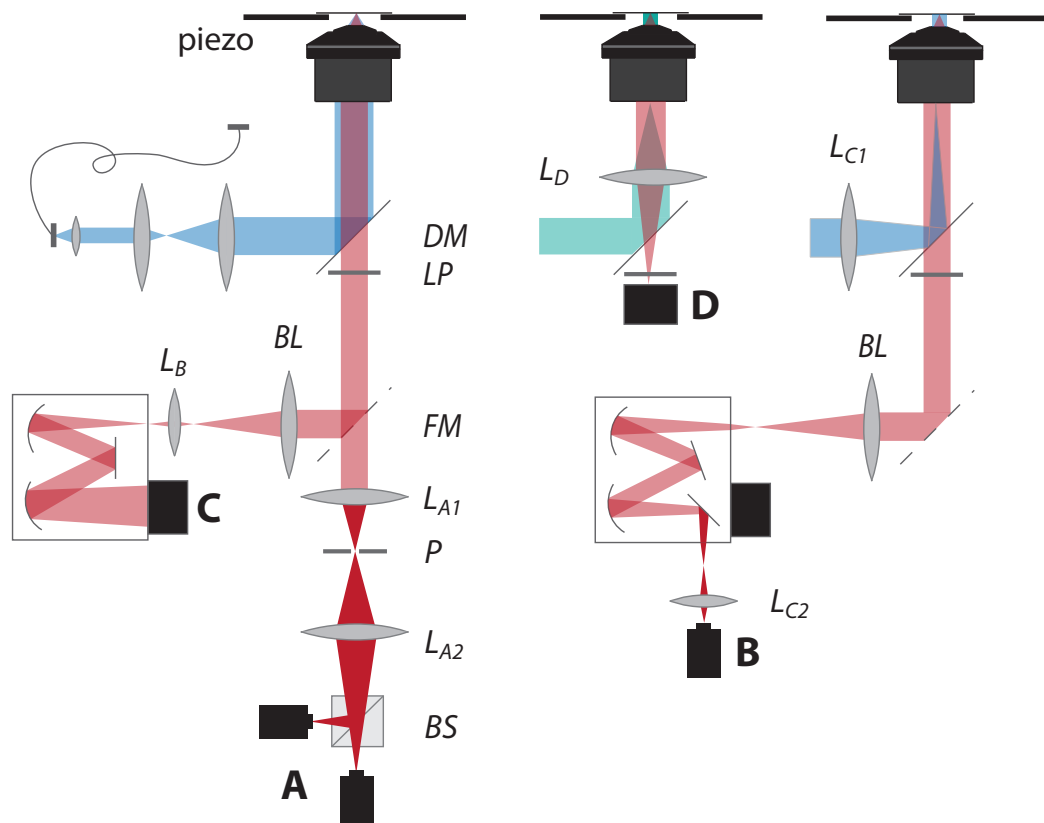


Figure 4.5: Different operating modes of the microscope setup. A: confocal detection. B: Time-resolved ensemble detection. C: Spectroscopy. D: Single QD widefield detection. The initial excitation path (top left) is followed for all variations. Fluorescence light is colored in red, excitation in blue (470 nm) or green (488 nm). For further description see text.

- B) Time-Resolved Ensemble Detection:** For most electrochemical measurements in Chap. 6 an ensemble of QDs at low concentrations is investigated with time-resolved detection. A lens ($L_{C1} = 700\text{mm}$) is placed in the excitation path in front of the dichroic to assure illumination of a broader field of ca. $10\mu\text{m}$ in diameter (see Fig. 4.6). As the confocal path would only image one spot of approximately 500nm , the fluorescence of this area is instead reflected toward the spectrometer with a flip mirror (FM). A Bertrand lens (BL , $L_{BL} = 400\text{mm}$), which is fixed to the setup, images the objective's back focal plane onto the spectrometer's entrance slit. When the spectrometer's internal flip mirror is used at zero order setting, this image is reproduced on the side exit of the spectrometer instead of the CCD chip. It has decreased intensity compared to the original image as only the zeroth order is included. The complete image at the side exit is then focused ($L_{C2} = 19\text{mm}$) onto the detection area of a third APD (SPCM-AQR-13, PerkinElmer), thus collecting all light coming from the illuminated area.
- C) Spectroscopy:** For ensemble spectra the same widefield excitation with lens L_{C1} is used as in setup B. The fluorescence is also directed with the flip mirror FM

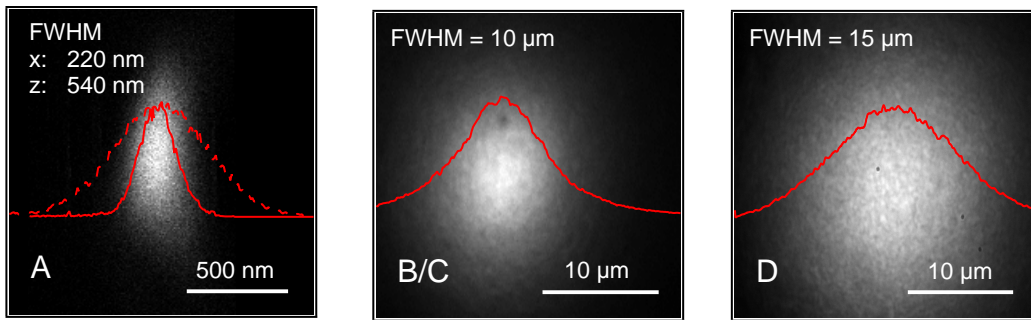


Figure 4.6: Excitation foci of the three different excitation modes in setups A-D. A: Confocal excitation of setup A with lateral and axial direction on abscissa and ordinate, respectively. B/C: Widefield excitation of setup B and C with lens L_{C_1} . D: Widefield excitation of setup D with lens L_D . Line profiles in lateral direction are plotted in red solid lines, the axial direction for confocal measurements as a dashed line. Corresponding FWHMs of Gaussian fits are indicated in the figures.

to the spectrometer (Acton SpectraPro-300i, princeton instruments with liquid nitrogen cooled CCD (1340×100 px)). Behind the Bertrand lens (BL) the light is focused onto the spectrometer entrance slit with a second lens $L_B = 40$ mm. With a 300 g/mm blazed grating (blaze wavelength 300 nm) a spectrum of 0.2 nm/px is obtained. An entrance slit of 130 μ m leads to a resolution of ≈ 2 nm. Spectra are recorded with the accompanying software WinSpec. Setup C is used for measurements in Sec. C.6 of the appendix.

- D) **Single QD Widefield Detection:** For simultaneous detection of the intensity of several single QDs, a lens $L_D = 400$ mm is placed behind the dichroic in the excitation path for wide field illumination. The same lens is used to image the focal plane on a CCD camera (Andor Luca S), placed directly behind the dichroic in the detection path. Images are recorded with the accompanying software Andor Solis. Setup D is used for measurements in Secs. 6.5 and 6.6.

The illumination foci of the three excitation paths for setups A-D are shown in Fig. 4.6. Line profiles in lateral direction are included in red and the FWHMs of fitted Gaussians are indicated. For confocal detection (A) also the axial direction is shown (dashed line). With the measured excitation power P , the illuminated area $A = \pi(\text{FWHM}/2)^2$ and the absorption cross section σ of Eq. (4.3) (see Tab. 4.1) the excitation rate at wavelength λ_{exc} is given by

$$R_{\text{exc}} = x \cdot \frac{\lambda_{\text{exc}} \sigma}{hc} \frac{P}{A} \quad (4.14)$$

The factor x is the relative power per measured excitation power passing the objective and has been determined to ≈ 0.3 for confocal (due to overfilling of the objective) and ≈ 0.7 for widefield excitation. For pulsed excitation at pulse rate R this can be converted in absorptions per pulse $n_p = R_{\text{exc}}/R$ and for continuous wave (cw) excitation with an excited state lifetime τ_{eff} in absorptions per lifetime $n_{\text{cw}} = R_{\text{exc}} \tau_{\text{eff}}$. Absorptions per pulse and per lifetime allow an estimation of the creation probability of multiple excitons. Typical excitation intensities used in setup A and B/C

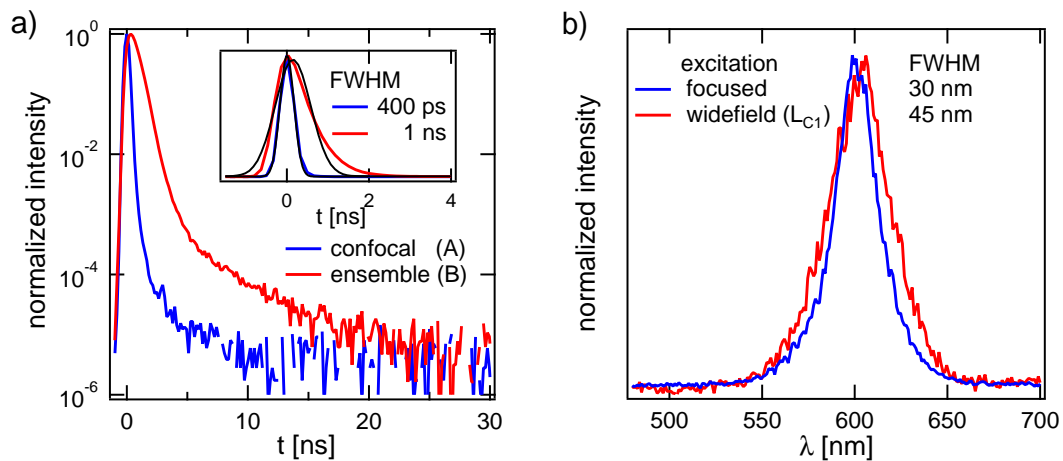


Figure 4.7: a) Measured instrument response functions for setup A (confocal) and B (ensemble). Inset: IRF on a linear scale with Gaussian fits and indicated FWHMs. b) Fluorescence spectra of a film of QDs on a ZnO/ITO electrode at focused and widefield (lens L_{C1} in Fig. 4.5) excitation.

(100 nW, $R = 2$ MHz, $\lambda_{\text{exc}} = 470$ nm) are 80 W/cm^2 ($R_{\text{exc}} = 500 \text{ kHz}$, $n_p = 0.05$) and 90 mW/cm^2 ($R_{\text{exc}} = 560 \text{ Hz}$, $n_p = 2.8 \cdot 10^{-4}$), respectively. In setup D (200 μW , $\lambda_{\text{exc}} = 488$ nm, $\tau_{\text{eff}} \approx 20$ ns), it is 80 W/cm^2 ($R_{\text{exc}} = 400 \text{ kHz}$, $n_{\text{cw}} = 8 \cdot 10^{-3}$). Excitation intensities for single QD investigations are a factor of 1000 higher than those used for ensemble measurements.

Instrument Response and Fluorescence Spectra

Due to experimental limitations, the exact time of zero delay cannot be directly extracted from the microtime histogram (see Sec. 4.2.3). Laser pulse width, detector response time, time resolution of the counting card and different optical path lengths of photons influence the detected microtimes. All these are represented in the instrument response function (IRF). The IRF describes the system's answer to a delta pulse of zero delay between excitation and emitted photons. All measured microtime histograms are convolved with this IRF. The IRF can be recorded with a mirror at the focal plane and without the long pass filter LP in the detection (see Fig. 4.5). Fig. 4.7 a) shows the measured IRFs reflected from a chromium coated glass cover slip for setup A (confocal, blue) and B (ensemble widefield, red). They are fitted with Gaussians which show FWHMs of 400 ps (A) and 1 ns (B), respectively. The broader FWHM for setup B results from the lower time resolution of the PerkinElmer APD and the different optical path lengths of light from different angles on the sample. The time resolution of fluorescence decays is thus limited to this IRF width. A higher time resolution can be obtained with a deconvolution of the measured histogram with the IRF, which is not applied here.

Fluorescence spectra are taken with a slit width of $130 \mu\text{m}$ at the spectrometer entrance. At wide field excitation with lens L_{C1} (see Fig. 4.5, setup B) the observed spectrum (see Fig. 4.7 b), red) shows the same FWHM ($\approx 45 \text{ nm} \equiv 150 \text{ meV}$) as that in solution (see Fig. 4.1). With focused excitation the spectrum is often more narrow as only few QDs

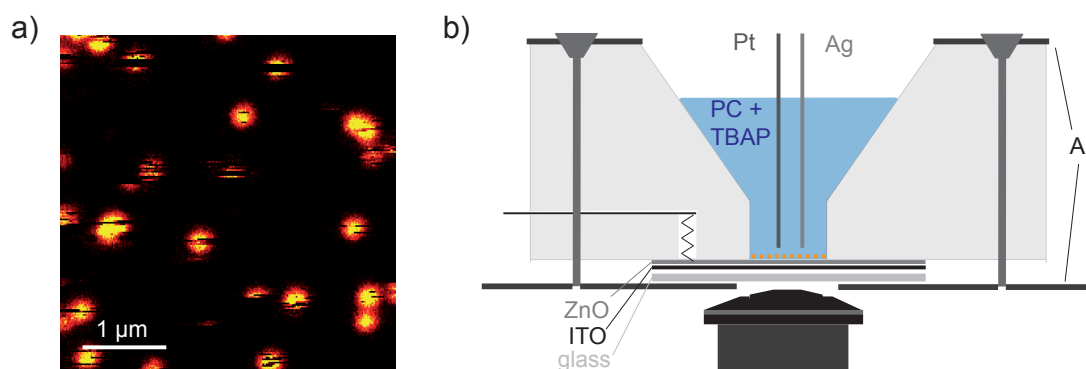


Figure 4.8: a) Confocally scanned $4 \times 4 \mu\text{m}$ image of single QDs (Fort Orange Evidots) on glass in a polystyrene matrix. Dark stripes in single QD images result from blinking off-periods. b) Sketch of the electrochemical cell.

are sampled. A corresponding spectrum with a FWHM = 31 nm is shown in blue in Fig. 4.7 b).

4.4.2 Voltage Application and Current Detection

Voltage is supplied via one of the analog outputs of an ADwin-Gold (Jäger Computergesteuerte Messtechnik). It is input to a home-built potentiostat (circuit see Fig. B.1 of the appendix) which applies the desired potential to the working electrode with respect to the reference silver wire. The functionality of the potentiostat was verified by comparison to a commercial potentiostat (PalmSens, kindly provided by the Kurt-Schwabe-Institut für Mess- und Sensortechnik). Current between working and counter electrode is measured with a Keithley 2400 SourceMeter as voltage over a resistor in the potentiostat. A specifically designed Labview program controls the applied voltage and records voltage, current and fluorescence intensity. Timing with the time-resolved fluorescence data collected by the photon counting card is achieved by comparison of the two fluorescence signals at the same bin size. It is thus limited to the typically chosen bin time of 200 ms.

4.5 Sample Preparation

4.5.1 Single Quantum Dots on Glass

$2 \times 2 \times 0.15 \text{ mm}$ glass slides (Menzel Gläser No. 1) are thoroughly cleaned with technical grade acetone, ethanol and Millipore water and dried in a nitrogen flow. They are then placed in a plasma cleaner (PDC-3XG Harrick, air plasma) for 10-30 minutes. The original solution of Evidots of $20 \mu\text{M}$ concentration is diluted in two steps to a $\approx 0.5 \text{ nM}$ concentration in a 5 mg/ml polystyrene/toluene solution. The solution is sonicated for 15 – 30 s prior to and after dilution to avoid aggregation. $10 \mu\text{L}$ of the final QD-polystyrene solution are spin cast (Laurell, WS-650S-6NPP/Lite) onto the cleaned glass slides at 8000 rpm. This procedure yields a film of single QDs protected from air in a polystyrene matrix. A typical confocal image is displayed in Fig. 4.8 a).

4.5.2 Electrochemical Cell

The design of the electrochemical cell to be placed onto the piezo scanner of the microscope setup is depicted in Fig. 4.8 b). Working electrodes are ITO-coated glass cover slips (18 x 18 x No. 1, diamond coatings). Those are either directly used or coated with a 20 nm ZnO film via pulsed laser deposition (kindly prepared by Mr. Hochmuth in the PLD-laboratory of Prof. Lorenz in the semiconductor physics group of Prof. Grundmann). Also ZnO films of 0.1% or 1% Ga doping are used. The QDs are diluted to the desired concentration in toluene (ca. 200 nM for ensemble and 40 nM for single QD concentration⁴) and spin cast onto the electrodes. Ensemble measurements are performed with the same solution for several weeks. For each single QD measurement a fresh dilution of the original solution is prepared.⁵ The working electrode is placed glass down onto an aluminium sample holder with a 9 mm hole for the objective. A film of adhesive tape ensures complete isolation of the working electrode from the sample holder metal plate. A funnel shaped teflon vessel is placed on the working electrode. It has a small tunnel allowing a contact to the working electrode via a copper spring (see Fig. 4.8 b)). A thin teflon ring serves as a seal. The area of the working electrode in contact with the solution has a diameter of 7 mm. The cell is held together by screwing another metal plate on top of the vessel to the sample holder, pressing the working electrode against the teflon ring. The top of the cell is open to air. Reference and counter electrode, a 0.5 mm silver and a 0.25 mm platinum wire (both Chempur), respectively, are taped to the vessel insuring complete isolation with the adhesive tape. The sample holder is screwed onto the piezo with the working electrode on the objective separated by a drop of oil. All electrodes are connected to the potentiostat. A 0.1 M solution of 140 mg tetrabutylammonium perchlorate (TBAP, 342 g/mol) in 4 mL propylene carbonate (PC) is prepared and filled into the vessel. The TBAP/PC solution is either directly used or priorly dried (at least over night) over molecular sieves (0.4 nm, Merck).

Between experiments, counter and reference electrode as well as the teflon seal are cleaned in ultrasonic baths (5-10 min) of technical grade acetone, isopropanol, ethanol and Millipore water. The vessel is rinsed with the same solvents and dried with the electrodes in the oven. The ZnO and Ga:ZnO coated electrodes are cleaned between experiments in toluene (ultrasonic bath for 1h) and 12-16 h at 80° in spectroscopy grade ethanol (Merck). They are rinsed before storage with Millipore water. Before use they are again rinsed with Millipore water and placed in the plasma cleaner for 20 – 30 min. Pure ITO electrodes are rinsed with technical grade acetone, isopropanol, ethanol and Millipore water and also placed in the plasma cleaner before use. They are discarded after the measurement. Molecular sieves are dried for about 12 h at 200°C and 0.15 mbar prior to use.

⁴Spin cast single QD concentrations for electrochemical measurements are higher than on glass. This results partially from quenching of many single QDs on the electrodes. Different adhesion can also lead to different concentrations sticking to the substrates.

⁵Dilution always leads to a detachment of passivating ligands from the QD surface [107]. Fluorescence of single QD concentrations thus quickly decreases over the first minutes after dilution. Ensemble concentrations still contain enough ligands in access for highly luminescent well passivated QDs over several days or even weeks.

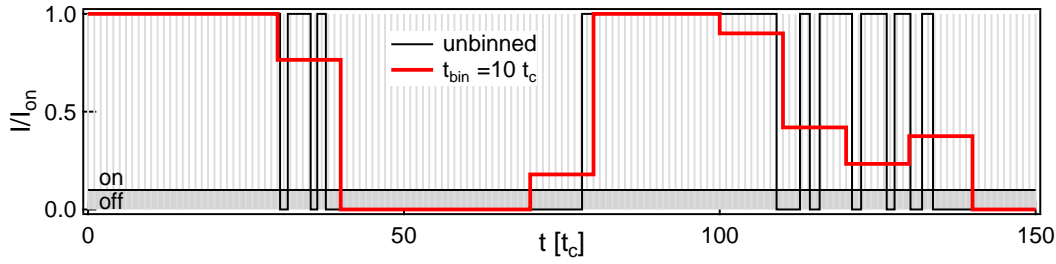


Figure 4.9: Simulation of a binned time-trace. The original data of alternate on- and off-events following a power law distribution with $\alpha_{\text{on/off}} = 1.8$ is shown in black. Units of t_c are marked as gray vertical lines. The resulting binned time-trace with $t_{\text{bin}} = 10 t_c$ is shown in red. A threshold at $0.1 I_{\text{on}}$ demonstrates the sorting in on- and off-events.

4.6 Data Analysis

4.6.1 Excited State Lifetime

The transition times between to well-defined states (excited and ground) are usually exponentially distributed. When different distinct states are involved a multiexponential distribution can be observed. The transition time is given by the delay between fluorescence photon and the prior laser pulse, thus the microtime (see Sec. 4.2.3). Average decay times τ_i can be extracted with a multiexponential fit to the microtime histogram.

$$p(\tau) = \sum_i A_i e^{-\tau/\tau_i} \quad (4.15)$$

For highest time resolution a deconvolution of the measured histogram with the IRF (see Sec. 4.4.1) or fitting of Eq. (4.15) convolved with the IRF is necessary. The decays here are mostly > 5 ns. A direct fit to the still convolved microtime histogram thus serves as a good approximation. For a rough quantification of multiexponential ensemble decays an average lifetime τ_{avg} is calculated from the decay according to

$$\tau_{\text{avg}} = \frac{1}{N} \sum_{k=1}^N \tau_k \quad (4.16)$$

with the total number of photons N and the respective delay time to the excitation pulse τ_k for each photon. This average allows no information on the contribution of different decay constants.

For intensity time-traces of single QDs microtime histograms are observed to change over time. For time intervals of only a few milliseconds often monoexponential decays are observed within the measurement accuracy. For the investigation of lifetime fluctuations single exponential functions are fitted to the decay of each bin. Extracted decay times are then correlated to the corresponding bin intensity.

4.6.2 Simulation of Two-State Blinking

To determine the effect of unresolved events on the threshold method, the method is applied to time-traces of simulated power law blinking. For these time-traces power

law distributed numbers $t_{\text{on/off}}$ are obtained by a transformation of equally distributed random numbers $r \in [0, 1)^6$ via [198]

$$t_{\text{on/off}} = r^{1/(1-\alpha_{\text{on/off}})} \quad (4.17)$$

This yields power law distributed random numbers $t_{\text{on/off}} > 1$, thus in units of the shortest blink time t_c , the onset of blinking. For simplicity it is set to 1. When examining an on-state cut-off at $\tau_{\text{cut-off}}$, the generated time t_{on} is rejected with probability $1 - e^{-t_{\text{on}}/\tau_{\text{cut-off}}}$ by comparison with another random number $r \in [0, 1)$. On-times and off-times are now alternately drawn from the respective distributions. Each of these times $t_{\text{on/off}}$ represents a corresponding evolution in time. The intensity during the drawn on-times is set to 1, that during off-times to zero. A segment of such an unbinned time-trace with $\alpha_{\text{on/off}} = 1.8$ is presented in Fig. 4.9 in black. Units of t_c are indicated as gray vertical lines. This time-trace is then binned, thus divided into equal time intervals $t_{\text{bin}} > t_c$. The intensity of each consecutive bin of length t_{bin} is set to the fraction of its time spent in the on-state. This yields a time-trace of intensities between 0 and 1 with the time given in units of t_c . It can easily be scaled to corresponding intensities or bin times of experiments. Power law numbers are limited to $t_{\text{on/off}} < t_{\text{max}} = 2 \cdot 10^4 t_{\text{bin}}$ as experiments rarely show longer events.⁷ Different bin times of $t_{\text{bin}}[t_c] = 1 - 10^5$ are investigated. It should be noted that even $t_{\text{bin}} = t_c$ does not yield the original time-trace as original power law numbers are not limited to discrete multiples of t_c . An example of $t_{\text{bin}} = 10t_c$ is shown in red in Fig. 4.9. To investigate the influence of Poisson noise, an average intensity I_{avg} is assigned to on-state and off-state. The probability to find k photons per bin for either state then follows

$$p_{I_{\text{avg}}}(k) = \frac{I_{\text{avg}}^k}{k!} e^{-I_{\text{avg}}} \quad (4.18)$$

Poisson distributed photons are statistically independent. Poisson noise is thus simply added after the simulation of the time-trace. The simulated binned time-trace is multiplied by the average on-state count rate I_{on} , offset by a background (off-state) count rate I_{bg} and each bin transformed to a Poisson distributed random number following Eq. (4.18). Poisson distributed random numbers are generated with the integrated random number generator of IGOR Pro. The simulation is implemented in C with the basic script written by André Heber in the course of his bachelor thesis.

4.6.3 Probability Distributions via Thresholding

Simulated binned time-traces and experimental time-traces are investigated with IGOR Pro. A threshold is chosen and bins above the threshold defined as *on* and below as *off*. This is demonstrated for a threshold of $0.1 I_{\text{on}}$ in Fig. 4.9. The number of consecutive bins in the on- or off-state mark the length of an on- or off-time, respectively. A histogram over these lengths gives the probability to find an on- or off-time of a specific

⁶Pseudorandom numbers are obtained with a 64-bit Mersenne twister (<http://www.math.sci.hiroshima-u.ac.jp/~m-mat/MT/emt64.html>).

⁷This limit does not affect occurrence histograms (see below) up to t_{max} . It simply avoids time-traces dominated by just one event.

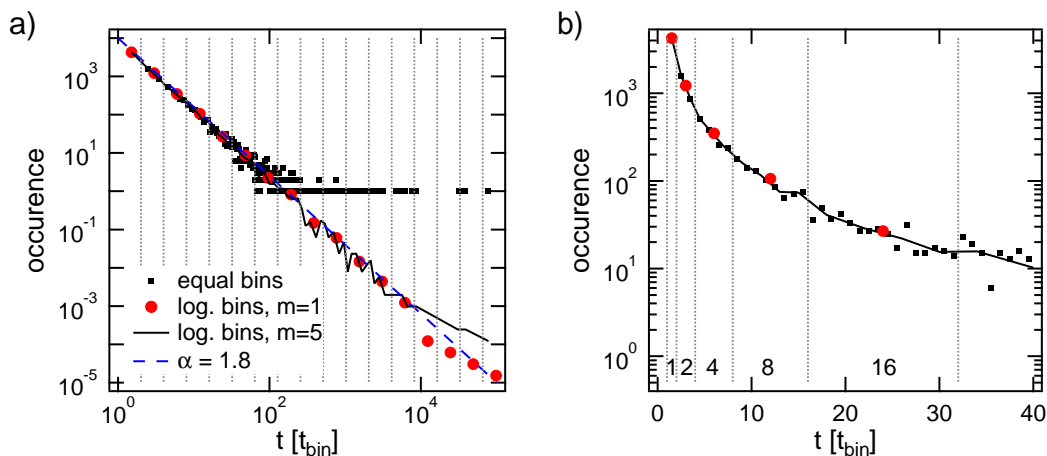


Figure 4.10: Difference between equal and logarithmic binning of histograms of 10^4 power law distributed random numbers on a) log-log and b) log-linear scale. Black dots show the histogram with equally spaced bins, red markers with logarithmically increasing bin width of $2^n t_{\text{bin}}$ and black line with the adjusted logarithmic binning with $m = 5$ (see text). Bin edges for logarithmic binning with $m = 1$ are shown as vertical dotted lines. The blue dashed line represents the underlying power law of exponent 1.8.

length. Such a histogram of 10^4 power law distributed random numbers is displayed as black dots in Fig. 4.10 a). The power law slope is well observed for about two decades. Long events, however, are very rare and noisy. An averaging procedure is thus necessary. The time resolution of short events can be maintained with an increasing bin width for longer times. Logarithmic binning has been shown to be well suited for this purpose [199]. The bin width is increased according to $2^n t_{\text{bin}}$, $n = 0, 1, 2, \dots$, thus each bin is two times as wide as the prior bin. This is shown on a linear scale in b). Vertical dotted lines indicate the bin edges. They are also included in a) where they appear equally spaced on the logarithmic scale. Averaging events over those bins allows the observation of a much broader time and occurrence range of the power law as shown by the red markers. To allow more details of possible deviations from power laws, binning can be slightly adjusted. For example a doubling of the bin size not after each bin but after m bins of equal length can be chosen. In Fig. 4.10 this is shown for $m = 5$ as black line.

The extraction of power law exponents from this histogram can be obtained with a linear least squares fit to $\log(\text{occ.})$ and $\log(t)$. It can depend on the chosen binning procedure in the histogram. For truly power law distributed numbers a maximum likelihood estimation (MLE) without the need of a histogram is shown to give better results [198, 200, 201]. However, when the data deviates from a power law distribution, the results of an MLE quickly become arbitrary. If obtained data likely follows a power law distribution can be tested with the Kolmogorow-Smirnow-Test. With histograms as in Fig. 4.10, the power law hypothesis and possible deviations can be inspected visually. This allows the selection of suitable regions for a power law fit, when deviations are observed.

5 Power Law Blinking of Single Quantum Dots

With the development of single particle microscopy unexpected intensity fluctuations of single emitters became visible. Under continuous excitation, single fluorophores were found to randomly switch between an emitting (bright) and a non-emitting (dark) state. This intermittent fluorescence behavior, also referred to as blinking (see Sec. 2.2.2), turned out to be even more intriguing when examining dwell time statistics in bright and dark states. When thresholds T are used to define on- (above T) and off-state (below T) intensities, single molecules typically show exponential distributions. Dwell times in off-states lie at the microsecond scale and are assigned to transitions to the triplet state. However, especially semiconductor quantum dots but also some proteins and molecules [39–42] show much longer off-times. Most importantly, instead of exponential distributions linear slopes are observed in log-log histograms of occurrence vs. dwell time lengths. They are characteristic for power law distributions with exponents ranging from 1.1 to 2.2 [47, 48, 140]. For off-states of semiconductor quantum dots linear slopes in dwell time histograms cover at least six decades in time and more than eight in occurrence [37]. On-time distributions are truncated at long times, typically a few seconds. A linear slope is thus only reported for less than three decades in time.

Such power law statistics cannot simply be described with the transition between two well-defined states. Quantum dots also do not possess a triplet state turning the QD off. To explain observations, a charged QD was soon postulated as a candidate for the off-state [46]. The unusual power law statistics, however, evoked several different models to describe possible mechanisms generating this random switching (see Sec. 2.2.2.1). So far no consensus has been reached on a best description of all observations.

Power law statistics in QD fluorescence have been observed with several different methods [43, 44, 156, 172, 202–204]. The explicit separation in on- and off-state statistics, however, has primarily been investigated with binning and thresholding. Binning is limited to a time resolution of the bin time t_{bin} of typically 1 – 100 ms. Shortest dwell times and thus the onset of power law blinking t_c are, however, expected on the microsecond or even nanosecond scale [43–45]. Such short blink events are not only unresolved and neglected. They also influence dwell time histograms of longer events. They lead to intermediate intensity bins in the time-trace which are mistakenly sorted as on or off by the threshold. Also experimental noise can lead to threshold crossings even for events far above the time resolution. It can thus be questioned if underlying dwell time statistics can be rigorously extracted with binning and thresholding. This implies the question if power law statistics, the key feature of blinking models, can

really be identified.

With the help of simulations it could be shown that for low power law exponents close to 1.5 the underlying statistics can be rigorously extracted at bin times close to the onset of blinking and thresholds outside of noise [43, 49, 55, 135, 136, 159, 205]. Higher exponents and longer bin times, however, are more influenced by averaging. A performance test of the threshold method for these parameter ranges is thus performed in the following. With the help of simulated time-traces, the results of binning and thresholding are tested for exponents between 1.5 and 2 and bin times up to 10^5 times longer than shortest blink events. First, influences purely arising from averaging of the power law distribution are investigated. Second, effects of cut-off, noise and intermediate intensity levels are regarded. Third, selected experimentally recorded intensity traces of single QDs are presented and compared to the results of simulations. Except for the experimental comparison results are summarized in Ref. [206].

5.1 Artifacts of Thresholding Due to Unresolved Blinking

When an intensity time-trace is recorded, the resolution of intensity fluctuations is limited by the chosen bin time t_{bin} . All fluctuations faster than the bin time will be accumulated to an average bin intensity. Also two state fluorescence blinking as described above will thus lead to bins of intermediate intensity when the shortest blink events are shorter than the bin time. The threshold method as described in Sec. 4.6.3 assigns these “mixed” bins to on- or off-state dependent on their average intensity relative to the chosen threshold. The resulting histograms of on- and off-times are thus inherently biased. The extend of this bias depends on the importance of short blink events which are given by the underlying blinking statistics with respect to the bin time. For different thresholds, bin times and power law exponents the introduced bias in extracted statistics by binning and thresholding of simulated time-traces is thus investigated in the following. Details to the simulations are described in Secs. 4.6.2 and 4.6.3.

5.1.1 Threshold Placement

A representative time-trace generated from power law blinking with $\alpha_{\text{on/off}} = 1.8$ and a resolution of $t_{\text{bin}} = 10^4 t_c$ is depicted in Fig. 5.1 a). The corresponding intensity histogram (black line) is shown in b). It is zoomed to the intermediate intensities, which in total add to 17% of the total time. Most bins are found at intensity 1 or 0, each representing $\approx 40\%$ of the total time. Here no transition occurred during the complete bin time. A local maximum is observed at intensity $0.5 I_{\text{on}}$. For this time-trace the off-state dwell time histograms for three different thresholds are shown in Fig. 5.1 c). In the case of equal exponents, the on-state histogram at threshold 0.9 (thresholds are referred to by their on-state fraction) follows the off-state histogram at threshold 0.1 and vice versa. Thus, only off-state histograms are shown. The blue dashed line represents the input power law exponent $\alpha_{\text{on/off}} = 1.8$. Only a threshold of 0.1 close to the off-state (0.9 for the on-state) leads to these input statistics over the complete time range. For higher thresholds deviations at short times are observed

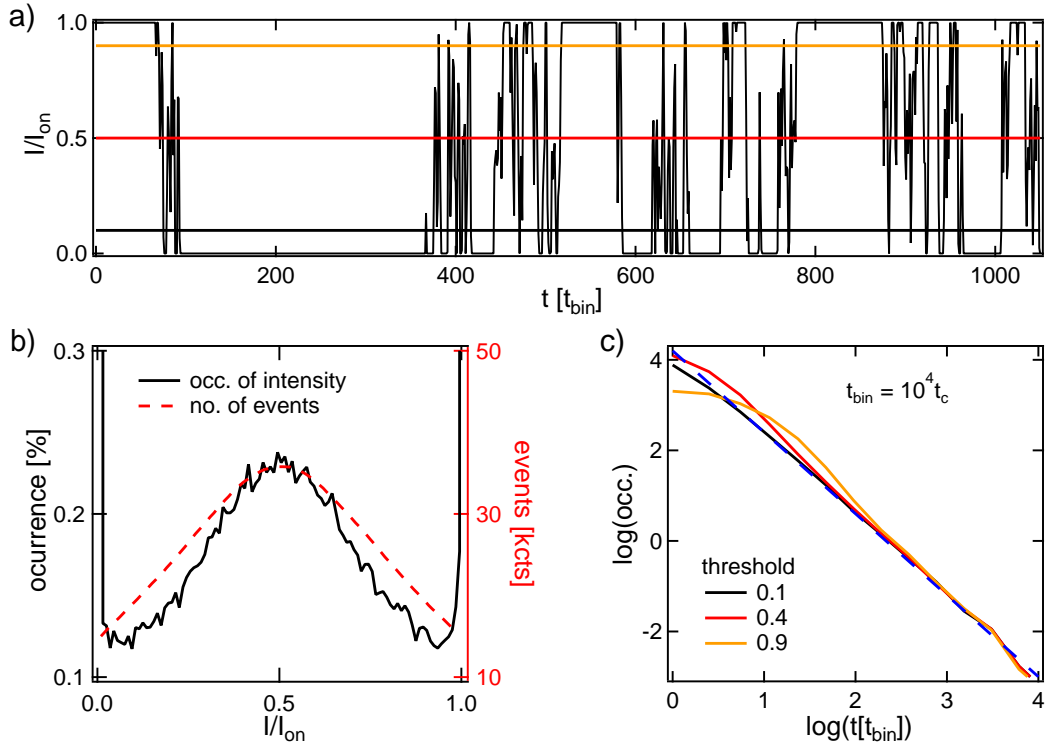


Figure 5.1: Simulation of power law blinking with exponents $\alpha_{on/off} = 1.8$ and $t_{bin} = 10^4 t_c$. a) Segment of the time-trace consisting of $10^6 t_{bin}$ in total. b) Intensity histogram of the time-trace (black line) and number of detected events at different thresholds (red dashed line). c) Dwell time histograms of the off-state for the thresholds indicated in a). A slope corresponding to $\alpha = 1.8$ is indicated as a blue dashed line.

which increase and extend to longer times with increasing threshold. The power law tail robustly follows the input distributions for all thresholds. The number of detected events is also dependent on the threshold and indicated by the red dashed line in b). It resembles the distribution of intermediate intensities. The threshold 0.5 shows almost twice as many events as thresholds 0.1 or 0.9. These additional events are very short events as observed in c) (red line).

5.1.2 Bin Time

The effect of different time resolutions, thus different t_{bin} , for $\alpha_{on/off} = 1.8$ is depicted in Fig. 5.2. Fig. 5.2 a) shows the intensity histograms and b) the dwell time histograms for different thresholds of the off-state. On-state histograms are again omitted as they are identical to off-state histograms when exchanging thresholds 0.1 and 0.9. Intensity histograms are plotted on a logarithmic scale to show occurrence of intermediate levels as well as the peak occurrence in on- and off-state. Simulated intensity histograms in a) show no intermediate intensities $I < \frac{t_c}{t_{bin}} I_{on}$ and $I > (1 - \frac{t_c}{t_{bin}}) I_{on}$. This is best observed for $t_{bin} = 10 t_c$ (dark brown) for intensities $< 0.1 I_{on}$ and $> 0.9 I_{on}$. Instead a higher probability of intensities close to $0.1 I_{on}$ and $0.9 I_{on}$ is detected. This simulation arti-

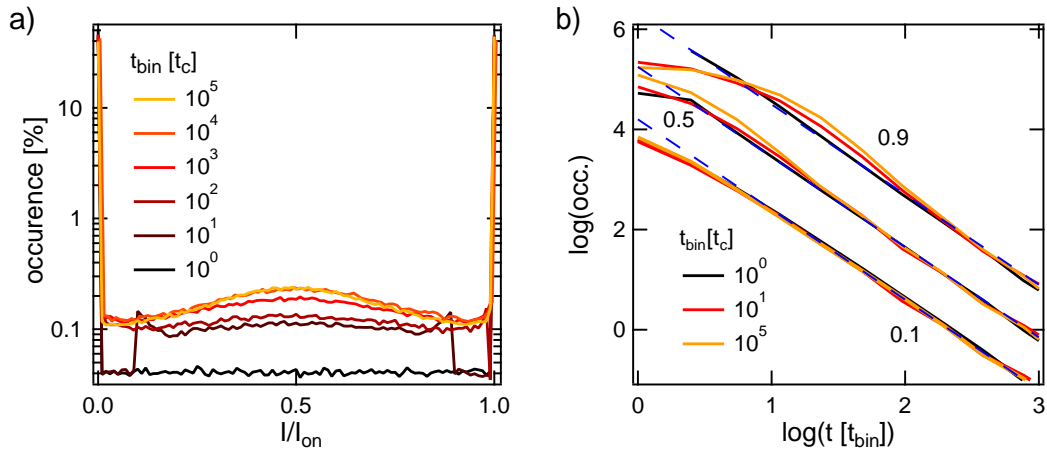


Figure 5.2: Simulations of power law blinking with exponents $\alpha_{\text{on/off}} = 1.8$ for different bin times t_{bin} . a) Intensity histograms for time-traces of different t_{bin} . b) Corresponding dwell time histograms for the off-state at thresholds 0.1, 0.5 and 0.9 (offset for clarity). Dashed blue lines indicate slopes corresponding to $\alpha = 1.8$.

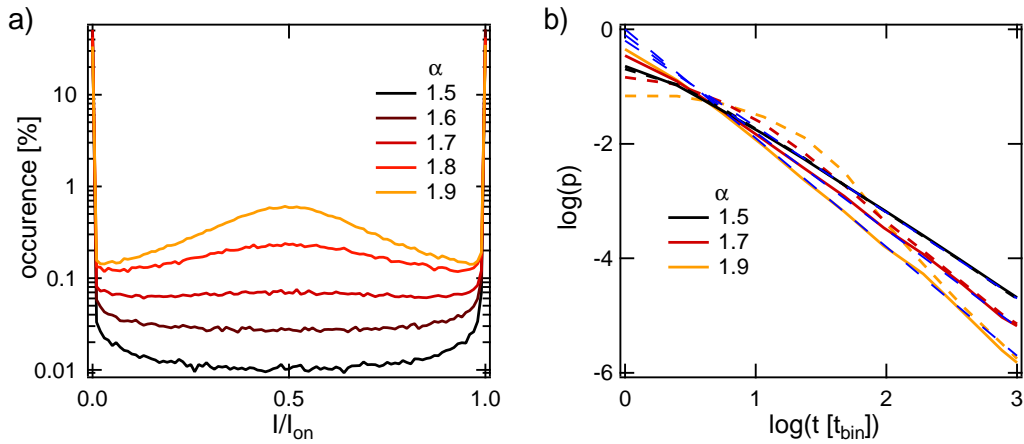


Figure 5.3: Simulations of power law blinking for $t_{\text{bin}} = 10^4 t_c$ and different exponents $\alpha_{\text{on}} = \alpha_{\text{off}}$. a) Intensity histograms. b) Probability dwell time histograms for thresholds 0.1 (solid lines) and 0.9 (dashed lines), normalized by the number of detected events. Slopes corresponding to $\alpha = 1.5, 1.7$ and 1.9 are indicated as blue dashed lines.

fact results from the definition of the minimum dwell time t_c , thus minimum possible values of $t_{\text{on/off}} > t_c = 1$. Intermediate intensities in the mentioned intervals are thus only possible with participation of exactly two events, which limits their occurrence. Interval extensions decrease with $\frac{t_c}{t_{\text{bin}}}$. The occurrence of bins at intensity $0.5 I_{\text{on}}$ is increasing with t_{bin} , but saturates at long bin times. Blue dashed lines in Fig. 5.3 b) again mark the input power law. With increasing t_{bin} also deviations of the detected dwell time histograms from this slope increase. However, most deviations already occur for a bin time of $10 t_c$. Deviations similarly saturate at longer bin times.

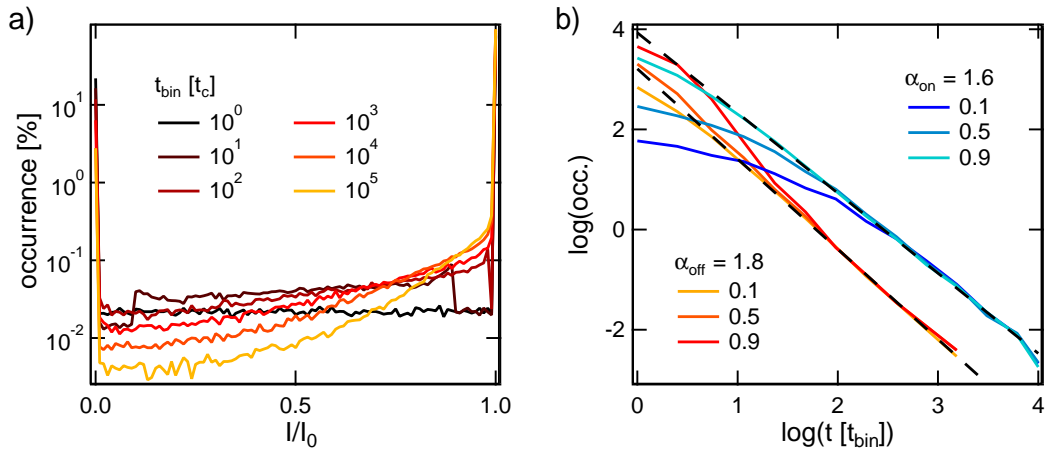


Figure 5.4: Simulations of power law blinking for $\alpha_{\text{on}} = 1.6$ and $\alpha_{\text{off}} = 1.8$ for different bin times t_{bin} . a) Intensity histograms. b) Dwell time histograms of on- (blue color scale) and off-states (red color scale) for thresholds 0.1, 0.5 and 0.9 at a bin time $t_{\text{bin}} = 10^4 t_c$. Dashed lines indicate slopes corresponding to $\alpha_{\text{on}} = 1.6$ and $\alpha_{\text{off}} = 1.8$, respectively.

5.1.3 Different Power Law Exponents

At a bin time $t_{\text{bin}} = 10^4 t_c$ the same simulation is performed for different exponents $\alpha_{\text{on}} = \alpha_{\text{off}}$ between 1.5 and 2. Corresponding intensity histograms are depicted in Fig. 5.3 a). They show an increasing amount of intermediate intensities with increasing exponent $\alpha_{\text{on/off}}$, forming a local maximum at $0.5 I_{\text{on}}$. The corresponding off-state probability histograms for thresholds 0.1 (solid line) and 0.9 (dashed line) are depicted in 5.3 b). For a time-trace of equal length the number of events also increases with the power law exponent. Histograms are thus normalized by the number of detected events and presented as the probability p of a given dwell time. The threshold dependence of the observed dwell time histograms strongly increases with the exponent. For $\alpha_{\text{on/off}} = 1.5$ no difference between thresholds 0.1 and 0.9 is found. For $\alpha_{\text{on/off}} = 1.9$ observed statistics deviate strongly except for events $> 400 t_{\text{bin}}$. Again for a threshold of 0.1 and the tail of long events the input power law distributions (blue dashed lines) are closely followed for all exponents. The onset of this power law tail shifts to longer times for higher thresholds and higher exponents.

5.1.4 Distinct On- and Off-State Exponents

In several experiments very similar exponents for on- and off-states were found, suggesting them to be equal. However, from most measurements distinct exponents are extracted, that can differ considerably. When two different exponents describe on- and off-states, the occupation of the state with the lower exponent will eventually dominate in time and blinking will be suppressed. Fig. 5.4 a) shows intensity histograms for $\alpha_{\text{on}} = 1.6$ and $\alpha_{\text{off}} = 1.8$ at different t_{bin} . The histogram at $10 t_{\text{bin}}$ (dark brown line) shows the same artifact as discussed in Sec. 5.1.1. Not only the occupation of the on-state increases with longer t_{bin} . Also the number of bins at intensities close to the on-state increases and with it the number of detected events. For $t_{\text{bin}} = 10^4 t_c$ on- and

off-state histograms for thresholds 0.1, 0.5 and 0.9 are displayed in 5.4 b). A close threshold for both states (0.1 for the off-, 0.9 for the on-state) still ensures an extraction of input statistics. Deviations from this threshold (e. g. a threshold of 0.5) appear stronger for the on-state histogram, the one with the lower exponent. With decreasing threshold the number of short events in both histograms decreases. This is observed as a bending of the on-state histogram while the off-state histogram approaches slope corresponding to the input exponent.

5.1.5 Discussion

Simulations here show that at a limited time resolution of $t_{\text{bin}} \gg t_c$ binning and thresholding will only reliably return input power law statistics for exponents $\lesssim 1.6$ and equal for on- and off-state. Else a threshold dependence will be observed that strongly depends on the actual time resolution and exponents. Input statistics are only returned for long events or low thresholds for the off-state and high thresholds for the on-state. Detected short time statistics at unsuitable thresholds can completely mask underlying dynamics.

5.1.5.1 Threshold Dependence

A threshold dependence of the determined power law exponent has also been observed in experiments [49, 55]. For comparison between measurements of different QDs a common threshold of several times the standard deviation of the off-states is often defined [55, 134]. It is expected that such a threshold works equally well for all QDs. It is further assumed that any threshold will work equally well for both, on- and off-states. As simulations show here, this is not the case. Only low thresholds are found suitable for extraction of off-state statistics and high thresholds for on-state statistics. Unresolved blinking events sum up to intermediate intensities in the time-trace. The threshold determines whether they are counted as on or off. A low threshold assigns all bins of intermediate intensity as on-events. It will thus ignore off-events shorter than the bin time. Not only unresolved events, but also switching between longer on- and off-events leads to a bin of intermediate intensity. Thus, all detected off-events are randomly shortened at beginning and end, which can add up to a maximum of $2t_{\text{bin}}$. This will slightly shift the observed off-states histogram on the time axis by $\approx 1t_{\text{bin}}$. On the logarithmic scale such a shift is only relevant for the shortest events comparable to t_{bin} . Those show a slightly lower occurrence than expected. At a threshold of $0.1I_{\text{on}}$ this deviation is only observed for the first two bins in the histograms of Figs. 5.1 c) and 5.4 b), thus off-events $\leq 2t_{\text{bin}}$. No further deviations are expected for the off-state at low or the on-state at high thresholds. Input statistics are thus reliably extracted. At high thresholds all intermediate intensities are assigned as off-events. Here unresolved short on-events that would separate two off-events are ignored. Adjacent off-events are thus combined to longer events. This reduces the probability of short and increases that of long events in the histogram. A bending is observed (orange line in Fig. 5.1 c)). While on-events shorter than the bin time are ignored, short off-events are all registered at least with a length of one bin. This leads to an increase of short events especially at a threshold of $0.5I_{\text{on}}$ (red line in Fig. 5.1 c)). Thus, at low thresholds a much stronger

distortion of the on-state distribution is observed than of the off-state distribution. The opposite applies at high thresholds. A first rule for good threshold placement can thus be extracted.

1. The best threshold to obtain on- or off-state distributions lies *as close as possible* to the on- or off-state intensity, respectively. This implies choosing different thresholds for on- and off-state distributions.

For time-series analysis and correlations between subsequent events such independent thresholds are not possible as the order of events is important. The phrase *as close as possible* further indicates the limit of good threshold placement in experiments. It is set by the inherent shot-noise (see Sec. 5.2.2 and 5.2.4) and in some cases also an unknown on-state intensity. The on-state intensity can be unknown, when no clear peak is observed in the intensity histogram e. g. due to a very short cut-off. However, the absence of such a peak already indicates an insufficient time resolution for on-state statistics. Typical thresholds of a few times the off-state's standard deviation lie close to the off-state. They are thus only suitable for determination of off-state statistics and often completely inadequate for on-state statistics.

Simulations further show, that the influence of the threshold is characterized by its on-state fraction T/I_{on} . For identical parameters identical distributions will only be obtained with a threshold at the same on-state fraction. A second important rule can thus be stated.

2. When comparing statistics of different emitters, a threshold should be chosen at the same on-state fraction.

This again is experimentally limited by a reliable determination of the on-state intensity and different noise levels for different emission intensities. Typical thresholds at the same total intensity (e. g. a few times the off-state's standard deviation) lie at a completely different on-state fraction for emitters of high intensity than those of low intensity. The determined on- and off-state distributions then show deviations simply due to the threshold dependence without any physical relevance.

A power law fit always suffers from low statistics at long dwell times. Short times are a lot more frequent and usually appear as more reliable. Unresolved events, however, exclusively distort these most frequent events. The number of detected events at a given threshold closely follows the number of intermediate intensities at that threshold. A higher number of events at a given threshold thus only feigns better accuracy. The seemingly better statistics can even destroy the accordance of underlying and detected distributions. For increasing thresholds from 0.1 to 0.5 in Fig. 5.1 b) the number of detected events more than doubles. The histogram in c) shows that merely short off-events are added that do not follow the input power law distribution. A third rule can thus be formulated for the extraction of power law exponents.

3. Highest emphasis should be laid on the longest events as they are the least distorted.

For high statistics as in the simulations here, the power law tail is always observed and a fitting to this tail is intuitive. However, when the number of detected events is low or statistics exhibit a cut-off, those long events are hardly observed. Only short events can be and commonly are evaluated. Those often do not reflect the underlying statistics.

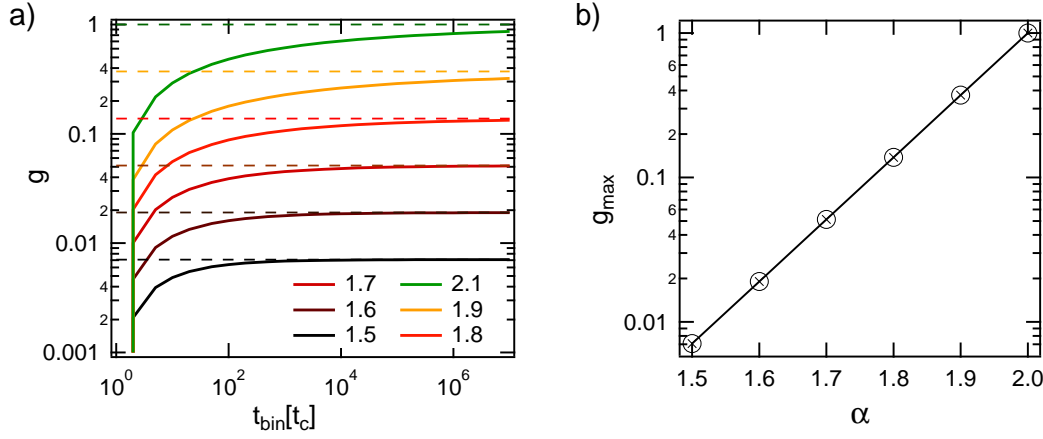


Figure 5.5: a) Fraction of time spent in events shorter than the bin time t_{bin} for different t_{bin} according to Eq. (5.1). Maximum time is set to $t_{\text{max}} = 10^4 t_{\text{bin}}$. Different exponents $\alpha_{\text{on}} = \alpha_{\text{off}}$ are plotted in the indicated colors. Asymptotic limits of Eq. (5.2) are indicated as dashed lines and plotted in dependence on exponent in b).

5.1.5.2 Bin Time Dependence for Different Exponents

With increasing power law exponent the relative amount of short dwell times increases with respect to long dwell times. For exponents ≥ 2 a time average would be obtained at long bin times, leading to an average constant intensity at $0.5 I_{\text{on}}$. The influence of averaging thus also increases for exponents approaching 2, which is observed in the increasing local maximum at $0.5 I_{\text{on}}$ with bin time (Fig. 5.2 a)) and exponent (Fig. 5.3 a)). The relative amount of bins at intermediate intensity in a time-trace is closely related to the time spent in blinking events shorter than the bin time. At given t_{bin} , α and t_{max} the fraction g of the total time spent in states shorter than t_{bin} is given by

$$g = \frac{\int_{t_c}^{t_{\text{bin}}} t \cdot t^{-\alpha} dt}{\int_{t_c}^{t_{\text{max}}} t \cdot t^{-\alpha} dt} = \frac{(t_{\text{bin}}/t_c)^{2-\alpha} - 1}{(t_{\text{max}}/t_c)^{2-\alpha} - 1} \quad (5.1)$$

For long $t_{\text{bin}} \gg t_c$ the fraction g asymptotically reaches

$$g \rightarrow g_{\text{max}} = \left(\frac{t_{\text{bin}}}{t_{\text{max}}} \right)^{2-\alpha} \quad t_{\text{bin}} \rightarrow \infty \quad (5.2)$$

Eq. (5.1) and (5.2) are demonstrated in Fig. 5.5 a) and b) for different exponents and $t_{\text{max}} = 2 \cdot 10^4 t_{\text{bin}}$ as in the simulations. The relative time spent in events shorter than t_{bin} increases with bin time and approaches g_{max} . This saturation at g_{max} implies a decreasing influence of an increasing t_{bin} also on dwell time histograms. This is observed in Fig. 5.2. At a threshold 0.9 the strong distortion after binning to $10 t_c$ only slightly increases for binning to $10^5 t_c$. The time needed for saturation is longer for high exponents. For $\alpha_{\text{on/off}} = 1.5$ unresolved events never amount to more than $g = 0.7\%$ of the total time, while they reach up to $g = 14\%$ for $\alpha_{\text{on/off}} = 1.8$. All time spent in unresolved events will be found in intermediate intensity bins and inevitably result in false occurrence data. Consequently, statistics for higher exponents are distorted more

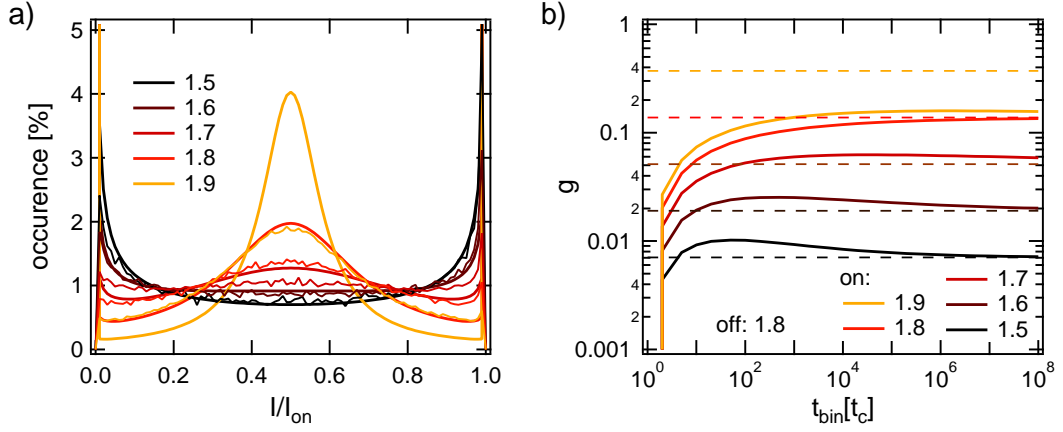


Figure 5.6: a) Comparison of intensity histograms of Fig. 5.3 a) at $t_{\text{bin}} = 10^4 t_c$ (thin lines) with the long-time limit of Eq. (5.3) (thick lines). Histograms of Fig. 5.3 a) are normalized to their total number of bins at intermediate intensity. b) Fraction of time spent in events shorter than the bin time for an off-state exponent $\alpha_{\text{off}} = 1.8$ and different indicated on-state exponents at $t_{\text{max}} = 2 \cdot 10^4 t_{\text{bin}}$ according to Eq. (A.4) of the appendix. Dashed lines are limits of Eq. (5.2) for the on-state exponent.

severely as observed in Fig. 5.3 b). They will additionally show a remaining bin time dependence even for $t_{\text{bin}} \gg t_c$ as saturation takes longer.

The long-time limit, thus $t_{\text{bin}} \rightarrow \infty$, of the intensity histogram for two-state power law blinking has analytically been investigated by Margolin et al. [205] and Sibatov and Uchaikin [207]. For $1 < \alpha_{\text{on}} = \alpha = \alpha_{\text{off}} < 2$ the distribution of intermediate intensities $p(i)$ with $i = I/I_{\text{on}}$ and $0 < i < 1$ follows the Lamperti equation ($m = \alpha - 1$)

$$p(i) = \frac{\sin(\pi m)}{\pi} \frac{i^{m-1}(1-i)^{m-1}}{i^{2m} + (1-i)^{2m} + 2\cos(\pi m)i^m(1-i)^m} \quad (5.3)$$

which for $\alpha = 1.5$ is abbreviated to

$$p(i) = \frac{1}{\pi \sqrt{i(1-i)}} \quad (5.4)$$

For all $\alpha \lesssim 1.5946$ [208] a minimum is observed at the intuitive average intensity $i = 0.5$. For higher α a local maximum emerges leading to a divergence in the ergodic regime ($\alpha \geq 2$), due to the existence of a time average. For $\alpha < 2$ the probability, that either one state dominates the average, is still highest and divergence is observed for $i = 0$ and $i = 1$.

Eq. (5.3) (thick solid lines) is plotted in Fig. 5.6 a) together with the integral-normalized histograms of Fig. 5.3 c) (thin solid lines). For $\alpha = 1.5$ and 1.6 the simulated histograms for $t_{\text{bin}} = 10^4 t_c$ agree well with the distribution of the long-time limit. Simulated histograms of higher exponents show increasing deviations. As was observed in Fig. 5.5 a), for higher exponents a longer time is needed to reach the asymptotic limit. At $t_{\text{bin}} = 10^4 t_c$ the contribution of unresolved events is already close to this maximum limit for exponents ≤ 1.6 . Thus, intensity histograms agree well. For higher exponents saturation is only reached at longer t_{bin} .

5.1.5.3 Distinct Exponents for On- and Off-State Distributions

The data extraction for power law blinking with different exponents for on- and off-state has not yet been examined before. In experiments, however, very different exponents are often assigned to the two states. Fig. 5.4 b) shows that especially such a difference corrupts the performance of the threshold method. Most importantly, it specifically distorts the extracted distribution of the lower exponent.

Like for $\alpha_{\text{on}} = \alpha_{\text{off}}$ in Eq. (5.1), the fraction of time spent in unresolved states for a given t_{max} can also be determined for $\alpha_{\text{on}} \neq \alpha_{\text{off}}$ (see Eq. (A.4) of the appendix). The result is displayed in Fig. 5.6 b) for $t_{\text{max}} = 2 \cdot 10^4 t_{\text{bin}}$, an off-state exponent of 1.8 and different on-state exponents. Dashed lines are solutions to Eq. (5.2), thus the asymptotic limits g_{max} for $\alpha_{\text{on}} = \alpha_{\text{off}}$. At long times, the fraction of time spent in unresolved events is determined by the same g_{max} of the lower exponent. The state of the lower exponent will dominate and blinking will be suppressed. This domination is also observed for bins of intermediate intensity. In Fig. 5.4 a) more bins are observed at intensities close to the on-state intensity. Sibatov and Uchaikin [207] also analytically describe the long-time limit of the intensity histogram for different exponents ($1 < \alpha_{\text{on}} \neq \alpha_{\text{off}} < 2$). Qualitatively the same shape is described by the histograms in Fig. 5.4 a) with an accumulation of bins close to the on-state intensity. A threshold at $0.5 I_{\text{on}}$ thus assigns most intermediate intensity bins as on-events. Those bins are biasing the extracted distributions as discussed above. Consequently, the off-state distribution remains almost unaffected, while the on-state distribution is strongly distorted as observed in Fig. 5.4 b). Only thresholds close to the on-state intensity start sorting more and more intermediate intensity bins as off and bias the off-state histogram. The range of suitable thresholds for the state of the lower exponent thus strongly decreases. The performance of binning and thresholding for power law blinking thus strongly depends on the underlying statistics. The determination is less reliable when higher exponents are involved. Similar distortions of extracted statistics from simulations as those presented here have in fact been observed before [43, 49, 159] but mostly ignored. Different performances are especially critical for examinations to changes of the exponent with experimental parameters. Distortions due to a change in exponent might even be more visible in a histogram than the corresponding change in the slope. In addition, they can appear as a different exponent, like a histogram bending. Especially the combination of different on- and off-state exponents should quickly hinder the correct extraction of statistics for both states at the same time. Thus, even without typical experimental limitations (see below) an investigation of power law blinking with binning and thresholding is strongly limited.

5.2 Additional Influences in Experiments

In the previous section strong limitations to the correct observation of power law statistics with binning and thresholding are shown. Reliable observation of underlying power law distributions is only possible at thresholds close to on- or off-state and long events. Experiments, however, show further limitations that even prevent these choices. Next to limited statistics of long events, the most important are an on-time cut-off, noise and real intermediate intensity levels. Influences are discussed below.

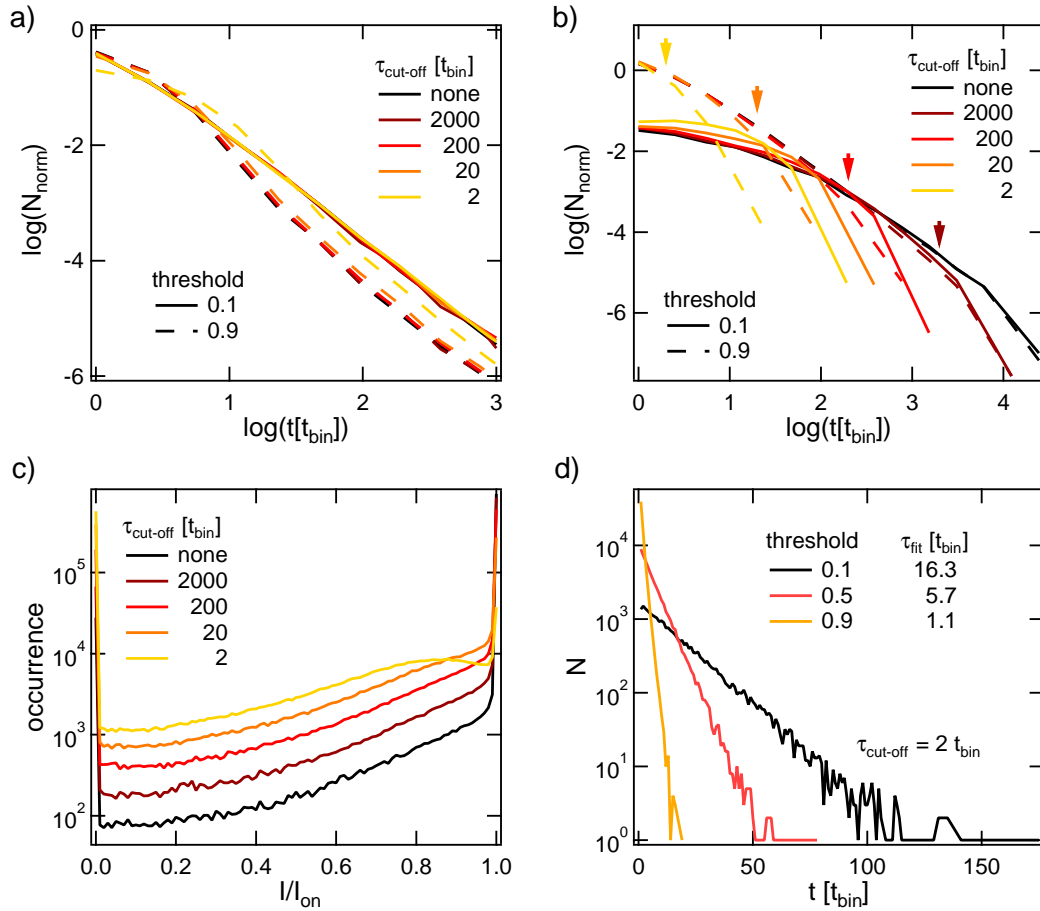


Figure 5.7: Influence of an on-state cut-off on intensity and dwell time histograms. a) Off-state and b) on-state dwell time histograms for $\alpha_{\text{off}} = 1.8$, $\alpha_{\text{on}} = 1.6$, $t_{\text{bin}} = 10^4 t_c$ and different $\tau_{\text{cut-off}}$ at thresholds 0.1 (solid lines) and 0.9 (dashed lines). Histograms are normalized to the number of detected events at threshold 0.1. c) Corresponding intensity histograms. d) On-state histograms on a semi-log scale for $\tau_{\text{cut-off}} = 2 t_{\text{bin}}$ at different thresholds. Results from exponential fits are indicated in the graph.

5.2.1 On-Time Cut-Off

While the power law distribution for off-states is typically found to extend beyond the longest measurement times, the on-state distribution shows an exponential cut-off. In experiments this cut-off shifts to shorter times with higher excitation and temperature [38, 135, 142, 143, 145], representing an activated process. Such a cut-off is also included in the simulations (see Sec. 4.6.2). For a simulation of the same parameters as used for Fig. 5.4 ($t_{\text{bin}} = 10^4 t_c$, $\alpha_{\text{on}} = 1.6$, $\alpha_{\text{off}} = 1.8$) long on-times are eliminated according to different cut-off times $\tau_{\text{cut-off}}$. Effects on dwell time and intensity histograms are shown in Fig. 5.7. Cut-off times $\tau_{\text{cut-off}}$ are given in t_{bin} . Fig. 5.7 a) shows the off-state histograms for different on-time cut-offs and thresholds 0.1 (solid lines) and 0.9 (dashed lines). A cut-off decreases the appearance of long on-events thus increases the total number of events. For a better comparison of histograms, they are thus normalized for each cut-off to the number of detected events at threshold 0.1. No

influence in the shape of off-state histograms is observed except for very short cut-off times ($\tau_{\text{cut-off}} = 2t_{\text{bin}}$) at high thresholds (0.9). The on-state histograms in Fig. 5.7 b) naturally lack long on-events. Events shorter than the cut-off are not influenced except for very short cut-offs and low thresholds (0.1). An on-state cut-off decreases the occurrence of the maximum intensity in a time-trace and increases that of zero and intermediate intensities (see intensity histograms in c)). Very short cut-offs $\lesssim t_{\text{bin}}$ even shift the occurrence maximum of intermediate intensities away from 1^1 (yellow line), due to the existence of a time average. This increase of intermediate intensity bins eventually further distorts on- and off-state histograms depending on the threshold falsely assigning them to either state.

For $\tau_{\text{cut-off}} \lesssim 200t_{\text{bin}}$ a shift is observed of the apparent cut-off time to longer times with lower thresholds (compare solid and dashed lines in Fig. 5.7 c)). The determined on-state distribution for very short $\tau_{\text{cut-off}}$ of only $2t_{\text{bin}}$ appears purely exponential for all thresholds. The apparent average dwell time increases with decreasing threshold (see Fig. 5.7 d)). At high thresholds (0.9, yellow line) it is shorter ($1.1t_{\text{bin}}$) at low thresholds (0.1, black line) longer ($16.3t_{\text{bin}}$) than the real cut-off time ($2t_{\text{bin}}$).

5.2.2 Poisson Noise

In contrast to the simulations presented above, the measurement of intensity time-traces in experiments is always accompanied by noise. On- and off-state are characterized by an average intensity. Noise results in a distribution of intensity bins around this average intensity in the time-trace. As is intuitively expected and has been stressed [55, 56] for correct statistics a threshold needs to lie outside of the noise of either state. In single particle spectroscopy, when single photons are counted, this noise is dominated by the photon statistics of the excitation laser. It follows a Poisson distribution (see Eq. (4.18)). Also electronic shot noise is Poisson distributed. Poisson noise for a typical signal to background ratio of 100 : 2 (10 ms binning, 200 cps background (off-state at 2 cpb), 10 kcps signal (on-state at 102 cpb)) is added to the simulation of $\alpha_{\text{on}} = 1.6$ and $\alpha_{\text{off}} = 1.8$ at $t_{\text{bin}} = 10^4$ (see Fig. 5.4 without noise). The resulting analysis is shown in Fig. 5.8. Like in experiments a linear axis is chosen for the intensity histogram in a). To compare occurrence histograms of different thresholds with those without noise, the same on-state fraction is chosen. While a threshold of 12 cpb (0.1) already exceeds the noise of the off-state, all thresholds above 62 cpb (0.6) still fall in the on-state noise. Fig. 5.8 b) demonstrates that thresholds outside the noise (markers) lead to the same histograms as the corresponding thresholds to traces without noise (dashed lines). The effect of higher thresholds in the on-state noise is depicted for the off-states in Fig. 5.8 c) and for the on-states in d). Dashed lines are again without noise. The off-states show an increasing amount of very short events with thresholds deeper in the noise. Long events are unaffected. The on-state histograms immediately show a cut-off when the threshold enters the noise. Long on-events are suppressed as during long on-states the threshold is crossed by the noise. Instead these longer events, that are “cut off” by the noise are found at intermediate length. A small hump is observed

¹For equal exponents $\alpha_{\text{on}} = \alpha_{\text{off}}$ or a lower off-state exponent $\alpha_{\text{on}} > \alpha_{\text{off}}$ the occurrence maximum is found at $0.5I_{\text{on}}$ (see Fig. 5.3 a)) or 0, respectively.

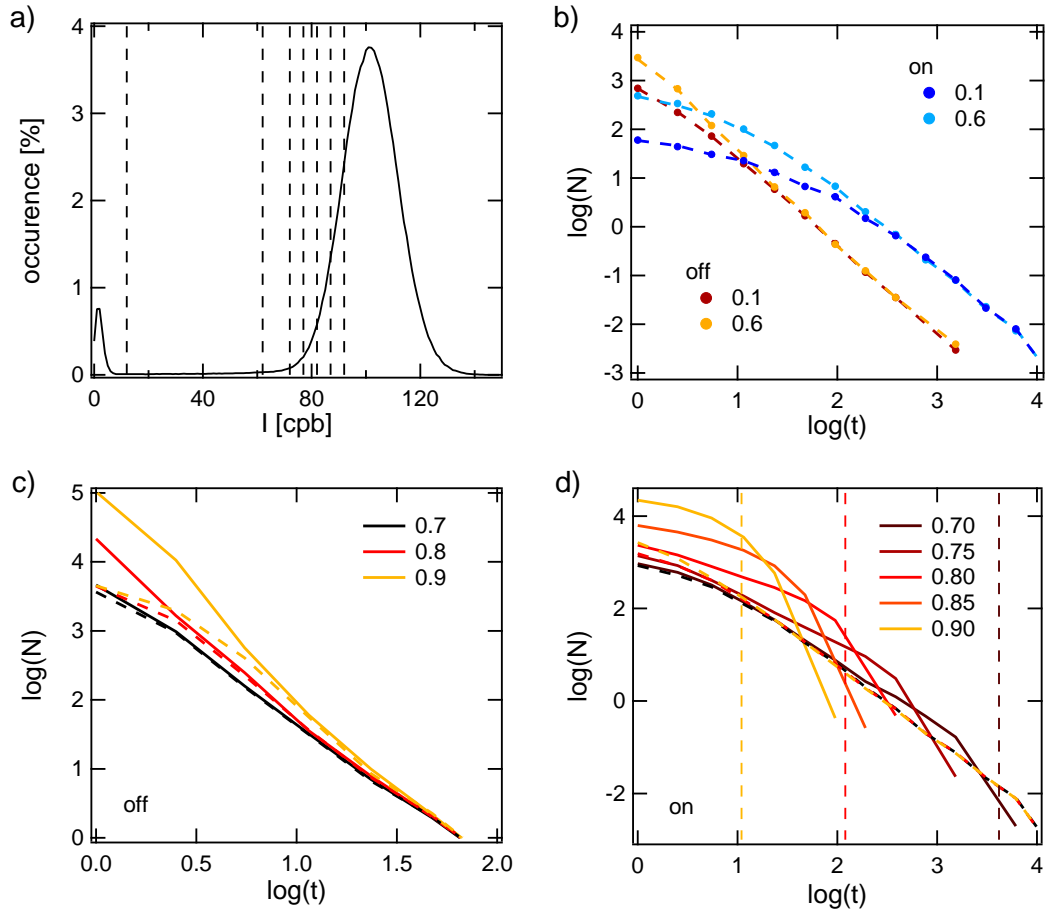


Figure 5.8: Influence of Poisson noise with 100 signal and 2 background counts per bin on a time-trace with $\alpha_{\text{off}} = 1.8$, $\alpha_{\text{on}} = 1.6$ and $t_{\text{bin}} = 10^4 t_c$. a) Intensity histogram with the investigated thresholds in b)-d) as dashed vertical lines. b) On- and off-state histograms for thresholds outside of the noise (markers) compared to simulations without noise (dashed lines). c) Off-state and d) on-state histograms at thresholds in the on-state noise (solid lines). Dashed lines show histograms without noise. Dashed vertical lines are estimated cut-offs with Eq. (5.6). Thresholds are referred to by their on-state fraction.

in the histogram just before the cut-off. Hump and cut-off move to shorter times with increasing threshold and mask the underlying power law statistics.

5.2.3 Intermediate Intensity Levels

In experiments also “real” intermediate intensity levels are observed in addition to merely unresolved blinking events. They can be distinguished from unresolved blinking events by different excited state decays [172, 173]. Sometimes a fixed intensity level just above the background intensity exists, like the one found in this work (see Sec. 5.3.4 and [209] as well as [75, 210]). Typically a continuous distribution of intensity levels between maximum and background intensity is observed [172, 173]. Such continuous distributions are expected to stem from charges in the close environment

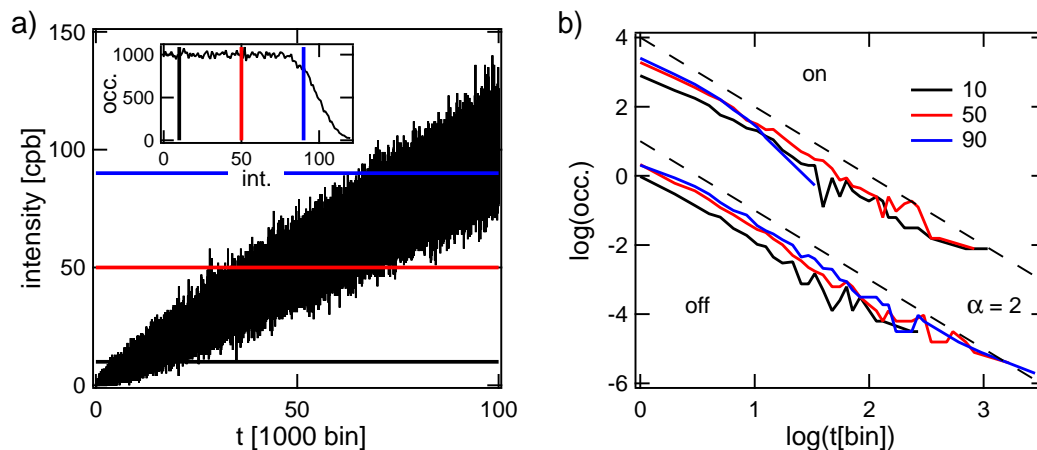


Figure 5.9: a) Time-trace of $10^5 t_{\text{bin}}$ length with linearly increasing intensity from 0 to 100 cpb exhibiting Poisson noise. Inset: Corresponding intensity histogram. b) Dwell time histograms of on- and off-state (offset for clarity) obtained with the threshold analysis at the thresholds marked in a). Dashed lines indicate slopes corresponding to $\alpha = 2$.

leading to Auger decay and spectral diffusion. Their dwell time statistics have not yet been modeled. To get an idea of a possible influence of a continuous distribution of intensity levels a simple time-trace of $10^5 t_{\text{bin}}$ length with linearly increasing intensity from 0 to 100 cpb and Poisson noise (see Fig. 5.9 a)) is investigated at different thresholds. The intensity histogram is shown in the inset and thresholds at 10, 50 and 90 cpb shown in black, red and blue, respectively. The resulting dwell time histograms in the same colors are displayed in Fig. 5.9 b). They all resemble an inverse power law of exponent $\alpha \approx 2$ (black dashed lines) for up to three decades.

5.2.4 Discussion

If a limited time resolution was the only experimental limitation, true power laws would still reliably be observed at suitable thresholds or for long events. Experimental noise, however, prevents the choice of suitable thresholds close to on- and off-intensities as it introduces a cut-off for long events. Good choices for thresholds are more limited for the on-state distribution due to its higher total noise (see below). In addition, also the examination of long events at other thresholds is limited for the on-state. They are cut off by an activated process. The more robust observation of off-state power laws is thus not surprising. For the definition of thresholds as “out of the noise” and a reliable separation of noise-induced and real cut-offs, noise contributions to dwell time histograms have to be estimated.

5.2.4.1 Noise-Induced Cut-Offs

When single photons are counted the detected signal will always suffer from inherent noise with statistics given by the Poisson distribution (Eq. (4.18)). For an average count rate per bin N the standard deviation of the Poisson distribution is given by \sqrt{N} . It is thus considerably higher for the on-state with respect to the off-state, albeit with

an increasing signal to noise ratio N/\sqrt{N} . When a threshold needs to be placed at a distinct on-state fraction the reference signal is the count rate of the on-state N_{on} . With a count rate N_{off} of the off-state the ratio $\sqrt{N_{\text{off}}}/N_{\text{on}}$ defines possible threshold placements close to the off-state and $\sqrt{N_{\text{on}}}/N_{\text{on}}$ those close to the on-state. As $\sqrt{N_{\text{off}}} \ll \sqrt{N_{\text{on}}}$, suitable thresholds are inherently better accessible for the off-state. Binning the data to longer t_{bin} also reduces \sqrt{N}/N and allows thresholds at higher and lower on-state fractions. If the number of events remains high enough, this can reduce distortions of the histogram, despite the longer bin time.

Fig. 5.8 b) shows that thresholds outside the noise of either state do not influence the determined dwell time histograms. As soon as they are placed in the noise of the on-state, long on-events and short off-events start to be affected. Thresholds in the off-state noise accordingly affect long off- and short on-events (not shown). As becomes obvious in Fig. 5.8 and has been discussed before [55, 56], placing the threshold in the on-state noise leads to an exponential cut-off in the on-state histogram. Thus, a placement outside the noise is imperative. Assuming pure Poisson noise, the induced cut-off $\tau_{\text{on/off}}(T, N)$ for a threshold at count rate T and a given on- or off-state count rate N can be estimated with the sum over Eq. (4.18)

$$P(T, N) = \sum_{k=0}^{T-1} p_N(T) = \frac{\Gamma(T, N)}{\Gamma(T)} \quad (5.5)$$

with the incomplete and ordinary gamma functions $\Gamma(T, N)$ and $\Gamma(T)$, respectively. Intensities $< T$ are counted as off and those $\geq T$ as on. $P(T, N)$ gives the fraction of bins that lie below the threshold during on-events. As their appearance is completely independent they are exponentially distributed in time. Long events are thus interrupted at a rate $R(T, N) = P(T, N)/t_{\text{bin}}$. For a given count rate N_{on} and threshold T the noise-induced on-time cut-off will thus be found at $\tau_{\text{on}} = R^{-1}(T, N_{\text{on}})$ and accordingly the off-time cut-off at $\tau_{\text{off}} = [1 - P(T, N_{\text{off}})]^{-1}t_{\text{bin}}$ leading to

$$\tau_{\text{on}}[t_{\text{bin}}] = \frac{\Gamma(T)}{\Gamma(T, N_{\text{on}})} \quad \tau_{\text{off}}[t_{\text{bin}}] = \left[1 - \frac{\Gamma(T, N_{\text{off}})}{\Gamma(T)}\right]^{-1} \quad (5.6)$$

Cut-offs appearing at $\tau_{\text{on/off}}$ are thus simply noise induced. Only shorter cut-offs can describe physical processes.

The observed additional short off-events in Fig. 5.8 c) will accordingly follow an exponential distribution of time constant $\tau'_{\text{off}} = (1 - \tau_{\text{on}}^{-1})^{-1}$. Thresholds close to the off-state will equally induce short on-events with time constant $\tau'_{\text{on}} = (1 - \tau_{\text{off}}^{-1})^{-1}$ (not shown). The weight of this additional exponential distribution increases with the time spent in the corresponding state close to the threshold. For the example of Fig. 5.8 with count rates 2 cpb and 102 cpb for off- and on-state, respectively, the expected cut-off times $\tau_{\text{on/off}}$ and additional time constants $\tau'_{\text{on/off}}$ are plotted dependent on threshold in Fig. 5.10 a). The predicted on-time cut-offs at $11t_{\text{bin}}$ for $T = 0.9I_{\text{on}}$, $120t_{\text{bin}}$ for $T = 0.8I_{\text{on}}$, and $4170t_{\text{bin}}$ for $T = 0.7I_{\text{on}}$ correspond well to those observed in Fig. 5.8 d) (dashed vertical lines). The estimation of noise induced cut-offs according to Eq. (5.6) has not been reported before. It is expected to be very helpful with the confirmation of the assignment of physical cut-offs. Especially for overlapping Poisson peaks of on- and off-state, thresholds completely outside of noise are not possible. Cut-off times shorter than those given in Eq. (5.6) can then still be assigned.

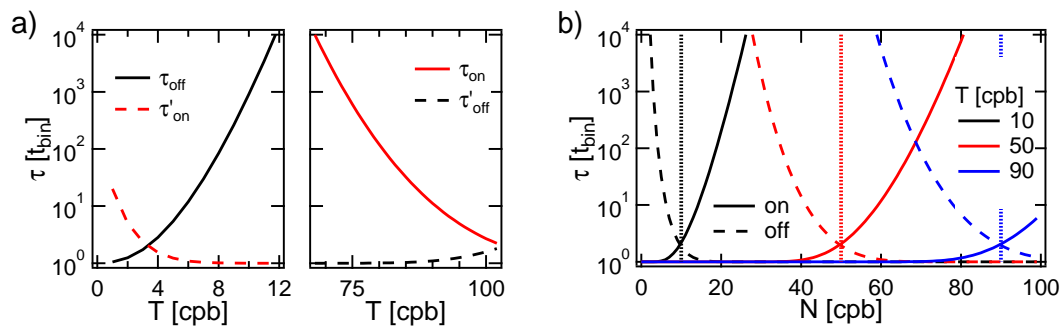


Figure 5.10: a) Estimated on- and off-state cut-off times $\tau_{\text{on/off}}$ as well as time constants $\tau'_{\text{on/off}}$ according to Eq. (5.6) for an off-state count rate of 2 cpb (left) and an on-state count rate of 102 cpb (right) for different thresholds T . b) Estimated times $\tau_{\text{on/off}}(T, N)$ according to Eq. (5.6) for three different thresholds and count rates N between 0 – 100 cpb.

5.2.4.2 Determination of the On-State Cut-Off

The appearance of an on-state cut-off not only limits accessible time-scales to determine power law distributions. Its sensitivity to experimental conditions also introduces a new parameter to manipulate and characterize intermittency. A correct determination of $\tau_{\text{cut-off}}$ is thus desired. As discussed above, a threshold T needs to be chosen such that the determined cut-off time is shorter than those given in Eq. (5.6). Due to limited statistics the total measurement time τ_{tot} additionally limits the accessible range of cut-off times to $< 0.1 \tau_{\text{tot}}$. Cut-off times shorter than $10 t_{\text{bin}}$ do also not allow enough sampling [55, 56]. They still lead to exponential statistics as in Fig. 5.7 d) but do not allow the correct extraction of the underlying $\tau_{\text{cut-off}}$. Even for $10 t_{\text{bin}} < \tau_{\text{cut-off}} < 0.1 t_{\text{tot}}$ and $\tau_{\text{cut-off}} < \tau_{\text{on/off}}$ an increase of the extracted cut-off can be observed with decreasing threshold (compare solid and dashed lines in Fig. 5.7 b)) when it lies in the distorted short events. Only a threshold independent cut-off, thus in the power law tail, ensures the correct determination of $\tau_{\text{cut-off}}$. Else, the extracted cut-off time at high threshold still serves as an upper limit for $\tau_{\text{cut-off}}$. An extraction of power law exponent and cut-off time with Eq. (2.29) requires low distortions, thus usually high thresholds.

5.2.4.3 On-State Power-Laws and the Onset of Blinking

Simulations show that the determination of on-state power law distributions is inherently more difficult than the determination of off-state power laws. The on-state cut-off eliminates the unperturbed long events and the higher noise enforces less suitable thresholds. It almost appears surprising that on-state power law distributions are still observed when exponents are not both close to 1.5. Several extracted power law distributions can only stem from power law switching if the onset of switching is close to the bin time ($t_{\text{bin}} \approx t_c$). A slightly higher time resolution should then reveal a change in statistics, thus the onset t_c of the power law. Longer bin times would lead to the described distortions here. Such a determination of t_c should be very interesting. There are indeed observations that expect t_c on the typical millisecond scale [156], but mostly it is expected to lie at microseconds [43, 44] or even nanoseconds [45]. The knowledge

of a power law onset t_c is interesting for all blinking models. Depending on the model it can be related to the excitation rate, shortest tunnel distances, lowest tunnel barriers, closest trap states or simply a change in power law exponent as for diffusive electron transfer (see Sec. 2.2.2.1). A further investigation to assign t_c , possibly even different t_c for on- and off-state, should thus be interesting.

If typically chosen bin times, however, do not coincide with t_c , other reasons that can lead to the observation of power law distributions have to be considered. Here especially the contribution of intermediate intensity states should be investigated. They are typically found as a continuous distribution between on- and off-intensity. Equal amounts of time are thus spent at each intensity like for the linear increase in Fig. 5.9 a). Each intensity leads to a different induced cut-off according to Eq. (5.6). This is plotted in Fig. 5.10 b) for the three applied thresholds in Fig. 5.9. A time range over four decades is quickly covered within the intensity interval from 0 – 100 cpb. Fig. 5.9 b) shows that the average over those different exponentials can also appear as a power law distribution over several decades in times. The contribution of real intermediate intensity levels to observed dwell time distributions is often neglected. However, depending on their order of occurrence, especially continuously distributed states can quickly lead to power laws themselves.

In addition, particular care should be taken when summing statistics of several QDs. Averaging over different cut-off times or thresholds in the noise of different QD intensities might also leads to power laws. For single QDs, drift or intensity fluctuations can also lead to similar effects as display in Fig. 5.9. All of these effects should be excluded before assigning power law dwell times in on- and off-state. While off-state power laws extend over at least four decades in time, on-state power laws rarely extend over three decades. Often only two are observed, typically limited by the cut-off. Those can easily be obtained from a combination of the described averaging processes here.

5.3 Comparison to Experiments

Simulations show that binning and thresholding should be applied very carefully on experimental data. Several artifacts have been demonstrated that should be observed for power law statistics of on- and off-state. These expectations will now be compared to experimental data. As discussed in the previous chapter, the summing of statistics from multiple QDs could induce power law appearance simply due to different exponential cut-offs (real or noise-induced). Thus, statistics of two single QDs are representatively investigated. Time-traces are recorded in the confocal setup with a pulsed 470 nm blue laser diode. This not only allows more flexible binning of the single photons than wide field detection. It also allows the determination of the excited state lifetime for an estimation of the contribution from intermediate intensity levels.

5.3.1 Influence of Bin Time and Threshold

The evaluation of a typical QD at 100 nW excitation power in the on-state is shown for bin times of 5 ms and 0.5 ms in Fig. 5.11. For both bin times dwell time distributions

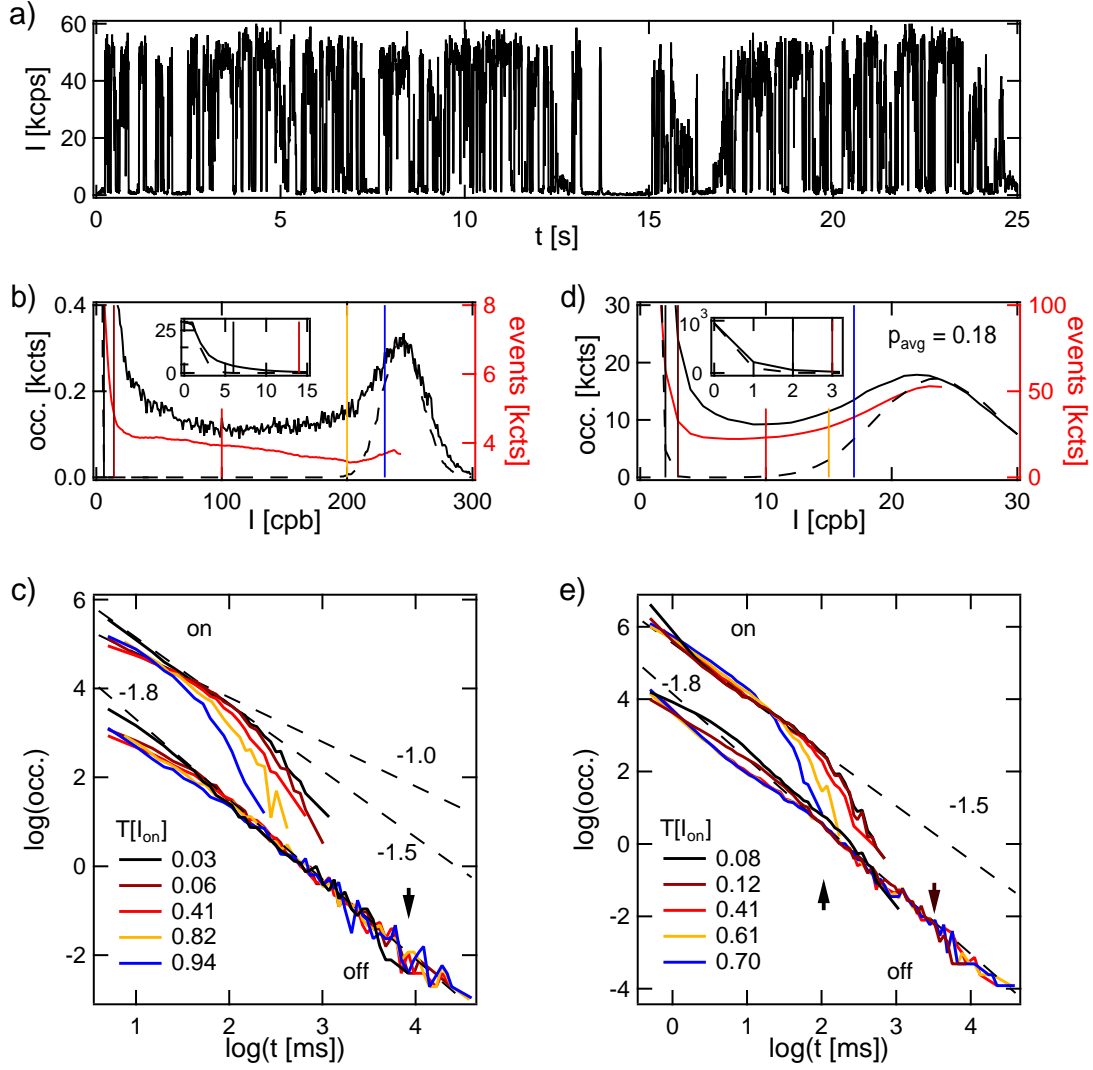


Figure 5.11: Analysis of an 800 s time-trace of a single QD (Fort Orange, $\lambda_{\text{em}} = 600$ nm) excited at 100 nW. a) Segment of the time-trace at 5 ms binning. b) & d) Histograms at 5 ms and 0.5 ms binning (black lines), respectively. They are zoomed in to show the on-state peak. Red lines mark the number of detected events at different thresholds. Insets show a zoom to the off-state peak. Black dashed lines indicate Poisson distributions of average off- and on-state count rates. c) & e) Dwell time histograms for on- and off-state at 5 ms and 0.5 ms binning, respectively. On-states are offset for clarity. Dashed lines indicate slopes of -1.8 , -1.5 and -1 as guide to the eye. Thresholds are indicated by the same color in b) & d) and referred to by their on-state fraction.

are extracted with different thresholds and presented in c) and e).

Dwell time histograms for the off-state follow a robust linear dependence in the log-log plot for dwell times $t_{\text{off}} > 100$ ms independent of threshold or bin time. A slope of ≈ -1.8 is observed (dashed line).² Deviations from this slope are observed for short times. At 5 ms binning they decrease with thresholds below $T < 0.06 I_{\text{on}}$ (brown

²Per definition, in Eq. (1.1) positive power law exponents correspond to negative slopes in log-log plots.

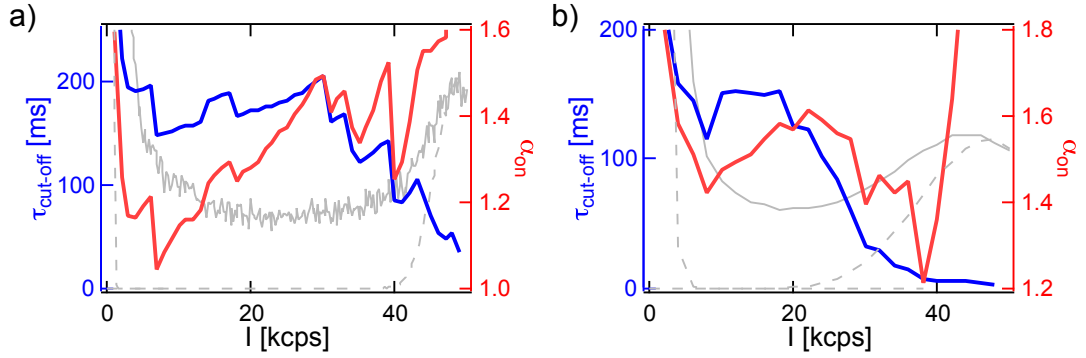


Figure 5.12: Fit results of Eq. (5.7) to on-state distributions of Fig. 5.11 at different thresholds for a) 5 ms binning and b) 0.5 ms binning. Thresholds are referred to by their total count rate I in kcps. Intensity histograms are included in arbitrary units in gray for comparison.

and black). At thresholds in the off-state noise (black, for 0.5 ms binning also brown) long events are missing as indicated by the arrows. At the same time the number of extracted short dwell times $t_{\text{off}} < 100$ ms increases. At thresholds in the on-state noise (yellow and blue) the number of very short events $t_{\text{off}} \approx t_{\text{bin}}$ increases.

On-state dwell time distributions show the well-known on-time cut-off which is close to 100 ms. They also show an increasing number of very short events $t_{\text{on}} \approx t_{\text{bin}}$ for thresholds in the off-state noise (black, for 0.5 ms binning also brown) and a decreasing number of long events for thresholds in the on-state noise (yellow and blue). The number of long on-events is decreasing with decreasing threshold also for thresholds outside of the on-state noise ($T \gtrsim 0.4I_{\text{on}}$, red line). At 0.5 ms binning a linear slope close to -1.5 (dashed line) is observed for times shorter than the cut-off. At 5 ms binning the short cut-off of only $\approx 20t_{\text{bin}}$ dominates the distribution without a robust linear slope at short times.

A power law with exponential cut-off is fitted to the on-state distributions of both bin times at different thresholds with the variables $\log(t_{\text{on}})$ and $\log(\text{occ.})$ according to

$$\log(\text{occ.}) = A - \alpha_{\text{on}} \cdot \log(t_{\text{on}}) - \frac{10^{\log(t_{\text{on}})}}{\tau_{\text{cut-off}}} \cdot \log(e) \quad (5.7)$$

Fit results are plotted in Fig. 5.12 a) and b). The fitted cut-off time $\tau_{\text{cut-off}}$ strongly decreases with increasing threshold above 30 kcps for 5 ms binning and above 20 kcps for 0.5 ms binning. Fitted exponents are correlated to the cut-off time and mostly increase with increasing threshold. They lie between 1.5 and 1 for 5 ms binning and close to 1.5 for 0.5 ms binning as indicated by the dashed lines in Fig. 5.11 c) and e). The observed on- and off-state peaks in the intensity histograms in Fig. 5.11 b) and d) are only slightly broader than the corresponding Poisson distributions (dashed lines). The expected noise-induced cut-offs are thus also estimated with Eq. (5.6) at different thresholds for the on-state count rates 24 cpb and 240 cpb and off-state count rates 0.1 cpb and 1 cpb, respectively. They are plotted in Fig. 5.13 a) with the corresponding intensity histograms replicated in b) for comparison. The range of thresholds that do not induce a cut-off decreases with decreasing bin time. For cut-offs $\tau_{\text{cut-off}} > 10$ s,

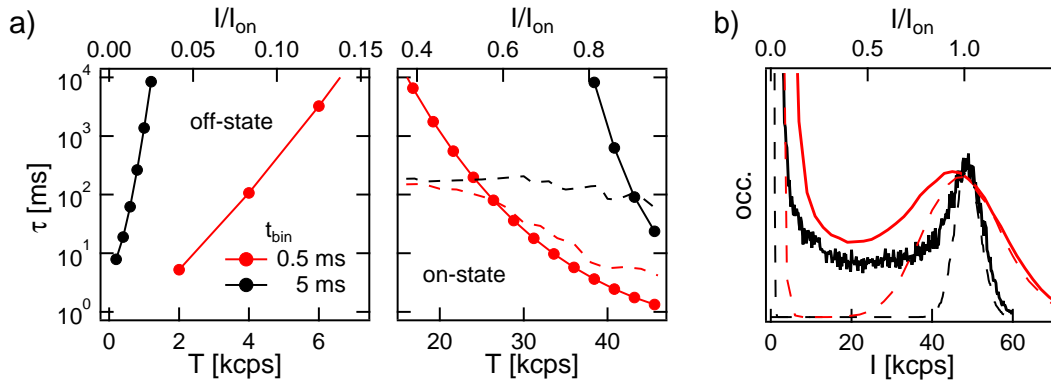


Figure 5.13: a) Expected cut-off times for on- and off-state according to Eq. (5.6) at different thresholds for the QD of Fig. 5.11. Fitted on-state cut-offs of Fig. 5.12 are included as dashed lines. Except for the on-state cut-off at 5 ms binning, the plotted markers increase by 1 cpb, thus mark the only possible thresholds. For the on-state cut-off at 5 ms binning, markers increase by 10 cpb. b) Intensity histograms at different bin times (solid lines) and Poisson distributions of the corresponding count rates of on- and off-state (dashed lines). Data for 0.5 ms binning is plotted in red, for 5 ms in black.

it comprises a range of $0.03 - 0.8I_{\text{on}}$ at a bin time of 5 ms and only $0.15 - 0.4I_{\text{on}}$ at 0.5 ms. Fitted on-state cut-offs of Fig. 5.12 (dashed lines in Fig. 5.13 a)) are mostly shorter than the estimated noise induced cut-off at 5 ms binning. They decrease with the estimated cut-off at 0.5 ms binning for $T > 25$ kcps, but remain a factor of two higher.

5.3.2 Excitation Dependence

The QD in Fig. 5.11 is also investigated at lower excitation powers of 20 nW and 10 nW as presented in Fig. 5.14. Dwell time histograms of all three powers are shown in e). An increasing cut-off time for the on-state with decreasing excitation power is observed as reported in the literature. The QD spends relatively more time in the bright state as also indicated in the time-trace segments and the relative areas of on-state and off-state peak in the intensity histograms. The average on-state fraction $p_{\text{avg}} = I_{\text{avg}}/I_{\text{on}}$, as calculated from the average intensity of the complete time-trace I_{avg} , increases with decreasing excitation power as indicated in the intensity histograms.

Dwell time histograms are demonstrated for two thresholds, one at a low common count rate and the other at a common intermediate on-state fraction. They lie outside of the influence of estimated noise-induced cut-offs according to Eq. (5.6). The off-state distribution is very robust against changes in excitation power with a slope of -1.8 for long times. Deviations from this slope at short times decrease with decreasing excitation power.

The on-state distribution resembles the off-state distribution at short times and also approaches the linear slope of -1.8 at low excitation power. Long times increase in probability with respect to the off-state distribution leading to a long-time hump.

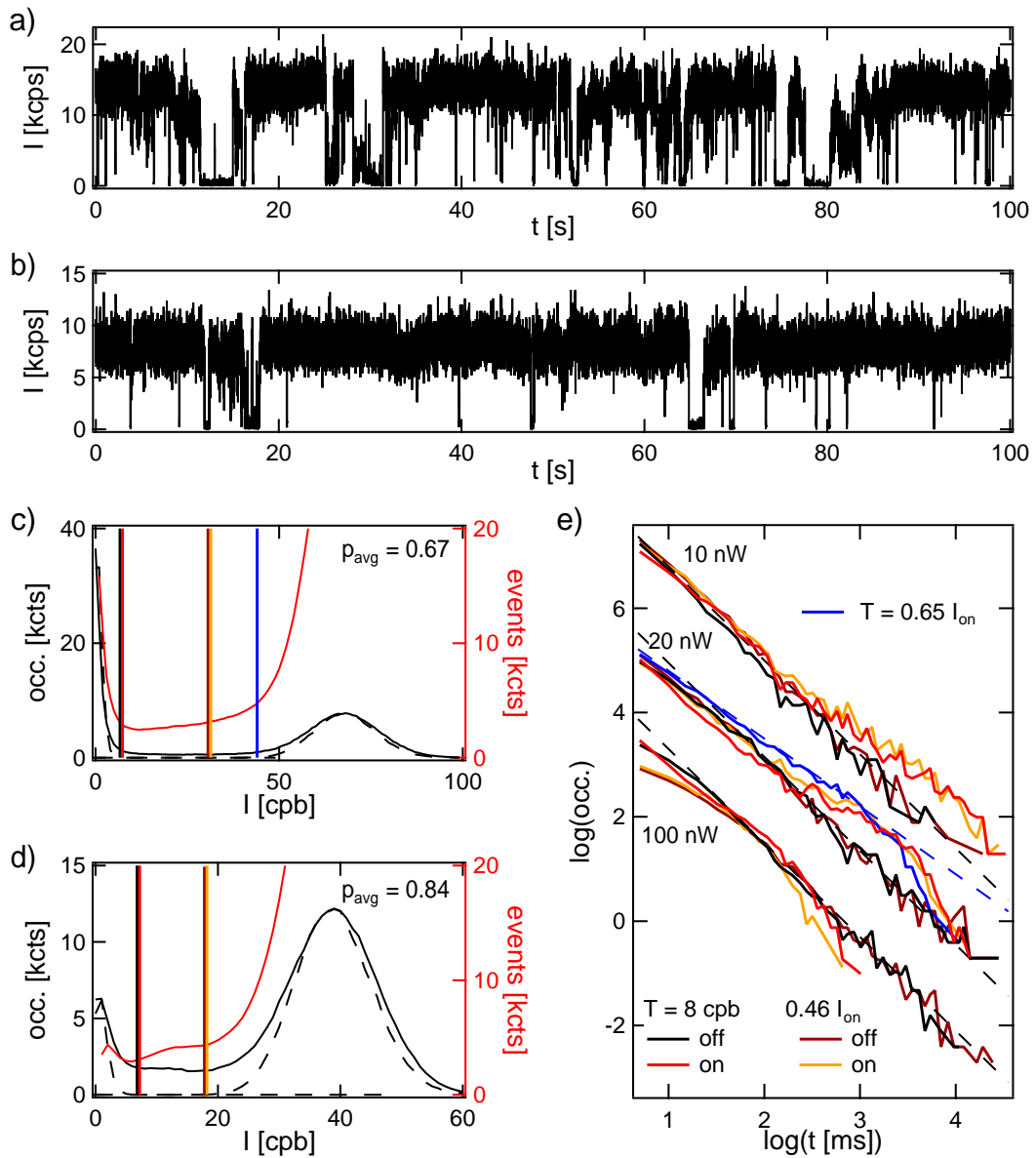


Figure 5.14: Analysis of the same QD as in Fig. 5.11 excited at 20 nW for 1500 s and 10 nW for 1400 s at 5 ms binning. a) & b) 100 s segments of time-traces at 20 nW and 10 nW, respectively. c) & d) Corresponding intensity histograms (black lines) and number of detected events at different thresholds (red lines) at 20 nW and 10 nW, respectively. Black dashed lines indicate Poisson distributions of average off- and on-state count rates. e) Dwell time histograms at different thresholds for all excitation powers. Different excitation powers are offset for clarity. Dashed black lines indicate slopes of -1.8, the blue dashed line a slope of -1.3.

A threshold in the noise of the on-state at 20 nW³ (blue line) resembles a power law with exponential cut-off with $\alpha_{\text{on}} = 1.3$ and $\tau_{\text{cut-off}} = 3$ s.

³The chosen threshold at $0.65 I_{\text{on}}$ induces a cut-off at 6.5 s according to Eq. (5.6).

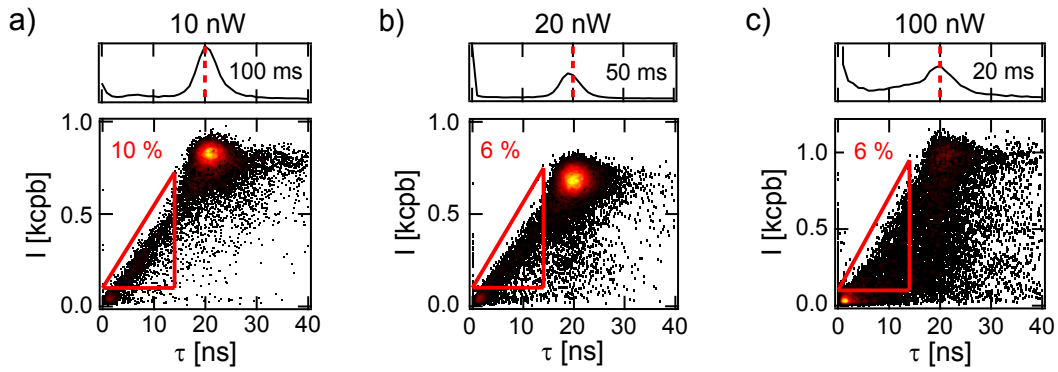


Figure 5.15: Analysis of fluctuations in the excited state lifetime at the different excitation intensities of Fig. 5.14. Correlations of bin intensity and fitted lifetimes at a) 10 nW, $t_{\text{bin}} = 100$ ms b) 20 nW, $t_{\text{bin}} = 50$ ms and c) 100 nW, $t_{\text{bin}} = 20$ ms. Hot colors represent high occurrence. Top: corresponding histograms of the fitted lifetimes. Red dashed lines mark the most frequent lifetime of 20 ns.

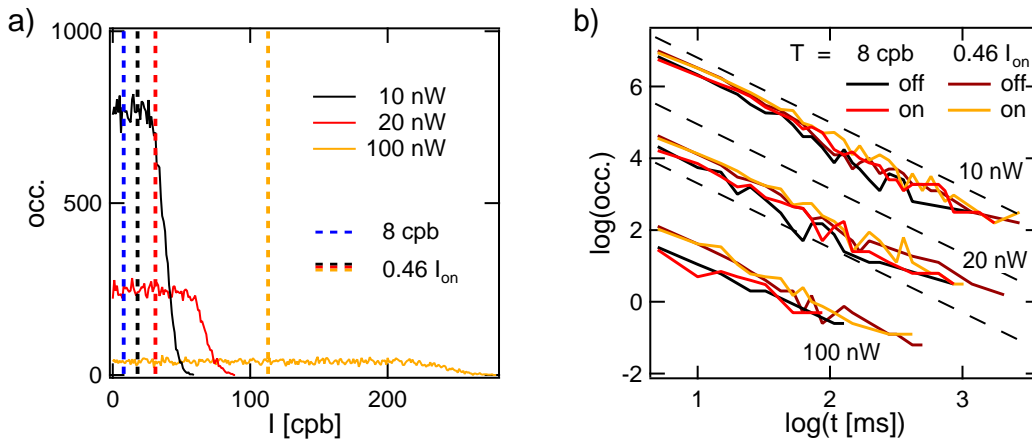


Figure 5.16: Estimation to the influence of intermediate intensity levels as in Sec. 5.2.3. Time-traces of linearly increasing intensity are evaluated. Number of bins per time-trace and bin intensities are taken from experimental data (see text). a) Intensity histograms of the time-traces corresponding to the different excitation intensities of Fig. 5.14. b) Dwell time histograms at the indicated thresholds in a). Excitation intensities are offset for clarity. Black dashed lines possess the same slope of -1.8 and offsets as those in Fig. 5.14 e).

5.3.3 Continuous Distribution of Intermediate Intensity Levels

As discussed in Sec. 5.2.3, next to unresolved blinking another influence on dwell time statistics can be found in real intermediate intensity levels. A discrimination between unresolved events and real intermediate intensity levels can be achieved with the simultaneous detection of lifetime fluctuations (see Sec. 2.2.3.1). For the three time-traces in Figs. 5.11 and 5.14 this is presented in Fig. 5.15. Time-traces are binned to 100 ms, 50 ms and 20 ms for 10 nW, 20 nW and 100 nW, respectively, to obtain similar count rates. Single exponential fits are performed for each bin. Bin intensities are plotted over these extracted lifetimes for each excitation power. Histograms of fitted lifetimes

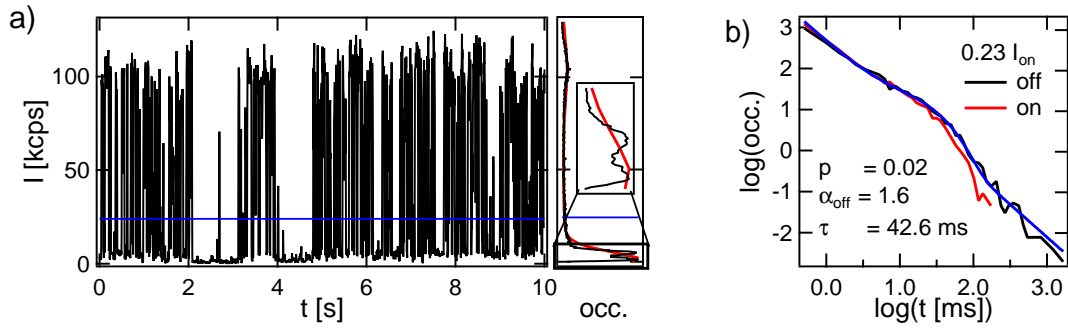


Figure 5.17: Segment of a 100s time-trace of a single QD (Maple Red Orange, $\lambda_{em} = 610\text{nm}$) at 180nW and 5ms binning. The corresponding intensity histogram is shown on the right side (black line) with a zoom to the off-state peak in the inset. A histogram at 0.5ms binning is included as red line. b) Dwell time histograms for on- and off-state at 0.5ms binning at a threshold of $0.23I_{on}$ (blue line in a)). A fit with Eq. (5.8) is shown in blue with parameters indicated in the graph.

(top) show a peak at 20ns. It is correlated to the average on-state intensity. Next to this most frequent lifetime also shorter and longer lifetimes are observed. Longer lifetimes than 20ns are also mostly found at the on-state intensity. With increasing excitation intensity, the occurrence of bins of intermediate intensity and lifetimes $\tau \gtrsim 20\text{ns}$ increases. For $\tau \lesssim 20\text{ns}$, a linear correlation of intensity and lifetime is observed (red triangles). Within this region of higher intensity than 100 cpb and shorter lifetime than 14ns 6% of all bins are found for 20nW and 100nW while 10% are found for 10nW.

With these fractions of intermediate intensity levels an influence on dwell time histograms is estimated like in Sec. 5.2.3. A continuously increasing intensity between zero and I_{on} is evaluated at the same thresholds as in Fig. 5.14 e). According to the determined percentage of the measurement time, the number of bins in the evaluated time-traces is set to 9600, 16800 and 30000 at 100nW, 20nW and 10nW, respectively. Intensity histograms for these time-traces are depicted in Fig. 5.16 a). At lower maximum intensity, i.e. lower excitation, a higher total number of bins at each intensity is found. In Fig. 5.16 b) dwell time histograms are depicted at the same thresholds as those in Fig. 5.14 e). Black dashed lines also have the same slope of -1.8 and offsets as those in Fig. 5.14 e), for a comparison of the total number of events. The offset between these lines and the extracted dwell time histograms from the traces in Fig. 5.16 a) decreases for lower excitation intensities. The number of experimentally detected events exceeds those in Fig. 5.16 b) by a factor of 50-150 at 100nW. This factor decreases with decreasing intensity to 5-15 at 20nW and only 2-3 at 10nW.

5.3.4 Dim-State Above the Background Intensity

Next to on- and off-state peaks and continuously distributed intermediate intensities, an additional peak slightly above the background intensity is observed in intensity histograms for bigger QDs, see Fig. 5.17. In intensity traces of QDs of different diameter

it is mostly observed for Maple Red Orange ($\lambda_{\text{em}} = 610\text{nm}$, QD in Fig. 5.17), rarely for Fort Orange ($\lambda_{\text{em}} = 600\text{nm}$, QD in Figs. 5.11 to 5.15) and not for Birch Yellow ($\lambda_{\text{em}} = 576\text{nm}$) and Hops Yellow ($\lambda_{\text{em}} = 556\text{nm}$).⁴ It can only be separated from the background counts for high signal to noise ratios, thus long bin times and/or high excitation and low background intensity. The “dim” level above the background counts for the Maple Red Orange QD in Fig. 5.17 shows a relative quantum yield of 4%. Dwell time histograms for 0.5 ms binning at $0.23 I_{\text{on}}$ are displayed in b). The on-time distribution is dominated by the short cut-off of less than 100ms due to the high excitation. The observed off-state histogram is not linear on the log-log plot. It can be fitted with a power law and an additive exponential according to

$$P(t) \propto (1 - p) \cdot t^{-\alpha} + p \cdot e^{-t/\tau} \quad (5.8)$$

with $\alpha_{\text{off}} = 1.6$, $\tau \approx 40\text{ms}$ and $p = 0.02$. Instead of $\log(\text{occ.})$ and $\log(t)$ the variables occurrence and dwell time have to be fitted directly. Logarithmic binning is maintained and suitable weights increasing with dwell time are chosen for the fit.

5.3.5 Discussion

The examined QD in Figs. 5.11-5.15 allows an investigation of almost 20 min for each of the presented excitation intensities differing by a factor of 10. In each measurement, the number of on- and off-events detected by the threshold (red lines in intensity histograms of Figs. 5.11 and 5.14) exceeds the 2500 needed for a reasonable determination of power law statistics according to Crouch et al. [55]. The QD shows the typical characteristics often observed in experiments: a robust linear slope for the off-state mostly independent of bin time, threshold or excitation power, an on-time cut-off that shifts to shorter time with higher excitation power, linear on-state slopes for rarely more than two decades and a continuous distribution of intermediate intensity levels. At low excitation a hump on the on-state distribution is observed as also reported in Ref. [211]. Slightly bigger QDs show a dim intensity level that is accompanied by a hump on the off-state distribution as also observed for CdSe/CdS QDs [210].

In agreement with the simulations of the previous two sections, only short events (here approximately one decade) are influenced by different thresholds and bin times. At 5 ms binning and 100 nW excitation, deviations from the off-state slope also increase with increasing threshold as in the simulations. The observed linear slopes, however, mostly do not agree with simulations to corresponding power law exponents. Together with an off-state exponent of 1.8, the fitted on-state exponents between 1 and 1.6 of Fig. 5.12 would not yield the corresponding linear slopes in on-state distributions in Fig. 5.11 due to distortions (see Fig. 5.4). Also the histograms at lower excitation with a steeper on-state slope of -1.8 do not show the simulated threshold dependence of Fig. 5.2. At the low threshold of 8 cpb in Fig. 5.14 the on-state distribution is not bend downwards at short times as in the simulations. These expected deviations from linear slopes at short times have not been considered before. The observed linear slopes up to almost three decades thus do not represent underlying power law dwell time distributions down to the microsecond scale or below. The observed linear slopes thus

⁴For absorption and emission spectra see Fig. 1.1.

have another origin which is further discussed in Sec. 5.3.5.1.⁵ Also for the off-state, deviations from a plain power law distribution are observed. A hump which can be expressed as an additional exponential distribution (see Fig. 5.17) indicates different kinds of blinking off-states which is discussed in Sec. 5.3.5.2. The estimation for noise-induced cut-offs as deduced from the Poisson distribution in Eq. (5.6) is used to set an upper limit to the cut-off time as demonstrated in Sec. 5.3.5.3.

The observed deviations of extracted dwell times from underlying distributions clearly demonstrate the limits of the threshold method in determining QD dwell time statistics. Other methods like the change point analysis as applied in Ref. [212] are expected to be more adequate to examine on-state statistics. In Ref. [212] the on-state power law hypothesis was rejected as well. Instead, the existence of only three to four different on-states with well-defined average dwell times was indicated in accordance with the model of multiple recombination centers (see Sec. 2.2.2.1 and [49]). Also the distribution of intermediate intensity levels was investigated. A similar performance test of the change point analysis as applied here to the threshold method is still in order to verify the extracted distributions.

5.3.5.1 Linear Slopes Unrelated to Power Law Distributions

With the detection of lifetime fluctuations an estimation of the time spent at intermediate intensities can be found. All bins exhibiting lower intensity and at the same time a different excited state lifetime than the on-state can in principal be attributed to moderately quenched states. Also the dim trion state discussed above shows a shorter excited state lifetime [209]. Next to this dim state a continuous distribution of intermediate intensity levels is found. For the QD in Fig. 5.15 intermediate intensity bins with lifetimes $\tau \gtrsim 20\text{ns}$ are attributed to unresolved blinking. They increase in number with excitation, thus a shortening of on-times, and show no correlation between τ and I . Only the linear correlation within the red triangles is positively assigned to moderately quenched intensities. Their contribution to dwell time histograms is estimated in Fig. 5.16 and compared to the experimentally extracted histograms. From this comparison it can be concluded that for the histogram at 100nW the influence of intermediate levels is not significant. At 10nW the estimated number of events induced by intermediate levels amounts to half of all experimentally detected events. This higher contribution not only results from the higher total number of bins used for the time-trace. It especially results from the spread of these intermediate intensities over a smaller intensity range. Contributions of intermediate intensity levels increase with decreasing signal counts, i.e. lower excitation or shorter bin times. Estimated dwell time histograms also show the same slope as those detected in the experiment. Considering that intermediate states in experiments are usually short, an even higher contribution to short events can be expected. This suggests, that short state statistics are completely determined by the noise of intermediate intensity levels. It can thus be expected as the origin of many apparent power laws. Such a strong effect of intermediate intensities on dwell time histogram is so far neglected in the literature. For better

⁵In some cases a power law onset close to the bin time ($t_{\text{bin}} \approx t_c$) might agree with the observed linear slopes in on-state histograms (also see Sec. 5.2.4.3). For the QD in Figs. 5.11 to 5.15 this would additionally imply a strong excitation dependence of the on-state power law exponent.

estimations, also a modeling of the dwell time lengths and occurrences of these states is necessary. Only recently first information to their dwell times was gathered with the change point analysis [212].

Estimations to noise-induced effects of intermediate intensity levels in Fig. 5.16 show steep linear slopes close to -2. In Fig. 5.14 it is demonstrated how flat linear slopes over more than two decades can appear that also do not represent power law dwell time distributions. At 20 nW dwell time distributions are extracted at a threshold in the on-state noise (blue line), thus splitting long on-events. Split on-times of intermediate length merge with the short time statistics which leads to a histogram resembling a flat power law with exponential cut-off (blue line). A similar influence could also be expected for real instead of noise-induced cut-offs at higher excitations and lead to histograms as in Fig. 5.11.

5.3.5.2 Different Kinds of Blinking

A distinct intermediate intensity level above the background level is observed in intensity time-traces of larger QDs at high excitation (see Fig. 5.17). It clearly shows the participation of at least two different processes leading to strongly quenched luminescence. The observation of such a dim state above the background level is accompanied by a hump in the off-state distribution, which can be described by Eq. (5.8). Off-state distributions can thus be separated in a power-law and an additional exponential. The latter is ascribed to the dim state. The same behavior has also been observed for CdSe/CdS QDs [75, 210]. Due to a similar lifetime and the lack of a dim state on electron accepting ZnO, Qin et al. [75] assigned the dim level to the negative trion. Trion emission is also argued in Ref. [210] and here.⁶ The quantum yield of the negative trion for Fort Orange QDs (4.1 nm), as the one of Figs. 5.11 to 5.15, is determined to $\approx 1\%$ in Sec. 6.4 of the next chapter. This would hardly be resolved in the time-traces here, even at 100 nW. The QD in Fig. 5.17 (Maple Red Orange, 4.6 nm) shows a dim level quantum yield of 4%, which is in agreement with lower Auger efficiencies. The lack of a dim level should thus not directly imply that no trion is formed. The deviation from the linear slope in off-state distributions in Fig. 5.11 at 50 ms indeed resembles a hump on a power law distribution as well. It is clearly no binning effect as it remains at 50 ms independent of the chosen bin time. It can thus also be assigned to the same process of trion neutralization. High excitation intensity will not only allow a discrimination from the background. It can also enhance charge ejection and thus promote the formation of a trion. As has often been argued, the on-state cut-off can stem from such trion formation. This explains a missing hump at lower excitation intensities (see Fig. 5.14 e)). A comparison between the QD in Fig. 5.11 and that in Fig. 5.17 also shows a longer on-time cut-off in Fig. 5.11. A lower probability of trion formation, i. e. a lower hump, is thus reasonable.

⁶As in Ref. [210], in Ref. [209] we also argued with a positive trion. The kind of trion was, however, not specifically investigated. All observations equally agree with the formation of a negative trion instead, which is further supported by the electrochemical investigations in Chap. 6.

5.3.5.3 Estimation of Noise-Induced Effects

In agreement with predictions to the noise-induced cut-off by Eq. (5.6), a decrease of the fitted cut-off time for thresholds $T < 25$ kcps is observed at 0.5 ms binning and 100 nW excitation power (see Fig. 5.12). Also estimated noise-induced off-state cut-offs correspond well to the missing long events in off-state distributions as marked by the arrows in Fig. 5.11. The additional noise-induced short times of $\tau'_{\text{off/on}} = (1 - \tau_{\text{on/off}}^{-1})^{-1} \approx 1 t_{\text{bin}}$ correspond well to the observed increase of short events in both distributions for thresholds in the noise of the opposite state. The amplitude of this additional exponential distribution scales with the time spent in this state. At 100 nW more time is spent in the off-state. Consequently, the influence is higher in the on-state distribution.

The fitted on-state cut-off time, however, remains a factor of 2 higher than the estimated cut-off. As noise-induced cut-offs set an upper limit to detectable cut-offs, this is attributed to an artifact of the fitting procedure. It can result from the correlations of fit parameters (see Fig. 5.13) or the suitability of Eq. (5.7) to describe the data in general. Fit results are thus regarded as an upper bound for the real cut-off. Fitted cut-off times further increase with lower thresholds without an influence of noise. Such a threshold dependence is also observed in the simulations of Fig. 5.7 b) and d). It stems from contributions of intermediate intensity bins that are regarded as on. The real cut-off is then approached at high thresholds. An upper limit for the real cut-off is found at the highest threshold that does not lead to a noise induced cut-off. It is determined to $\tau_{\text{cut-off}} < 100$ ms.

6 Electrochemical Charging of Quantum Dots

The observation of blinking in single QD time-traces is still far from being understood. The extraction of power law statistics for dwell times of dark and bright states present a high challenge to models of underlying mechanisms. In the previous chapter it is shown that these extracted statistics themselves are highly questionable. Even more desirable than better methods to describe fluctuations, however, are methods that directly access the mechanism itself. The nature of the off-state is still highly debated. The first assumption of a singly charged QD could be disproved as the origin of all dark states [53, 54]. It is, however, assigned to a low emissive state just above the background level that was first observed for CdSe/CdS QDs in Ref. [210] and for CdSe/ZnS QDs here (see Sec. 5.3.4 and [209]). This indicates contributions of multiple distinct processes in dark state statistics. Next to singly charged QDs, multiple charges have been suggested as dark states as well as different kinds of trap relaxation via electron or hole traps. The trapping of an electron in a trap state can be described by the reduction of the trap and the oxidation of the conduction band. Trapping of holes then corresponds to the oxidation of a trap and reduction of the valence band. Reduction and oxidation potentials can be identified with electrochemistry. A combination with simultaneous fluorescence detection then allows to directly record the influence of filling and emptying of traps and bands on excited state relaxation. An access of blinking dynamics still demands for the examination of single QDs. A method is thus developed to achieve this optical detection of redox processes on single particles. An electrochemical cell is designed with a transparent working electrode to be placed on an inverted microscope. This cell is described in Sec. 4.5.2. Transparent electrodes are typically highly doped semiconductors with a band gap in the visible spectrum. Often ITO is chosen [51, 76, 78]. QD measurements have also been performed on a nanoparticulate ZnO film on ITO [72–75, 77] or FTO [66, 67]. When semiconductors are used as working electrodes in electrochemistry, observations depend strongly on the alignment of the semiconductor bands as well as defect states at the electrode surface (see Sec. 3.3). To capture electrode dependencies different electrodes are tested here. Those are pure ITO and ITO with a deposited 20 nm film of ZnO. The deposited ZnO is either undoped or gallium doped by 0.1% or 1% and referred to as ZnO/ITO or Ga:ZnO/ITO, respectively.

Investigations to the voltage dependent QD fluorescence are mostly performed with the application of triangular voltage scans as in common cyclic voltammetry. Instead of the current, the fluorescence is recorded and displayed in dependence on this applied potential. Those plots are referred to as fluorescence voltammograms. If not men-

tioned otherwise all scans are taken at a scan rate of 10 mV/s and an excitation power of 100 nW.

The outline of this chapter is as follows: First fluorescence of QD films in air and the electrochemical performance of the cell are characterized for ITO, ZnO/ITO and Ga:ZnO/ITO in Sec. 6.1. The proper operation of the setup is verified with standard redox couples, from which also the reference potential is determined. In Sec. 6.2 reduction and oxidation potentials are identified optically on QD ensembles. A dependence of fluorescence voltammograms on scan parameters is presented in Sec. 6.3. In Sec. 6.4 the excited state lifetime is evaluated to further characterize different quenching mechanisms. Measurements on single QDs are presented in Sec. 6.5 with an evaluation of the distribution of reduction potentials in Sec. 6.6. Involved photoinduced processes are examined in Sec. 6.7. Voltage dependent spectra are included in the appendix in Sec. C.6.¹

6.1 Characterization of Sample and Cell

Prior to electrochemical measurements, the investigated QD films on semiconductor electrodes are characterized by film morphology of intensity scans in the confocal setup and ensemble intensity and lifetime of an approximately 80 μm^2 segment. Ensemble intensity and lifetime are compared to films on glass and on PVA spacer layers of different thickness. This allows information on the distance dependent influence of the electrode's presence close to the QDs and the underlying mechanisms.

The operation of the cell is further verified by measurements on the standard redox couples ferrocene/ferrocenium (Fc/Fc^+) and cobaltocene/cobaltocenium (Cc/Cc^+). They also allow the determination of the reference potential of the silver wire. A comparison between measurements on platinum and the different semiconductor electrodes allows a first estimation to the band alignment at the surface.

6.1.1 Film Morphology

The prepared QD films on the electrodes are mostly homogeneous in density (intensity) throughout 100 \times 100 μm scans of the sample as demonstrated in Fig. 6.1 a). Images in Fig. 6.1 show confocal scans of submonolayer QD films that are spin cast from an approximately 200 nM concentration. The zoom in b) still allows the identification of closely arranged single QDs. Electrochemical investigations are primarily performed on such submonolayer QD concentrations. Image c) is collected after a few ensemble measurements in TBAP/PC. The bright spot indicates the investigated area of 10 μm in diameter which was illuminated during each measurement. Fluorescence of QDs in the examined spot is typically enhanced with respect to surrounding QDs. This difference, however, is dependent on the voltage that has been applied, as especially discussed in Sec. 6.7.

¹Part of the data on different ZnO/ITO substrates in Secs. 6.2 to 6.6 and the appendix have been collected with the assistance of David Plotzki in the course of his master thesis.

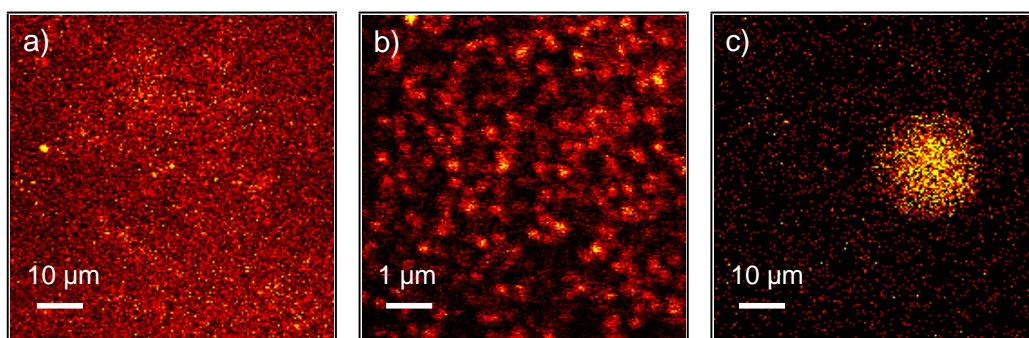


Figure 6.1: Confocal scans of a QD film on a ZnO/ITO electrode at different resolutions at 100 nW excitation. c) Scan after ensemble measurements with wide field illumination. The bright spot represents photo-brightened QDs that have been continuously illuminated during the measurements.

6.1.2 Quenching Close to a Conducting Interface

To investigate the effect of energy or electron transfer to the ITO or ZnO/ITO electrodes fluorescence intensity and lifetime are recorded of QD films directly placed on ITO and compared to films on PVA spacer layers as well as on glass.² To achieve different PVA spacer layer thicknesses, different PVA concentrations dissolved in water are spin cast on ITO prior to spin casting the QD solution. Layer thicknesses of 1% and 0.25% PVA are determined to measure approximately 15 nm and 2 nm, respectively, with the help of an AFM (see Sec. B.2). A 10% PVA solution is expected to produce layers of several 100 nm [213]. Fig. 6.2 a) shows normalized fluorescence decays of QD films of the same concentration placed on ITO, PVA on glass and PVA on ITO of different layer thicknesses. A similar concentration placed on ZnO/ITO is shown in blue. Decays on glass and a 10% PVA layer on ITO coincide (black line is hardly visible behind brown line). For thinner PVA layers the decay time decreases and is shortest without a spacer layer. On ZnO/ITO fluorescence decays even faster. An average lifetime τ_{avg} is calculated according to Eq. (4.16). The corresponding film fluorescence intensity is plotted in dependence on τ_{avg} in b). It is normalized to the intensity detected on the thick PVA film on ITO. This normalization accounts for the lower transmission through the ITO electrode.³ A second measurement (gray markers) of similar QD concentration shows the same behavior. Lifetime and intensity are lowest on ZnO/ITO, higher on ITO and increase with increasing PVA layer thickness.

The quantum yield on PVA without any influence of the electrode is assumed to be similar to the one in toluene solutions which is about 30% (see Fig. 4.1 in 4.1). On ITO QDs are further quenched (see Fig. 6.2 b)) to a total quantum yield of $\approx 9\%$. On doped and undoped ZnO/ITO a total quantum yield of only 3% is observed. Non-radiative rates thus strongly increase close to the electrode surface. Such an increase close to a conducting interface can result from energy or electron transfer (see Sec. 2.2.1.3). The

²No difference in lifetime or intensity is found between QDs on PVA on glass and QDs directly placed on glass.

³The relative intensity on glass is only higher due to higher transmission, i.e. slightly higher excitation and fluorescence collection.

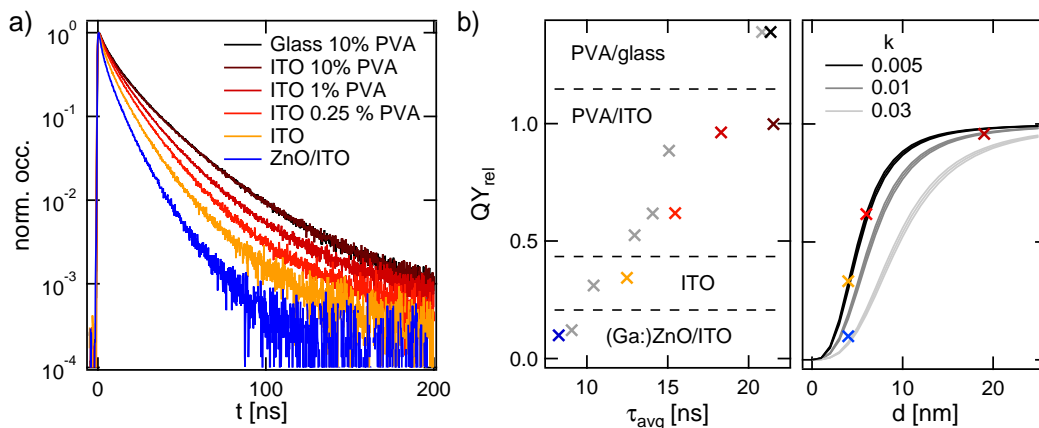


Figure 6.2: Fluorescence decays and intensities on different substrates. a) Influence of different PVA spacer layers on the fluorescence decay on an ITO electrode. Samples are excited at 50 nW. The shown curve on ZnO/ITO (blue) is excited at 100 nW and differs slightly in QD concentration. b) Left: Relative quantum yield QY_{rel} on the different substrates dependent on the calculated average lifetime τ_{avg} with Eq. (4.16). QY_{rel} is normalized to the intensity on a thick PVA/ITO film (10% PVA). Colored markers correspond to the curves in a). Gray (and blue) markers represent a slightly different concentration and unknown PVA thickness excited at 100 nW. They are normalized to show the same intensity on bare glass. Right: Relative intensity QY_{rel} dependent on the estimated distance from the ITO electrode. Lines are given by Eq. (2.24).

electron transfer probability decays exponentially with distance and will already be inhibited by very thin PVA layer thicknesses, see Eq. (2.27). A rough estimate of the energy transfer probability and therefore the corresponding quantum yield of the QDs on ITO can be obtained from the theory presented in Sec. 2.2.1.3. Eq. (2.24) presents the expected ratio $b_{ET} = \Gamma_{nr}/\Gamma_r \propto d^{-3}$ between the induced non-radiative rate by an electrode surface and the radiative rate. The quantum yield, which is proportional to the fluorescence intensity, will then be given by $QY = \frac{1}{1+b_{ET}}$ (Eq. (2.22)). The required value of the dielectric function of ITO $\epsilon_2 = (n_2 + ik_2)^2$ varies in the literature and depends on the deposition technique [214, 215]. At the QD emission wavelength of 600 nm, the real and imaginary parts of the refractive index are found in a range of 1.9 – 2.1 for n_2 and 0.005 – 0.03 for k_2 . Following these parameter ranges, $n_1 = 1.53$ for PVA and $\theta = 1$ for isotropic dipole orientation, a relative quantum yield is obtained as plotted over the distance of the QDs from the ITO surface on the right of Fig. 6.2 b). Influences of different n_2 in the reported range are hardly observed. The measured relative quantum yields (left graph of Fig. 6.2 b)) are included as markers in the corresponding colors as well. Here a QD radius of 4 nm is estimated (including shell and ligands) and the determined PVA layer thicknesses of 2 nm (0.25% PVA) and 15 nm (1% PVA) added. Together with the normalization to the value at $d > 100$ nm layer thickness, they follow the expected distance dependence for an extinction coefficient $k_2 = 0.005$. Quenching on ITO can thus be attributed to energy transfer. Intensity and lifetime are found to decrease even stronger on ZnO/ITO than on ITO alone. For pure and doped ZnO n_2 and k_2 are expected in a similar range as for ITO or lower [216, 217]. Energy transfer should thus be similar or reduced on ZnO/ITO

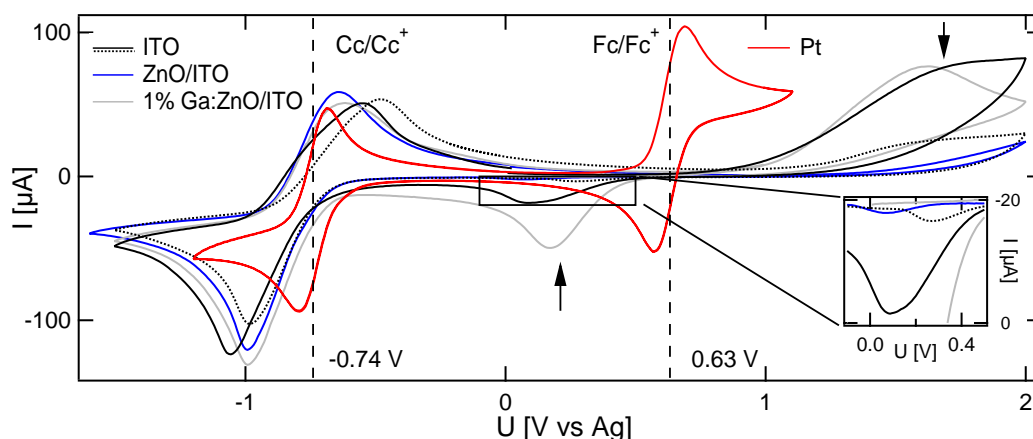


Figure 6.3: Current voltammograms at 40 mV/s of the Fc/Fc^+ and Cc/Cc^+ couples (5 mM concentration) on the indicated working electrodes in dried TBAP/PC solution. Reference electrode is a silver wire, counter electrode a Pt wire except for the measurement on Pt where it is ITO. Inset: Magnification of the reduction peak region for Fc/Fc^+ on the semiconductor substrates. Dashed lines indicate redox potentials of Fc/Fc^+ and Cc/Cc^+ as mean of reduction and oxidation peaks measured on Pt.

substrates. A reduction was indeed observed by Qin et al. [74]. They detected higher intensities and longer lifetimes of QDs when a spacer layer of linked ZnO nanocrystals was placed between ITO and the QD film. In the present work stronger quenching is observed on an evaporated layer of ZnO, clearly showing a different effect than a layer of ZnO QDs. Another non-radiative decay channel is opened. Any involvement of charge transfer can be identified with the control over the electrode potential as employed in the following.

6.1.3 Determination of the Reference Potential

The proper operation of the established electrochemical cell can be verified with the measurement of standard references such as the ferrocene/ferrocenium (Fc/Fc^+) redox couple. Due to its known redox potential vs. the standard hydrogen electrode (SHE) of 0.64 V [218] it allows the determination of the silver reference potential. Also the cobaltocene/cobaltocenium (Cc/Cc^+) couple shows very robust electrochemical behavior with a potential of ≈ -1.3 V vs Fc/Fc^+ [218]. Both components are added at 5 mM (4 mg/4 mL, $M_{\text{Fc}} = 186$ g/mol, $M_{\text{Cc}} = 189$ g/mol) concentration to a 0.1 M solution of tetrabutylammonium perchlorate (TBAP) in propylene carbonate (PC). Different voltammograms are taken on the same solution with the working electrodes ITO, ZnO/ITO and 1% doped Ga:ZnO/ITO as well as Pt. They are displayed in Fig. 6.3. The measurement on Pt (red) shows a typical voltammogram with reduction and oxidation peaks of equal heights and a peak difference of 100 mV, close to the theoretically predicted value of 59 mV (see Sec. 4.3.1). The potential difference between the two components lies close to the expected -1.3 V. From the Fc/Fc^+ peak (0.63 V vs Ag) the potential of the silver wire is estimated to ≈ 0 V vs SHE. It thus lies at the absolute electrode potential of the SHE of -4.44 V. This potential is found to

drift over the course of time and differs between measurements (also see Fig. C.4 b) of the appendix). It should best be determined for each measurement separately and repeatedly over time. For more quantitative results also the change from ambient to inert (e.g. nitrogen, argon or helium) atmosphere is required which has not been installed here. In the following all potentials are reported in reference to this silver wire. Despite potential drifts first characterizations of QD films are possible.

6.1.4 Band Alignment at the Electrode Surface

The measurements on the different transparent electrodes in Fig. 6.3 look considerably different from the one on platinum. Oxidation and reduction of the Cc/Cc⁺ couple is reproduced with almost symmetric peak heights and shapes. The peak difference of 0.3 – 0.5 V is still larger, indicating slower charge transfer on the semiconductors (see Sec. 4.3.1). A much stronger difference is observed for the Fc/Fc⁺ couple. Reduction and oxidation peaks are far from symmetric and separated by more than 1.4 V (black arrows). The oxidation peak, when observed, is much broader than the reduction peak and shows a stronger offset to the determined redox potential on Pt. On ZnO/ITO no oxidation peak is observed at all. Also reduction peaks are typically lower than the peak on Pt. The inset in Fig. 6.3 shows a zoom to the region of the reduction peak. Observations to reduction and oxidation of Fc/Fc⁺ can vary considerably for different measurements. Two different measurements of the same solution on different ITO substrates are shown as black solid and dotted lines. ZnO/ITO typically does not show an oxidation peak. The reduction peak can be of similar height as the one on ITO but typically appears slightly shifted to more negative potentials. Doping ZnO with Gallium increases observable reduction and oxidation features, for 1% doping sometimes even beyond those of ITO as shown in blue in Fig. 6.3.

These observations of strongly differing reactions of Cc/Cc⁺ and Fc/Fc⁺ directly result from the semiconducting nature of the electrodes as theoretically described in Sec. 3.3. Also ITO, which is commonly approximated as showing metallic behavior, reveals its semiconducting nature at potentials approaching its intrinsic band gap. On an ideal semiconductor electrode reversible reduction and oxidation of species are only possible for redox energies above the semiconductor surface conduction band edge $E(\text{CB}_S)$. Oxidation and reduction of species with redox energies in the semiconductor band gap can only proceed from this energy $E(\text{CB}_S)$ independent of the electrode's Fermi level. Reduction and oxidation rates thus strongly depend on the accessible density of unoccupied and occupied states at $E(\text{CB}_S)$. Those decrease with decreasing redox energies in the band gap. The distribution of reduced (occupied) states lies at lower energies thus deeper in the band gap (see Sec. 3.3). Consequently, oxidation is hindered more strongly.

This behavior is also observed here in Fig. 6.3. The reaction of Cc/Cc⁺ is not influenced by the electrode's band gap. Its redox potential thus lies above $E(\text{CB}_S)$. The strongly irreversible reaction of Fc/Fc⁺ indicates that its redox potential lies below $E(\text{CB}_S)$. The oxidation peak is broader and further offset than the reduction peak or not present at all. Frank and Bard [187] observed the same effect in a study comparing voltammograms on n-type titanium dioxide (TiO₂) and Pt of compounds with different redox potentials. For redox potentials 200 mV above the TiO₂ conduction band

edge reversible reactions were found resembling those on Pt. Below the TiO_2 conduction band edge electrode reactions were completely irreversible and in the transition region nearly reversible or nearly irreversible. Reductions of species with redox potentials in the band gap were typically observed slightly above the conduction band edge. From Fig. 6.3 conduction band edges close to 0.4 V vs Ag, and slightly less negative for ZnO/ITO, would thus be expected. Such a higher conduction band edge for ZnO also agrees with a missing oxidation peak of ferrocene on ZnO/ITO. The higher electron density in Ga:ZnO/ITO (typically two to three orders of magnitude higher than in undoped ZnO [219, 220]) decreases the electron depletion at the surface, and thus increases charge transfer rates.

All measured substrates are n-doped semiconductors. Even pure ZnO carries electron donor defects just below the conduction band. The band gap of ZnO is well established at 3.4 eV [87, 219]. The fundamental band gap of ITO has recently been determined to about 2.9 eV [221].⁴ Values for work functions, electron affinities and ionization potentials for ITO and ZnO vary considerably in literature and are dependent on deposition technique, surface orientation and doping [219, 223–226]. The work function of ZnO is typically reported similar to but lower than that of ITO. It lies in the range of 3.5 – 5 eV [219, 224, 225], often reported as 4.2 eV, while that of ITO is observed between 4.2 – 5.2 eV [223, 224, 226–228], generally reported at 4.7 eV. Due to their n-type nature, work functions approximately yield the conduction band energy, when surface defects can be neglected. A higher surface conduction band edge of ZnO is therefore reasonable.

In the following, measurements on ZnO/ITO are compared to those on ITO. Primarily electrodes of undoped ZnO are used. Some measurements on doped ZnO/ITO are included which qualitatively resemble those without doping (see Fig. C.4 a) of the appendix). All voltages are reported relative to the silver reference electrode (vs Ag).

6.2 Cyclic Voltammetry on a Quantum Dot Film

In cyclic voltammetry the current through an electrode is monitored during cycles of increasing and decreasing electrode potential. The electrode is in contact with an analyte which is reduced or oxidized via charge exchange with the electrode. The net charge transfer to (oxidation) or from (reduction) the electrode is detected as a current. It shows peaks associated with maximum and minimum net transfer rates, which increase and decrease with the species' concentration at the electrode. When this concentration is too low the corresponding current is no longer detectable. Charge transfer can still take place, but requires other means of detection. As QD fluorescence is very sensitive to reduction and oxidation it is used as the observable here. For QDs the injection and ejection of charges is particularly interesting as it is expected to play a role in observations of QD blinking.

To test the observation of charge transfer in the setup and identify redox potentials triangular voltage scans are applied to the QD film on the electrode like in conventional cyclic voltammetry. Current through the electrode and fluorescence of the QD film are

⁴Its absorption gap is still larger (3.75 eV [222]) due to very low dipole transitions for the highest valence band states.

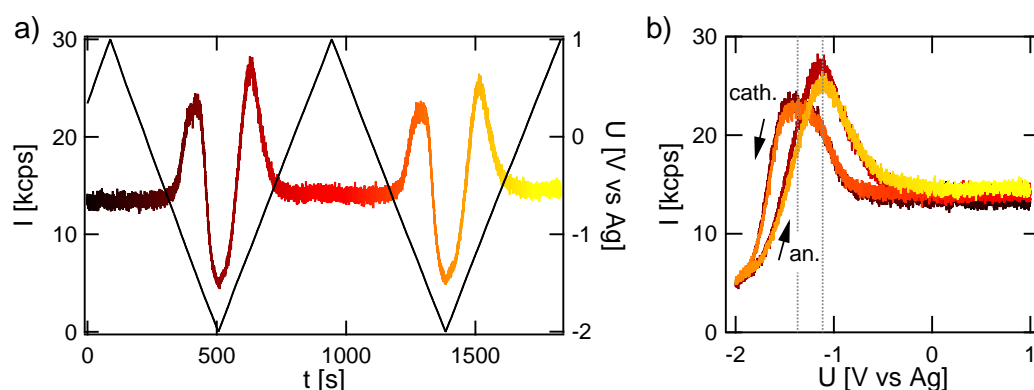


Figure 6.4: a) Intensity trace of a triangular voltage scan on ZnO/ITO at a scan rate of 10 mV/s. b) Fluorescence voltammogram for the same scan. Cathodic and anodic sweep are labeled. Time development is indicated with a black-red-yellow color scale.

simultaneously recorded. No redox peaks of the QD film are observed in the current. The reduction peak that appears in undried solution (see Sec. C.2.2) is independent of the presence of the QD film on the electrode. The observed voltage dependent fluorescence is presented below.

6.2.1 ZnO/ITO Electrode

A triangular voltage scan over time on ZnO/ITO is shown in Fig. 6.4 a) and the analog of a voltammogram as luminescence dependent on voltage in 6.4 b). After a few scans, a reproducible reaction of QD luminescence to the applied voltage is observed. Luminescence is brightest at a preferred potential, here between -1 V and -1.5 V. At higher negative and higher positive voltages luminescence decreases. High negative potentials completely quench the luminescence. At positive potentials the luminescence decreases to a constant value, here approximately half the peak intensity. This intensity varies between measurements, especially dependent on the spin cast concentration of QDs as shown in Sec. C.1 of the appendix. It decreases with decreasing QD concentration.

The total scan is reproducible in shape. The scan to negative potential (cathodic sweep), however, differs from the return scan to positive potential (anodic sweep). The voltammograms show a hysteresis. As in current-voltage diagrams, both sweeps show a luminescence peak but occurring at different potentials, with a more negative peak potential in the cathodic sweep, marked by dotted lines in Fig. 6.4 b).

6.2.2 ITO Electrode

The luminescence-voltage dependence on ITO in an undried solution is shown in Fig. 6.5. A similar behavior is observed as on ZnO/ITO. Intensity decreases to positive and negative potential. Compared to the measurement on ZnO/ITO (Fig. 6.4), the decrease in the cathodic sweep starts at a similar potential close to -1.5 V. The decrease

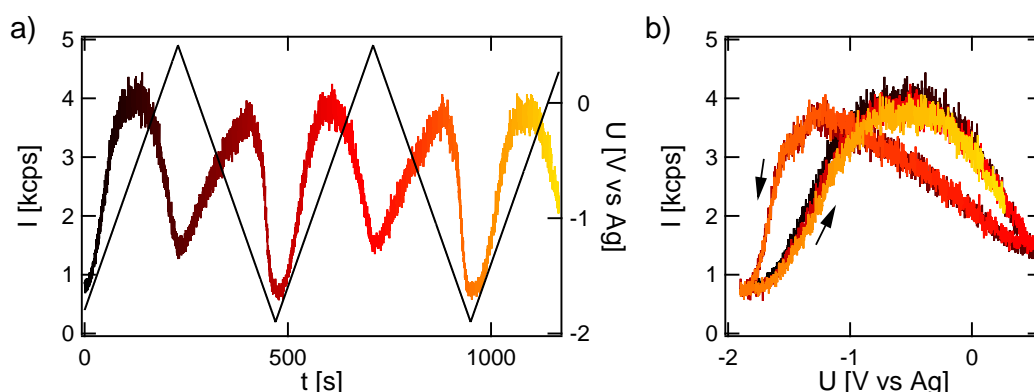


Figure 6.5: a) Intensity trace of a triangular voltage scan on ITO at a scan rate of 10 mV/s. b) Fluorescence voltammogram for the same scan. Time development is indicated with a black-red-yellow color scale.

in the anodic sweep, however, starts at a more positive potential close to 0 V instead of -1 V as on ZnO/ITO. A similar hysteresis between anodic and cathodic sweep is also observed on ITO.

6.2.3 Discussion

During the applied triangular voltage scans the current through the electrode does not show QD related features of reduction or oxidation. The concentration of QDs on the electrode is too low for detectable contributions to the current. QD fluorescence, however, is observed to depend strongly on the applied electrode potentials. Like in conventional voltammetry, fluorescence voltage diagrams, termed as fluorescence voltammograms, show reproducible features at increasing and decreasing voltage sweeps. First fluorescence enhancement, and then quenching is observed when lowering the electrode potential to more negative values. Different from current voltammograms, such a peak in fluorescence voltammograms cannot be ascribed to a single process. While a current peak indicates a maximum of change in the concentration of oxidized and reduced species, a luminescence peak is directly related to the concentration or quantum yield of luminescent species. The observed increase and decrease thus involves at least two different processes responsible for enhancement and quenching, respectively. In the following all intensities are referenced to the maximum intensity. Instead of discussing enhancement and quenching with increasing negative potential, in the following all intensities are referenced to the maximum intensity. Thus, only quenching mechanisms are reported. At least two different quenching processes are found, one to more negative and another to more positive potentials.⁵ They are influenced by the material of the working electrode, leading to different shapes of fluorescence voltammograms. Their origin is discussed below and further verified and characterized in the following sections. For this purpose the setup not only allows the

⁵In the literature intensity is often compared to the intensity at the reference potential (0 V). Then the fluorescence change between the peak potential and 0 V would be reported as enhancement with negative potential instead of quenching with positive potential.

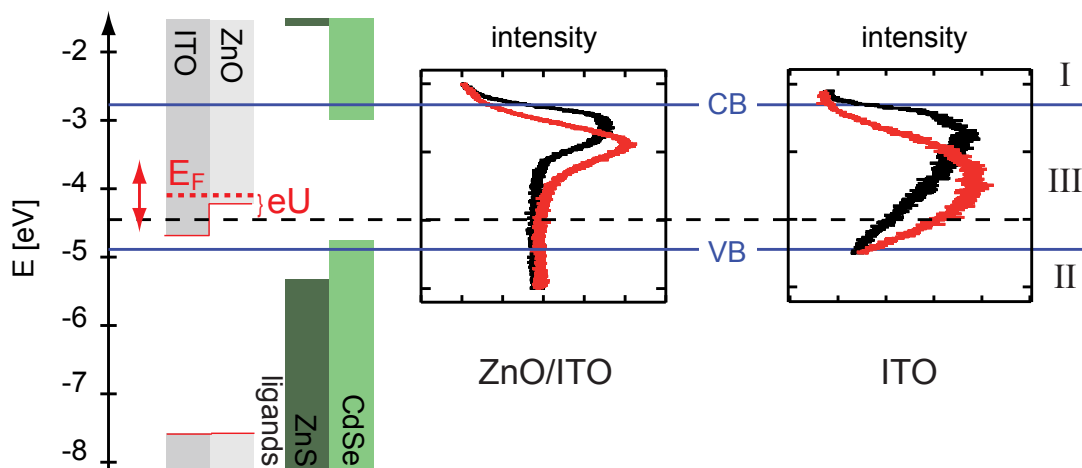


Figure 6.6: Left: Schematic energy diagram of bulk ITO, ZnO, ZnS and CdSe. Right: Respective potential region accessed in the measurement on ZnO/ITO and ITO. Blue lines: Expected QD conduction and valence bands. Black dashed line: pseudo-reference potential of the silver wire. The electrode's Fermi level E_F is shifted with respect to the reference by eU according to the applied potential U .

detection of ensemble intensities (Secs. 6.3 and 6.7). Also lifetime (Sec. 6.4) and emission spectra (Sec. C.6) can be recorded, as well as the intensities of single QDs (Secs. 6.5 and 6.6). Interesting information can also be found when investigating the absence of illumination (Sec. 6.7).

6.2.3.1 Reduction and Oxidation of Quantum Dots

Quantum Dots possess at least two redox potentials that can separately be addressed. One corresponds to the conduction and the other to the valence band. Quenching at high negative potentials (< -1.5 V, region I) shows the same voltage dependence on ZnO/ITO and ITO. A steep decrease of the fluorescence intensity is observed. With the determined reference potential corresponding to ≈ -4.4 eV (see Sec. 6.1.3) an absolute energy level of -2.9 eV is obtained for the onset of fluorescence quenching. This lies very close to the conduction band edge (≈ -3 eV) of similar sized QDs deduced from photoelectron spectroscopy [229]. The fluorescence decrease in region I is thus assigned to the reduction (electron injection) of the conduction band and subsequent Auger relaxation of the exciton. This is further supported by investigations to the excited state lifetime and the absence of illumination in Secs. 6.4 and 6.7, respectively. Such quenching of single QDs and QD films due to the injection of electrons into the conduction band has also been observed by other groups [67, 68, 75, 76, 78]. The average conduction band edge of all QDs will then approximately be found at the center between maximum and completely quenched luminescence, here at -1.7 V. Fig. 6.6 shows a comparison of the detected luminescence from Fig. 6.4 and 6.5 with the expected band edges of CdSe, ZnS, ZnO and ITO. The determined reference potential is indicated as dashed line. The CdSe valence band is inferred from the first absorption peak at 2.115 eV and the bulk band gap (1.75 eV) drawn correspondingly. ZnS is indicated with a valence band offset of -0.6 eV to CdSe (calculated in Ref. [230]) and a

bulk band gap of 3.78 nm [87]. ZnO and ITO are indicated with conduction band edges of -4.7 eV and -4.2 eV, respectively, as reported in the literature (see Sec. 6.1.4). The potential of the negative turn-off edge is observed to shift over time and depend on the QD concentration and electrolyte solution, e.g. prior drying with molecular sieves (see Secs. C.1 to C.3 of the appendix). This is suggested to result from changes in the charge transfer due to ligands and adsorptions at the surface. For more quantitative investigations an elimination of those drifts is required.

According to the first QD absorption peak at 2.115 eV (586 nm), the average valence band edge is expected at 0.435 V. No indication of quenching due to electron extraction is observed at this voltage (region II) on ZnO/ITO. Hole injection is not observed. On bare ITO fluorescence indeed decreases to more positive potentials and hole injection appears possible. The potential of the QD valence band is expected to lie close to or below the conduction band edges of the electrodes (see Fig. 6.6). Those potentials cannot well be accessed from n-type semiconductor electrodes (see Sec. 3.3.1). Oxidation and reduction critically depend on the actual offset to the electrode conduction band edge. A higher conduction band edge of ZnO with respect to ITO then leads to less efficient oxidation. Also on ITO, the fluorescence decrease at the QD valence band is not as steep as the decrease at the conduction band. Hole injection rates still appear lower than electron injection rates. The ITO conduction band is thus expected very close to the QD valence band. Further indications for hole injection in region II on ITO are given in Secs. 6.3 and 6.7.

Differences in accessibilities of QD conduction and valence band levels can thus be well described by the influence of the electrode band gap. An inhibited valence band access has, however, also been observed on metals [70, 231]. Additional reasons, like the hole's higher effective mass, might thus also limit hole injection rates. Reversible hole injection into CdSe QDs in general has not been reported before. It could only be observed for PbSe QDs with a much smaller band gap (0.278 eV in bulk) and similar effective masses for holes and electrons [232]. CdSe QDs are generally reported unstable under oxidizing conditions [68, 76, 78]. It is expected that holes decompose the CdSe surface or hot electron traps are introduced, which degrades the fluorescence permanently. Here high positive potentials are also observed to degrade luminescence permanently. Degradation of the QDs could, however, not be separated from a degradation of the electrode, as ZnO detached from the surface.

The established setup thus allows the observation of reduction and oxidation of the QD's conduction and valence band, respectively. Both are recorded as fluorescence quenching after charge injection. Oxidation of the valence band is only observed on ITO as its potential falls below the ZnO surface conduction band of the electrode. Reduction and oxidation of QD bands is further verified in the following sections.

6.2.3.2 Quenching at Mid-Gap Potentials

Quenching in region III involves potentials in the QD band gap, which are here referred to as "mid-gap" potentials. It is stronger on ZnO/ITO than on ITO without significant differences between Ga:ZnO/ITO and ZnO/ITO (see Fig. C.4 a) of the appendix). Similar quenching below the conduction band has been observed for doped or undoped ZnSe QDs [66, 72], as well as CdSe/CdS/ZnS QDs [68] or CdTe/CdSe QDs

[77]. It was not observed for the CdSe/ZnS QDs studied in Ref. [77] as well. A strong dependence on the QD material is thus expected. The CdSe/ZnS QDs investigated here are quenched on ZnO/ITO but not on ITO, showing an additional influence of the electrode material. Very different substrates have also been used in the literature like ITO [76], fluorine tin oxide (FTO) [66], gold [68] or a film of ZnO nanoparticles on ITO [72, 77]. An influence of the electrode material has, however, never been considered. Observed quenching at mid-gap potentials is typically suggested to originate from the reversible activation of mid-gap electron traps on the QD surface [66, 68, 72, 233]. Non-radiative relaxation of the exciton due to fast electron trapping and recombination with the hole then also leads to a decrease of the excited state lifetime. The lack of quenching on ITO here, however, does not support the idea of intrinsic QD surface traps. Instead, only extrinsic traps can be involved, i.e. trapping sites that are characteristic to the ZnO surface. Such surface specific non-radiative relaxation might also arise from a similar non-FRET⁶ process as observed in QD-porphyrin and QD-perylene bisimide assemblies [234–237]. It was argued, that in these assemblies the attachment of the dyes at the QD surface distorts the electron wave function. This distortion was suggested to induce a non-radiative decay path of the electron. Interactions of the electron wave function with the electrode surface strongly depend on the specific surface sites at the electrode, i.e. the electrode material. Such electron localization at the surface would also be less favored for higher negative potentials. It can thus similarly be described as a trap activation and passivation mechanism.

Without any applied voltage, the electronic potential of n-type semiconductor electrodes is approximately given by their conduction band edges. Electrode conduction band potentials are found close to 0 V (-4.4 eV, see Fig. 6.6). These potentials are thus sensed by QDs in air. Like in fluorescence voltammograms at 0 V, in air considerably stronger quenching is observed on ZnO/ITO with respect to ITO (see Fig. 6.2). The same quenching mechanism of surface-induced quenching is thus involved. This is further supported by investigations of the excited state lifetime in Sec. 6.4.

The dependence on the electrode material at mid-gap and valence band potentials (regions II and III) clearly shows, that not only QD properties are probed but always the combination with the substrate. Influences of the electrode material arise due to the band alignment of semiconductor electrodes and might also involve specific sites at the surface. This leads to a fluorescence response that is not only linked to QD properties. Various different substrates have also been used in the literature. The identification of relevant differences is thus essential for the understanding of the observed fluorescence.

6.3 Dependence on Scan Parameters

In triangular voltage scans fluorescence is observed to strongly depend on the applied electrode potential. Three regions are identified for different fluorescence behavior. A steep edge to negative potential (region I) is assigned to electron injection to the QD conduction band. From this edge, the QD band potentials are deduced. The applied

⁶Förster Resonance Energy Transfer (FRET) [109] is based on non-radiative energy transfer between two fluorophores.

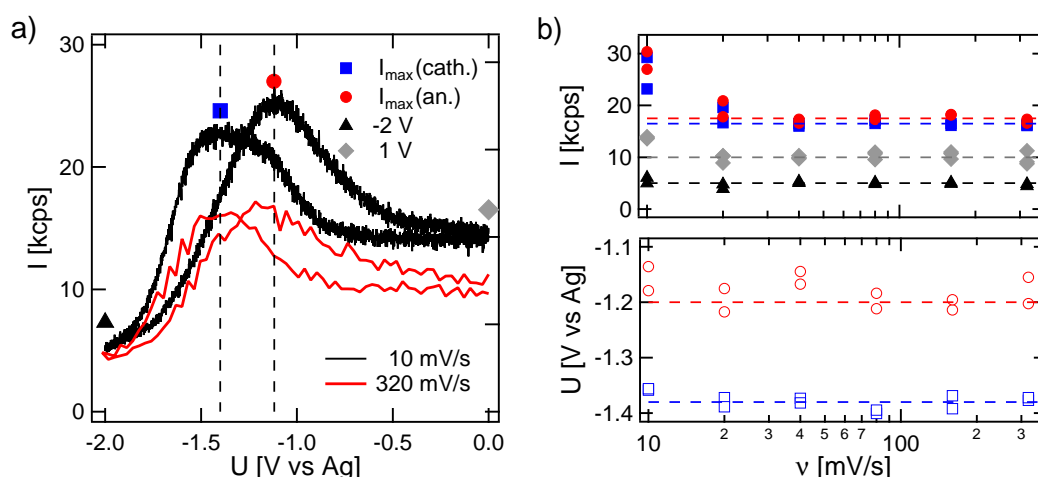


Figure 6.7: a) Intensity-voltage diagram at 10 mV/s as in Fig. 6.4 (black) and at 320 mV/s (red). Voltammograms extend to 1 V. b) Evaluation of the positions (empty symbols) and intensities (filled symbols) of anodic (red circles) and cathodic (blue squares) peak as well as the intensities at the reversal potentials at 1 V (gray diamonds) and -2 V (black triangles, background intensity) dependent on scan rate. Marker legend is included in a).

voltage scans are characterized by three parameters: scan rate v , negative (minimum) reversal potential U_{\min} and positive (maximum) reversal potential U_{\max} . The deduced QD band alignment should be independent of these parameters. Influences of parameter variations on the fluorescence voltammogram are thus investigated in the following. Investigations to the scan rate further give information on charge transfer rates and first characterizations of fluorescence dynamics. With higher positive and negative potentials also multiple charges can be injected.

6.3.1 ZnO/ITO Electrode

Selected measurements are presented on electrodes of different doping levels and water content of the TBAP/PC solution. Voltammogram shapes do not differ between doped and undoped ZnO/ITO substrates or dried and undried solution as shown in Fig. C.4 a) of the appendix. After drying of the TBAP/PC solution only an offset of the negative turn-off edge is detected. The same effects are thus involved on all ZnO/ITO substrates independent of doping.

6.3.1.1 Scan Rate Dependence

The scan rate of the voltammogram in Fig. 6.4 on ZnO/ITO is successively increased up to an increase of a factor of 30. The results are depicted in Fig 6.7. The black line in 6.7 a) shows the scan of Fig. 6.4 at 10 mV/s, the red line a scan at 320 mV/s. In b) the intensities and positions of the peaks in anodic (anodic peak) and cathodic (cathodic peak) sweep, as well as the intensities at the reversal potentials are depicted in dependence on scan rate. Except for an initial decrease in intensity of all components, peak positions and intensities do not change with scan rate.

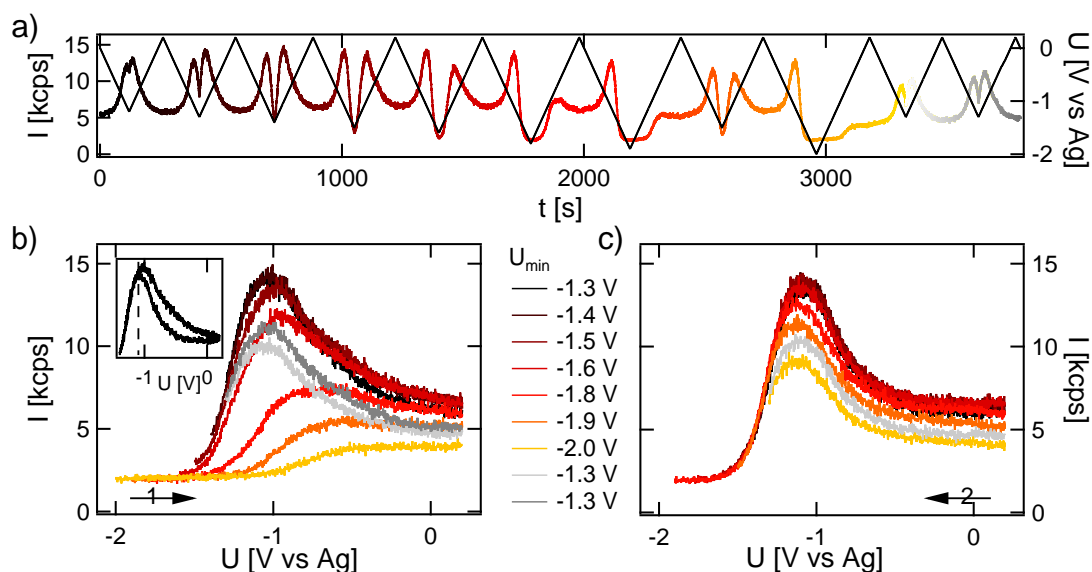


Figure 6.8: a) Intensity-trace of a triangular voltage scan with different negative reversal potentials to and from 0.3 V on 0.1% Ga:ZnO/ITO. b) Intensity-voltage diagrams for anodic sweeps. Inset: Complete cycle from 0.3 V to -1.4 V and back. c) Intensity-voltage diagrams for cathodic sweeps. Arrows indicate the scan direction, numbers the order in time. Measurements are taken at a scan rate of 10 mV/s.

6.3.1.2 Dependence on the Negative Reversal Potential

To investigate the effect of different reversal potentials, consecutive triangular voltage sweeps are recorded keeping one reversal potential fixed while varying the other after each cycle. Measurements on 0.1% doped Ga:ZnO/ITO in dried solution are presented in Figs. 6.8 to 6.10. The time-trace of increasing negative reversal potential U_{\min} is depicted in Fig. 6.8 a). The positive reversal potential U_{\max} is kept at 0.2 V over the whole measurement, while U_{\min} is varied between -1.3 V and -2 V. The measurement is taken on a dried TBAP/PC solution leading to a cathodic fluorescence peak at -1 V. Corresponding anodic and cathodic sweeps are depicted in Fig. 6.8 b) and c). Especially for the anodic sweep in b) a strong influence of the different U_{\min} is observed. The more negative the potential, the longer it takes for luminescence to recover. The peak of the anodic sweep shifts to more positive potentials or longer times, respectively. At very moderate U_{\min} no hysteresis in the quenching process is observed as shown in the inset for $U_{\min} = -1.4$ V, only -0.3 V below the peak potential. Fluorescence is still quenched by more than 70%. For the highest applied $U_{\min} = -2$ V fluorescence does not fully recover over one cycle. Even after two cycles to only -1.3 V fluorescence is still reduced. The voltammogram shape of these two final cycles resembles that of the first cycle to -1.3 V, only at lower intensity. The shape of the cathodic scans in 6.8 c) remains completely independent of U_{\min} and only differs in intensity. Peak intensities and positions are again evaluated as in Fig. 6.7 and presented in Fig. 6.9 a). The shift of the anodic peak with increasing U_{\min} (red empty circles) grows stronger above -1.6 V, when all QDs are dark (see black triangles). It increases from approximately 30 mV per -0.1 V change in U_{\min} to 150 mV/0.1 V (red

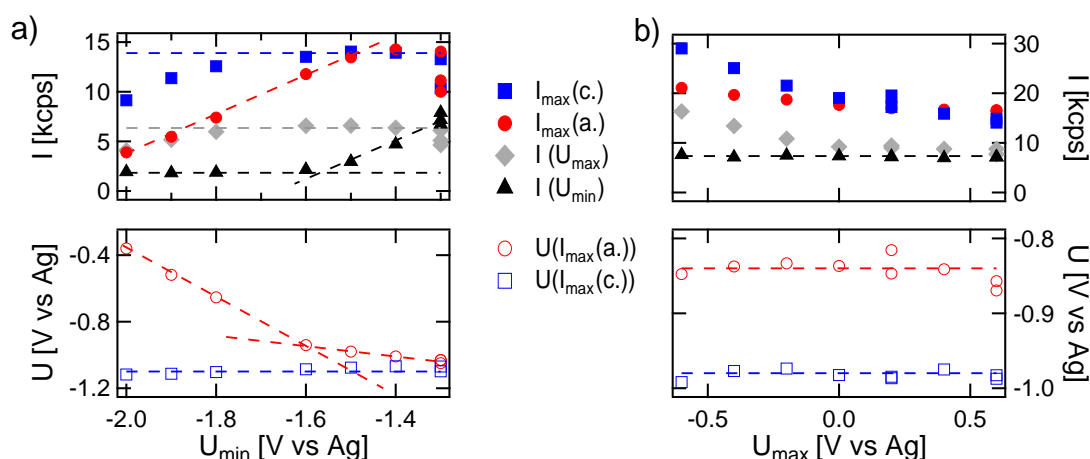


Figure 6.9: Evaluation of the positions (empty symbols) and intensities (filled symbols) of anodic (red circles) and cathodic peak (blue squares) as well as the intensities at the positive (gray diamonds) and negative (black triangles) reversal potentials as in Fig. 6.7 for the voltammograms in Fig. 6.8 and 6.10 in a) and b), respectively. Dashed lines are guides to the eye.

dashed lines). The shift is accompanied by a strong decrease in intensity in the anodic peak (red filled circles). Eventually also the intensity in the subsequent cathodic sweep (blue squares and gray diamonds) decreases for $U_{\min} < -1.8$ V. The cathodic peak remains at the same position throughout.

6.3.1.3 Dependence on the Positive Reversal Potential

The same experiment is conducted for different positive reversal potentials U_{\max} also on 0.1% Ga:ZnO/ITO in dried solution. Results are demonstrated in Fig. 6.10 and 6.9 b). Here U_{\min} is kept at -1.6 V and U_{\max} is varied between -0.6 V and 0.6 V. The shape of the voltammogram, and thus also peak positions (empty symbols in 6.9 b)) and hysteresis, is hardly altered by the different U_{\max} . A normalization of the cathodic sweeps, as shown in the inset of Fig. 6.10 c) confirms equal sweep shapes independent of intensity. Only a small broadening to negative potentials is indicated with increasing U_{\max} (black vs yellow line). Peak intensity of cathodic sweeps, however, decreases strongly with increasing U_{\max} (blue squares in 6.9 b)). Also the anodic peak (red filled circles) shows a lower intensity after high U_{\max} .

6.3.2 ITO Electrode

The effect of different U_{\min} and U_{\max} is also evaluated on ITO and depicted in Fig. 6.11 in undried solution. Anodic (left) and cathodic (right) sweeps are again separated for variations of U_{\min} (top) and U_{\max} (bottom). One potential is fixed while the other is consecutively increased until a moderate potential is repeated (gray line). This order is only slightly changed in a) and b), see voltage trace on the top. Here the last measurements to -1.8 V, -2.0 V and -1.2 V are recorded after a few cycles (gray dashed lines) following the measurements from -1.3 V to -1.9 V. This leads to the low lumi-

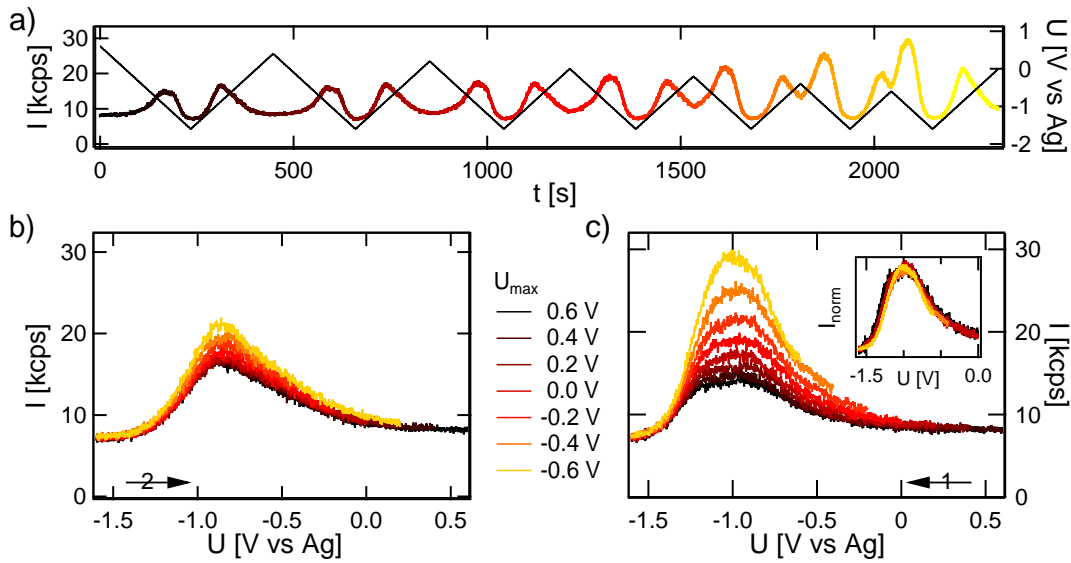


Figure 6.10: a) Intensity-trace of a triangular voltage scan with different positive reversal potentials to and from -1.8 V on 0.1% Ga:ZnO/ITO. b) Intensity-voltage diagrams for anodic sweeps, c) for cathodic sweeps. Inset: normalized cathodic sweeps. Arrows indicate the scan direction, numbers the order in time. Measurements are taken at a scan rate of 10 mV/s.

nescence for the cycle of $U_{\min} = -1.8$ V.

The effect of increasing U_{\min} resembles that observed on ZnO/ITO in Fig. 6.8. Higher potentials lead to stronger hysteresis. In contrast to ZnO/ITO, an increasing U_{\max} on ITO shows a similar effect like an increasing U_{\min} . Higher U_{\max} not only reduce the intensity but also change the shape of the cathodic sweep. The measurement is more symmetric in U_{\min} and U_{\max} . Final measurements to moderate potential (gray lines) equally show decreased luminescence, but identical shape like the initial measurement to the same potential. Differences between variations in U_{\min} and U_{\max} are a steeper negative than positive turn-off edge and relatively shorter recovery times from negative potentials. The insets in 6.11 b) and c) mark the reversal potentials up to which no hysteresis is observed. Recovery, thus, proceeds within the bin time between $U_{\min} = -1.7$ V and $U_{\max} = 0$ V. Those potentials correspond to an intensity quench of more than half (-1.7 V) and less than one third (0 V), respectively.

6.3.3 Discussion

Variations of the scan parameters show that the steep edge to negative potential that is associated with electron injection to the QD conduction band does not change with scan parameters. It thus remains as a good reference to determine the QD band alignment. Only a small shift with increasing U_{\max} (inset in Fig. 6.10) is observed due to superposing recovery and quenching of QDs. The high symmetry with positive and negative reversal potentials on ITO (see Fig. 6.11) additionally supports the access of both QD bands which is not observed on ZnO/ITO.

The insets in Fig. 6.8 b) and 6.11 c) show voltammograms with the minimum U_{\min}

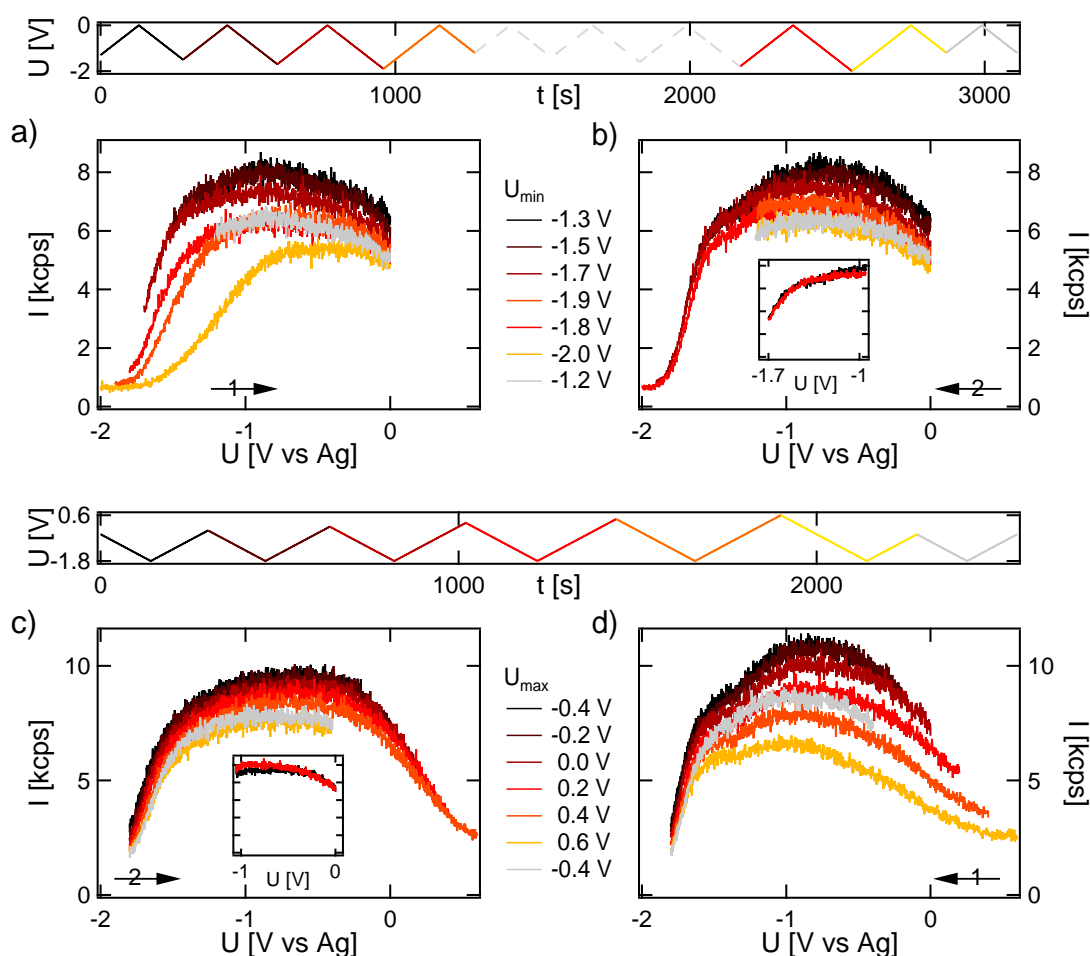


Figure 6.11: Investigations to different reversal potentials on ITO. a) Cathodic and b) anodic sweeps between 0 V and different negative reversal potentials. Inset in b): Complete cycle from 0 V to -1.7 V and back. c) Cathodic and d) anodic sweeps between -1.8 V and different positive reversal potentials. Inset in c): Complete cycle from -1.8 V to 0 V and back. Arrows indicate the scan direction, numbers the order in time. Measurements are taken at a scan rate of 10 mV/s. Time dependent voltage is shown on the top of the corresponding graphs.

and maximum U_{\max} up to which quenching is reversible within the bin time. Charge transfer between QD conduction band and the electrode thus is faster than the bin time for up to 70% of all QDs in Fig. 6.8 b) and at least 50% in Fig. 6.11 b). This is only found for 30% of the QDs at hole injection potentials on ITO (see inset in Fig. 6.11 c)).

For higher potentials U_{\min} and U_{\max} a hysteresis is observed between cathodic and anodic sweep. Fluorescence remains lower after voltage reversal. Such a hysteresis could be expected from charge transfer rates lower than the scan rate. The reaction at the electrode then is delayed like in current voltammograms (see Sec. 4.3). Such a delay leads to voltammogram peaks that broaden and separate with increasing scan rate. A shift with scan rate is indeed observed for the current reduction peak of the undried solution (see Fig. C.3 of the appendix). Fluorescence peaks in Fig. 6.7 are,

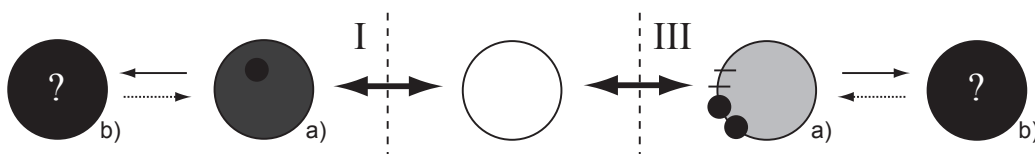


Figure 6.12: The variation of the reversal potentials U_{\min} and U_{\max} indicates the participation of different quenching mechanisms in region I and III of Fig. 6.6. At potentials above the conduction band edge a second process (I b)) develops in negatively charged QDs (I a)) with lower recovery rates indicated by the arrow thickness. Also at mid-gap potentials (in region III) the participation of two process is found. Next to trap activation (III a)) a fraction of QDs is completely quenched by another process (III b)).

however, not observed to shift with scan rate. The hysteresis is thus not dominated by slow charge transfer rates. Indeed, 70% of all QDs in Fig. 6.8 show fast charge transfer within the bin time to and from the QD conduction band (see inset in b)). After high $U_{\min} = -2\text{V}$ not even these 70% recover in the complete anodic sweep. Recovery within the bin time is not observed at all. A more complex origin for recovery from negative potentials is thus responsible. QDs are first quenched due to electron injection to the conduction band. Electron ejection is fast as well. Fluorescence can thus be quickly recovered within the bin time. From this negatively charged state QDs can now cross over to another quenched state that recovers more slowly (see left of Fig.6.12). The transition probability to the state with slow recovery increases with higher negative potentials U_{\min} . The data at the bottom of Fig. 6.9 a) indicate a threshold potential (crossing of the two red dashed lines) at which a stronger shift is observed for the anodic peak. This threshold coincides with the complete quenching of fluorescence (see black diamonds at the top). Almost complete quenching is already observed after the injection of only a single charge due to the high efficiency of the Auger process. The hysteresis thus strongly increases when multiple charges are injected. Next to Auger quenching due to electrons in the conduction band, there is thus another quenching process observed in region I (see Fig. 6.12). This process is further discussed in Sec. 6.7.

The symmetry of positive and negative charging on ITO suggests a similar process also for positively charged QDs in region II. The separation from influences of slower charge transfer rates is, however, not as clear. Recovery within the bin time is only observed for 30% of fluorescence quenching (see inset of Fig. 6.11 c)).

On ZnO/ITO cathodic sweeps for different U_{\max} coincide after normalization. This means that in contrast to variations of U_{\min} , variations of U_{\max} on ZnO/ITO do not change recovery rates. They only change the number of participating QDs. This means that some QDs are turned off at high U_{\max} and do not recover at potentials below the QD conduction band. Two different quenching processes are thus also involved in region III (see right of Fig. 6.12). Only one recovers at mid-gap potentials, which can be associated with the activation of electron traps (see Sec. 6.2.3.2). The other only reduces the number of fluorescent QDs in the cathodic sweep.

The analysis of the dependence on scan parameters in this section reveals the participation of at least two different quenching mechanisms at potentials above the conduction band edge (region I) and two at mid-gap potentials (region III). A second process at

potentials below the QD valence band (region II) on ITO is suspected as well but not clearly distinguished. To identify their origins, they are further characterized by their corresponding lifetimes, fluorescence fluctuations and illumination dependence in the following sections. Recovery times from charge-induced quenched states are found to reach from below the bin time of 200ms over the scan rate to the cycle time of several minutes. Their connection to the blinking phenomenon is of special interest and specifically addressed with examinations on single QDs in Sec. 6.5.

6.4 Potential Dependence of the Excited State Lifetime

The previous sections demonstrate the successful operation of the optical detection of reduction and oxidation of QD films. Next to Auger relaxation after charge injection to the bands three other charge-induced quenching mechanisms are revealed. Two proceed at mid-gap potentials (region III), the third develops at high negative potentials (region I). For a further characterization of the different processes also time-resolved information of the recorded fluorescence intensity can be evaluated. This is demonstrated below.

With pulsed excitation and time-tagged detection of single photons (see Sec. 4.2.3) voltage dependent excited state decays can be extracted. Whenever fluorescence is quenched it either results from increasing non-radiative rates Γ_{nr} , decreasing radiative rates Γ_r or a decreasing population of the excited state. The first two will lead to a change of the effective excited state lifetime according to Eq. (2.22) $\tau_{eff} = (\Gamma_{nr} + \Gamma_r)^{-1}$. The population of the excited state is mostly determined by the absorption cross section which should not change except for irreversible bleaching of QDs [238]. However, it has also been argued to decrease due to a participation of hot carrier traps (see Sec. 2.2.1) at mid-gap potentials [76]. An examination of fluorescence decays allows to distinguish between the different contributions of fluorescence quenching. This provides further insight to the origin of the involved mechanisms. For a first estimation of the multiexponential ensemble decays an average lifetime τ_{avg} is calculated (see Eq. (4.16) in Sec. 4.6.1).

6.4.1 ZnO/ITO Electrode

Fig. 6.13 a) shows two voltammogram cycles of fluorescence intensity I (red) and average lifetime τ_{avg} (blue). Like the fluorescence intensity, the average lifetime first increases then decreases when the voltage is lowered from -0.2V to -2V . Cathodic and anodic sweep almost coincide with only small deviations. The maximum of τ_{avg} is slightly shifted to more negative potentials with respect to the peak in I . The direct correlation of I and τ_{avg} in Fig. 6.13 b) shows monotonic behavior in the cathodic sweep (black arrows). I and τ_{avg} simultaneously increase and decrease, only with changing slopes. The stronger hysteresis in I leads to a non-monotonic correlation in the anodic sweep (gray arrows). The complete decays are normalized and depicted in Fig. 6.14 for various potentials negative a) and positive b) to the peak of the cathodic scan. As indicated by τ_{avg} , fluorescence is decaying faster with decreasing intensity.

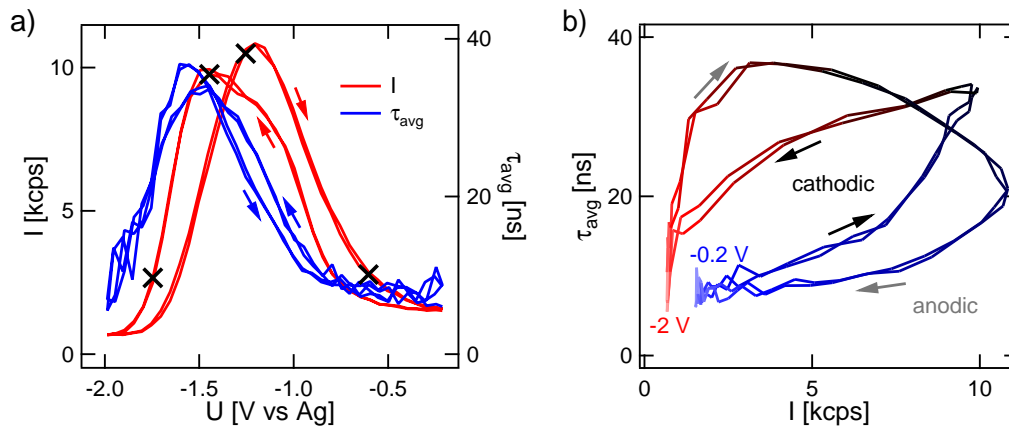


Figure 6.13: a) Voltammograms of intensity I (red) and average lifetime τ_{avg} (blue) calculated with Eq. (4.16) for a triangular voltage scan of 5 s bin time on ZnO/ITO. Black crosses mark instants of decays in Fig. 6.14 d). Arrows indicate the scan direction. b) τ_{avg} dependent on I . The color scale indicates the corresponding negative (red) and positive (blue) voltage with respect to the peak luminescence (black). Arrows indicate the scan direction in the cathodic (black) and anodic (gray) sweeps.

6.4.1.1 Lifetime at the Negative Turn-Off Edge

A normalization of the decays in Fig. 6.14 a) to times > 10 ns in c) shows that the faster decay at negative potential can simply be ascribed to an arising short component. The residual decay is unchanged compared to the decay at -1.5 V, thus the peak in τ_{avg} . At very high negative voltages < -1.8 V (gray) decays are dominated by background luminescence⁷. The lower inset shows the resulting decays after the subtraction of a weighted decay at -1.45 V. The intensity in the short component first increases then decreases to higher negative potentials. Its decay time is < 1 ns and not resolved here. A relative quantum yield is estimated by comparing the number of photons detected in the short component with the “missing” number of photons in the long decay. Accordingly, for each potential < -1.45 V the integral over the short decay component I_{short} (lower inset) up to 6 ns is calculated, as well as the integral over the complete decay I_{tot} . With the integral I_{max} over the decay at -1.45 V the relative quantum yield is obtained by $QY_{rel} = I_{short}/(I_{max} - (I_{tot} - I_{short}))$. This relative quantum yield is displayed in the upper inset. It amounts to $\approx 10\%$ and decreases to higher negative potentials.

6.4.1.2 Lifetime at Positive Potentials

Decays to positive potentials cannot similarly be normalized to the long decay components. In Fig. 6.14 d) selected decays at different voltages are presented for comparison. They are marked in the voltammogram of Fig. 6.13 b) as black crosses. Decays for similar intensity (blue and red) and similar average decay time (blue and orange) are compared. They differ strongly between positive and negative potential. The decay at -1.55 V (maximum τ_{avg} , black solid and dashed lines) corresponds to the long

⁷The prior subtraction of the background luminescence leads to the same results as those presented here, but higher noise.

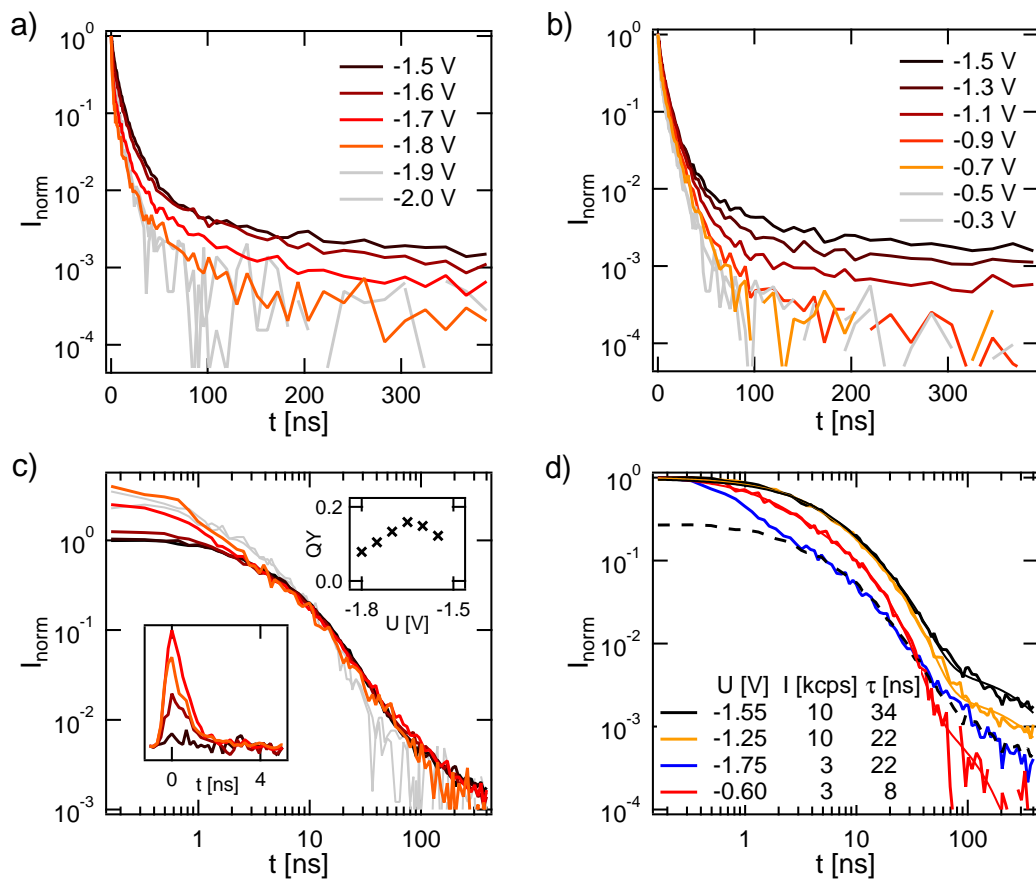


Figure 6.14: Normalized fluorescence decays for different negative a) and positive b) potentials with respect to the intensity peak of Fig. 6.14. Decays dominated by background fluorescence are gray. c) Decays at negative potential normalized to times > 10 ns. Lower inset: Residual fluorescence decay after subtraction of a scaled decay at -1.45 V (linear scale). Upper inset: Calculated relative quantum yield of the negatively charged QD (see text). d) Selected normalized fluorescence decays at different negative and positive potentials at similar intensity I and average lifetime τ_{avg} . Instants are marked as crosses in Fig. 6.13 c). Values of I and τ_{avg} are given in the legend. Dashed line is offset by a multiplicative factor to demonstrate similarities and differences of decay components. Thin lines are triexponential fits to the data.

decay at -1.75 V (blue) but not at -0.6 V (red) nor -1.25 V (orange) despite of the same intensity I or average lifetime τ_{avg} , respectively. Instead of showing an increasing short component, all decay components shorten with increasing positive potential (orange and red). While the decay at -1.55 V (black) can be fitted with three exponentials of 4 ns, 13 ns and 300 ns, those three lifetimes decrease with similar weights to 1.6 ns, 8 ns and 60 ns at -0.6 V (red).

6.4.2 ITO Electrode

The average lifetime τ_{avg} is also calculated for a voltage scan on ITO and presented together with the ensemble intensity in Fig 6.15 a). The measurement is performed at a similar QD concentrations as that in Figs. 6.13 and 6.14. The behavior of τ_{avg}

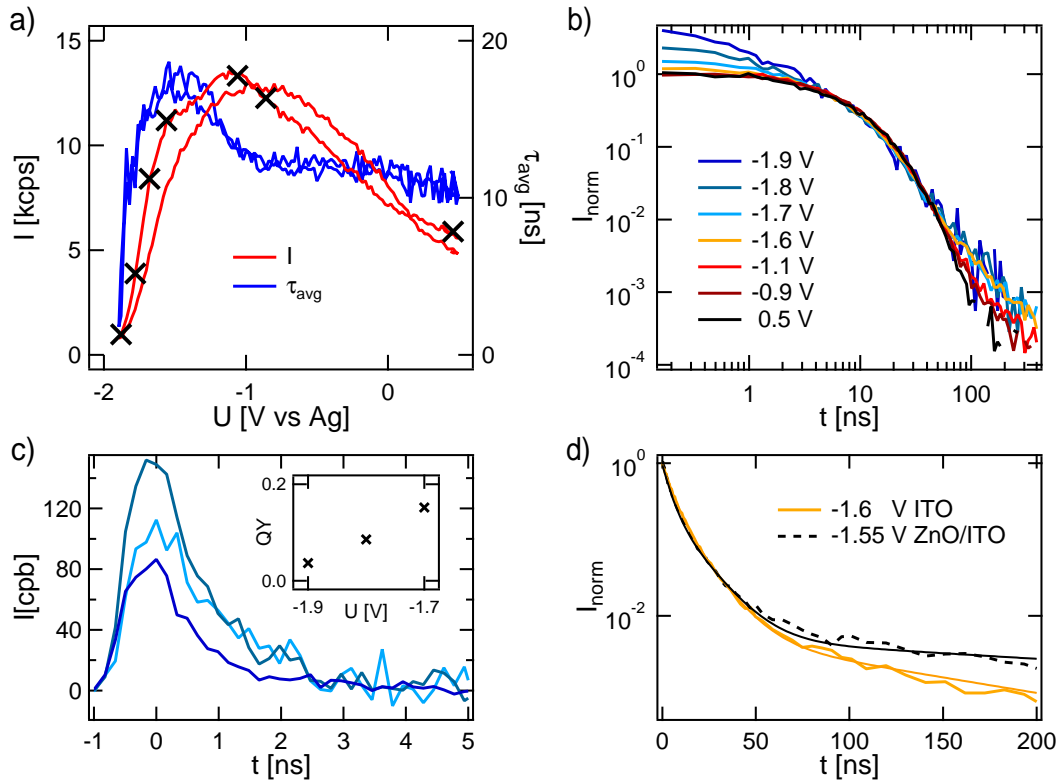


Figure 6.15: a) Voltammograms of intensity I (red) and average lifetime τ_{avg} (blue) for a triangular voltage scan of 2 s bin time on ITO. b) Selected normalized fluorescence decays at the marked instants in a) (black crosses). Blue lines are normalized for times > 10 ns, yellow to black lines to the maximum intensity. c) Residual fluorescence decay after subtraction of a scaled decay at -1.6 V (linear scale). Inset: Calculated relative quantum yield of the negatively charged QD (see text). d) Comparison of fluorescence decays on ITO and ZnO/ITO (of Fig. 6.14) close to the negative turn-off edge. Thin lines are triexponential fits to the data.

resembles that observed on ZnO/ITO with a peak close to -1.6 V. This peak corresponds well to the steep decrease in intensity to negative potential in the cathodic scan. A decrease in τ_{avg} is also observed for positive potentials but only until ≈ -1 V. At more positive potentials τ_{avg} remains constant despite the observed decrease in intensity. The average lifetime is completely reversible with voltage. Only the intensity shows the discussed hysteresis.

Selected fluorescence decays on ITO are depicted in Fig 6.15 b). Like on ZnO/ITO, the decrease in τ_{avg} to negative potential at the turn-off edge (blue) results from the increasing weight of a short component. Fig. 6.15 c) shows the decay of this short component after subtraction of the long time decay. The calculated relative quantum yield is presented in the inset. It also lies at $\approx 10\%$ and decreases with increasing negative potential. As also expected from the average lifetime τ_{avg} , decays at more positive potentials than -1 V do not change. A shortening of long decay components as for ZnO/ITO is only observed between -1.6 V and -1 V, leading also to the peak in τ_{avg} in a). In 6.15 d) the normalized decay on ITO at -1.6 V is compared to the peak decay on ZnO/ITO of Fig. 6.14. They almost coincide for short times < 50 ns.

Triexponential fits for both decays can be obtained with the shorter decay components of 4 ns and 13 ns. Only the longer component shows a lower weight and shorter time (160 ns) on ITO than on ZnO/ITO (300 ns).

6.4.3 Discussion

The recorded fluorescence decays show different features in the different potential regions. These features also depend on the electrode substrate. They can be used to characterize the different involved quenching mechanisms. Contrary to the hysteresis in fluorescence intensity, τ_{avg} shows almost identical values in cathodic and anodic sweeps. This demonstrates the relevance of a varying fraction of dark QDs. Dark QDs only reduce the observed ensemble intensity. The excited state lifetime of the residual bright QDs remains unchanged.

6.4.3.1 Negative Charging

On both types of electrodes the initial intensity decrease above the expected conduction band (region I) can entirely be ascribed to a very efficient quenching mechanism for some QDs, while others are unaffected. This strongly supports the assignment of electron injection into the conduction band. Subsequent Auger relaxation is expected on the picosecond timescale [114, 117]. The mechanism is demonstrated on the top left of Fig. 6.16. The increasing number of charged QDs leads to an increasing short decay component with a lifetime below the resolution limit here. The determined relative quantum yield is the same in Figs. 6.14 and 6.15 indicating a similar quantum yield close to the conduction band on both electrodes.⁸ With the determined relative QY and the reference QY of neutral QDs ($\approx 9\%$,⁹ see Sec. 6.1) a total QY of $\approx 0.9\%$ is estimated. The apparent decrease of the QY to higher negative potentials results from the injection of multiple charges leading to even more efficient quenching.

For CdSe/CdS QDs Qin et al. [75] found the same lifetime for the negative trion and a dim state in blinking time-traces. They thus assigned this state to the negative trion. Such a dim state has also been observed here for CdSe/ZnS QDs (see Fig. 5.17 in Sec. 5.3 and [209]). The QD of Fig. 5.17 is bigger (with a diameter of 4.6 nm instead of 4.1 nm) than the ones investigated electrochemically here. Auger processes are thus expected to be less efficient and the trion QY higher. The observed dim state quantum yield has been determined to 4%. This is indeed higher than the 1% QY of the negative trion for the smaller QDs here. The QD in Figs. 5.11 to 5.15 is of the same set as those used here. A dim state is not observed despite the same indication of two independent off-states in the dwell time distribution at high excitation (see Fig. 5.11 e) and corresponding discussion in Sec. 5.3.5.2). A dim state of only 1% quantum yield would, however, not be resolved from the background level, like in most single QD blinking experiments. Observations here thus agree with the assignment of the negative

⁸The determined relative QY also depends on QD concentration which is very similar for the two measurements here and the one in Sec. 6.1.2. Higher concentrations of QDs that are observed to show less quenching by the electrode (see Sec. C.1 of the appendix) also exhibit a lower relative QY.

⁹As the QY on ITO does not change considerably with increasing negative potential, it is expected to be the same in air and at potentials close to the conduction band edge for both electrodes.

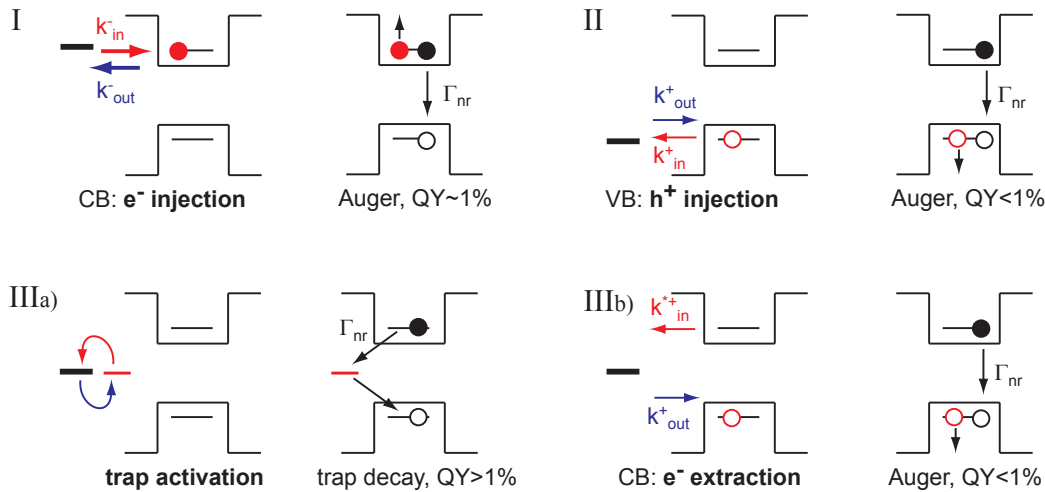


Figure 6.16: Four potential induced quenching mechanisms in the regions I-III. The left band diagram of each graph indicates the creation (red) and elimination (blue) of the quenching mechanism, the right diagram the corresponding non-radiative decay of the exciton with rate Γ_{nr} . Charging rates are denoted with k_{in} , neutralization rates with k_{out} .

trion to the dim state as well as its contribution to blinking time-traces even when it is not resolved.

The faster recovery of the average lifetime with respect to the intensity confirms the participation of an additional quenching process after multiple charging as suggested in Sec. 6.3 (see I b) in Fig. 6.12). As mentioned above, it indicates that a fraction of QDs remain completely dark with low recovery rates. The second quenching process developing in negatively charged QDs is thus more efficient than the negative trion ($QY < 1\%$). With additional information on its illumination dependence, its origin is further discussed in Sec. 6.7.

6.4.3.2 Positive Charging

On ITO hole injection (region II) is expected for potentials $> 0V$. A similar short decay component as for Auger relaxation of the negative trion would also be expected for the positive trion (see top right of Fig. 6.16). However, intensity decreases without a change in excited state decays. The absence of a short component can indicate more efficient Auger relaxation of the positive trion. This was indeed observed in CdSe/CdS QDs [51, 71, 239], which are, however, quasi type II QDs (see Sec. 2.1.3). This means they show stronger hole than electron confinement and, thus, a stronger interaction of multiple holes. An asymmetry in Auger decay rates can still be expected also for CdSe/ZnS QDs due to the higher density of hole states. In contrast to the conduction band, the valence band edge is formed from multiple bands (see Sec: 2.1.2) with higher effective masses of holes. A more efficient process than negative Auger quenching ($QY < 1\%$) would hardly be detected in fluorescence decays here. The ensemble intensity is then simply reduced by the fraction of positively charged QDs while decays of neutral QDs are unaffected.

Intensity on ITO also decreases at mid-gap potentials (region III). For potentials $>$

-1 V this decrease is also not observed in excited state decays (see Fig. 6.15). Considering the higher charge transfer rates between electrode and conduction band ($k_{\text{in}}^-, k_{\text{out}}^- > k_{\text{in}}^+, k_{\text{out}}^+$) as well as the strong quenching of the positive trion, this intensity decrease can be explained with positive charging as well (see III b) in Fig. 6.16). Here, however, holes are not injected into the valence band but excited electrons extracted from the conduction band. Such a photoinduced charging process is especially supported by investigations to the illumination dependence in Sec. 6.7 but also by measurements on single QDs. It also contributes to the quenching on ZnO/ITO and can be identified as the additional quenching process indicated in Sec. 6.3 (see III b) in Fig. 6.12).

6.4.3.3 Trap Relaxation

The increasing decay rates on ZnO/ITO at mid-gap potentials (region III) as found in Fig. 6.14 b) and d) are also found for the additional quenching mechanism in air. This confirms that the same mechanism is involved. In Sec. 6.2.3.2 it has been assigned to trap relaxation due to the activation of electron traps at the ZnO surface (see III a) of Fig. 6.16). The higher quenching on ZnO/ITO in air is thus related to its intrinsic Fermi level and can be eliminated with the application of a negative potential. This is shown by a comparison of the two measurements on ITO and ZnO/ITO at potentials close to the QD conduction band (see Fig. 6.15 d)). The difference in long decay components in Fig. 6.15 d) can be found to result from a broad red emission band on ZnO/ITO (see Sec. C.6.3 of the appendix). It shows the same voltage dependence as band edge emission and is not observed on ITO. It is expected to result from trap emission which is thus more important on ZnO/ITO. This also agrees with the assignment of electron trap activation to this additional quenching process on ZnO/ITO as typically suggested for mid-gap quenching [66, 68, 72, 233]. Dependent on the trap accessibility from the QD core trapping efficiencies can be found at all time-scales. They can thus explain the observed decrease in all decay components. On ITO a minor lifetime decrease at mid-gap potentials $U < -1$ V (see Fig. 6.15 a) and b)) indicates the presence of a similar but much weaker mechanism as well.

6.5 Cyclic Voltammetry on Single Quantum Dots

In the previous sections it is shown that fluorescence can be used to detect and characterize reduction and oxidation processes of very low concentrated QD films. These measurements on ensembles, however, average over differences between single QDs as well as intensity fluctuations such as blinking. To obtain information about the spread of QD characteristics or fluctuating relaxation channels, the investigation of single QDs is required and demonstrated in the following. Due to the low quantum yield on the electrode ($< 10\%$, see Sec. 6.1), excitation intensities are used that are higher by a factor of 1000 than those of ensemble measurements. The probability of biexciton creation per absorbed photon is still lower than 5%. With wide field images the intensity of a large number of QDs is accessed simultaneously. Time averages of single QDs over several cycles as well as the average over many single QDs are compared to ensemble measurements on ITO and ZnO/ITO. A confocal measurement, allowing higher time resolution and signal to background ratio, is demonstrated as well.

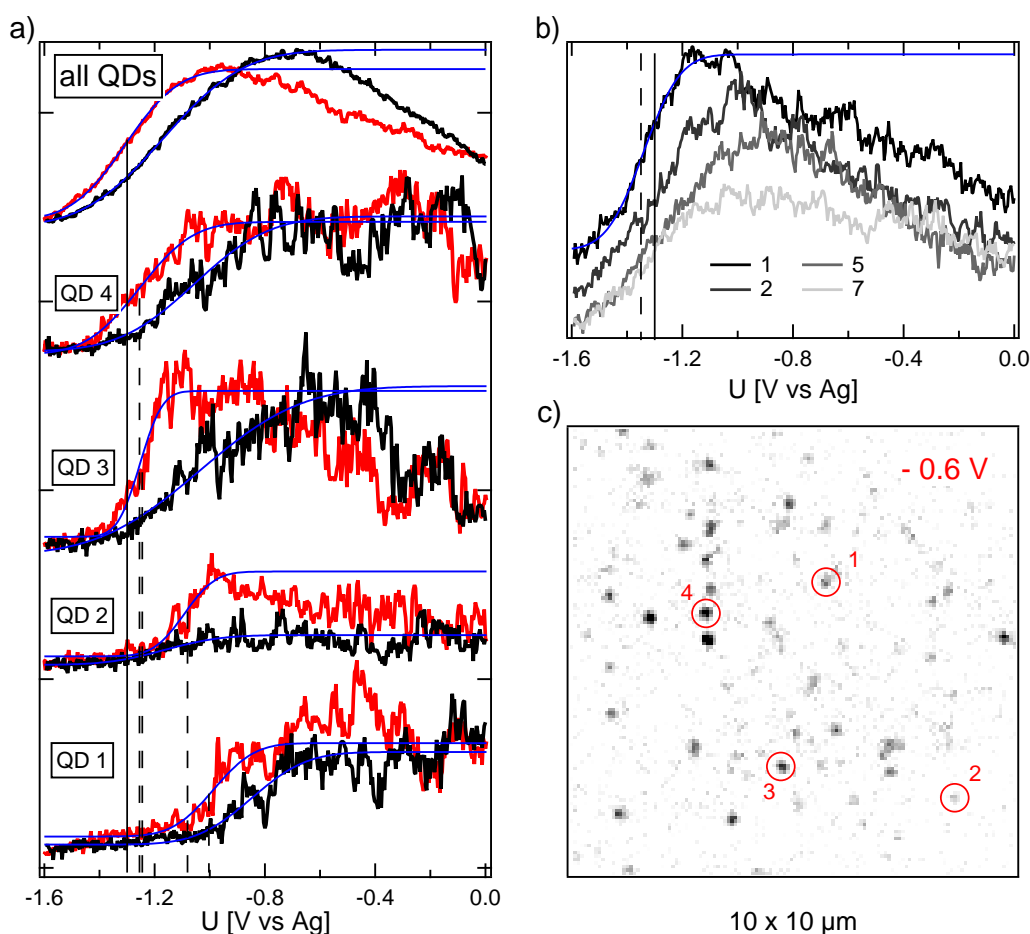


Figure 6.17: Time and ensemble averages of a total of 220 single QDs on 1% Ga:ZnO/ITO. Seven consecutive voltage scans at 20 mV/s between 0 V and -1.6 V are averaged. The measurement is taken in dried solution at $180 \mu\text{W}$ excitation in the wide field setup (D). a) Time averages of the ensemble of all QDs (top) and four single QDs over all seven cycles, offset for clarity. Cathodic sweeps are displayed in red, anodic sweeps in black. Blue lines indicate fits with Eq. (6.1). The average turn-off potentials are marked as dashed vertical lines. b) Ensemble averages of all QDs for four selected cathodic sweeps. Fitted turn-off potentials for the first cycle and the total time average are marked as dashed and solid lines, respectively. c) Wide field image at -0.6 V. The four QDs in a) are marked with red circles.

6.5.1 ZnO/ITO Electrode

Results of a wide field measurement on 1% Ga:ZnO/ITO in dried solution are demonstrated in the following. A measurement of single QDs in undried solution on an undoped ZnO/ITO substrate with the same characteristics is additionally included in the appendix (see Fig. C.7).

6.5.1.1 Averaged Cycles of Single Quantum Dots

Figs. 6.17 and 6.18 show a measurement recorded over seven cycles between 0 V and -1.6 V and more than 200 QDs. The time and ensemble average of all QDs (top of

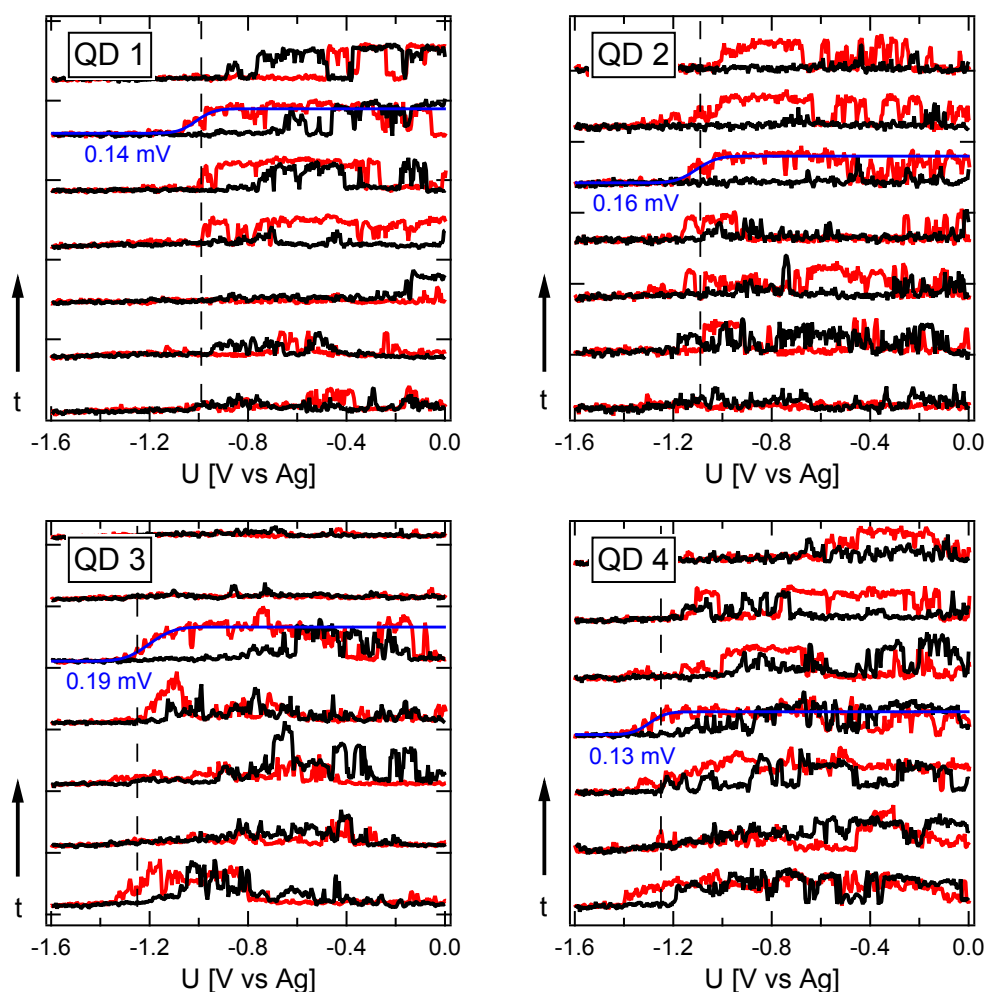


Figure 6.18: Individual cycles of the four QDs of Fig. 6.17. Cycles are offset for clarity with the first cycle at the bottom. Cathodic sweeps are displayed in red, anodic sweeps in black. Dashed lines indicate the average turn-off potential of all seven sweeps. Blue lines and indicated parameters for the fwhm result from fits with Eq. (6.1) to a single sweep.

Fig. 6.17 a)) as well as ensemble averages of single cycles (Fig. 6.17 b)) show the same features as the ensemble measurements of the previous sections. The average intensity of consecutive cycles decreases within the cycle time of 5 min. This strong decrease is not observed at the lower excitation intensities of ensemble measurements and indicates bleaching of QDs (also see Sec. C.4 of the appendix). Consecutive cycles show a shift of the negative turn-off edge to more positive potentials over time, see first cycle (dashed line) and time average (solid line). A similar shift in time is also observed for all ensemble measurements, albeit weaker due to the lower excitation (see Secs. C.3 and C.4 of the appendix). The time averages over all seven cycles for four single QDs in 6.17 a) show a similar behavior as the ensemble as well. Only fluctuations are stronger. All QDs turn off at negative potentials. The specific turn-off potential is characteristic for each QD and differs between QDs, as indicated by the dashed lines. At positive potential a decrease of the average luminescence is only observed for some QDs (QD 2, QD 3). Others remain at a fixed intensity (QD 1, QD 4).

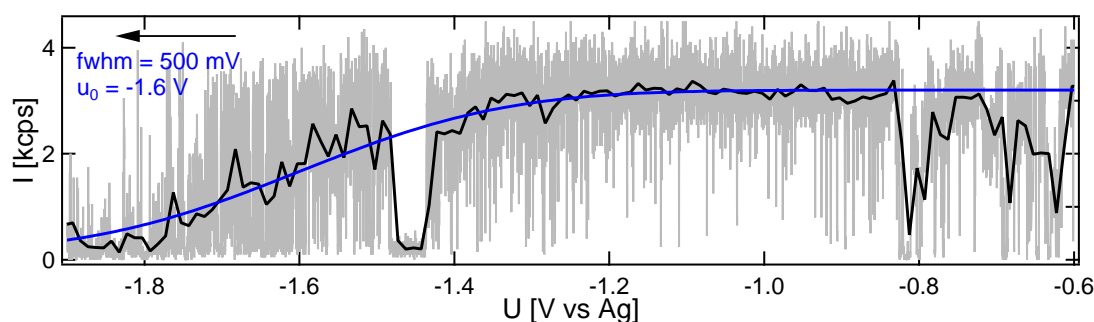


Figure 6.19: Cathodic sweep of a single QD on ZnO/ITO with 1 s (thick black line) and 20 ms (thin gray line) bin time. The measurement is taken in undried solution at 200 nW excitation in the confocal setup (A). Blue line and indicated parameters result from a fit with Eq. (6.1) to the intensity at 1 s binning (black).

6.5.1.2 Individual Cycles of Single Quantum Dots

All consecutive cycles for the four QDs of Fig. 6.17 are separately displayed in Fig. 6.18. Due to QD blinking and flickering consecutive sweeps can differ considerably. The negative turn-off potentials (dashed lines), however, remain approximately fixed and distinct for each QD. The shift of the turn-off edge to more positive potentials over time is also indicated for single QDs, see first cycle (bottom) and time average (dashed line). Despite intensity fluctuations, several scans show a gradual decrease of the maximum intensity at this edge (blue lines). This is most pronounced for QD 3 and 4 but also QD 1 and 2 show intermediate intensities before turning off completely. No such intensity decrease is observed to positive potential. Instead, all QDs still show periods of high luminescence even at 0 V.

A representative QD investigated in the confocal setup is depicted in Fig. 6.19. A very broad gradual decrease is observed for 1 s binning (black). Binning at 20 ms (gray) shows that with more negative potentials fluctuations between high and low luminescence increase. The average intensity decreases due to a shortening of the times at high intensity.

6.5.2 ITO Electrode

Measurements of single QDs on ITO also show a time and ensemble average like that in ensemble measurements of the last sections. A measurement of a total of 150 QDs and three cycles in undried solution is included in the appendix (see Fig. C.8). The same features are observed as on ZnO/ITO. The decreasing time-averaged intensity is also determined by increasing intensity fluctuations instead of a decrease of the bright state intensity. However, in contrast to ZnO/ITO, on ITO many single QDs show a very long linear decrease of intensity before turning off at negative potentials and an increase after turning on again. This is demonstrated for two QDs in Fig. 6.20. The linear decrease can reach over the whole measured voltage range. At the ensemble turn-off edge it steepens before turning off completely.

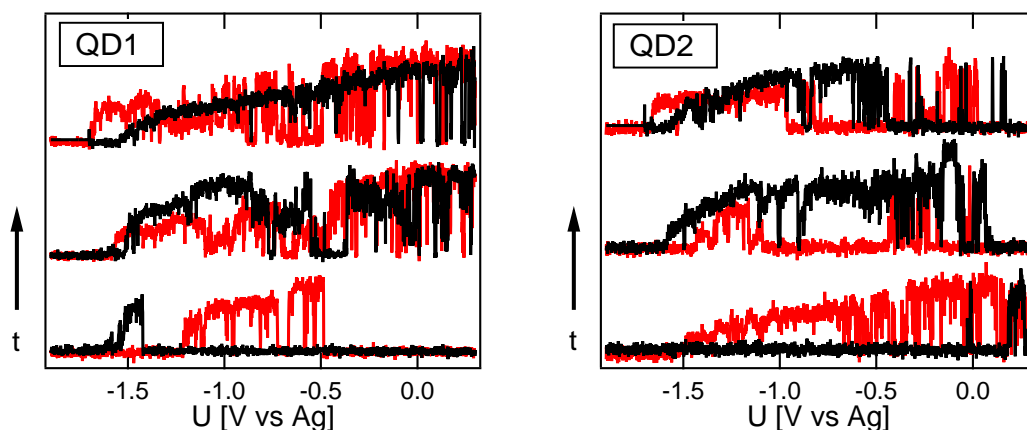


Figure 6.20: Fluorescence over three consecutive voltage cycles of two single QDs on ITO. The measurement is taken in undried solution at $200\ \mu\text{W}$ excitation in the wide field setup (D). Cathodic sweeps are displayed in red, anodic sweeps in black. First cycle is at the bottom, last at the top.

6.5.3 Discussion

In the established setup reduction and oxidation processes can also be observed on single QDs as shown in Figs. 6.17 to 6.20 as well as C.7 and C.8 in the appendix. The time average and ensemble average yield the same results as observed for ensemble measurements (see previous sections). Single QD investigations show that the involved mechanisms that quench ensemble luminescence all fluctuate in efficiency over time. Non-fluctuating quenching mechanisms would also decrease the QD maximum intensity. Such a decrease is not observed for any of the involved mechanisms. The decrease at the negative turn-off edge for a bin time of 200 ms only appears to involve a decreasing maximum intensity as fluctuations are not resolved. At a higher time resolution of 20 ms blinking is resolved with decreasing on-state lengths (see Fig. 6.19). Ensemble measurements average over these fluctuations, that can only be revealed with single QD investigations. At least two types of blinking mechanisms are observed, like in Ref. [76]. Both can be influenced with the electrode potential. One increases above (region I), the other below (region III) the expected QD conduction band edge. They are further discussed in Secs. 6.5.3.1 and 6.5.3.2 below.

All QDs are observed to turn off at negative potential, associated with electron injection to the QD conduction band. Turn-off potentials and transition widths differ for different QDs, representing a distribution of individual QD characteristics. This distribution is further evaluated in the next section (Sec. 6.6).

6.5.3.1 Transition of Electron Injection (A-Type Blinking)

The observed intensity decrease to negative potential in region I is associated with electron injection. It is not abrupt but continuous for most QDs at 200 ms bin time. At lower bin times (20 ms, see Fig. 6.19) this continuous decrease is revealed to stem from blinking between high and low luminescence with a decreasing amount of time spent at high intensity. This corresponds well to an increasing electron injection rate k_{in}^- (ren-

dering the QD dark) and a decreasing ejection rate k_{out}^- (recovering fluorescence), see top left of Fig. 6.16. The length of the bright periods is determined by k_{in}^- , that of the dark periods by k_{out}^- . The decreasing length of bright periods in Fig. 6.19 thus directly reflects the increase of k_{in}^- . Close to the injection edge both rates are in the range of 100 Hz. Similar blinking at negative potential with exponential dwell time distributions has also been found in the groups of Klimov [76] and Guyot-Sionnest [73].¹⁰ in Ref. [76] it was denoted as A-type. A relevance in the typically observed blinking phenomenon is not directly evident. Typical blinking experiments do not show exponential dwell time statistics, especially not for the off-state. Furthermore, the quantum yield of the negative trion is too high for typical dark states [53]. Therefore, this kind of A-type blinking is not the dominating blinking mechanism observed for QDs on glass or in polymers. It is, however, assigned to an exponential contribution to blinking statistics as found here (see Secs. 5.3.4 and [209]) and by others [75, 210]. This contribution is an exponential hump on the off-state dwell time distribution at several milliseconds. It is typically accompanied by a dim intensity level with a quantum yield corresponding well to that of the negative trion (see Sec. 6.4.3.1). Qin and Guyot-Sionnest [75] also found a correspondence of trion and dim state lifetimes in CdSe/CdS QDs.

6.5.3.2 Fluctuations at Mid-Gap Potentials (B-Type Blinking)

Not all QDs show a decrease of their average fluorescence to positive mid-gap potentials (region III). Even those that do, do not show a continuous quenching in individual scans. The lower intensity results from intensity fluctuations with a decreasing time spent at the QD maximum fluorescence. This decrease is observed on both substrates and indicates another on-off blinking mechanism. It corresponds well to quenching due to photoinduced positive charging as suggested in Sec. 6.4.3.2. Photoinduced electron ejection rates from the conduction band k_{in}^{*+} and subsequent injection rates to the valence band k_{out}^+ (see Fig. 6.16) are considerably lower than those of A-type blinking. A-type blinking corresponds to dwell times shorter than the bin time of 200 ms (see above). This is not observed at mid-gap potentials. Lower rates for photoinduced positive charging are comprehensible. Photoinduced electron ejection is strongly limited by the time the excited electron spends in the conduction band. It scales with the excitation rate R_{exc} ($\approx 0.4 \mu\text{s}^{-1}$ for confocal excitation) and the excited state lifetime $\tau_{\text{eff}} \approx 10 \text{ ns}$. For confocal excitation as in Fig. 6.19 the fraction of time in the excited state it is limited to $R_{\text{exc}}\tau_{\text{eff}} = 0.4\%$. Electron injection into the valence band is also slow due to the unfavorable band alignment at the electrode (see Sec. 6.2.3.1). Blinking is thus determined by longer dwell times than the bin time. A large spread of different rates can result from the strong dependence of tunneling barriers on inhomogeneities of the substrate and HDA layers. The presence of QDs without considerable quenching (QD 1 and 4 in Fig. 6.17) is thus comprehensible as well. Galland et al. [76] observe similar blinking at mid-gap potentials for thick shell CdSe/CdS QDs which they denote as B-type blinking. They argue with the creation of and relaxation over hot electron

¹⁰The determined exponential dwell time distributions in Refs. [73] and [76] might be questioned as intensity peaks in the presented intensity histograms are partially overlapping. This leads to noise-induced exponential cut-offs (see Chap. 5). The decreasing average intensity observed here still indicates the existence of a real cut-off for the length of bright and dark state.

traps, which would be conceivable as well. Illumination dependent measurements in Sec. 6.7, however, rather support photoinduced positive charging for the QDs here.

The relevance of photoinduced positive charging in common time-traces had long been accepted. Its illumination dependence agrees well with typical observations (see Sec. 6.7). It was, however, challenged by Zhao et al. [53] and Rosen et al. [54] in 2010 who found off-states that were not govern by trion relaxation. The observation of different distinct blinking and quenching mechanisms here as also found by others [75, 76, 210] indicates that different off-states exist. They are not all governed by the same quenching mechanism. Photoinduced positive charging can thus still be expected to lead to blinking in QDs. It is just not responsible for all off-states. This has also recently been suggested by Park et al. [239], who assigned negative and positive trion to dim and dark state of single thick shell CdSe/CdS QDs. For these QDs quantum yields and lifetimes of the dim and dark state were in good agreement with those of the trions.

In addition to the increase of blinking, an increase of time spent at intermediate intensity levels (flickering) can also contribute to the average intensity decrease. The observed lifetime decrease on ZnO/ITO indeed suggests the presence of only partially quenched states with $QY > 1\%$ (see III a) of Fig. 6.16). When comparing single QD measurements on ZnO/ITO and ITO (Figs. 6.18, 6.20, C.7 and C.8), intermediate intensity levels that increase in occurrence with positive potential appear to be more relevant on ZnO/ITO. Without lifetime information they can, however, not be separated from unresolved blink events (see Sec. 2.2.3.1). Single QD measurements still reveal, that also the suggested trap relaxation mechanism on ZnO/ITO is not static but subject to fluctuations. As stated before, a static process would also lead to a decrease of the maximum QD intensity.

6.5.3.3 Single Quantum Dots on ITO

Like single QDs on ZnO/ITO, single QDs on ITO (Figs. 6.20 and C.8) show a steep decrease to negative potential at the expected conduction band edge (region I). The average valence band is expected at the very edge of the scan close to 0.3 V (region II). No corresponding decrease of the maximum QD intensity is found. In contrast to charge exchange with the conduction band, hole injection and ejection do thus not proceed within the bin time. Corresponding rates k_{in}^+ and k_{out}^+ are lower than k_{in}^- and k_{out}^- (see Fig. 6.16). They lead to blinking even for binning at 200 ms, which can, however, not be separated from the photoinduced positive charging discussed above.

The notable difference of single QD observations on ITO and ZnO/ITO lies at mid-gap potentials (region III). On ITO a long linear increase of the maximum QD intensity is observed to positive potentials. Starting from the conduction band edge the maximum intensity linearly increases over the whole applied voltage range of 1.5 V. Such a behavior has not been reported before. In time or ensemble averages it is also not evident. It is thus partially compensated by the enhanced intensity fluctuations discussed above (also see Fig. C.8 of the appendix). Ensemble measurements indeed show a slightly higher intensity at mid-gap potentials than at the conduction band edge (see Figs. 6.5 and 6.11). A third quenching process is thus found in region III. It is strongly substrate dependent and only observed on ITO.

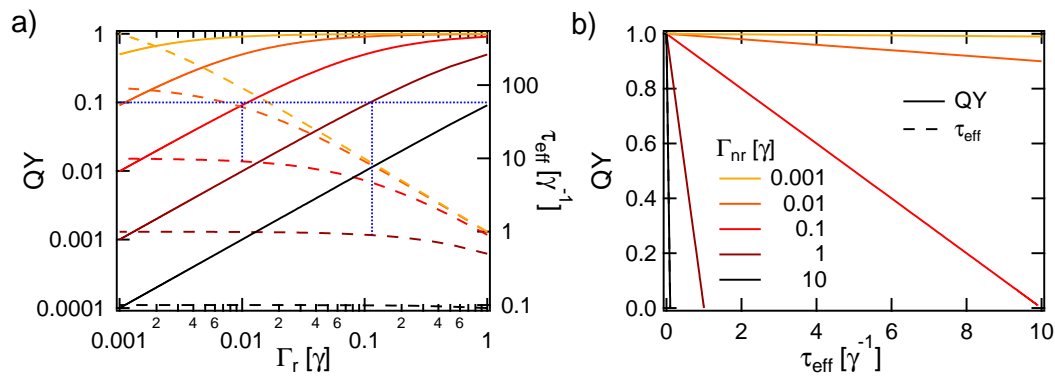


Figure 6.21: a) Dependence of quantum yield QY and lifetime τ_{eff} on the radiative rate Γ_r for different Γ_{nr} . Horizontal blue line indicates a quantum yield of 10%. Vertical blue lines the corresponding lifetimes τ_{eff} for $\Gamma_{\text{nr}} = 0.1$ or 1, respectively. b) Dependence of QY on τ_{eff} for different Γ_{nr} . The legend in b) corresponds to a) as well. All rates and times are given with respect to an arbitrary reference rate γ .

Such a quenching of the maximum intensity by a factor of two should intuitively be reflected in fluorescence decays. Those are, however, not found to change (see Fig. 6.15 for potentials > -1 V). As discussed before, an intensity change without a change in lifetime can involve a (third) blinking mechanism with dwell times much shorter than the bin time of 200 ms. Following the argument in Ref. [76] also the activation of hot hole traps might be proposed. For low quantum yields a change in the radiative rate Γ_r can also leave the effective lifetime τ_{eff} unaffected. A strong domination of non-radiative rates Γ_{nr} decreases the influence of Γ_r on $\tau_{\text{eff}} = (\Gamma_{\text{nr}} + \Gamma_r)^{-1}$. This is demonstrated in Fig. 6.21. For different non-radiative decay rates Γ_{nr} the quantum yield $\text{QY} = 1 - \Gamma_{\text{nr}} \tau_{\text{eff}}$ (see Eq. (2.22)) as well as the lifetime τ_{eff} are plotted in dependence on the radiative rate Γ_r in a). In b) the linear dependence of QY and τ_{eff} is plotted as well. Due to quenching by the electrode the quantum yield of the QDs here has been estimated to be below 10% (see Sec. 6.1.2), thus below the blue horizontal line in a). Up to these quantum yields τ_{eff} hardly changes for different Γ_r (left region up to the blue vertical lines). The same is observed in b) Due to a steeper slope given by Γ_{nr} large changes in QY can be observed for very small changes in τ_{eff} . A decrease of the radiative rate with potential could result from the quantum confined stark effect (QCSE) (see Sec. 2.2.3). The electrode on one side of the QD and counter ions on the other can lead to strong fields across the QD that linearly increase with potential (also see Sec. C.6.3 of the appendix). Electric fields reduce the overlap of electron and hole wave function and thus the radiative decay rate. However, it would not explain the lack of such an observation on ZnO/ITO. Furthermore, QD spectra should shift red with increasing field, thus negative potential, but are observed to shift blue (see Sec. C.6 of the appendix). Whether fast blinking, hot hole traps, electric fields or other changes in the radiative rate are involved, could not be determined here. Further studies involving lifetimes and spectra of single QDs are in order to identify the origin of this extraordinary observation and its relation to the electrode material.

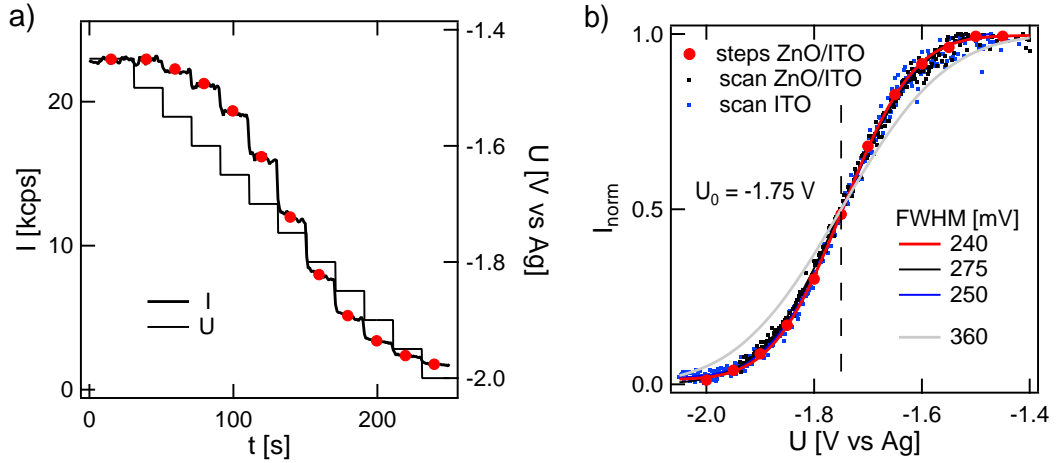


Figure 6.22: a) Fluorescence decrease I over time on ZnO/ITO for 20s steps of increasing negative potential U . Average fluorescence of each step is indicated as red markers. b) Normalized fluorescence intensity for representative cathodic voltage sweeps on ZnO/ITO (black dots, offset by -0.04 V) and ITO (blue dots, offset by -0.07 V). Red markers indicate the average intensity of each step in a). Curves are normalized to their corresponding maximum and minimum intensity. Fits with Eq. (6.1) are included as lines in the corresponding colors. Fitted FWHMs are indicated in the legend. A curve for FWHM= 360 mV is added in gray for comparison.

6.6 Distribution of Negative Turn-Off Characteristics

The investigation of single QDs as established in the previous section also allows the identification of varying characteristics between QDs. An example is the negative turn-off edge in region I. It features a characteristic turn-off potential and transition width. Both parameters are found to differ for individual QDs (see Figs. 6.17 and 6.18 or Figs. C.7 and C.8 of the appendix). For the measurement shown in Figs. 6.17 and 6.18 this distribution of turn-off potentials and transition widths is evaluated below and compared to the observed ensemble edge.

6.6.1 Transition Width of the Ensemble

The voltage steps in Fig. 6.22 a) show that quenching at negative potentials mostly takes place within the bin time of 200ms, as was also indicated in fast blinking of single QDs. Only a very slow decrease continues on the timescale of seconds after the first intensity drop. The average intensity for each step (red markers) is plotted over the applied voltage in b). A triangular scan at 10 mV/s of the same sample is also shown as black dots and a scan on ITO as blue dots. These scans are shifted in voltage by -0.04 V (ZnO/ITO) and -0.07 V (ITO), respectively. The luminescence decreases from its maximum to its minimum value over approximately 0.5 V. The width of the intensity decrease $I(U)$ with potential U can be determined with the error function

$$I(U) = \frac{I_{\text{max}}}{2} \left[1 + \text{erf} \left(\sqrt{2 \ln(2)} \frac{U - U_0}{\text{FWHM}} \right) \right] - I_{\text{BG}} \quad (6.1)$$

where I_{BG} and I_{max} are background and maximum intensity, respectively. Eq. (6.1) is a convolution of a step function and a Gaussian (see Sec. A.2) with its maximum prob-

Table 6.1: Fit Parameters to Eq. (6.1) for the Negative Turn-Off Edge

	QD 1	QD 2	QD 3	QD 4	sum	1 st cycle	mean
U_0, u_0 [V]	-1	-1.1	-1.25	-1.25	-1.3	-1.35	-1.29
FWHM, fwhm [mV]	275	210	150	360	360	280	240
U'_0, u'_0 [V]	-0.85	-1.15	-1.05	-1.05	-1.17	-1.25	-1.15
FWHM', fwhm' [mV]	370	380	685	505	540	400	340

ability at U_0 and a full width at half maximum FWHM. For a Gaussian distribution of turn-off potentials u_0 that immediately quench the fluorescence once $U < u_0$, Eq. (6.1) yields the distribution's average potential U_0 and width FWHM. When fitting Eq. (6.1) to the observed signal, a FWHM of 240 mV is obtained for the 20 s steps and 275 mV (250 mV) for the scan on ZnO/ITO (ITO). Fitted FWHMs typically scatter between 200 mV and 300 mV, slightly decreasing with time (see Fig. C.5 d) of the appendix).

6.6.2 Distribution of Negative Turn-Off Characteristics

A fit of Eq. (6.1) is also applied to the time and ensemble average of the single QD measurement in Fig. 6.17 a). It yields a FWHM_{sum} of 360 mV. This width is broader than that of typical ensemble measurements (< 300 mV), see Fig. 6.22 b). A fit to the first cycle yields a $\text{FWHM}_{1^{\text{st}} \text{ cycle}}$ of 280 mV.

The individual time-averaged intensity-voltage scans of all QDs are summarized in Fig. 6.23 a). For each QD the negative turn-off edges of cathodic (u_0 , fwhm) and anodic (u'_0 , fwhm') sweep are fitted with Eq. (6.1). Fit parameters for single QDs are here referred to with lowercase letters, fit averages and ensemble fits with uppercase letters. Histograms of the fit parameters are plotted on the right of Fig. 6.23. Values for maximum occurrences of U_0 , U'_0 , FWHM and FWHM' are specified in Tab. 6.1 (mean). Tab. 6.1 also includes fit parameters of the time averages for the four QDs of Fig. 6.17, the ensemble average of the first cycle (1. cycle) and the complete time and ensemble average of all cycles (sum). The spread in u_0 (see Fig. 6.23 b)) amounts to $\text{FWHM}_{\text{edges}} = 240$ mV with a $\text{FWHM}_{\text{mean}}$ of maximum occurrence also at 240 mV (see Fig. 6.23 c)). The plot of u_0 versus u'_0 on the bottom of 6.23 b) indicates a similar offset for all QDs (red line corresponds to $u_0 = u'_0$) and a weak correlation towards a higher offset for less negative u_0 (see blue line). QDs in a) are ordered according to their fitted u_0 values, marked by a white solid line. No correlation between this edge potential and an intensity decrease to positive potentials is visible. The fitted fwhms are broader in the anodic than in the cathodic scan.

For the single QDs in Fig. 6.18 also the least fluctuating transition of the seven individual cycles is fitted with Eq. (6.1). They yield $\text{fwhms}_{1 \text{ cycle}}$ that are between 130 meV and 190 meV as indicated in the graphs in blue.

6.6.3 Discussion

Quenching at high negative potentials is associated with electron injection from the electrode into the QD and subsequent Auger quenching. With increasing negative potential, more and more QDs are charged and become dark. An ensemble transition

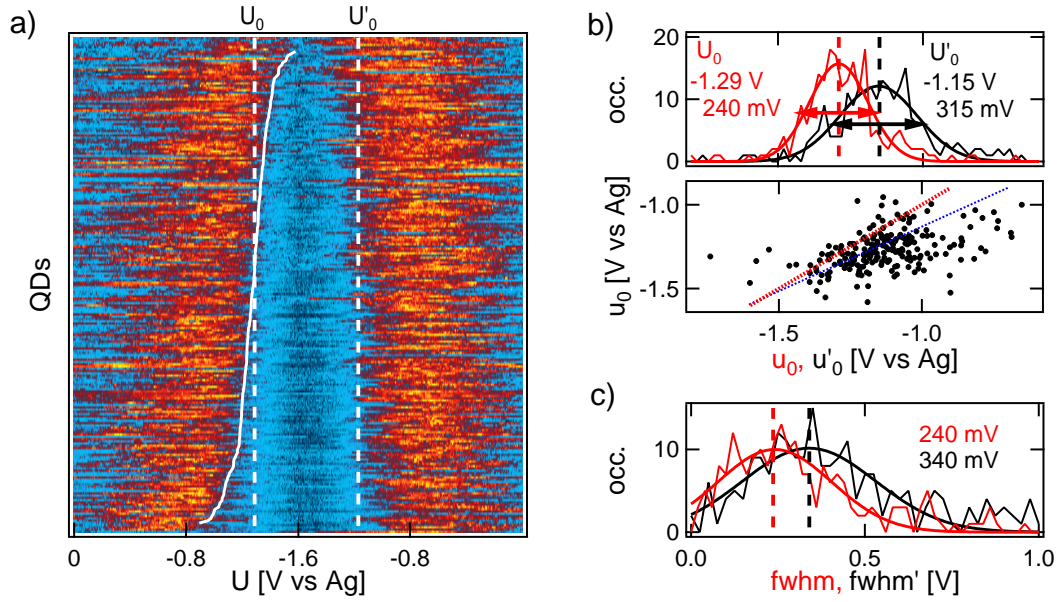


Figure 6.23: Distribution of widths and potentials of the negative turn-off edge for all single QDs of the measurement of Figs. 6.17 and 6.18. a) Individual time averages of all QDs over all seven cycles. Each line on the y-axis corresponds to one QD. The x-axis indicates the applied voltage, cathodic sweep on the left, anodic sweep on the right. The normalized intensity is given in the color scale. QDs are ordered according to their fitted turn-off potentials u_0 of Eq. (6.1) (white solid line). The white dashed lines indicate U_0 and U'_0 of maximum occurrence. Fit parameters are summarized for u_0 (red) and u'_0 (black) on the top of b) and the corresponding $fwhm$ and $fwhm'$ in c). Bottom of b) shows the correlation of u_0 and u'_0 . Red dotted line represents $u_0 = u'_0$, blue dotted line a slope of 100 mV/ 30 mV.

with a FWHM of $200 - 300$ mV is observed. The ensemble time average of the single QDs in Fig. 6.17 shows a broader $FWHM_{\text{sum}}$ of 360 mV (see Tab. 6.1 and Fig. 6.22 b)). This broadening results from the shift of the injection edge over time (see Fig. C.5 d) of the appendix). A fit to only the first cycle yields a width of $FWHM_{1\text{st cycle}} = 280$ mV as typically obtained from single scan ensemble measurements. Without this drift, the ensemble width results from a convolution of the single QD transition with a distribution of edge potentials u_0 for different QDs. To obtain information on the respective contributions, Eq. (6.1) is also fitted to the time-averaged single QD transitions. This yields a distribution of single QD injection edges u_0 as well as transition widths $fwhm$ (see histograms in Fig. 6.23). The distribution of u_0 peaks at -1.3 V (sum) which agrees with the mean of the distribution for single QDs -1.29 V (mean), see Tab. 6.1. Again, the shift of the injection edge is reflected in the fitted $fwhm$. Single QD time averages show a $fwhm$ peaking at 240 mV. The width of selected cycles of single QDs is typically smaller $fwhm_{1\text{ cycle}} \approx 160$ mV (see Fig. 6.18), which corresponds to the same 80 mV broadening of the ensemble transition. Still, large variations between QDs are observed (see histogram in Fig. 6.23 c) and the QD investigated in Fig. 6.19).

The fitted $fwhm$ and $fwhm_{1\text{ cycle}}$ do not correspond to any additional Gaussian distribution of injection edges for single QDs. They thus do not have any immedi-

ate physical relevance in this context. If, however, the extracted contributions of a distribution of u_0 with $\text{FWHM}_{\text{edges}} = 240\text{mV}$ and an average transition width of $\text{FWHM}_{\text{mean}} = 240\text{mV}$ are describing the situation well, a convolution of two Gaussians with $\text{FWHM} = 240\text{mV}$ should still approximately yield a width of $\text{FWHM}_{\text{sum}} = 360\text{mV}$. In a convolution the widths add up as follows $\text{FWHM}_{\text{AVG}} = \sqrt{240^2 + 240^2}\text{mV} = 340\text{mV}$, which is in good agreement with FWHM_{sum} . Also for a second Gaussian with $\text{fwhm}_{1\text{cycle}} = 160\text{mV}$, the $\text{FWHM}_{\text{avg}} = \sqrt{240^2 + 160^2}\text{mV} = 290\text{mV}$ corresponds well to typical ensemble averages like that of the first cycle $\text{FWHM}_{1\text{st cycle}} = 280\text{mV}$.

The evaluation of single QD characteristics thus shows that the width of the time-averaged ensemble originates from a distribution of injection edges for single QDs with $\text{FWHM}_{\text{edges}} = 240\text{mV}$ that each show a time-averaged transition width around $\text{FWHM}_{\text{mean}} = 240\text{mV}$ and an approximate single cycle transition width of $\text{fwhm}_{1\text{cycle}} = 160\text{mV}$. This spread in u_0 and the significance of the fitted $\text{fwhm}_{1\text{cycle}}$ are further discussed in the following sections.

6.6.3.1 Transition Width of Electron Injection

As mentioned before, the fitted transition width of $\text{fwhm}_{1\text{cycle}} \approx 160\text{mV}$ for a single QD does not correspond to a distribution of injection edges u_0 . The shape of the transition for a single QD is defined by the electron injection rate $k_{\text{in}}^-(U_F)$ and ejection rate $k_{\text{out}}^-(U_F)$ and their dependence on the applied potential U_F . The continuous intensity decrease at the electron injection edge in single cycles (see Fig. 6.18) indicates that $k_{\text{in}}^-(U_F)$ and $k_{\text{out}}^-(U_F)$ are high enough to lead to several injection and ejection processes within the bin time. The average bin intensity $I(U_F)$ is then proportional to the fraction of time p_N , in which the QD is neutral, given that the charged QD has a quantum yield close to zero ($\text{QY}^- \approx 0$).¹¹ This fraction p_N for charge injection and ejection in general (positive or negative) is given by (see Eq. (A.9) of the appendix)

$$I(U_F) \propto p_N = \frac{k_{\text{out}}(U_F)}{k_{\text{out}}(U_F) + k_{\text{in}}(U_F)} = \left(\frac{k_{\text{in}}(U_F)}{k_{\text{out}}(U_F)} + 1 \right)^{-1} \quad (6.2)$$

At each electrode potential U_F , the transition width is thus defined by the ratio of charge injection and ejection rates $k_{\text{in}}(U_F)/k_{\text{out}}(U_F)$.

The potential dependent ratio of $k_{\text{in}}^-/k_{\text{out}}^-$ is typically given by the Nernst equation as the ratio of reduced and oxidized concentrations $\rho_{\text{red}}/\rho_{\text{ox}}$ (see Eq. (4.13))

$$\frac{k_{\text{in}}^-}{k_{\text{out}}^-} = \frac{\rho_{\text{red}}}{\rho_{\text{ox}}} = e^{-\frac{e(U_F - u_{\text{CB}})}{k_B T}} \quad (6.3)$$

One might assume that a time-averaged distribution of conduction band edges u_{CB} due to solvent fluctuations leads to a broadening of the transition. Such potential fluctuations due to solvent reorganization are described in Marcus theory and in the Gerischer model¹² (see Sec. 3.3). These fluctuations, however, only represent fluctuations of energies of reduced and oxidized species, not the redox potential itself.

¹¹ $\text{QY}^- \approx 0$ is assumed for simplicity. The relative QY^- has been determined to 10% in Sec. 6.4. In this case it is $I \propto p_N + (1 - p_N)\text{QY}^-$.

¹²The Gerischer model is based on Marcus theory.

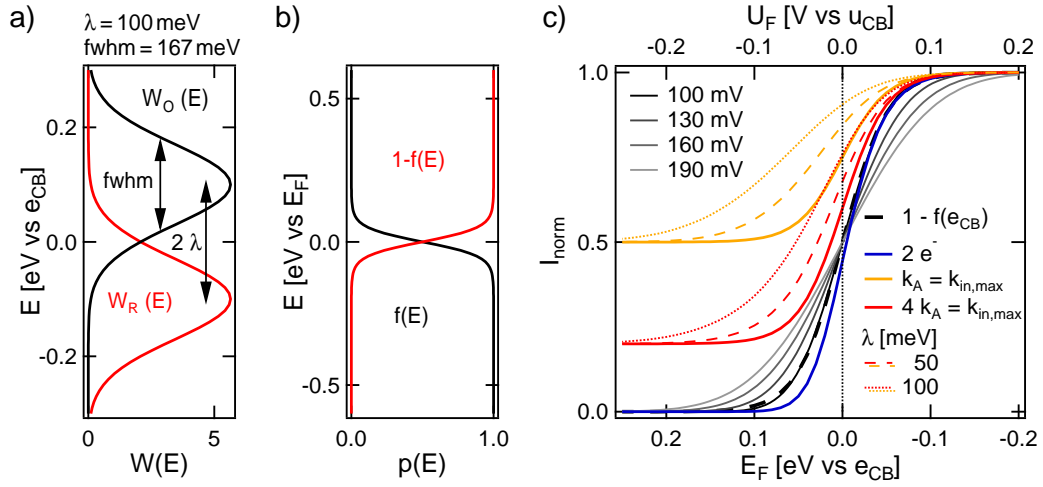


Figure 6.24: a) Time-averaged probability distributions of reduced state W_R and oxidized state W_O of the conduction band at e_{CB} in the Gerischer model (see Sec. 3.3) with an arbitrary reorganization energy λ . b) Probability density of occupied $f(E)$ and unoccupied $1 - f(E)$ states in the electrode of Fermi level E_F . c) Comparison of the theoretical intensity transition of single QDs for one electron injection $1 - f(e_{CB})$ with the measured transition widths (gray lines) given by equation Eq. (6.1). A curve with FWHM= 100 meV is included as guide to the eye. Two electron injection ($2e^-$, Eq. (6.7)) and the effect of additional Auger rates k_A for one electron injection are shown in blue, red and orange, respectively (see text).

This can be illustrated when directly looking at the ratio of injection to ejection rates at any energy E . In the Gerischer model the energy fluctuations of reduced and oxidized species are described by time-averaged Gaussian functions $W_{O/R}(E)$ (see Eq. (3.5)) with a width characterized by the reorganization energy λ (see Fig. 6.24 a), $\text{fwhm} = 4\sqrt{\ln(2)\lambda k_B T}$. Injection and ejection rates are proportional to these distributions, as well as the occupation level of states in the electrode, thus $f(E)$ and $1 - f(E)$, respectively (see Eq. (3.6), with $f(E)$ the Fermi-Dirac distribution of Eq. (3.8) depicted in Fig. 6.24 b)). Assuming the matrix element in Eq. (3.6) to be equal for reduction and oxidation, the ratio of injection and ejection rate at each energy E is given by

$$\frac{k_{\text{in}}^-(E)}{k_{\text{out}}^-(E)} = \frac{f(E)W_O(E)}{(1-f(E))W_R(E)} = \frac{f(e_{CB})}{1-f(e_{CB})} = e^{\frac{E_F - e_{CB}}{k_B T}} \quad (6.4)$$

with the redox energy $E_{F,\text{redox}} = e_{CB}$ in $W_{O/R}(E)$ (see Eq. (3.5)). It is thus independent of E and λ . The different sign in the exponents of Eqs. (6.4) and (6.3) results from the correspondence of higher electron energies to more negative voltages. Eq. (6.4) is also directly obtained simply assuming a non-fluctuating e_{CB} with $k_{\text{in}}^- \propto f(e_{CB})$ and $k_{\text{out}}^- \propto 1 - f(e_{CB})$.

Without any additional injection or ejection rates, the transition of each single QD

should thus be described by Eqs. (6.2) and (6.3) or (6.4) according to

$$I(E_F) \propto \left(e^{\frac{E_F - e_{CB}}{k_B T}} + 1 \right)^{-1} = 1 - f(e_{CB}) \quad (6.5)$$

$$I(U_F) \propto \left(e^{-\frac{e(U_F - u_{CB})}{k_B T}} + 1 \right)^{-1} \quad (6.6)$$

This intensity decay is plotted in Fig. 6.24 c) (black dashed line). Selected plots of Eq. (6.1) (gray) corresponding to typical single QD transition widths, as well as a curve with a $\text{fwhm} = 100 \text{ mV}$, are included for comparison. The latter resembles the decay from Eq. (6.6). Typical $\text{fwhm}_{\text{cycle}}$ are broader than this transition. This implies additional changes in $k_{\text{in}}^-/k_{\text{out}}^-$. Possible origins are discussed in Sec. 6.6.3.3.

6.6.3.2 Distribution of Electron Injection Potentials

A distribution of turn-off potentials u_0 with a $\text{FWHM}_{\text{edges}} = 240 \text{ mV}$ is observed in the single QD measurement in Fig. 6.23. This directly corresponds to a spread in energy of 240 meV . One origin of a distribution of injection edges is expected from the QD size distribution. The size distribution leads to different conduction band edges for single QDs. Smaller QDs show stronger confinement, thus higher transition energies. The valence band edge is lowered and the conduction band edge lifted, inversely dependent on the effective mass of hole and electron, respectively (see Eq. (2.6) in Sec. 2.1.1.1). Due to the electron's lower effective mass ($m_h^* \approx 10 m_e^*$), the spread of conduction band edges due to the size distribution is much broader. Different transition energies are thus mostly determined by different energies of the conduction band edges. The distribution of transition energies is directly observable in emission and absorption spectra. Emission and absorption peaks in Fig. 4.1 a) show a FWHM of 150 meV . This FWHM includes any differences in transition energy due to size, shape or spectral diffusion. The determined spread in injection edges $\text{FWHM}_{\text{edges}} = 240 \text{ meV}$ is considerably broader, as also found by Jha and Guyot-Sionnest [73]. The size distribution thus only contributes to the distribution of u_0 . Like for the single QD transition widths, additional processes are involved that broaden the distribution of injection edges. A broadening of the distribution of u_0 also indicates that no direct correlation between u_0 and the transition energy should be expected, which was also found in Ref. [73]. The fitted u_0 yields the potential where half the intensity is quenched (see Eq. (6.1)). It thus corresponds to $k_{\text{in}}(u_0) = k_{\text{out}}(u_0)$. When additional injection and ejection rates are involved, this equality quickly leads to $u_0 \neq u_{CB}$. The origin of possible additional injection and ejection rates are discussed in the following.

6.6.3.3 Multiple Charging and Auger Ejection

The electron injection edge is described by Eq. (6.2). Additional injection rates k_{in}^- and ejection rates k_{out}^- will thus influence its shape and position. Two effects are discussed in the following. The first is an additional contribution to k_{in}^- due to the injection of a second electron in the QD 1S state. The second is a contribution to k_{out}^- due to Auger ejection of electrons.

At high negative electrode potentials not only one but multiple charges can be injected into the QD. The lowest conduction band state (1S, see Fig. 6.25 a)) can be occupied by two electrons, while higher states can take even more electrons. To examine the effect on the intensity decrease, the injection of the second electron into the 1S state is considered. It is assumed to show the same injection and ejection rate as the first electron, only weighted by the different occupation levels of the 1S state (see Sec. A.3 of the appendix). The injection edge is then given by (see Eq. (A.11))

$$I(U_F) = I_0 \left(1 + e^{-\frac{e(U_F - u_{CB})}{k_B T}} + \frac{1}{4} e^{-2\frac{e(U_F - u_{CB})}{k_B T}} \right)^{-1} \quad I(u_{CB}) = 0.45I_0 \quad (6.7)$$

Eq. (6.7) is also plotted in Fig. 6.24 c) (blue). It is even more narrow than Eq. (6.5) and shows a potential u with $I(u) = I_{\max}/2$ slightly shifted to more negative energies (positive potentials). The injection of multiple charges itself thus cannot considerably increase the width of the distribution of u_0 and does not broaden the transition width.

An additional contribution to electron ejection rates can be found in an Auger-assisted process with rate k_{out}^{A-} (see Fig. 6.25). In the negatively charged QD, the transition energy of excitons is transferred to the extra electron, which leads to the observed quenching. The electron is lifted to a higher energy level e_A with a higher tunneling probability to the electrode. Such Auger-assisted electron ejection is independent of U_F and only depends on the excitation rate R_{exc} . The resulting total ejection rate is then given by $k_{\text{out}}^- = k_{\text{out}}^-(U_F) + k_{\text{out}}^{A-}(R_{\text{exc}})$, with the contribution of the electrode $k_{\text{in}}^-/k_{\text{out}}^-(U_F)$ still given by Eq. (6.4) and $k_{\text{in}}^- = k_{\text{in}}^-$. The intensity decrease of Eq. (6.2) then yields

$$I(E_F) \propto \left(\left(e^{-\frac{E_F - e_{CB}}{k_B T}} + \frac{k_{\text{out}}^{A-}}{k_{\text{in}}^-} \right)^{-1} + 1 \right)^{-1} \quad (6.8)$$

with the total rate k_{in}^- integrated over all E for a given E_F . For the simple idea of $k_{\text{in}}^- \propto f(e_{CB})$ and $k_{\text{out}}^- \propto 1 - f(e_{CB})$ for a fixed conduction band edge at e_{CB} , the effect of two different k_{out}^{A-} is also plotted in Fig. 6.24 (red and orange, $k_A = k_{\text{out}}^{A-}$). When the injection into higher energy levels is neglected, $I(U_F)$ no longer decays to zero at high negative potentials. The residual intensity is given by the ratio of the maximum injection rate $k_{\text{in,max}}$ and the Auger ejection rate k_{out}^{A-} . Due to the resonant tunneling process, $k_{\text{in,max}}$ corresponds to Fermi levels with a full occupation of electrode states at e_{CB} , thus $f(e_{CB}) = 1$. Eq. (6.2) then yields $I(E_F) = A(1 - f(e_{CB})) + (1 - A)$ with $A = k_{\text{out}}^{A-}/(k_{\text{out}}^{A-} + k_{\text{in,max}}^-)$, thus an offset and compression of Eq. (6.5). The transition width is unchanged. In reality, additional electron injection rates $k_{\text{in}}^{P,D-}$ into higher QD energy levels (see Fig. 6.25 a)) would eventually quench fluorescence. This effectively broadens and shifts the transition to more negative potentials even without solvent fluctuations. With the introduction of k_{out}^{A-} , however, not only the ratio of electrode injection and ejection rates is important, but also k_{in}^- itself (see Eq. (6.8)). Thus, also the actual shape of $W_O(E)$ in the Gerischer model influences the transition. With $k_{\text{in}}^-(E_F) \propto \int f(E)W_O(E)dE$, this is demonstrated for the same k_{out}^{A-} and two different reorganization energies λ in Fig. 6.24 (dashed and dotted lines). The transition is considerably broadened and shifted to more negative potential. A significant Auger

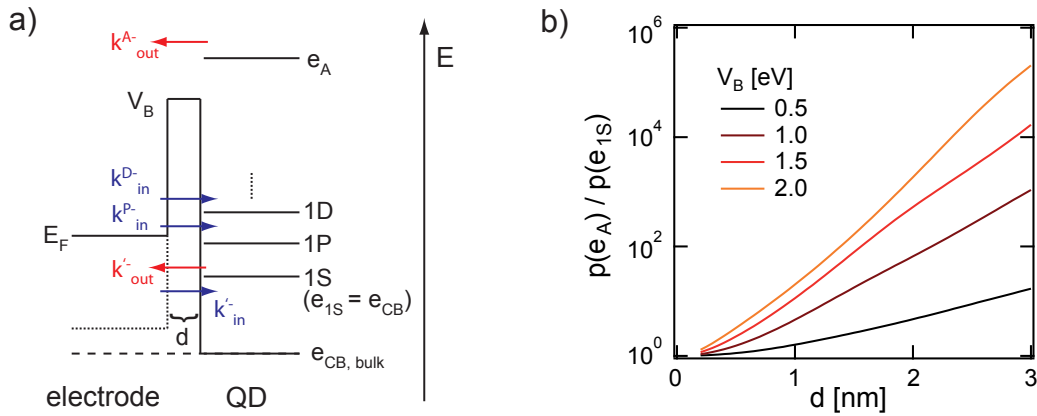


Figure 6.25: Relative probability of Auger-assisted and ground-state electron ejection to the electrode. a) Scheme of the tunneling process between QD and electrode at Fermi level E_F with tunneling barrier V_B and width d . First QD energy levels and that of the Auger-excited state are marked relative to the bulk conduction band edge at 0 eV. b) Ratio of the electron ejection probabilities to the electrode from the Auger excited state $p(E_A)$ and the ground state $p(E_{1S})$ for different V_B and d . An effective electron mass of $m^* = 0.11m_e$ is assumed. For a higher m^* than for the hole an even stronger increase with d and V_B is found.

ejection rate can thus markedly influence the transition width and determined edge potential simply due to the increasing relevance of solvent fluctuations.

Relative Auger Ejection Efficiencies Auger ejection efficiencies depend on the probability of electron ejection from the excited state and the time spent in this state. Relative probabilities for Auger-assisted and ground-state electron ejection to the electrode can be estimated with Eq. (2.27). Auger ejection to the electrode has to overcome the same barrier V_B as ejection from the 1S level e_{1S} . It simply proceeds from an energy $e_A > V_B$ as shown in the sketch in Fig. 6.25 a). The transition probability is still given by Eq. (2.27) only with an imaginary κ as $V_B - e < 0$. The QDs' emission energy (2.07 meV) lies 320 meV above the bulk band gap (1.75 meV). The energy difference mostly results from confinement, thus, kinetic energy of the electron and the hole. As $m_h^* \approx 10m_e^*$, the kinetic energy of the 1S electron is estimated to $e_{1S} = \frac{m_e^*}{m_h^*} \Delta E = 290$ meV. After an Auger process the electron will be lifted by the transition energy to $e_A = 2.35$ eV. The relative ejection probability from the Auger excited state compared to the one from the 1S state then depends on the barrier width d and height V_B . For different barrier widths and heights the ratio of ejection probabilities $p(e_A)/p(e_{1S})$ calculated from Eq. (2.27) is plotted in Fig. 6.25 b). With increasing barrier or distance also the relative transfer probability $p(e_A)/p(e_{1S})$ increases exponentially. The relative time spent at e_A is given by the excitation rate R_{exc} and the dwell time τ_A at e_A . The decay to the ground state for an excited electron was found to take place within picoseconds or faster [115, 116]. The excitation rate is given by Eq. (4.14). For confocal excitation at 200 nW as in Fig. 6.19 an excitation rate of $R_{\text{exc}} = 0.4 \mu\text{s}^{-1}$ is obtained. For a dwell time of $\tau_A = 1$ ps the fraction of time spent at e_A for a single negative charge in the conduction band is $R_{\text{exc}} \cdot \tau_A = 4 \cdot 10^{-7}$. For

ensemble excitation ($R_{\text{exc}} = 0.5 \text{ ms}^{-1}$) it is only $5 \cdot 10^{-10}$. Thus, for Auger ejection to the electrode to be able to compete with electron injection at the conduction band edge, the potential barrier for electron injection should be considerably higher than 2 eV and wider than 3 nm (see Fig. 6.25 b)). In Sec. 6.1 the average width from the electrode due to ZnS shell and HDA ligand is estimated to 2 nm. Considerable contributions of Auger ejection to the electrode are thus not expected. Auger-excited electrons might however also be ejected to the environment e.g. into hot electron traps as recently suggested in Ref. [76]. Ejection into the environment might also be possible from the ground state. Such ejection rates can also strongly differ for individual QDs and lead to a spread in u_0 and fwhm. For significant additional ejection rates, independent of the mechanisms, a broadening of the distribution of u_0 will also be found for a distribution of k_{in}^- , e.g. due to different tunneling barriers to the electrode. Such a distribution can result from inhomogeneities at the electrode surface or in the HDA film. Contact inhomogeneities on ZnO/ITO have also been found by Holman et al. [240].

6.6.3.4 Charge Extraction Potentials

The recovery of fluorescence after negative charging (u'_0 , fwhm') is found to follow a transition that is considerably broader (fwhm' > fwhm) and shifted to more positive potentials ($u'_0 > u_0$) than the electron injection edge (u_0 , fwhm), see Fig. 6.23. This hysteresis has also been found for ensemble measurements where shift and broadening increase with higher negative reversal potentials U_{min} (see Sec. 6.3). A weak correlation of u_0 and u'_0 is observed for single QDs as well (see blue line in Fig. 6.23 b)). The blue line corresponds to the slope (100 mV/30 mV) obtained in ensemble measurements for a difference between peak and reversal potential of $\Delta U = U(I_{\text{max}}(\text{c.})) - U_{\text{min}} < 0.6 \text{ V}$ (see Fig. 6.9 and corresponding Sec. 6.3.1.2). For the single QD measurement here it is $\Delta U \approx 0.6 \text{ V}$. The observed weak correlation is thus in agreement with ensemble measurements. A stronger correlation between u_0 and u'_0 would be expected for higher ΔU , also accompanied by stronger quenching. The process leading to this offset is attributed to another very efficient quenching process in negatively charged QDs with slow recovery rates (see I b) in Fig. 6.12 and corresponding discussion in 6.3.3). The dependence on $\Delta u = u_0 - U_{\text{min}}$ supports the relevance of charges in the QD core for the process causing the hysteresis, instead of e.g. stronger electric fields. This process is elucidated in the next section.

6.7 Illumination Dependence of Fluorescence Quenching and Recovery

Fluorescence voltammograms on single QDs and QD films convincingly show the injection of electrons into the QD conduction band which is followed by Auger quenching of the exciton. A hole injection edge is only indicated on ITO. Inhibited hole injection on ZnO/ITO is explained with a valence band potential in the ZnO band gap. Except for the intensity decrease on ITO, which is very similar to the one for electron injection, no further indications of hole injection have yet been given. A short decay component of Auger relaxation is only observed for the negative trion, not the

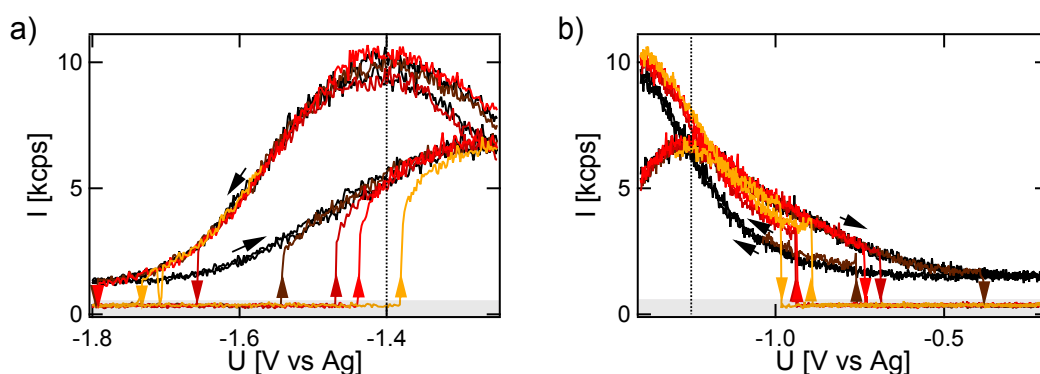


Figure 6.26: Illumination dependence of the fluorescence voltammogram on ZnO/ITO. Excitation is blocked at different a) negative and b) positive potentials of several consecutive cycles. A scan under continuous illumination is shown in black. Different colors indicate different consecutive scans. Colors differ in a) and b). Arrows mark the scan direction. Excitation is blocked where fluorescence drops into in the shaded area.

positive trion. The intensity decrease, however, already starts above the valence band edge. This mid-gap quenching is also attributed to positive charging but via electron extraction from the conduction band after excitation. A clear separation of the two processes is still necessary. As electron extraction from the conduction band requires a preceding excitation, a separation is possible with a study of the illumination dependence. Such a study can also separate photoinduced positive charging from trap relaxation mechanisms at mid-gap potentials. Influences of the presence and absence of illumination in the different regions are therefore studied in this section. As in the absence of illumination no light is emitted, the effect of blocked illumination can only be examined on subsequent fluorescence. Further investigations to a dependence on illumination intensity are presented in Sec. C.4 of the appendix. Next to influences on the fluorescence voltammogram, specific potentials are also addressed directly with voltage steps. Furthermore, this section presents an interplay of illumination and selected positive potentials in the recovery process after electron injection.

6.7.1 Photoinduced Quenching and Recovery

The influence of interrupted illumination on a fluorescence voltammogram is shown in Fig. 6.26. In a) excitation is blocked at negative and in b) at positive potential of the same scan. When excitation is blocked at negative potential, QD fluorescence starts at a lower intensity after excitation return. It then quickly increases to the intensity it also follows under continuous illumination. When blocking the excitation at positive potential, fluorescence remains offset at a higher level until the peak fluorescence at -1.4 V is reached. From there it again follows the same path independent of prior illumination (see Fig. 6.26 a)).

This dependence on illumination in the specific potential regions is more explicitly addressed with potential steps in Fig. 6.27. As a reference point the potential of maximum intensity is chosen. For ZnO/ITO this is the peak in the cathodic sweep. For ITO it is approximately mid-way between negative and positive turn-off edges. From this

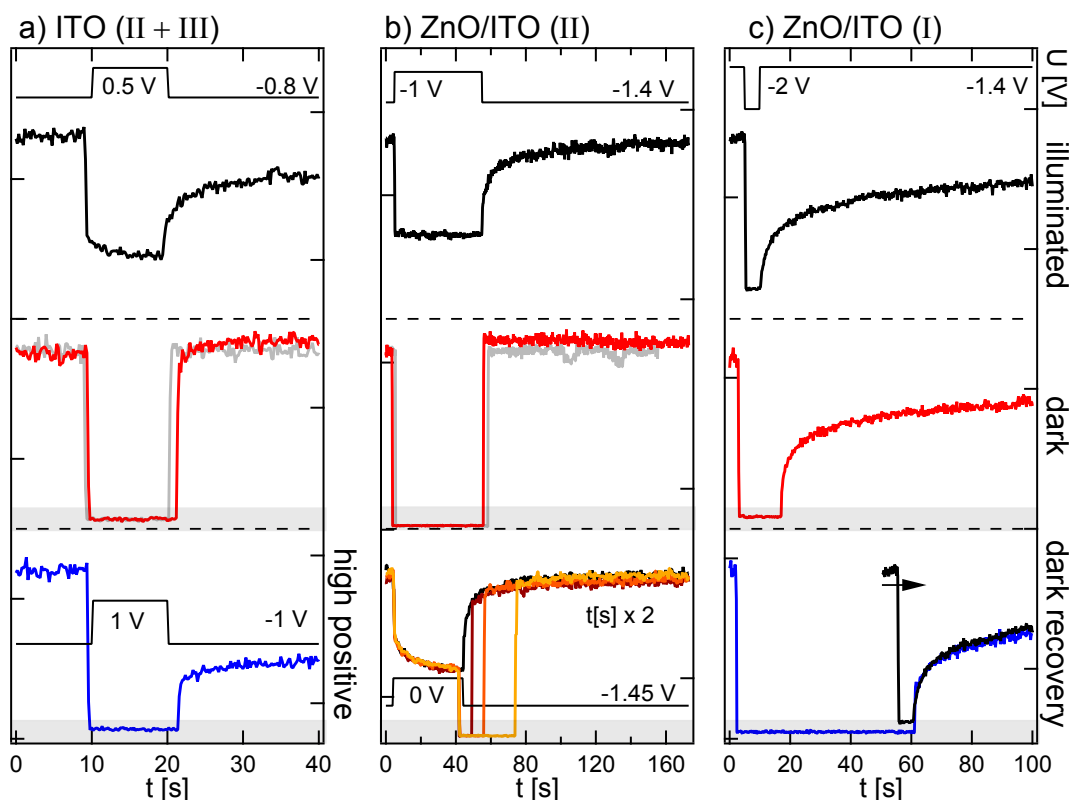


Figure 6.27: Illumination dependence of fluorescence quenching and recovery for positive (region II and III in Fig. 6.6) and negative (region I) quenching potentials on ZnO/ITO and ITO. The thick black lines on the top indicate measurements under continuous illumination. The red lines in the middle show measurements with blocked luminescence during the quenching potential. Gray lines are obtained from blocking illumination at the peak potential. The bottom of a) shows the same for a higher quenching potential. At the bottom of b) and c) illumination is blocked during the recovery period shown as brown to yellow lines in b) or in blue in c), respectively. Curves at the bottom of b) are scaled by a factor of 2 in time to suit the same time axis. The black line at the bottom of c) is the same as the black line on top shifted by 50 s and normalized to the fit initial intensity of the blue line at 0 s. The applied voltage for all measurements is indicated as thin black line at the top or, when different, directly in the graph. Curves are offset for clarity. Excitation is blocked where fluorescence drops into in the shaded area.

peak potential a step to positive or negative potentials is applied for a short period of time and then reversed to the peak potential. The corresponding fluorescence quenching and recovery are examined in the presence and absence of concurrent illumination. Results are shown for positive potentials on ITO in a) and ZnO/ITO in b) and negative potentials on ZnO/ITO in c) with measurements under continuous illumination at the top (black). When illumination is blocked during moderate positive potential on ITO in a) (middle, red) fluorescence hardly changes. Higher positive potentials (bottom, blue) quench the fluorescence also in the dark. On ZnO/ITO neither moderate positive potentials (middle, red) nor high positive potentials (see Fig. 6.29) quench the fluorescence in the dark. Negative potentials show illumination independent quenching as shown on ZnO/ITO in c) (middle, red).

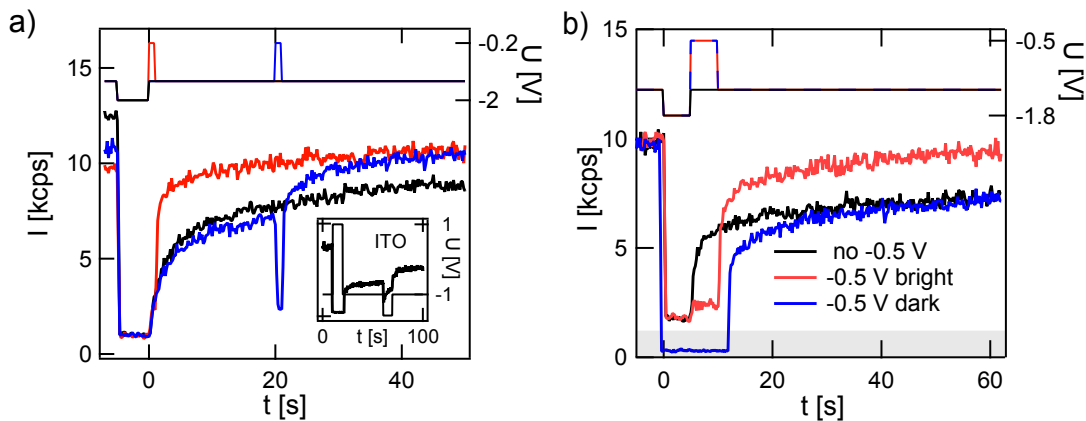


Figure 6.28: a) Following the application of -2 V on ZnO/ITO fluorescence is left to recover at the peak potential of -1.4 V (black). The effect of a short step of 2 s to -0.2 V either preceding recovery or interrupting it after 20 s is shown in red and blue, respectively. Inset: Recovery after high positive potential (1 V) on ITO interrupted by a short application of -1.6 V . b) Measurement as in a) at similar potentials with (red) and without (blue) concurrent illumination at -0.5 V . Black line is taken under continuous illumination without the application of -0.5 V . It is multiplied by a factor of 1.1 to match the same initial intensity. Applied voltages are indicated at the top. Excitation is blocked where fluorescence drops into in the shaded area.

Luminescence recovery in the absence of illumination on ZnO/ITO is shown at the bottom of b) and c). Recovery from positive potentials in b) does not show an illumination dependence. In contrast, luminescence recovery from high negative potentials is strongly inhibited in the dark (bottom blue line in c)). After 50 s in the dark luminescence is still much lower than the corresponding luminescence after continuous illumination (top, black line). When directly comparing recovery under continuous illumination with that after the 50 s dark period (black and blue line), the same intensity increase is observed.

6.7.2 Recovery Acceleration with Selected Potential Steps

The influence of selected positive potentials on the recovery process from negative potential is investigated in Figs. 6.28 and 6.29. In Fig. 6.28 a) the effect of a short application of -0.2 V after high negative potentials is studied. It is shown to enhance subsequent fluorescence intensity at the peak potential of -1.4 V . The specific instant at which the -0.2 V is applied is irrelevant for the long-time recovery. Different initial intensities stem from the order of measurements with a recovery time longer than 100 s (first 50 s shown), starting with the black curve. Fluorescence is similarly enhanced when steps to negative potentials are applied after high positive potentials on ITO, as shown in the inset. However, without concurrent illumination during the step, intensity is not enhanced as shown in b). Recovery without concurrent illumination (blue) resembles that without the positive voltage step (black). Only the application of much higher positive potentials leads to recovery enhancement also in the dark as presented in Fig. 6.29. A potential of 2.2 V for 5 s in the dark (yellow) reaches the same fluores-

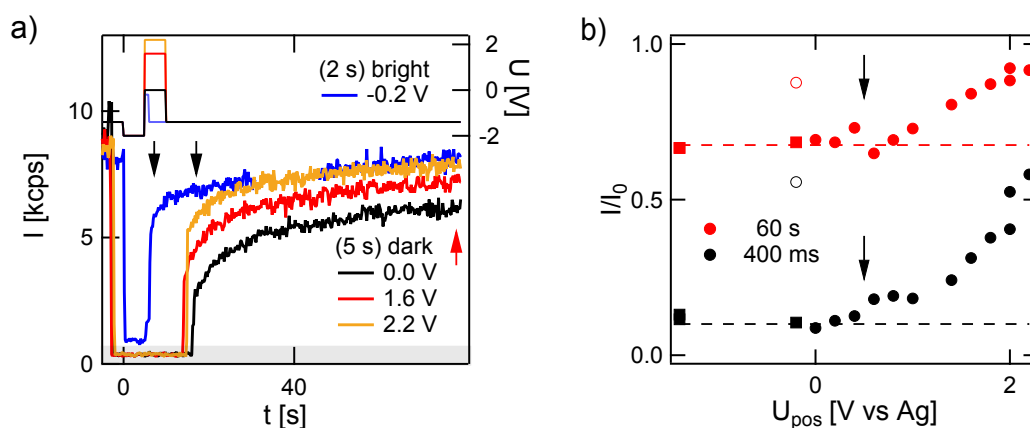


Figure 6.29: a) Fluorescence recovery at the peak potential of -1.4 V after quenching at -2 V. Prior to recovery, different positive potentials $U_{\text{pos}} \geq 0$ V are applied for 5 s in the dark or a potential of -0.2 V for 2 s under continuous illumination (blue). Applied voltages are shown at the top. Excitation is blocked where fluorescence drops into in the shaded area. b) Relative recovered fluorescence intensity of the measurements in a) at 400 ms (black markers) and 60 s (red markers) after the return of illumination for the different applied U_{pos} . Instants are indicated by the black and red arrows in a), respectively. Empty symbols indicate the measurement under continuous illumination. Intensity is normalized to the same maximum intensity. Squares are results from an earlier measurement of higher fluorescence and are normalized to the same corresponding initial intensity. Black arrows indicate 0.5 V.

cence as 2 s at -0.2 V during illumination (blue). In b) the relative recovered intensity after the first 400 ms (black markers) and after 60 s (red markers) is plotted dependent on the applied positive step-potential U_{pos} . Considerable enhancement in the dark starts increasing for potentials ≥ 0.5 V (black arrows).

After measurements with repeated and longer application of such high positive potentials the ZnO coating has been observed to be partially removed from the ITO surface. High positive potentials have therefore usually been avoided.

6.7.3 Discussion

With an illumination dependent study, photoinduced processes can be separated from illumination independent mechanisms. In the study here, subsequent luminescence after completely blocked excitation is investigated. This only addresses long-lived mechanisms. Processes proceeding within the bin time of 200 ms are not accessible with this procedure. Among these long-lived mechanisms several illumination dependencies are observed that depend on the specific potential region. Apart from a separation between different processes below the conduction band edge, they also allow further characterization of the quenching mechanism developing in negatively charged QDs.

6.7.3.1 Distinction of Mechanisms via Illumination Dependence

Mid-gap potentials only lead to long-lived quenching under concurrent illumination (see Fig. 6.27 a) and b)). This observation confirms the assignment to photoinduced

positive charging. Without excitation, the electron cannot be extracted and the QD remains neutral (see III b) Fig. 6.16). In voltammograms this leads to the offset of cathodic sweeps in Fig. 6.26 b). At potentials above the their conduction band QDs are neutralized. The fluorescence voltammogram then follows the same path independent of prior illumination (see Fig. 6.26 a)).

A clear distinction can thus also be made from potentials below the valence band on ITO. Here quenching is observed even in the dark (see bottom of Fig. 6.27 a)), confirming the injection of holes into the valence band. It is again not observed on ZnO/ITO even for very high positive potentials (see Fig. 6.29). As expected, also electron injection into the conduction band (region I) proofs to be illumination independent (see Fig. 6.27 c)).

A distinction can also be made from the process of trap activation. Quenching and recovery due to activation and passivation of traps would only depend on charge transfer rates to and from the traps, which should not depend on illumination. The lack of quenching in the dark limits these processes to time-scales of the bin time. They are thus not responsible for long-lived quenching. Also the suggested non-FRET relaxation mechanism as described in Sec. 6.2.3.2 and [234–237] is not expected to show a long-lived component. An interaction of the electron wave function with ZnO surface states is photoinduced, but limited to the time the electron spends in the excited state. The absence of quenching at mid-gap potentials in the dark, as observed here, has not been reported before. The observed luminescence recovery¹³ from positive to negative potential by other groups [66, 68, 72, 77] was rarely investigated in dependence on illumination. Weaver et al. [66] reported an excitation induced faster luminescence recovery of ZnSe QDs on fluorine doped tin oxide (FTO). Here, no such influence is observed as shown in the illumination independent recovery from positive potentials at the bottom of Fig. 6.27 a). These discrepancies can involve differences between CdSe/ZnS and ZnSe nanocrystals as well as FTO and ZnO/ITO.

6.7.3.2 Hole Trap Creation in Negatively Charged Quantum Dots

As concluded from several observations in the sections before, another quenching mechanism is developing in negatively charged QDs (see I b) in Fig. 6.12). It is characterized by a quantum yield $QY < 1\%$ and recovery times that can exceed many minutes. Illumination dependent observations here reveal that this recovery is strongly photoinduced. After electron injection into the conduction band and a return to the peak potential, photoluminescence recovers only during illumination (see bottom of Fig. 6.27 c)). It could be shown in the previous sections that electron transfer between the QD conduction band and the electrode mostly proceed within the bin time. Thus, even if electron ejection is supported by an Auger process as argued in Sec. 6.6.3.3, it should be completed quickly after illumination return. The slowly recovering intensity is further observed to be enhanced by the application of mid-gap potentials, but only under illumination (see Fig. 6.28). On ZnO/ITO recovery is also accelerated in the dark, when potentials below the expected valence band are applied (≈ 0.5 V, see arrows in Fig. 6.29 b)). These observations lead to the following model of this quenching mechanism, which is illustrated in Fig. 6.30.

¹³They term it luminescence enhancement as it is compared to the luminescence at 0 V.

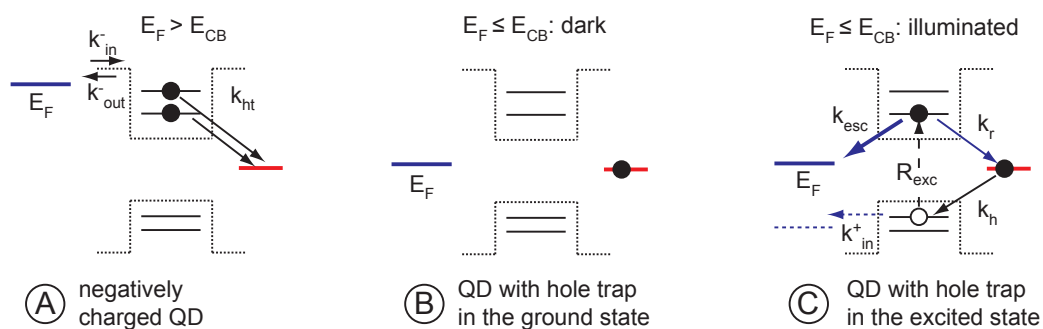


Figure 6.30: Processes leading to quenching and photoinduced recovery at high negative potentials in region I (see I b) of Fig.6.12). A: Electrons from a highly charged conduction band relax to mid-gap states not accessible from the electrode. B: Without illumination electrons cannot be extracted from the electrode at mid-gap potentials. C: Trapped electrons act as efficient hole traps with rate k_h . Retrapping of the excited conduction band electron at the same site proceeds with rate k_r , ejection to the electrode with $k_{esc}(E_F)$. At Fermi levels below the QD valence band, holes are injected with k_{in}^+ .

At high negative potentials some electrons from the QD conduction band are forced to occupy mid-gap states (A). These trapped electrons cannot directly be accessed from the electrode (B). Under illumination they act as efficient hole traps and quench QD luminescence (C) with a rate $k_h \gg \Gamma_r$. QDs with active hole traps remain dark until the electron is extracted from the trap. Extraction is not directly possible from the electrode or extremely slow (B). Under illumination, the trap is quickly depleted by the valence band hole. The electron in the conduction band can now escape to the electrode with rate k_{esc} or relax to the old trapping site with $k_r > R$ depending on the ratio of k_{esc}/k_r . Mid-gap potentials U enhance extraction rates $k_{esc}(U)$ from the conduction band and thus fluorescence recovery as observed in Fig. 6.28. At potentials below the QD valence band on ZnO/ITO, holes are slowly injected with an increasing rate $k_{in}^+(U)$. They quickly relax to the trapping site, which recovers fluorescence also in the dark.

Very slow hole injection does not contradict the observations of inhibited valence band access, when hole injection rates are still much lower than possible hole ejection rates e.g. to the environment. Only such slow injection rates prevent subsequent quenching of fluorescence due to positive charging. In the described model here recovery is initiated by illumination and should scale with the excitation rate R_{exc} . An acceleration of recovery with higher excitation rates is indeed observed as shown in Fig. C.6 b) of the appendix. Possible sites for electron trapping at the QD surface are Zn^{2+} sites. Like Cd^{2+} for uncapped QDs they are mostly but not completely passivated with HDA ligands [103]. Conduction band electrons could thus be populating unpassivated Zn^{2+} sites or even drive away passivating ligands as suggested by Gooding et al. [68].

The model in Fig. 6.30 is also supported by several observations in the literature. Wang et al. [70] directly monitored the presence of electrons in the conduction band via the IR absorption of the 1S-1P transition (see Fig. 6.25 a)). This IR absorption increased with the injection of electrons to the conduction band and quickly vanished at voltages below the conduction band edge. In contrast, fluorescence quenching persisted much longer, thus even without electrons in the conduction band. A depletion of electrons

from the conduction band after charging also agrees with low or missing oxidation peaks of the conduction band in cyclic voltammograms [58–62, 64, 65].¹⁴ Kuçur et al. [60] were able to detect trap state oxidation peaks in the band gap, when measuring in highly conductive ionic liquids. Those were found to vanish under UV-excitation, while the conduction band oxidation peak was enhanced. This directly supports a photoinduced depletion of trapped electrons through the conduction band, a process as described in Fig. 6.30. Lifting of trapped electrons to the conduction band with illumination is further supported by illumination enhanced electron extraction rates and conductivities in QD films [231, 241].

6.7.3.3 Relation to Photoinduced Processes in Blinking

Photoinduced positive charging, as found here at mid-gap potentials, has long been believed to be responsible for fluorescence intermittency. The shortening of on-periods (see Sec. 5.3.2) agrees well with photoinduced ejection of a charge. Dark states typically do not show an illumination dependence, as also observed here (see bottom of Fig. 6.27 b)). In 2010 two groups independently challenged this idea [53, 54]. In CdSe(CdZnS) QDs dark state quantum yields were observed that were lower than those of trions [53], as well as dark state decay dynamics that do not agree with the size and illumination dependence of an Auger process [54]. Park et al. [239], however, recently observed dark and dim states in thick-shell CdSe/CdS QDs with quantum yields that are in good agreement with the assignment to positive and negative trion. The observation of a dim state itself, as also shown here (see Sec. 5.3.4), already demonstrates the contribution of different types of quenched states. Measurements in Refs. [53, 54] and [239] further suggest the relevance of additional distinct dark states in different QDs or even in the same QD. The multitude of processes identified here with electrochemistry also supports this idea. A possible candidate for a dark state with lower quantum yield than a trion as observed in Ref. [53] could for instance be a hole trap as proposed in Fig. 6.30. It develops in negatively charged QDs and can thus also be accessible in single QD time-traces after hole ejection. A similar fast trapping mechanism was also proposed for the observations in Ref. [54]. The illumination dependence observed here shows that the mechanism is not dominating typical QD blinking traces. A weak indication of a photoinduced shortening of dark states has however been observed by Baker et al. [242]. Next to off-periods in blinking, photoinduced fluorescence enhancement due to hole trap elimination as described in Fig. 6.30 can also be involved in photobrightening of QDs [66, 68, 243].

¹⁴The missing reduction peak of the valence band then indicates a similar process after hole injection.

7 Summary and Outlook

7.1 Summary

Single semiconductor nanocrystals, also referred to as quantum dots (QDs), are bright and stable nanoemitters that are easily tunable in emission wavelength with variations of the crystal size. Investigations of single QDs show high luminescence which is, however, randomly interrupted by dark periods lasting up to several minutes. This phenomenon, which is only revealed at the single particle level, is also found in other single emitters and typically referred to as blinking. An examination of dwell time statistics of bright (on) and dark (off) periods shows power law characteristics that are even found at the microsecond scale or below. A long-time limit of dwell time lengths (an exponential cut-off) is only found for the on-state, not the off-state. Such long and non-exponential transition times are highly extraordinary for two seemingly well-defined states. They have soon been attributed to tunneling processes of charges into and out of the QD, as charged QDs are typically non-fluorescent. The observed power law statistics were approached with several models which range from a distribution of traps over diffusion of energy levels to fluctuating tunneling barriers. Most of them are based on the charge tunneling process and thus fluctuations of charges and charge accepting states close to the QD. None of them could be verified so far.

This thesis addresses the missing link between the observed single QD blinking and its proposed origin of fluctuating charges from two directions. First, in Chap. 5, the identification of power law statistics in the dwell time distributions is scrutinized. It is the key feature of blinking models and has been separately assigned for bright and dark states only from thresholding of intensity time-traces. This method suffers from a limited time resolution and several known, noise-induced artifacts. Its ability to correctly extract power law data therefore is tested against simulations and compared to single QD measurements.

Second, in Chap. 6, the nature of dark states is directly approached with electrochemistry. A setup is established for the optical detection of reduction and oxidation processes at the single particle level. It is used to directly access charges and charge accepting states while monitoring the effect on single particle intensity fluctuations. With different potentials, the two QD bands as well as the band gap region are specifically addressed to obtain information on electron, hole and trap state contributions.

7.1.1 Identification of Power Laws with Thresholding

The extraction of linear slopes in log-log plots of on- and off-time histograms is broadly confirmed in the literature. These slopes are assigned to power law distri-

butions of on- and off-state with an exponential on-time cut-off. The assignment of a power law distribution to linear slopes in log-log plots has been shown to be a difficult issue [201]. Not only the accuracy of extracted exponents but also a validity of the power law description itself is often not clear. For single QD time-traces even the accurate extraction of dwell times has been shown to suffer from artifacts of the threshold analysis [55, 56]. They stem from its limited time resolution and inherent single photon noise. The expected power law distribution of dwell times is believed to comprise dwell times that are several orders of magnitude below and above the typical resolution limit. The contribution of unresolved dwell times to extracted dwell time histograms is commonly neglected in the threshold analysis, without an estimation to its extend. This estimation has been addressed here with time-traces of simulated power law distributions. Additional effects of noise and often observed intermediate intensity levels have been examined to reproduce experimental observations.

With the simulation of switching between two well-defined intensity levels with power law distributed dwell times, intensity traces have been constructed at different time resolution. Influences for inverse power law exponents α between 1.5 and 2 have been investigated together with effects of an exponential on-time cut-off, noise and the contributions of intermediate intensity levels. The limited time resolution turns out to lead to considerable deviations from input power law distributions in extracted dwell time data. Deviations are limited to short dwell times and affect increasingly longer dwell times with higher bin times, higher power law exponents, higher differences between on- and off-state exponents and less suitable thresholds. For exponents $\alpha > 1.6$ these deviations exceed any fitting inaccuracies of power law distributions [198, 200]. Suitable thresholds are shown to be low for the off-state and high for the on-state. For comparisons between measurements they can be ranked according to their on-state fraction. Apart from long dwell times, only suitable thresholds allow the undistorted extraction of underlying power law statistics. The observation of long off-times and typically low thresholds thus allows the identification and assignment of off-state power laws as is also confirmed in presented experimental data. This is not possible for the on-state due to the exponential cut-off and higher on-state noise. An assignment of power law statistics for the on-state is concluded to be impossible in most experiments. Observed linear slopes in presented experiments could be exposed as misleading. Corresponding real power law distributions would have been distorted. Also the extraction of an unbiased cut-off time is shown to suffer from unresolved dwell times and noise-induced effects. The latter can be estimated (Eq. (5.6)), which allows a separation of noise-induced from real cut-offs. Due to unresolved dwell times only an upper limit to cut-off times can be extracted. It is further shown that a power law appearance of dwell time histograms can also be induced by noise of intermediate intensity levels. Their contribution increases with lower signal to noise ratios. Estimations to the presented experimental data suggest that they can be responsible for the observed linear on-state slopes at low excitation powers. Linear slopes at high powers are proposed to be induced by the exponential cut-off.

With the investigation of large QDs at high excitation a dim intensity level is revealed for the first time in CdSe/ZnS QDs. It is found to be accompanied by a hump on the off-state distribution. These observations indicate the existence of at least two distinct blinking processes while most blinking models assume only one underlying mecha-

nism. In agreement with electrochemical examinations, hump and dim intensity level are assigned to the formation and neutralization of the negative trion. Such distinct dark states and especially a questionable on-state power law challenge most models to the blinking phenomenon.

7.1.2 Controlling Quantum Dot Fluorescence with Charges

Single QD blinking and all fluctuations between moderately quenched states are typically attributed to fluctuating charges or trap states (i.e. charge accepting states) in and close to the QD. Valuable insight into specific mechanisms and a control of the blinking process is thus expected from the direct access of these charges and trap states. Such an access is possible by applying suitable potentials to an electrode close to the QD. A simultaneous observation of QD fluorescence, however, is challenging due to non-radiative energy transfer to the electrode. This transfer can be reduced with transparent electrodes, such as semiconductor layers with a high energy band gap. Their band alignment at the surface is known to determine reduction and oxidation rates, and needs to be considered in observations on each QD-electrode system. An investigation of blinking further requires observations at the single particle level and thus an integration of an electrochemical cell into a microscopic setup.

Such a setup has been successfully established and is shown to allow optical investigations of reduction and oxidation processes down to the single particle level. These concentrations are far below the detection limit of conventional cyclic voltammetry. Influences of specific QD-electrode systems are addressed by comparing two different electrode materials, ITO and ZnO/ITO, which are in a similar composition used for most spectroelectrochemical investigations on semiconductor quantum dots in other groups. The setup allows the detection of fluorescence intensity, excited state decays and emission spectra for a thorough characterization of all involved quenching mechanisms. Observations at the single particle level allow the detection of intensity fluctuations as well as variations in single QD characteristics. With a variation of the illumination also photoinduced mechanisms can be identified.

Several different quenching mechanisms are revealed, which are assigned to potentials above the QD conduction band (region I), below the valence band (region II) and in the band gap (region III). They are summarized and illustrated in Tab. 7.1.

- Ia) Electron injection into the QD conduction band is the most prominent feature in fluorescence voltammograms. It allows the deduction of the band alignment at the electrode. It is accompanied by fast blinking due to charging and neutralization on the millisecond time-scale. The fluorescence quantum yield of the negative trion is estimated to $QY^- \approx 1\%$ in agreement with an assignment to the dim level in single QD time-traces. The distribution of electron injection potentials and the observed injection transition widths for single QDs are broadened by additional electron ejection mechanisms, like Auger ejection or relaxation to the environment.
- Ib) After negative charging, a long-lived dark state is found to develop with a strongly photoinduced recovery process. It is assigned to the generation of hole traps and presents another candidate for a long strongly quenched blinking off-event.

- II At potentials below the QD valence band hole injection leads to quenching on ITO. On ZnO/ITO hole injection is inhibited due to a higher ZnO conduction band edge, thus a QD valence band in the ZnO band gap. Hole injection also leads to blinking but with longer dwell times (> 200 ms) due to lower charge transfer rates. The quantum yield of the positive trion is found to be lower than that of the negative trion $QY^+ < QY^-$, which is in agreement with recent observations [51, 71].
- IIIa) Electron trap relaxation pathways are induced at the ZnO surface of the ZnO/ITO electrode. They are attributed to an interaction of the electron wavefunction with specific ZnO surface sites. This observation stresses the sensitivity of the QD to its specific environment and the impact of the QD-electrode system on the detected fluorescence response.
- IIIb) The extraction of an excited electron from the QD leads to photoinduced positive charging and increased blinking at potentials in the QD band gap. This kind of blinking shows several characteristics also observed in typical experiments: photoinduced quenching, illumination independent recovery and a quantum yield $QY^+ < QY^-$. Consequently, a strong contribution of the positive trion to corresponding dark states in experiments is suggested, as recently proposed by Park et al. [239].
- IIIc) A last quenching process is observed as a linear voltage dependence of the QD bright state intensity level for single QDs on ITO. It is not observed on ZnO/ITO and does not show a corresponding change in the excited state lifetime. Whether hot hole traps, fast blinking or changes in the radiative rate are responsible could not be determined here. It is an interesting effect to address in future studies.

The identification of at least six distinct quenching mechanisms demonstrates the complexity of the seemingly well-defined system of a single quantum dot. Single QD fluorescence electrochemistry proves to be a powerful tool to investigate this system that is strongly determined by the presence of charges and trap states. A comparison of different QD-electrode systems allows to distinguish between extrinsic and intrinsic influences. Different blinking mechanisms are shown to be accessible with variations of the electrode potential. New candidates are revealed for dark and dim states in commonly observed single QD time-traces. The observed multitude of quenching and blinking mechanisms supports the participation of multiple mechanisms also in commonly observed blinking time-traces and dwell time histograms.

Table 7.1: Summary of the different observed quenching types in regions I-III with their characteristics C, origin O and mechanism M of quenching. Illustrations indicate origin (red) and mechanism (black arrows) as well as the corresponding electrode Fermi level (blue).

I a)		<p>C: $QY \approx 1\%$, fast blinking due to charging and neutralization O: Electron injection into the conduction band M: Energy transfer to the electron via an Auger process</p>
I b)		<p>C: $QY < 1\%$, photoinduced recovery O: Hole trap creation via relaxation of electrons to surface sites M: Hole capture by the trap and retrapping of the electron</p>
II		<p>C: $QY < 1\%$, blinking due to charging and neutralization (ITO) O: Hole injection into the valence band M: Energy transfer to the hole via an Auger process</p>
III a)		<p>C: $QY > 1\%$ (mainly ZnO/ITO) O: Creation of electron trap states at the electrode surface M: Relaxation via electron trapping</p>
III b)		<p>C: $QY < 1\%$, blinking due to charging and neutralization O: Photoinduced electron ejection from the conduction band M: Energy transfer to the hole via an Auger process</p>
III c)		<p>C: Quenching with linear voltage dependence (ITO) O: Hot hole traps / fast blinking / changes in Γ_r / \dots M: ?</p>

7.2 Outlook

Electrochemical investigations here clearly demonstrate the complexity of the single QD system and its sensitivity to its environment. Many quenching mechanisms could be identified with the optical investigation of single redox processes. They all still demand more detailed characterization, especially concerning their contributions to single QD intensity fluctuations. Several open questions arise that are left to be addressed in the future.

7.2.1 Investigating Quenching Dynamics with Electrochemistry

Most of the observed mechanisms could be attributed to charging or trap relaxation. An explanation for the linear voltage dependence on ITO (III c)) is still missing as well as evidence for the interaction with the ZnO surface on the single particle level. Also specific contributions of the different mechanisms to single QD blinking still need to be identified.

Several of these problems can be approached with the presented method of fluorescence electrochemistry. The voltage dependent increase on ITO and the observed surface induced relaxation pathways on ZnO can be addressed with confocal measurements of higher time resolution. On ITO, they allow to distinguish fast blinking from changes in the radiative rate. On ZnO, a study of lifetime fluctuations at different potentials will reveal changing contributions of moderately quenched states which are associated with the surface interaction.

A connection of positive and negative charging or of electron induced hole traps with the common blinking phenomenon can be investigated with dwell time statistics at

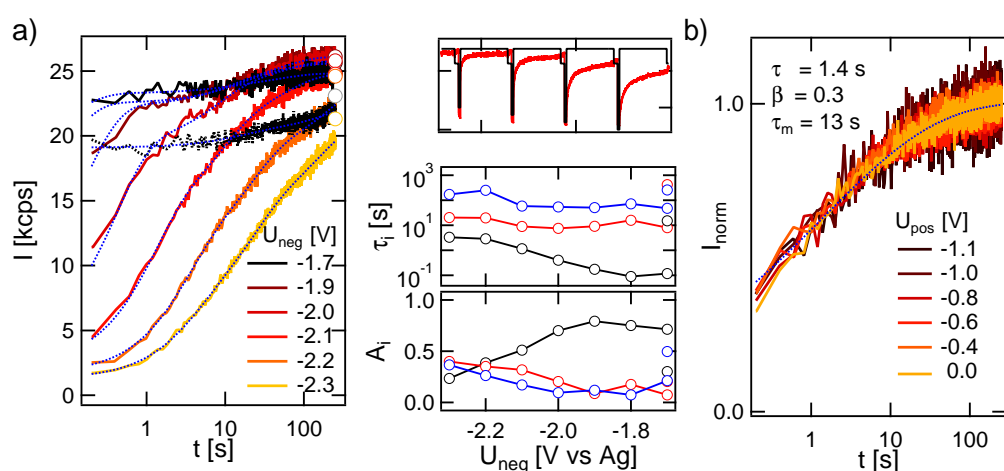


Figure 7.1: Investigation of fluorescence recovery at the peak potential after quenching for 10s at different potentials U_{neg} . Measurements are performed in undried solution on ZnO/ITO. a) Recovery after different potentials above the conduction band edge. The top right shows a segment of the intensity time-trace. Parameters of three exponential fits are plotted below. b) Recovery after the application of different mid-gap potentials. Curves are normalized to initial and final value. Parameters of a stretched exponential fit are indicated in the graph. Fits are shown as blue dotted lines.

specific charging potentials as indicated in Refs. [73, 76]. With the ability to deliberately turn QDs off electrochemically, blinking dynamics can also be extracted from ensemble measurements. With the application of step potentials recovery processes after QD quenching can be followed. This reveals information on the lengths of dark states as well as charge injection and ejection rates. First observations are presented in Fig. 7.1. In a) recovery is investigated after quenching at negative potentials above the conduction band edge (region I), in b) at mid-gap potentials (region III). While a normalization in b) reveals potential-independent recovery rates, recovery times strongly increase with the applied potential in a). Parameters of three exponential fits on the right show a resolution limited short component only for moderate potentials up to -1.9 V . It can be attributed to charge extraction from the conduction band which is no longer limiting recovery from higher potentials. The residual recovery times spread over several decades in time and collectively increase with higher negative potential indicating again more complex processes. The formation of multiple hole traps and its dependence on electron retrapping or ejection rates (see Fig. 6.30) can yield strong variations of recovery rates among QDs. The way in which those relate to the extracted recovery dynamics can be studied with more detailed modeling to the different contributions and a comparison to measurements like in Fig. 7.1.

7.2.2 Adjusting Fluorescence Electrochemistry to Other Systems

The method established here to optically detect reduction and oxidation of low concentrated analytes can be applied to any species that shows a detectable fluorescence change upon charging, e.g. also molecules or NV^- centers in nanodiamonds [244]. Its sensitivity lies considerably below the detection limit of conventional cyclic voltammetry. Detectable fluorescence changes do not only involve fluorescence intensity but also emission spectra, excited state lifetime or polarization. A similar combination of electrochemistry with absorption spectroscopy, as applied in Refs. [70, 245], can also yield optical information on redox dynamics of non-fluorescent processes. Measurements on QDs of different materials, sizes, shell thicknesses and surface treatments can further identify systematic variations in the contributions of specific quenching and blinking mechanisms. For a closer inspection of the QD valence band, electrodes with a lower conduction band edge or p-type semiconductors with a higher valence band edge need to be used. Such an adjustment of the electrode material allows for an optimization for the redox potentials of interest. An optimization of electrodes for low fluorescence quenching with remaining high charge transfer rates at the desired redox potentials will considerably improve the method's performance. The use of cross-linked ZnO nanoparticle films instead of a deposited layer of ZnO could for instance be shown to reduce electrode-induced quenching [73]. For quantitative investigations all systematic potential shifts (Secs. C.1 to C.3) still need to be addressed and best be eliminated.

7.2.3 Unbiased Extraction of Dwell Time Statistics

Models of QD blinking are all based on power law dwell time characteristics of on- and off-state. Here, those are shown to be highly questionable at least for the on-state

distributions. Better methods for a determination of accurate dwell times thus need to be found and blinking models will need to be adjusted accordingly. Due to a strong influence of the time resolution and intermediate intensity levels on the common dwell time analysis, questions are also raised concerning the true onset of blinking (shortest dwell times) and the nature and statistics of moderately quenched states.

A more adequate method to specifically access bright state fluctuation statistics is the change point analysis (CPA) [172]. The CPA relies on Poisson distributions of emitted photons and does not depend on prior binning to intensity time-traces. Its time resolution is not limited by a fixed bin time. Only recently it has been applied to QD time-traces with the same conclusion that there is no on-state power law [212]. An evaluation of the enzyme α -chymotrypsin with CPA and thresholding could similarly reveal the detection of dynamic disorder as a thresholding artifact [57]. Also intermediate intensity levels are directly accessible with the CPA. Its performance still needs to be scrutinized to rule out the influence of artifacts as found for the threshold analysis. Such artifacts might especially arise for low intensities as a minimum number of photons is necessary to assign an intensity level.

The onset of blinking is expected on a time-scale considerably below the time resolution of CPA and thresholding (at least for the dark state). It has been addressed with intensity correlations, power spectral densities and excited state decays [43–45, 156, 202], which mostly suggest an onset below the microsecond time-scale. These methods cannot directly separate on- and off-events and are often more difficult to interpret. With appropriate models they still yield valuable information on short time statistics and the onset of blinking.

A Mathematical Auxiliaries

A.1 Relative Time Spent in Unresolved Blinking Events

The probability p_b of an unresolved event at given t_{bin} , α and t_{max} for a shortest blink time $t_c = 1$ is given as

$$p_b = \frac{\int_1^{t_{\text{bin}}} t^{-\alpha} dt}{\int_1^{t_{\text{max}}} t^{-\alpha} dt} = \frac{t_{\text{bin}}^{1-\alpha} - 1}{t_{\text{max}}^{1-\alpha} - 1} \quad (\text{A.1})$$

The average time $t_{\text{avg,b}}$ of such an event is

$$t_{\text{avg,b}} = \frac{\int_1^{t_{\text{bin}}} t^{1-\alpha} dt}{\int_1^{t_{\text{bin}}} t^{-\alpha} dt} = \frac{1-\alpha}{2-\alpha} \cdot \frac{t_{\text{bin}}^{2-\alpha} - 1}{t_{\text{bin}}^{1-\alpha} - 1} \quad (\text{A.2})$$

while the average time for any events up to t_{max} is

$$t_{\text{avg,m}} = \frac{\int_1^{t_{\text{max}}} t^{1-\alpha} dt}{\int_1^{t_{\text{max}}} t^{-\alpha} dt} = \frac{1-\alpha}{2-\alpha} \cdot \frac{t_{\text{max}}^{2-\alpha} - 1}{t_{\text{max}}^{1-\alpha} - 1} \quad (\text{A.3})$$

The fraction of time spent in unresolved events then yields for independent exponents $\alpha_{\text{on/off}}$

$$g_{\neq} = \frac{p_{b,\text{on}} \cdot t_{\text{avg,b,on}} + p_{b,\text{off}} \cdot t_{\text{avg,b,off}}}{t_{\text{avg,m,on}} + t_{\text{avg,m,off}}} \quad (\text{A.4})$$

which is also displayed in Fig. 5.4 b). For equal exponents one simply finds

$$g_{=} = p_b \frac{t_{\text{avg,b}}}{t_{\text{avg,m}}} = \frac{\int_1^{t_{\text{bin}}} t^{1-\alpha} dt}{\int_1^{t_{\text{max}}} t^{1-\alpha} dt} = \frac{t_{\text{bin}}^{2-\alpha} - 1}{t_{\text{max}}^{2-\alpha} - 1} \quad (\text{A.5})$$

as given in equation (5.1) in section 5.1.5.2.

A.2 Distribution of Injection Edges

When an immediate and complete fluorescence bleach is assumed once a specific potential $U \leq u'$ is applied to the electrode, the fluorescence intensity I of a single QD follows a step function $I = I_{\text{max}} \cdot S(U - u')$ with

$$S(U - u') = \begin{cases} 0 & U \leq u' \\ 1 & U > u' \end{cases} \quad (\text{A.6})$$

The distribution of injection potentials u' in the ensemble is approximated with a Gaussian

$$g(u') = \frac{1}{\sigma \sqrt{2\pi}} e^{-\frac{(u'-U_0)^2}{2\sigma^2}} \quad (\text{A.7})$$

with a defined average potential U_0 and a standard deviation σ . The ensemble intensity $I(U)$ when decreasing the potential U then follows a convolution of the two functions

$$\begin{aligned} I(U) &\propto (g * S)(U) = \int_{-\infty}^{\infty} g(u') S(U - u') du' \\ &= \int_{-\infty}^{\infty} \frac{1}{\sigma \sqrt{2\pi}} e^{-\frac{(u'-U_0)^2}{2\sigma^2}} \cdot S(U - u') d\tau \quad S(U - u') = 0 \text{ for } U \leq u' \\ &= \int_{-\infty}^U \frac{1}{\sigma \sqrt{2\pi}} e^{-\frac{(u'-U_0)^2}{2\sigma^2}} du' \quad \int_{-\infty}^0 g(u') du' = \frac{1}{2} \\ &= \frac{1}{2} + \int_0^U \frac{1}{\sigma \sqrt{2\pi}} e^{-\frac{(u'-U_0)^2}{2\sigma^2}} du' \quad x = \frac{u' - U_0}{\sigma \sqrt{2}} \quad dx = \frac{du'}{\sigma \sqrt{2}} \\ &= \frac{1}{2} + \frac{1}{2} \operatorname{erf} \left(\frac{U - U_0}{\sigma \sqrt{2}} \right) \\ &= \frac{1}{2} \left[1 + \operatorname{erf} \left(\frac{U - U_0}{\sigma \sqrt{2}} \right) \right] \end{aligned} \quad (\text{A.8})$$

as used in Eq. (6.1) with the full width at half maximum $\text{FWHM} = 2\sigma \sqrt{2 \ln(2)}$.

A.3 Rate Equations for Charge Injection and Ejection

For potentials close to the QD conduction band edge charge injection from the electrode is possible and will proceed with a given rate $k_{\text{in}}(U)$ that increases with more negative potentials U . Injected electrons can be ejected again with another rate $k_{\text{out}}(U)$ that decreases with more negative potentials U . Injection rates depend on the available electron density at the QD conduction band edge E_{CB} and ejection rates on the availability of unoccupied states at the same potential. They thus scale with the Fermi-Dirac distribution (Eq. 3.8) $f(U)$ and $1 - f(U)$, respectively. For a simple two state system of a neutral and singly charged QD with populations N_0 and N_1 , respectively, the rate equations are given as follows

$$\begin{aligned} N_0'(t) &= -k_{\text{in}} N_0(t) + k_{\text{out}} N_1(t) \\ N_1'(t) &= k_{\text{in}} N_0(t) - k_{\text{out}} N_1(t) \\ 1 &= N_0(t) + N_1(t) \quad N_0'(t) = -N_1'(t) \\ 0 &= N_0'(\infty) = N_1'(\infty) \\ 0 &= -k_{\text{in}} N_0(t) + k_{\text{out}} (1 - N_0(t)) \\ \rightarrow N_0(\infty) &= \frac{k_{\text{out}}}{k_{\text{in}} + k_{\text{out}}} \end{aligned} \quad (\text{A.9})$$

$$\begin{aligned} N_0''(t) &= -k_{\text{in}} N_0'(t) - k_{\text{out}} N_0'(t) = -(k_{\text{in}} + k_{\text{out}}) N_0'(t) \\ \rightarrow N_0(t) &= N_0(\infty) + (N_0(0) - N_0(\infty)) e^{-(k_{\text{in}} + k_{\text{out}})t} \end{aligned} \quad (\text{A.10})$$

For fast charge transfer rates k_{in} and k_{out} and a negligible quantum yield for the charged QD the intensity for a given potential is proportional to $N_0(\infty)$. After a potential change it equilibrates to this intensity with $N_0(t)$.

When the possibility of charge injection of a second charge into the 1S state is regarded, a third state $N_2(t)$, that of the doubly charged QD needs to be considered. The same injection rate k_{in} can be assumed, only reduced by a factor of $\frac{1}{2}$ due to the occupation of the 1S state already by one electron. The ejection rate of a charge from N_2 is a factor of 2 higher than k_{out} . The rate equations are thus given by

$$\begin{aligned}
 N_0'(t) &= -k_{\text{in}}N_0(t) + k_{\text{out}}N_1(t) \\
 N_1'(t) &= k_{\text{in}}N_0(t) - (k_{\text{out}} + \frac{1}{2}k_{\text{in}})N_1(t) + 2k_{\text{out}}N_2(t) \\
 N_2'(t) &= \frac{1}{2}k_{\text{in}}N_1(t) - 2k_{\text{out}}N_2(t) \\
 0 &= N_0'(\infty) = N_1'(\infty) = N_2'(\infty) \\
 1 &= N_0 + N_1 + N_2 \\
 N_1(\infty) &= \frac{k_{\text{in}}}{k_{\text{out}}}N_0(\infty) \quad N_2(\infty) = \frac{1}{4} \frac{k_{\text{in}}}{k_{\text{out}}}N_1(\infty) = \frac{1}{4} \left(\frac{k_{\text{in}}}{k_{\text{out}}} \right)^2 N_0(\infty) \\
 1 &= N_0(\infty) + \frac{k_{\text{in}}}{k_{\text{out}}}N_0(\infty) + \frac{1}{4} \left(\frac{k_{\text{in}}}{k_{\text{out}}} \right)^2 N_0(\infty) \\
 \rightarrow N_0(\infty) &= \left(1 + \frac{k_{\text{in}}}{k_{\text{out}}} + \frac{1}{4} \left(\frac{k_{\text{in}}}{k_{\text{out}}} \right)^2 \right)^{-1} \tag{A.11}
 \end{aligned}$$

The intensity is again proportional to $N_0(\infty)$. Even more charges can be injected at the potential of the 1P state or any higher energy states of the QD as indicated in Fig. 6.25 a).

B Instrument and References of the Electrochemical Setup

B.1 Electric Circuit of the Home-Built Potentiostat

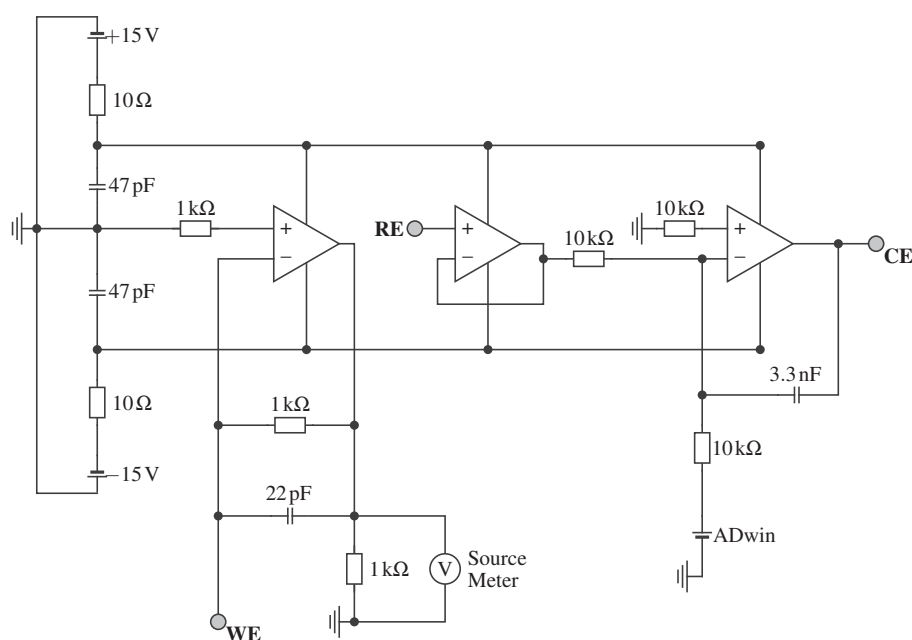


Figure B.1: Electric circuit of the home-built potentiostat, kindly assembled by Uwe Weber of our group. WE, RE and CE mark working, reference and counter electrode, respectively.

B.2 Thickness of Spin Cast PVA Spacer Layers

To test the distance dependence of electrode quenching on ITO, films of polyvinyl alcohol (PVA) are used as spacers between QDs and electrode. Different concentrations of PVA in water are prepared and spin cast at 8000 rpm on the electrodes before spin casting the QDs on top. Then intensity and fluorescence decays are measured as shown in Fig. 6.2. The thickness of spin cast 1% and 0.25% PVA solutions on glass are measured with an atomic force microscope at the edge of a deep cut in the surface. Measurements have been kindly taken by Martin Treß of the molecular physics group.

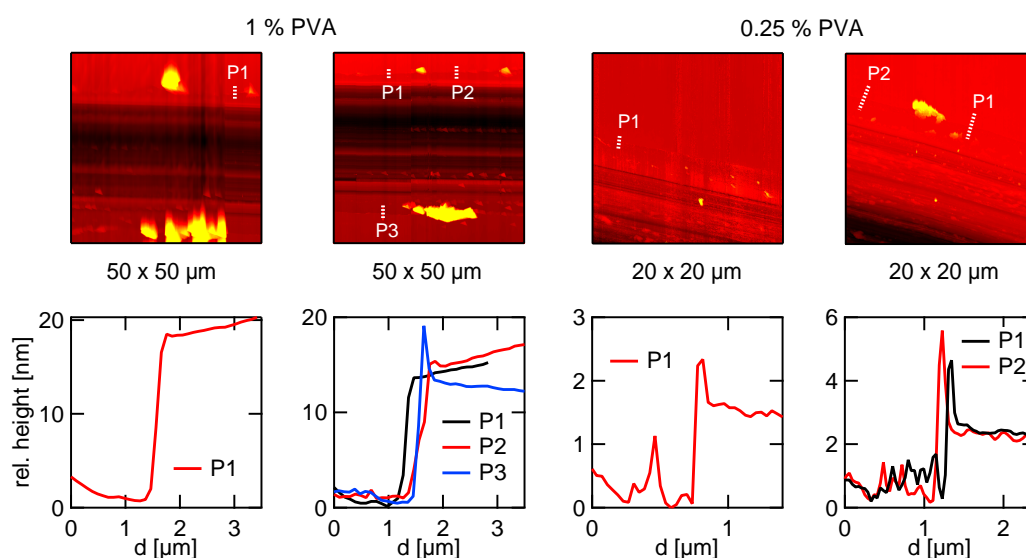


Figure B.2: Top: Topographic images of 1% (left) and 0.25% (right) spin cast PVA/water concentrations on glass. Bottom: Corresponding line profiles of the indicated white dotted lines in the images.

Topographic images of the two films are shown on the top of Fig. B.2 and line profiles of the indicated dotted lines on the bottom. From these line profiles thicknesses of 15 nm and 2 nm for the 1% and 0.25% PVA solutions are estimated, respectively. The thickness of spin cast PVA concentrations $> 1\%$ at 3000 rpm have been determined in Ref. [213] and yield approximately 20 nm and 800 nm for solutions of 1% and 10% PVA.

B.3 Transmission of ITO and ZnO/ITO Electrodes

In Fig. B.3 a) transmission spectra of the different electrodes are shown. They are measured with a Varian UV-Vis Spectrometer (Cary 1 Bio). A transmission $> 80\%$ is observed with a transmission peak at $\approx 500\text{nm}$ on ITO due to a minimum in the extinction coefficient [214]. It slightly shifts to $\approx 540\text{nm}$ on ZnO/ITO to $\approx 550\text{nm}$ on Ga:ZnO/ITO, possibly due to thin film resonances. Constructive interference is observed at $\lambda = 4nd$. A shift due to 20 nm of ZnO ($n \approx 2$) would shift a resonance by $\approx 80\text{nm}$. The thickness of the ITO ($n \approx 2$) substrate is not known. A resonance close to 500 nm would yield a reasonable thickness of $\approx 60\text{nm}$.

B.4 Fluorescence in Propylene Carbonate

With the addition of propylene carbonate onto the working electrode the detected fluorescence intensity is reduced approximately by a factor of two. This intensity decrease is accompanied by a decrease in the excited state lifetime as depicted in B.3 b). Black and red curves are taken at the different QD concentrations also depicted in Fig. C.1 b). Grey and pink curves are taken after the addition of PC. A decrease in lifetime is ex-

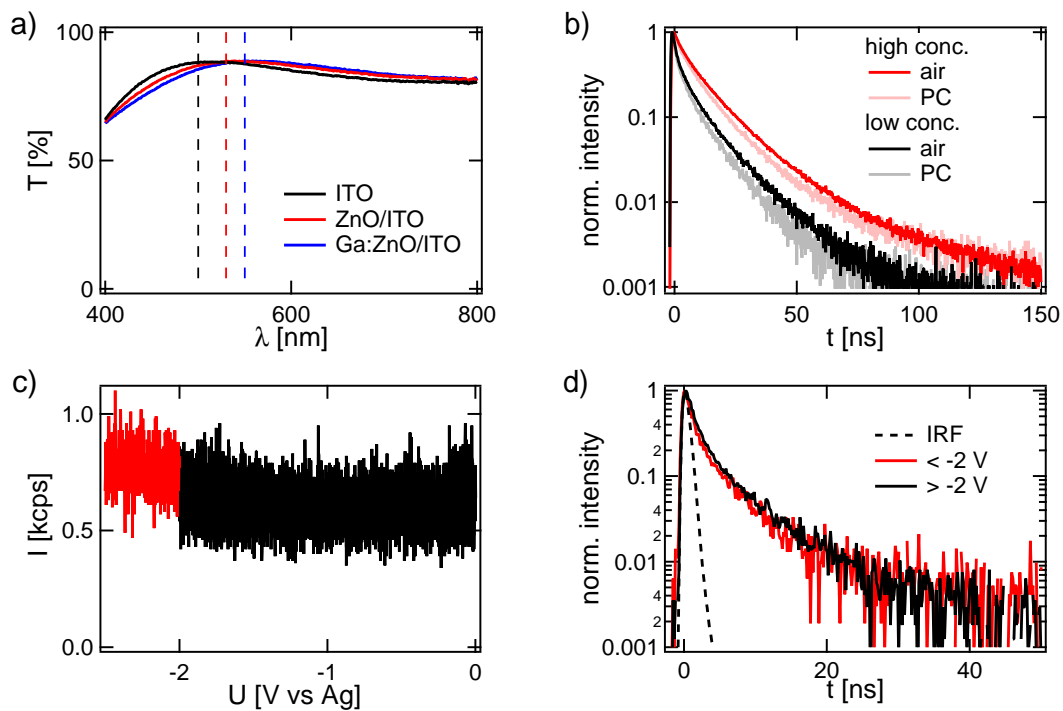


Figure B.3: a) Transmission spectra of the different indicated electrodes. Ga:ZnO/ITO is doped by 1% Ga. b) Fluorescence decays of QDs on ZnO/ITO at high (red) and low (black) concentration in air (strong colors) and TBAP/PC solution (pale colors). c) Voltage dependent fluorescence of a ZnO/ITO electrode in a TBAP/PC solution. d) Corresponding fluorescence decays for the fluorescence in c) at voltages higher and lower than -2 V.

pected due to an increase in the radiative rate Γ_r with an increase in the surrounding refractive index n . The radiative rate is approximately proportional to n [127, 246, 247]. With a change from air to PC ($n_{PC} = 1.42$) Γ_r thus increases accordingly. The effect on the effective excited state lifetime is observable but weak due to high non-radiative rates at the electrode (see Sec. 6.1). An increase in Γ_r should increase the quantum efficiency, thus intensity. However, the missing interface to air also decreases the surface enhanced emission towards the objective and thus the detectable emission intensity. Very close to an interface of two media of refractive indices $n_1 < n_2$ a higher fraction of light is emitted towards medium 2, increasing with increasing n_2/n_1 [248].

B.5 Background Fluorescence of ZnO/ITO Electrodes

Typical background counts at 100nW excitation in setup B (ensemble detection) are < 1 kcps for measurements in undried solution. Voltage dependent fluorescence of a ZnO/ITO electrode in TBAP/PC solution is shown in Fig. B.3 c). It slightly increases at very negative potentials which is not observed for pure ITO substrates. Intensity is still considerably lower than fluorescence of QD films. The observed lifetime at potentials lower and higher than -2 V is shown in b). It can roughly be approximated by a double exponential fit of 1 ns and 7 ns. This background luminescence dominates lifetime signals at strongly quenched QD luminescence.

C Electrochemical Investigations

C.1 Shift Due to Quantum Dot Concentration

At concentrations only a factor of two higher than those typically used, the observed negative turn-off edge is shifted considerably to more negative potentials as shown in Fig. C.1 a). The black voltammogram is taken on a typical 200 nM spin cast concentration, the red one at 400 nM. In addition to the shift of the negative turn-off edge, fluorescence hardly decreases to positive potentials. The fluorescence plateau that is reached at positive potential thus scales very sensitively with the spin cast concentration. At typically used concentrations it can almost decrease to zero (black). This difference is also observed in a 14 times higher fluorescence intensity in air for the higher concentrated films. Intensity per spin-cast QD thus increases by a factor of 7, assuming also twice the concentration on the electrode. Fig. C.1 b) shows fluorescence decays of the two corresponding QD concentrations on ZnO/ITO in air. The higher concentration also shows a longer excited state lifetime. Electrode quenching and the sensitivity to electrode potentials thus strongly decrease with an increase in QD concentration.

A higher concentration of QDs is always accompanied by a higher concentration of the HDA-ligand as well. Especially this additional HDA (≈ 2 nm when extended) but also the QDs themselves can be imagined to act as spacer between QDs and electrode. Electron transfer rates quickly decrease with higher separations from the electrode due to an exponential dependence on the tunneling distance (see Sec. 2.2.1.3). This shifts the electron injection edge to higher negative potentials. The stronger quenching on

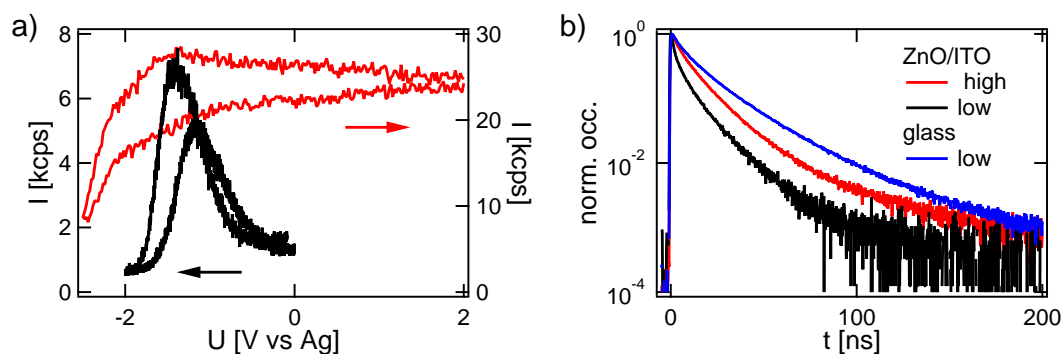


Figure C.1: a) Fluorescence voltammograms for a typically used QD concentration (black) and twice the concentration (red) on ZnO/ITO. b) Corresponding excited state decays in air. A decay on glass is shown in blue for comparison.

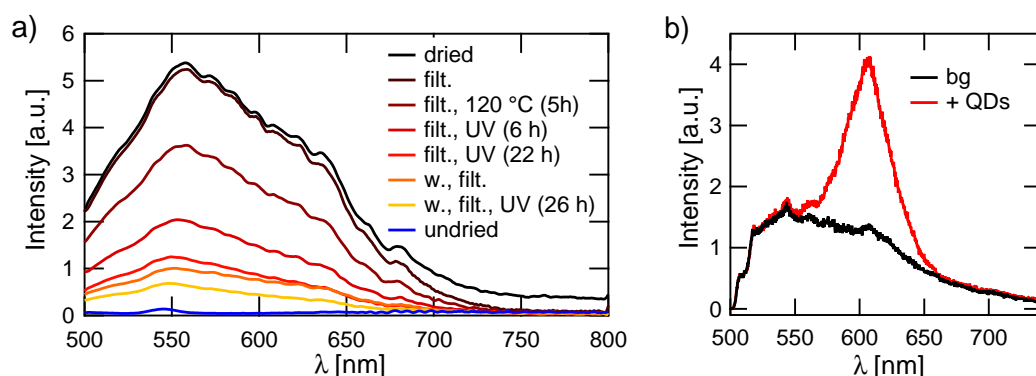


Figure C.2: a) Fluorescence spectra of a TBAP/PC solution undried (blue) and dried with molecular sieves for 24 h with several subsequent steps to reduce the fluorescence. It has been filtered (filt.), heated to 120°C, UV illuminated or molecular sieves have been washed (w.) prior to use. b) Spectra of an ensemble of QDs on a ZnO/ITO electrode in a dried TBAP/PC solution at the peak potential of -1.15 V (red) and for quenched QD luminescence at -1.75 V (black).

ZnO/ITO in air and at positive potentials is attributed to photoinduced charging and trap relaxation via traps induced by the ZnO surface. Efficiencies of both processes also decrease with a higher separation. The reduced quenching at positive potential and the shift of the negative turn-off edge thus show a strong reduction of charge transfer rates. Boehme et al. [245] observed a similar shift of the charge injection edge with film thickness, which they also attribute to inhibited charge transfer. As charge transfer is intended here, only submonolayers of QDs (black lines in Fig. C.1) are investigated.

C.2 Influences of Solvent Drying with Molecular Sieves

C.2.1 Background Fluorescence in Dried Solution

Completely dried solutions and a nitrogen atmosphere are generally preferred in electrochemistry and also when working with quantum dots. Even small amounts of water reduce the electrochemical potential window as water will get electrolyzed. Some measurements have thus also been performed in dried TBAP/PC solutions. Drying is achieved over molecular sieves (0.4 nm) for at least 12 h. During the drying process fluorescing contaminants are found to be released from the sieves to the TBAP/PC solution. Their fluorescence can be observed in a broad visible spectrum (see Fig. C.2). Fluorescence can be reduced but not eliminated by filtering through a syringe filter of 200 nm pore size, heating or UV illumination of the TBAP/PC solution as well as washing of the molecular sieves in acetone, isopropanol, ethanol and Millipore water prior to use (Fig. C.2 a)). After washing of the sieves they have been dried at 200°C and 0.15 mbar for 44 h. A spectrum of a QD film in dried solution is depicted in Fig. C.2 b) at maximum and background fluorescence. Apart from this background and a shift of the negative turn-off edge, measurements in dried and undried solutions are qualitatively alike (see below). Most measurements are thus performed in undried solutions to avoid this background fluorescence especially for time-resolved measurements.

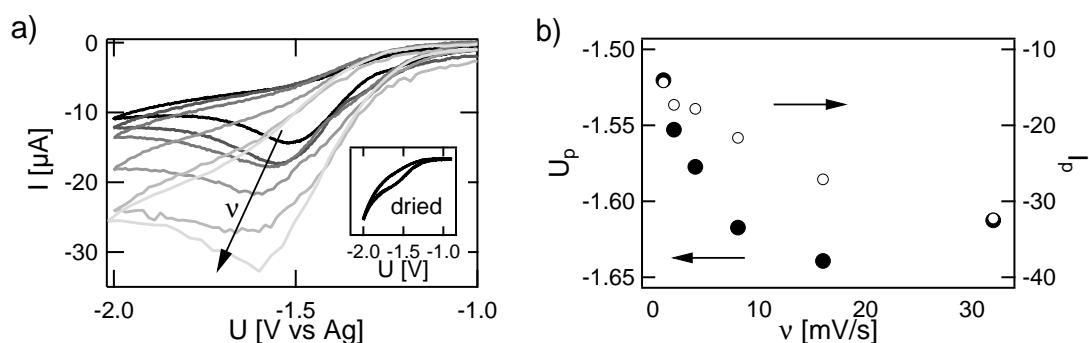


Figure C.3: Dependence of the reduction peak observed in the current of undried TBAP/PC solution on scan rate v . a) Current voltammograms at scan rates increasing from 10 mV/s (black) to 320 mV/s (light gray) recorded during the fluorescence voltammograms of Fig. 6.7. Voltammograms extend to 1 V. Inset: Voltammogram of a dried TPAB/PC solution at ambient condition. b) Dependence of peak position and amplitude on v . A shift of 0.1 V is observed.

C.2.2 Current Reduction Peak in Undried Solution

In current voltammograms of undried TBAP/PC solutions a reduction peak appears at $U_p \approx -1.7$ V as shown in Fig. C.3 a). This reduction peak is typical when working with undried solutions [249]. It is not or only marginally observed in the dried solution (see inset). In contrast to QD fluorescence, the peak shifts to more negative potentials U_p and increases in height I_p with increasing scan rate v as shown in Fig. C.3 b). This is in agreement with low electron transfer rates on time-scales of the scan rate (see Sec. 4.3.1).

C.2.3 Potential Shift in Undried Solution

The exchange of the solvent from an undried to a dried TBAP/PC solution does not change the shape of the fluorescence voltammograms. They are however shifted by approximately 0.4 V to more positive potentials. This is demonstrated in Fig. C.4 a) for different substrates. A corresponding 0.4 V shift between the undried and dried solutions is not observed in the reference potential as shown in b) for measurements on platinum. Drifts of the reference potential are however observed over time (compare dashed and solid lines for undried solutions). Differences in the negative turn-off potentials (dashed lines) between the different substrates in Fig. C.4 a) are not related to the respective electrodes. They result from slightly varying reference potentials, concentrations (see Sec. C.1) or the drift of the turn-off edge over time (see Sec. C.3 below).

When the first voltage scan in undried solutions is investigated it is clear that the 0.4 V shift happens during the initial decrease of voltage to negative potentials as shown in Fig. C.4 c) on ZnO/ITO and d) on ITO for the first cycles. The shift is also accompanied by a shift in the current voltammogram at negative potential, as shown in c) and d). Here the first cycles (black) show an earlier onset than later cycles (red). The onset is additionally not as steep, thus indicating the same shift during the increasing negative potential. Residual water or other impurities that can be eliminated with molecular

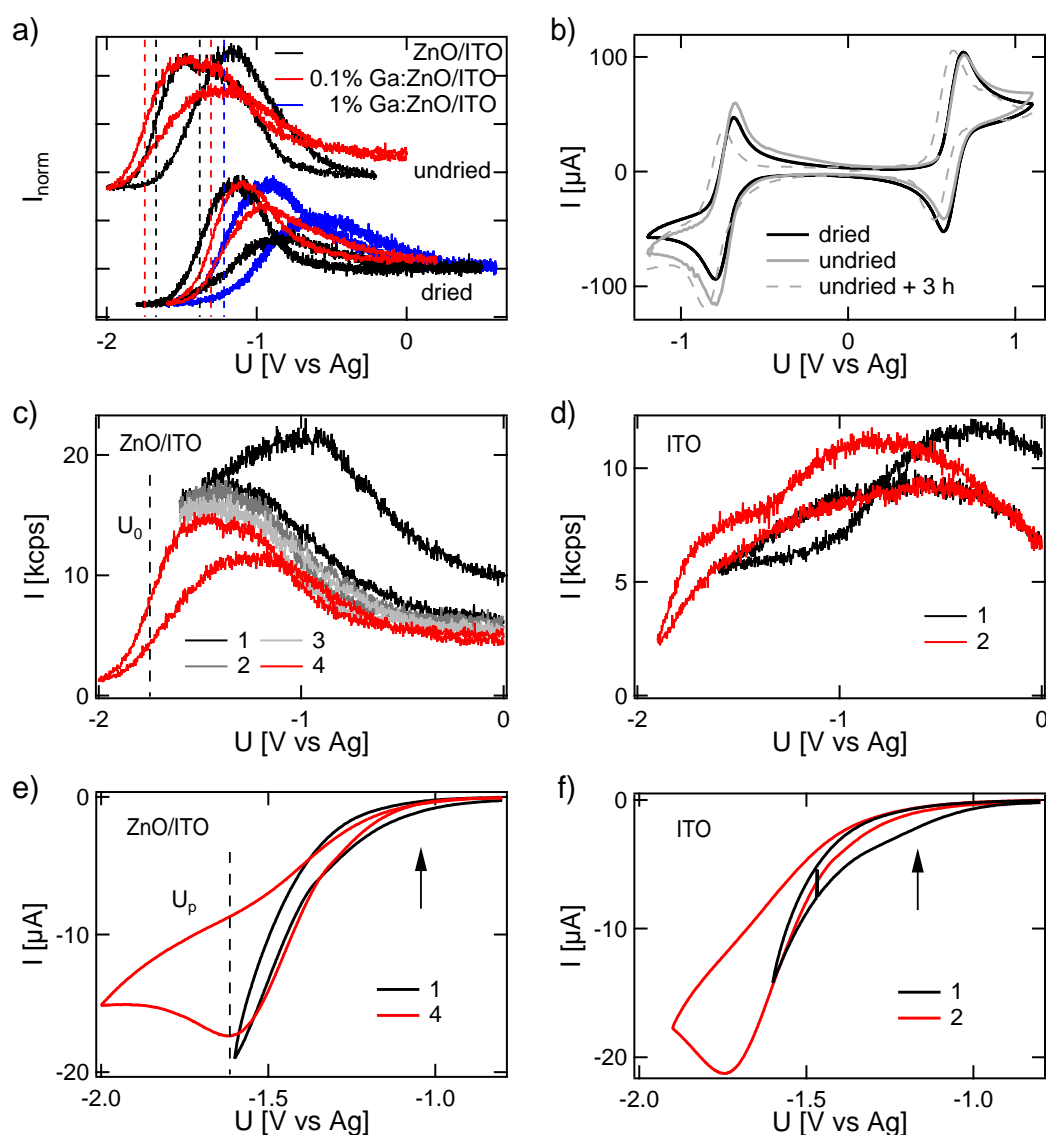


Figure C.4: a) Fluorescence voltammograms in undried and dried solution on ZnO/ITO substrates with different doping levels. Curves in undried solution are offset for clarity. Dashed lines indicate negative turn-off potentials. b) Current voltammograms of the Ce/Ce^+ and Fe/Fe^+ couples (5 mM solution) on a platinum working electrode in undried and dried solution. Dashed line is recorded after refilling the same undried solution to the cell after 3 h. c) First four cycles on ZnO/ITO and d) first two cycles on ITO of fluorescence voltammograms in undried solution. During the potential decrease in the first cycle, the voltammogram shifts by ≈ 0.4 V to more negative potentials. e) and f) Corresponding current voltammograms to c) and d) that show the same shift.

sieves thus change the observed negative turn-off edge. As the shift is also observed in the current peak, it is tentatively assigned to a change in the charge transfer rate between QD and electrode. Adsorption processes on electrode or QD, e. g. due to the incorporation of water molecules in the HDA-ligand layers, could increase tunneling barriers.

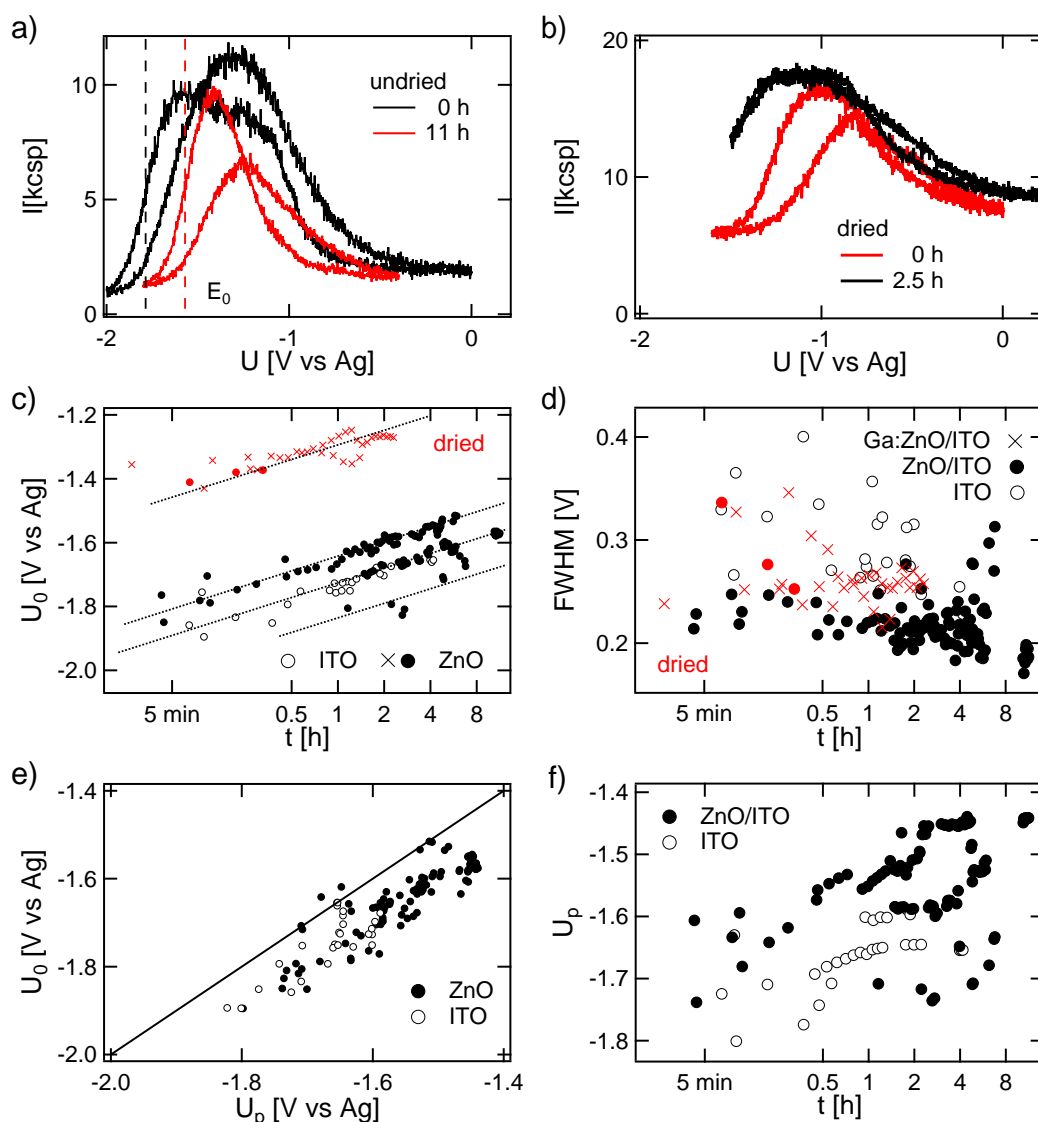


Figure C.5: Observed shifts of the negative turn-off edge over time. a) and b) First and last cycles of fluorescence voltammograms for two measurements in undried and dried solution, respectively. c) Evaluation of the edge potential U_0 with Eq. (6.1) for different measurements over time. Crosses mark Gallium doped ZnO electrodes. d) Corresponding fitted FWHM. e) Correlation of U_0 and the peak potential U_p of the reduction peak in current voltammograms of undried solution (see Fig. C.4 e)). f) Corresponding shift of U_p over time.

C.3 Shift of the Negative Turn-Off Edge over Time

Independent of this offset between dried and undried solution, the negative turn-off edge then shifts to more positive potentials over several hours. For two measurements in undried and dried solution the first and the last cycles are shown in Fig. C.5 a) and b), respectively. The much higher background fluorescence in dried solution in d) results from fluorescing contaminants of the molecular sieves in the electrolyte solution (see Sec. C.2.1). For a quantification of the shift, the potential dependent intensity

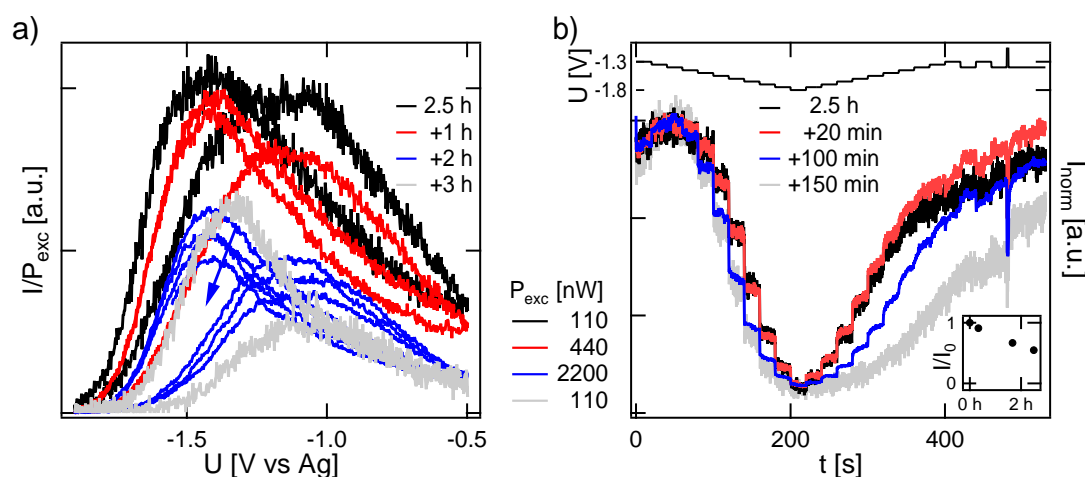


Figure C.6: a) Fluorescence voltammograms at different excitation powers P_{exc} normalized to the corresponding P_{exc} . b) Fluorescence intensity during 20s voltage steps of increasing and decreasing negative potential at the negative turn-off edge. Voltage is indicated at the top. Intensity is normalized to the initial peak intensity at -1.4 V. Inset: relative intensity decrease normalized to P_{exc} . The approximate time of each measurement after the corresponding first measurement (black) is indicated in the legend.

$I(E)$ of the turn-off edges is fitted with the error function (6.1). Results of the mid-edge potential U_0 are plotted for more than ten different measurements for consecutive cycles over time in c) and the corresponding FWHM in d). On a logarithmic time axis a linear shift is observed for U_0 of ≈ 0.3 V over 12 h with a shift of ≈ 100 mV over the first hour. No systematic difference is observed between the investigated substrates at illuminations close to 100 nW. Higher illuminations generally showed stronger shifts of the turn-off edge (see Sec. C.4). In undried solution different potential lines appear to be preferred which are attributed to different spin cast concentrations (see Sec. C.1). The FWHM slightly decreases over time. A narrowing of the transition over time can result from the loss of specific QDs e. g. with low or high turn-off potentials. High and low turn-off potentials are not directly correlated with different transition widths (see Sec. 6.6) and would thus not be detectable in the spectrum (see Sec. C.6). Stronger fluctuations for the fitted FWHM of initial measurements also result from lower fitting accuracies. Potentials are rarely decreased beyond -2 V which did not always cover the whole transition for very negative, thus initial U_0 . In undried solution the shift in U_0 can be correlated to the peak position U_p of the appearing reduction peak (see Sec. C.2.2). This is presented in e) and shows a linear correlation. The shift of U_p over time is plotted in f). Like the shift between undried and dried solution, the shift over time is also accompanied by a shift of the reduction peak U_p . Similar processes are thus expected to be responsible.

C.4 Dependence on the Excitation Intensity

Luminescence voltammograms at different excitation intensities are shown in Fig. C.6 a). Intensity is normalized to the excitation power P_{exc} . Voltammogram shapes are

qualitatively unchanged except for the shift of the turn-off edge and the narrowing over time (see Sec. C.3). The shift of the turn-off edge U_0 increases the difference between the negative reversal potential U_{\min} and U_0 , which also increases the hysteresis between cathodic and anodic sweep (see Sec. 6.3)). The observed shift over time in Fig. C.6 is unusually strong over the investigated 3 h. The first measurement at 110 nW is taken 2.5 h after the very first voltammogram. Fig. C.5 c) suggests only a shift of ≈ 60 mV from 2.5 h to 5.5 h. A shift of 150 mV over the 3 h and 80 mV over the last hour is observed. Also the single QD measurement in Figs. 6.17 and 6.18 is taken 2 h after the very first measurement and shows a detectable shift even over the 20 min of the seven measured cycles. There excitation rates are another factor of 100 higher. Higher excitation thus accelerates the shift of the turn-off edge. As observed on single QDs, higher excitation rates also lead to bleaching of QDs. Intensity strongly decreases over time which is hardly observed when only exciting at 100 nW (see Fig. C.5 c)). At 2200 nW (blue) an especially strong decrease over consecutive cycles is observed. A comparison to the later measurement at 110 nW, however, shows that most of this is reversible. Such an excitation induced reversible quenching at mid-gap potentials agrees well with the assignment to photoinduced positive charging.

Fig. C.6 b) shows the application of 20 s voltage steps (top) at the negative turn-off edge. They are applied before each of the cycles in a) at the same excitation rates. The shift of the turn-off edge leads to an earlier decrease and later increase (at less negative potentials) of fluorescence intensity for later measurements. It is however evident, that even when intensity is quenched at a similar potential (< 200 s) it recovers faster at higher excitation (compare red to black and blue to gray curves). Recovery from negative potentials (region I) can thus be accelerated with higher excitation rates.

C.5 Single Quantum Dots

In Fig. C.7 four representative single QDs are shown of a measurement on ZnO/ITO in undried solution. Four consecutive cycles between -2 V and 0.5 V are detected and plotted offset for clarity with the time average at the top. The QDs show the same features as those on Ga:ZnO/ITO in dried solution (see Sec. 6.5).

Fig. C.8 shows another measurements of a total of 150 single QDs in undried solution on ITO. Three consecutive cycles are recorded. The top left shows the time averages of all QDs, each displayed as line on the y-axis like in Fig. 6.23. The ensemble time average over all cycles and QDs is included as red line. It shows the same qualitative behavior as observed in ensemble measurements. The higher luminescence of the anodic sweep (black) simply results from the strong decrease of total luminescence at high excitation rates (e. g. bleaching of QD 2). Averaging starts with an anodic sweep at -1.9 V. The individual cycles of three QDs of this measurement are presented at the right and the bottom with the respective time average on the top. Despite the low averaging of only three cycles, also time averages of single QDs on ITO mostly show the qualitative ensemble behavior. Again the linear increase of the maximum fluorescence with more positive voltage is observed as in Fig. 6.20.

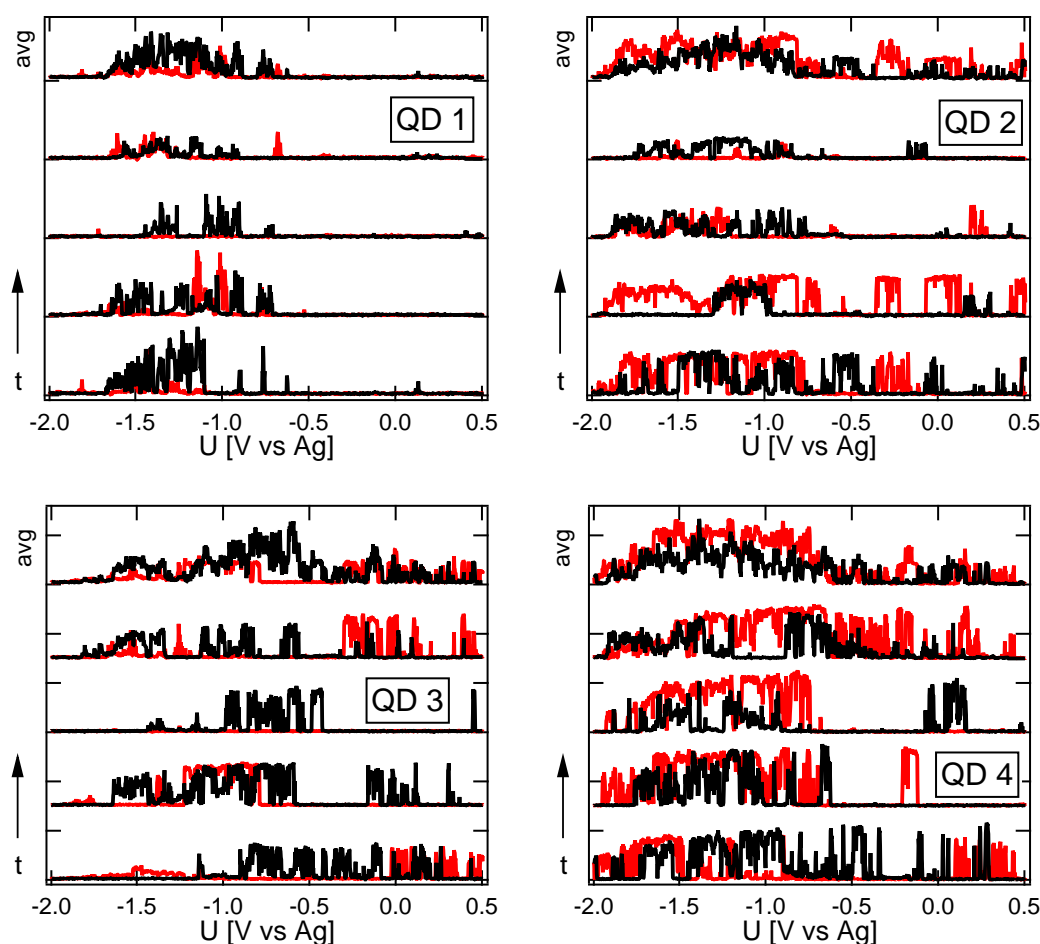


Figure C.7: Four consecutive cycles of fluorescence voltammograms of four single QDs on ZnO/ITO in undried solution at $200\ \mu\text{W}$ in setup D. Cycles are offset for clarity, starting with the first cycle at the bottom. At the top the time average over all four cycles is plotted. Cathodic sweeps are displayed in red, anodic sweeps in black.

C.6 Ensemble Fluorescence Spectra

Voltage dependent spectra on ITO and ZnO/ITO are depicted in Fig. C.9 and C.10, respectively. From the illuminated area of $10\ \mu\text{m}$ (see Fig. 6.1 c)) a thin stripe is chosen with the spectrometer entrance slit from which ensemble spectra are taken. An integral over the total intensity of each spectrum (Fig. C.9 a) and C.10 a)) leads to the same intensity-voltage diagrams as observed with the APD (see Secs. 6.2 to 6.4). Timing with the applied voltage is only approximate, as camera read-out times are not recorded.

C.6.1 Voltage Dependent Spectra on ITO

Selected spectra on ITO are shown in Fig. C.9 b) for the intensity decrease in the anodic (top) and cathodic sweep (bottom). Independent of the sign of the voltage, the fluorescence decrease results in a loss of short wavelength components. Gaussian fits

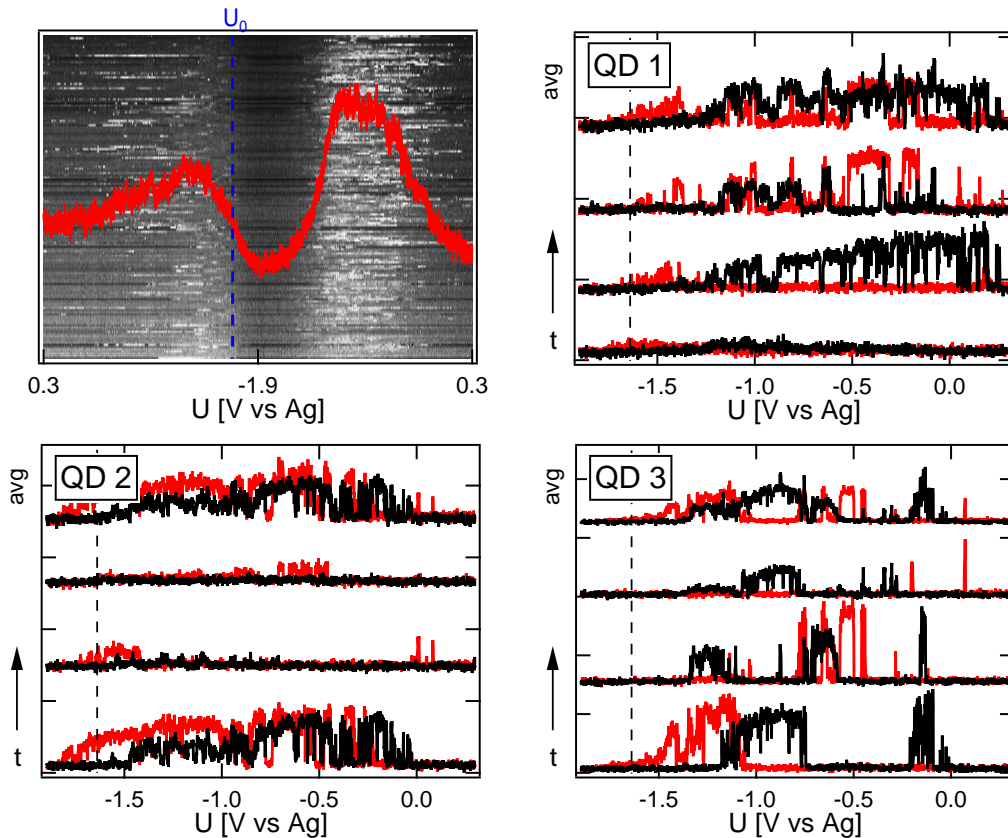


Figure C.8: Measurement of three consecutive voltage cycles of single QDs on ITO in undried solution at $200\ \mu\text{W}$ in setup D. Top left: Time averages of all QDs over all three cycles. Each line on the y-axis corresponds to one QD. The x-axis indicates the applied voltage, cathodic (anodic) sweep on the left (right). The normalized intensity is given in the gray scale. Red line is the ensemble time average of all QDs and all cycles. Blue dashed line indicates the fitted $U_0 = -1.64\ \text{V}$ of Eq. (6.1) for the cathodic sweep. Right and Bottom: The three individual cycles of three single QDs. Cycles are offset for clarity, starting with the first at the bottom. At the top the time average over all three cycles is plotted. Cathodic sweeps are displayed in red, anodic sweeps in black. Black dashed lines mark the average $U_0 = -1.64\ \text{V}$.

to the spectra yield a mean wavelength λ_{mean} increasing with decreasing intensity, as shown in c). A shift of up to 8 nm (25 meV) is observed. At the same intensity the observed red-shift is weaker for negative (blue) than for positive quenching potentials. For the latter a linear correlation is observed also between the fitted FWHM and λ_{mean} as depicted in d). For negative quenching potentials the FWHM does not follow this trend and tends to show broader values with higher scattering.

C.6.2 Voltage Dependent Spectra on ZnO/ITO

Similar spectra as on ITO are observed on ZnO/ITO in Fig. C.10 a) and b). They decrease in width with decreasing intensity due to a decrease in short wavelength components. A similar voltammogram is repeated five hours later, shown in C.10 c) and d). Luminescence has considerably decreased by approximately a factor of ten.

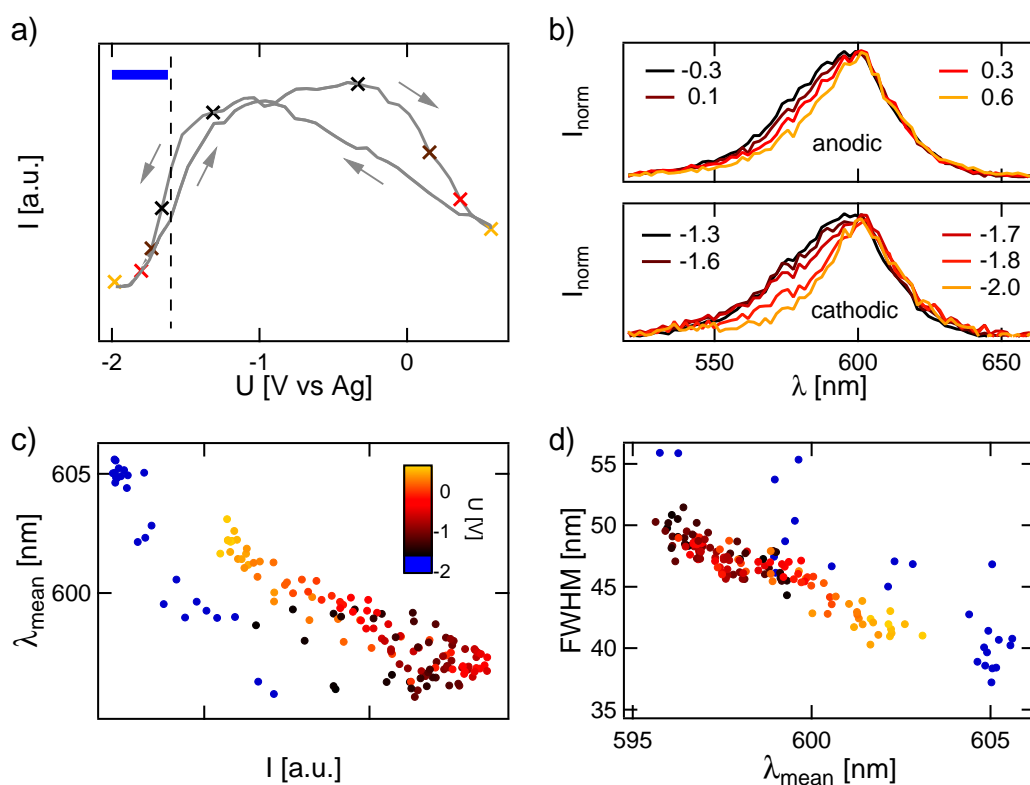


Figure C.9: Voltage dependent ensemble luminescence spectra on ITO at 100 nW. a) Integrated luminescence dependent on the applied voltage. Markers mark the instants in time for the spectra of the cathodic and anodic sweep in b). Colors correspond to the colors of the spectra. Spectra are displayed for the luminescence decrease of each sweep. c) Mean wavelength λ_{mean} of a Gaussian fit in dependence on the integrated luminescence I for two cycles. d) Fitted FWHM in dependence on λ_{mean} . The color scale of c) also indicates the applied voltage in d).

Notably, a red emission band has grown more important relative to band edge emission. It is also indicated in b), however, a lot weaker. Such red emission has not been observed on ITO or blank ZnO/ITO substrates. It correlates with QD luminescence and the applied voltage. When QD band edge luminescence is quenched the red emission band is quenched as well. Fig. C.11 a) shows a direct comparison of the spectra at -1.4V of the two measurements at the beginning and five hours later normalized to the excitation power. An initial spectrum divided by a factor of 10 is also shown as comparison (dashed line). In Fig. C.11 b) the corresponding QD excited state decays are depicted. With time, the relative weight of a long decay component is similarly enhanced as the red emission in the spectrum. A bandpass filter, centered at 605 nm of 60 nm width, cuts out most of the red emission (blue line in Fig. C.11 a)). For the initial measurement a comparison of excited state decays with and without the filter is shown. Blocking of the red emission decreases the long decay component.

C.6.3 Discussion

Observations of voltage dependent spectra show a $\text{FWHM} < 50\text{nm}$ at the expected QD conduction band edge (black in Fig. C.9). It corresponds to a spread in transition ener-

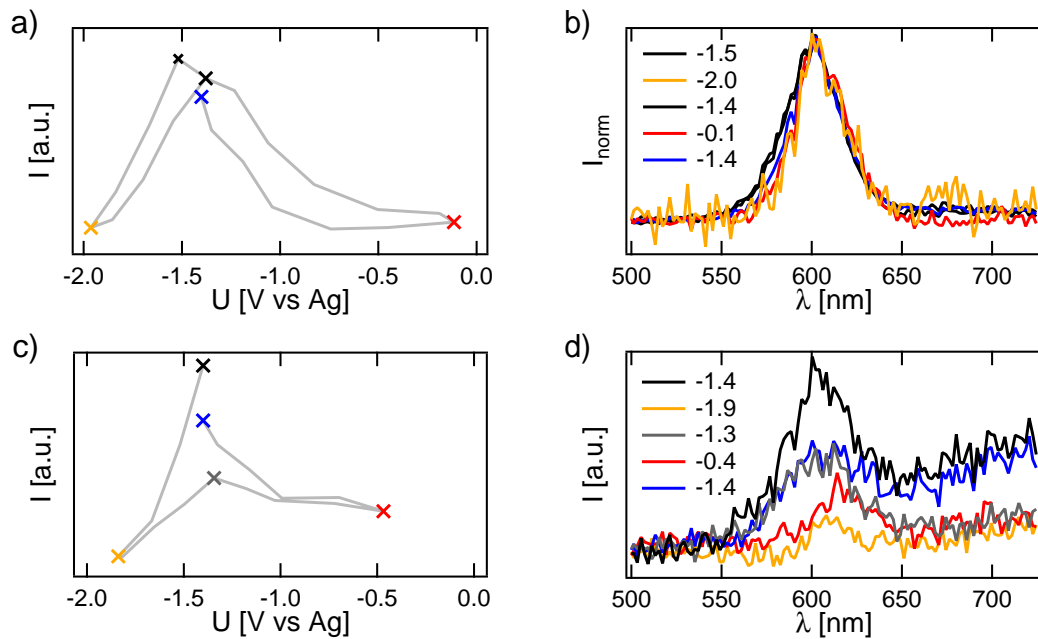


Figure C.10: Voltage dependent ensemble luminescence spectra on ZnO/ITO with setup C at the beginning of a measurement at 220 nW (top) and five hours later at 780 nW (bottom). a) and c) Integrated luminescence dependent on the applied voltage. Markers mark the instants in time for the spectra in b) and d), respectively. Colors correspond to the colors of the spectra.

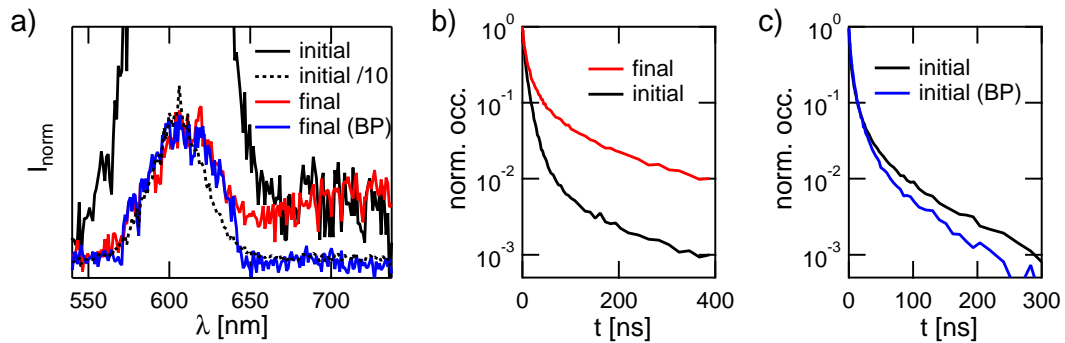


Figure C.11: a) Spectra of QDs on ZnO/ITO using a 605 nm bandpass filter (BP, blue) or a 502 nm long pass filter (LP, black and red), at the beginning of measurements (black) and 5 h later (red and blue). b) Excited state decays at the beginning (black) and after 5 h (red). c) Excited state decays at the beginning measured with a 502 nm long pass (black) and a 605 nm bandpass filter (blue). Decay histograms are logarithmically binned (see Sec. 4.6.3). Measurements are taken at the peak potential of -1.4 V.

gies of $E < 170$ meV which agrees well with the one found in absorption and emission spectra in solution (150 meV, see Fig. 4.1). A redshift is observed of the mean λ_{mean} and a decrease in the FWHM for decreasing luminescence in all three regions. Red shift and narrowing are stronger for the same intensity decrease to positive potentials (regions II and III).

Qin and Guyot-Sionnest [75] also observed spectral red shifts of 10 meV for the injec-

tion of multiple negative charges in single thin shell CdSe/CdS QDs. They interpret their observations with an attractive interaction of extra electrons with the exciton. In CdSe/CdS QDs Auger relaxation with negative charges is strongly suppressed leading to high quantum yields of the negatively charged QDs. Here a relative quantum yield of the negative trion is determined to $\approx 10\%$. An attractive interaction of the extra electron with the hole could thus also lead to a red-shift of the charged QD. It would however not lead to a narrowing of the spectrum or a red-shift to positive potentials.

At higher negative potentials also a participation of the quantum confined stark effect (QCSE) due to high electric fields at the electrode can be imagined. Empedocles and Bawendi [177] found shifts in the range of 10 meV per 100 kV/cm for single CdSe QDs. At the high electrolyte concentrations used (0.1 M TBAP in $\epsilon_{PC} = 64$) the Debye screening length is only $\lambda_D = 0.9$ nm (see Eq. 3.4). The whole potential thus drops across the ≈ 8 nm QD diameter, between TBAP ions and electrode. This could lead to fields of 1000 kV/cm. Due to the much lower polarizability of HDA most of the field will drop over the HDA shell. High fields can still be present across the QD. A red shift due to the QCSE, however, can also not explain the shift at more positive potentials close to 0 V.

Red shift and narrowing in all potential regions could originate from stronger quenching of QDs of shorter wavelength, thus smaller QDs. The intuitive assumption of higher injection edges for smaller QDs would lead to a blue shift of the spectrum at negative potentials. In Sec. 6.6 however it is demonstrated that injection edge and QD size are not directly correlated. Due to their higher wave function overlap with the environment smaller QDs are in general more sensitive to electronic states close to the core. Trap relaxation and charge ejection are thus more efficient.

Defect Emission Contrary to uncapped QDs, core-shell QDs generally do not show any red shifted defect or trap emission. Accordingly, spectra on ITO (Fig. C.9) and also on ZnO/ITO at the beginning of a measurement (Fig. C.10 b)) hardly showed any luminescence other than that of the QD band edge. However on ZnO/ITO five hours later (Fig. C.10 d)) most of the band edge emission is bleached while a red emission band around 700 nm is still strong. Fig. C.11 a) shows that it is already present in initial measurements but increases in relative weight as band edge luminescence decreases. Also bulk ZnO can show a broad spectrum of green and red defect luminescence apart from band edge emission at ≈ 370 nm (3.4 eV [87, 219]). The spectrum observed here however is not observed on blank ZnO/ITO electrodes and strongly correlates with QD emission. It is thus not pure substrate luminescence but an interaction of the QD with the ZnO surface. As expected for defect emission it is accompanied by a long lifetime component, which also increases in weight over time accordingly (Fig. C.11 b) and c)). The stronger participation of trap emission on ZnO/ITO with respect to ITO corresponds well to the observed longer decay components (see Fig. 6.15 d)) and the stronger decrease of QD intensity and lifetime below the QD conduction band edge (region III) on ZnO/ITO.

Bibliography

- [1] Y. Shirasaki, G. J. Supran, M. G. Bawendi, and V. Bulović, “*Emergence of Colloidal Quantum-dot Light-Emitting Technologies*”, *Nat. Photonics* **7**, 13–23 (2013).
- [2] A. L. Rogach, N. Gaponik, J. M. Lupton, C. Bertoni, D. E. Gallardo, S. Dunn, N. Li Pira, M. Paderi, P. Repetto, S. G. Romanov, C. O’Dwyer, C. M. Sotomayor Torres, and A. Eychmüller, “*Light-Emitting Diodes with Semiconductor Nanocrystals*”, *Angew. Chem. Int. Ed.* **47**, 6538–6549 (2008).
- [3] J. W. Stouwdam and R. A. J. Janssen, “*Red, Green, and Blue Quantum Dot LEDs with Solution Processable ZnO Nanocrystal Electron Injection Layers*”, *J. Mater. Chem.* **18**, 1889 (2008).
- [4] V. L. Colvin, M. C. Schlamp, and A. P. Alivisatos, “*Light-Emitting Diodes Made from Cadmium Selenide Nanocrystals and a Semiconducting Polymer*”, *Nature* **370**, 354–357 (1994).
- [5] J. Wu and Z. M. Wang, *Quantum Dot Solar Cells*. New York: Springer, (2013).
- [6] L. Etgar, “*Semiconductor Nanocrystals as Light Harvesters in Solar Cells*”, *Materials* **6**, 445–459 (2013).
- [7] I. Hod and A. Zaban, “*Materials and Interfaces in Quantum Dot Sensitized Solar Cells: Challenges, Advances and Prospects*”, *Langmuir* **30**, 7264–7273 (2014).
- [8] N. N. Ledentsov, “*Quantum Dot Laser*”, *Semicond. Sci. Technol.* **26**, 014001 (2011).
- [9] V. I. Klimov, A. A. Mikhailovsky, S. Xu, A. Malko, J. A. Hollingsworth, C. A. Leatherdale, H.-J. Eisler, and M. G. Bawendi, “*Optical Gain and Stimulated Emission in Nanocrystal Quantum Dots*”, *Science* **290**, 314–317 (2000).
- [10] M. Grundmann, “*The Present Status of Quantum Dot Lasers*”, *Physica E* **5**, 167–184 (1999).
- [11] M. Bruchez, M. Moronne, P. Gin, S. Weiss, and A. P. Alivisatos, “*Semiconductor Nanocrystals as Fluorescent Biological Labels*”, *Science* **281**, 2013–2016 (1998).

- [12] I. L. Medintz, H. T. Uyeda, E. R. Goldman, and H. Mattoussi, “*Quantum Dot Bioconjugates for Imaging, Labelling and Sensing*”, *Nat. Mater.* **4**, 435–446 (2005).
- [13] T. R. Pisanic II, Y. Zhang, and T. H. Wang, “*Quantum Dots in Diagnostics and Detection: Principles and Paradigms*”, *Analyst* **139**, 2968 (2014).
- [14] F. Pisanello, G. Leménager, L. Martiradonna, L. Carbone, S. Vezzoli, P. Desfonds, P. D. Cozzoli, J.-P. Hermier, E. Giacobino, R. Cingolani, M. De Vittorio, and A. Bramati, “*Non-Blinking Single-Photon Generation with Anisotropic Colloidal Nanocrystals: Towards Room-Temperature, Efficient, Colloidal Quantum Sources*”, *Adv. Mater.* **25**, 1973–1973 (2013).
- [15] A. Quattieri, G. Morello, P. Spinicelli, M. T. Todaro, T. Stomeo, L. Martiradonna, M. D. Giorgi, X. Quélin, S. Buil, A. Bramati, J. P. Hermier, R. Cingolani, and M. D. Vittorio, “*Nonclassical Emission from Single Colloidal Nanocrystals in a Microcavity: A Route Towards Room Temperature Single Photon Sources*”, *New J. Phys.* **11**, 033025 (2009).
- [16] X. Brokmann, G. Messin, P. Desbiolles, E. Giacobino, M. Dahan, and J. P. Hermier, “*Colloidal CdSe/ZnS Quantum Dots as Single-Photon Sources*”, *New J. Phys.* **6**, 99 (2004).
- [17] M. Fernández-Suárez and A. Y. Ting, “*Fluorescent Probes for Super-Resolution Imaging in Living Cells*”, *Nat. Rev. Mol. Cell Biol.* **9**, 929–943 (2008).
- [18] F.-C. Chien, C. W. Kuo, and P. Chen, “*Localization Imaging Using Blinking Quantum Dots*”, *Analyst* **136**, 1608 (2011).
- [19] Y. Wang, G. Fruhwirth, E. Cai, T. Ng, and P. R. Selvin, “*3D Super-Resolution Imaging with Blinking Quantum Dots*”, *Nano Lett.* **13**, 5233–5241 (2013).
- [20] M. Faraday, “*The Bakerian Lecture: Experimental Relations of Gold (and Other Metals) to Light*”, *Phil. Trans. R. Soc. Lond.* **147**, 145–181 (1857).
- [21] A. I. Ekimov, A. L. Efros, and A. A. Onushchenko, “*Quantum Size Effect in Semiconductor Microcrystals*”, *Solid State Commun.* **56**, 921–924 (1985).
- [22] P. Michler, *Single Quantum Dots: Fundamentals, Applications, and New Concepts*. Berlin New York: Springer, (2003).
- [23] D. Bimberg, M. Grundmann, and N. N. Ledentsov, *Quantum Dot Heterostructures*. John Wiley & Sons, (1999).
- [24] Klimov and V. I, *Nanocrystal Quantum Dots*. CRC Press, 2 ed., (2010).
- [25] C. Murray, D. J. Norris, and M. G. Bawendi, “*Synthesis and Characterization of Nearly Monodisperse CdE (E = S, Se, Te) Semiconductor Nanocrystallites*”, *J. Am. Chem. Soc.* **115**, 8706–8715 (1993).
- [26] M. Hines and P. Guyot-Sionnest, “*Synthesis and Characterization of Strongly*

- Luminescing ZnS-Capped CdSe Nanocrystals*”, J. Phys. Chem. **100**, 468–471 (1996).
- [27] U. Soni and S. Sapra, “*The Importance of Surface in Core-Shell Semiconductor Nanocrystals*”, J. Phys. Chem. C **114**, 22514–22518 (2010).
- [28] H. Zhu, N. Song, and T. Lian, “*Controlling Charge Separation and Recombination Rates in CdSe/ZnS Type I Core-Shell Quantum Dots by Shell Thicknesses*”, Journal of the American Chemical Society **132**, 15038–15045 (2010).
- [29] J. Vela, H. Htoon, Y. Chen, Y.-S. Park, Y. Ghosh, P. M. Goodwin, J. H. Werner, N. P. Wells, J. L. Casson, and J. A. Hollingsworth, “*Effect of Shell Thickness and Composition on Blinking Suppression and the Blinking Mechanism in ‘Giant’ CdSe/CdS Nanocrystal Quantum Dots*”, J. Biophotonics **3**, 706–717 (2010).
- [30] B. Chon, S. J. Lim, W. Kim, J. Seo, H. Kang, T. Joo, J. Hwang, and S. K. Shin, “*Shell and Ligand-Dependent Blinking of CdSe-Based Core/Shell Nanocrystals*”, Physical Chemistry Chemical Physics **12**, 9312 (2010).
- [31] S. Jeong, M. Achermann, J. Nanda, S. Ivanov, V. I. Klimov, and J. A. Hollingsworth, “*Effect of the Thiol-Thiolate Equilibrium on the Photophysical Properties of Aqueous CdSe/ZnS Nanocrystal Quantum Dots*”, J. Am. Chem. Soc. **127**, 10126–10127 (2005).
- [32] A. Issac, C. von Borczyskowski, and F. Cichos, “*Correlation Between Photoluminescence Intermittency of CdSe Quantum Dots and Self-Trapped States in Dielectric Media*”, Phys. Rev. B **71** (2005).
- [33] V. Fomenko and D. J. Nesbitt, “*Solution Control of Radiative and Nonradiative Lifetimes: A Novel Contribution to Quantum Dot Blinking Suppression*”, Nano Lett. **8**, 287–293 (2008).
- [34] T. Basché, S. Kummer, and C. Bräuchle, “*Direct Spectroscopic Observation of Quantum Jumps of a Single Molecule*”, Nature **373**, 132–134 (1995).
- [35] M. Nirmal, B. O. Dabbousi, M. G. Bawendi, J. J. Macklin, J. K. Trautman, T. D. Harris, and L. E. Brus, “*Fluorescence Intermittency in Single Cadmium Selenide Nanocrystals*”, Nature **383**, 802–804 (1996).
- [36] M. Davanço, C. S. Hellberg, S. Ates, A. Badolato, and K. Srinivasan, “*Multiple Time Scale Blinking in InAs Quantum Dot Single-Photon Sources*”, Phys. Rev. B **89** (2014).
- [37] M. Kuno, D. P. Fromm, H. F. Hamann, A. Gallagher, and D. J. Nesbitt, “*Non-exponential ‘Blinking’ Kinetics of Single CdSe Quantum Dots: A Universal Power Law Behavior*”, J. Chem. Phys. **112**, 3117–3120 (2000).
- [38] K. Shimizu, R. Neuhauser, C. Leatherdale, S. Empedocles, W. Woo, and M. Bawendi, “*Blinking Statistics in Single Semiconductor Nanocrystal Quantum Dots*”, Phys. Rev. B **63**, 205316 (2001).

- [39] P. Didier, L. Guidoni, and F. Bardou, “*Infinite Average Lifetime of an Unstable Bright State in the Green Fluorescent Protein*”, *Phys. Rev. Lett.* **95**, 090602 (2005).
- [40] J. Schuster, F. Cichos, and C. v. Borczyskowski, “*Blinking of Single Molecules in Various Environments*”, *Opt. Spectrosc.* **98**, 712–717 (2005).
- [41] M. Haase, C. G. Hübner, E. Reuther, A. Herrmann, K. Müllen, and T. Basché, “*Exponential and Power-Law Kinetics in Single-Molecule Fluorescence Intermittency*”, *J. Phys. Chem. B* **108**, 10445–10450 (2004).
- [42] J. P. Hoogenboom, E. M. H. P. van Dijk, J. Hernando, N. F. van Hulst, and M. F. García-Parajó, “*Power-Law-Distributed Dark States are the Main Pathway for Photobleaching of Single Organic Molecules*”, *Phys. Rev. Lett.* **95**, 097401 (2005).
- [43] R. Verberk, A. van Oijen, and M. Orrit, “*Simple Model for the Power-Law Blinking of Single Semiconductor Nanocrystals*”, *Phys. Rev. B* **66**, 233202 (2002).
- [44] J. Tang, D.-H. Lee, Y.-C. Yeh, and C.-T. Yuan, “*Short-time Power-Law Blinking Statistics of Single Quantum Dots and a Test of the Diffusion-Controlled Electron Transfer Model*”, *J. Chem. Phys.* **131**, 064506 (2009).
- [45] P. H. Sher, J. M. Smith, P. A. Dalgarno, R. J. Warburton, X. Chen, P. J. Dobson, S. M. Daniels, N. L. Pickett, and P. O’Brien, “*Power Law Carrier Dynamics in Semiconductor Nanocrystals at Nanosecond Timescales*”, *Appl. Phys. Lett.* **92**, 101111 (2008).
- [46] A. L. Efros and M. Rosen, “*Random Telegraph Signal in the Photoluminescence Intensity of a Single Quantum Dot*”, *Phys. Rev. Lett.* **78**, 1110–1113 (1997).
- [47] F. Cichos, C. von Borczyskowski, and M. Orrit, “*Power-law Intermittency of Single Emitters*”, *Curr. Opin. Colloid Interface Sci.* **12**, 272–284 (2007).
- [48] P. Frantsuzov, M. Kuno, B. Jankó, and R. A. Marcus, “*Universal Emission Intermittency in Quantum Dots, Nanorods and Nanowires*”, *Nature Phys.* **4**, 519–522 (2008).
- [49] P. A. Frantsuzov, S. Volkán-Kacsó, and B. Jankó, “*Model of Fluorescence Intermittency of Single Colloidal Semiconductor Quantum Dots Using Multiple Recombination Centers*”, *Phys. Rev. Lett.* **103**, 207402 (2009).
- [50] J. A. Hollingsworth, “*Heterostructuring Nanocrystal Quantum Dots Toward Intentional Suppression of Blinking and Auger Recombination*”, *Chem. Mater.* **25**(8), 1318–1331 (2013).
- [51] C. Galland, Y. Ghosh, A. Steinbrück, J. A. Hollingsworth, H. Htoon, and V. I. Klimov, “*Lifetime Blinking in Nonblinking Nanocrystal Quantum Dots*”, *Nat. Commun.* **3**, 908 (2012).

- [52] X. Wang, X. Ren, K. Kahen, M. A. Hahn, M. Rajeswaran, S. Maccagnano-Zacher, J. Silcox, G. E. Cragg, A. L. Efros, and T. D. Krauss, “*Non-Blinking Semiconductor Nanocrystals*”, *Nature* **459**, 686–689 (2009).
- [53] J. Zhao, G. Nair, B. R. Fisher, and M. G. Bawendi, “*Challenge to the Charging Model of Semiconductor-Nanocrystal Fluorescence Intermittency from Off-State Quantum Yields and Multiexciton Blinking*”, *Phys. Rev. Lett.* **104**, 157403 (2010).
- [54] S. Rosen, O. Schwartz, and D. Oron, “*Transient Fluorescence of the Off State in Blinking CdSe/CdS/ZnS Semiconductor Nanocrystals Is Not Governed by Auger Recombination*”, *Phys. Rev. Lett.* **104**, 157404 (2010).
- [55] C. H. Crouch, O. Sauter, X. Wu, R. Purcell, C. Querner, M. Drndic, and M. Pelton, “*Facts and Artifacts in the Blinking Statistics of Semiconductor Nanocrystals*”, *Nano Lett.* **10**, 1692–1698 (2010).
- [56] M. Lippitz, F. Kulzer, and M. Orrit, “*Statistical Evaluation of Single Nano-Object Fluorescence*”, *ChemPhysChem* **6**, 770–789 (2005).
- [57] T. G. Terentyeva, H. Engelkamp, A. E. Rowan, T. Komatsuzaki, J. Hofkens, C.-B. Li, and K. Blank, “*Dynamic Disorder in Single-Enzyme Experiments: Facts and Artifacts*”, *ACS Nano* **6**, 346–354 (2012).
- [58] S. K. Haram, B. M. Quinn, and A. J. Bard, “*Electrochemistry of CdS Nanoparticles: A Correlation Between Optical and Electrochemical Band Gaps*”, *J. Am. Chem. Soc.* **123**, 8860–8861 (2001).
- [59] E. Kuçur, J. Riegler, G. A. Urban, and T. Nann, “*Determination of Quantum Confinement in CdSe Nanocrystals by Cyclic Voltammetry*”, *J. Chem. Phys.* **119**, 2333–2337 (2003).
- [60] E. Kuçur, W. Bücking, R. Giernoth, and T. Nann, “*Determination of Defect States in Semiconductor Nanocrystals by Cyclic Voltammetry*”, *J. Phys. Chem. B* **109**, 20355–20360 (2005).
- [61] E. Kuçur, W. Bücking, and T. Nann, “*Electrochemical Determination of Mesoscopic Phenomena, Defect States in CdSe Nanocrystals and Charge Carrier Manipulability*”, *Mikrochim. Acta* **160**, 299–308 (2007).
- [62] S. N. Inamdar, P. P. Ingole, and S. K. Haram, “*Determination of Band Structure Parameters and the Quasi-Particle Gap of CdSe Quantum Dots by Cyclic Voltammetry*”, *ChemPhysChem* **9**, 2574–2579 (2008).
- [63] N. Gaponik, S. K. Poznyak, N. P. Osipovich, A. Shavel, and A. Eychmüller, “*Electrochemical probing of thiol-capped nanocrystals*”, *Microchimica Acta* **160**, 327–334 (2007).
- [64] X. Ma, A. Mews, and T. Kipp, “*Determination of Electronic Energy Levels*

- in Type-II CdTe-Core/CdSe-Shell and CdSe-Core/CdTe-Shell Nanocrystals by Cyclic Voltammetry and Optical Spectroscopy*", J. Phys. Chem. C **117**, 16698–16708 (2013).
- [65] M. Amelia, C. Lincheneau, S. Silvi, and A. Credi, "Electrochemical properties of CdSe and CdTe quantum dots", Chemical Society Reviews (2012).
- [66] A. L. Weaver and D. R. Gamelin, "Photoluminescence Brightening via Electrochemical Trap Passivation in ZnSe and Mn²⁺-Doped ZnSe Quantum Dots", J. Am. Chem. Soc. **134**, 6819–6825 (2012).
- [67] M. A. White, A. L. Weaver, R. Beaulac, and D. R. Gamelin, "Electrochemically Controlled Auger Quenching of Mn²⁺ Photoluminescence in Doped Semiconductor Nanocrystals", ACS Nano **5**, 4158–4168 (2011).
- [68] A. K. Gooding, D. E. Gómez, and P. Mulvaney, "The effects of Electron and Hole Injection on the Photoluminescence of CdSe/CdS/ZnS Nanocrystal Monolayers", ACS Nano **2**, 669–676 (2008).
- [69] L. Jin, L. Shang, J. Zhai, J. Li, and S. Dong, "Fluorescence Spectroelectrochemistry of Multilayer Film Assembled CdTe Quantum Dots Controlled by Applied Potential in Aqueous Solution", J. Phys. Chem. C **114**, 803–807 (2010).
- [70] C. Wang, M. Shim, and P. Guyot-Sionnest, "Electrochromic Nanocrystal Quantum Dots", Science **291**, 2390–2392 (2001).
- [71] P. P. Jha and P. Guyot-Sionnest, "Trion Decay in Colloidal Quantum Dots", ACS Nano **3**, 1011–1015 (2009).
- [72] S. Brovelli, C. Galland, R. Viswanatha, and V. I. Klimov, "Tuning Radiative Recombination in Cu-Doped Nanocrystals via Electrochemical Control of Surface Trapping", Nano Lett. **12**, 4372–4379 (2012).
- [73] P. P. Jha and P. Guyot-Sionnest, "Electrochemical Switching of the Photoluminescence of Single Quantum Dots", J. Phys. Chem. C **114**, 21138–21141 (2010).
- [74] W. Qin, R. A. Shah, and P. Guyot-Sionnest, "CdSeS/ZnS Alloyed Nanocrystal Lifetime and Blinking Studies under Electrochemical Control", ACS Nano **6**, 912–918 (2012).
- [75] W. Qin and P. Guyot-Sionnest, "Evidence for the Role of Holes in Blinking: Negative and Oxidized CdSe/CdS Dots", ACS Nano **6**, 9125–9132 (2012).
- [76] C. Galland, Y. Ghosh, A. Steinbrück, M. Sykora, J. A. Hollingsworth, V. I. Klimov, and H. Htoon, "Two Types of Luminescence Blinking Revealed by Spectroelectrochemistry of Single Quantum Dots", Nature **479**, 203–207 (2011).
- [77] W. Qin, H. Liu, and P. Guyot-Sionnest, "Small Bright Charged Colloidal Quantum Dots", ACS Nano **8**, 283–291 (2013).
- [78] P. P. Ingole, S. G. Hickey, C. Waurisch, N. Gaponik, and A. Eychmüller, "Effect

- of Electrochemical Charge Injection on the Photoluminescence Properties of CdSe Quantum Dot Monolayers Anchored to Oxide Substrates*", *Z. Phys. Chem.* **227**, 1173–1186 (2013).
- [79] A. Wachter and H. Hoerber, *Repetitorium Theoretische Physik*. Berlin Heidelberg New York: Springer, 2 ed., (2005).
- [80] L. E. Brus, "Electron–Electron and Electron–Hole Interactions in Small Semiconductor Crystallites: The Size Dependence of the Lowest Excited Electronic State", *J. Chem. Phys.* **80**, 4403–4409 (1984).
- [81] J. Luttinger and W. Kohn, "Motion of Electrons and Holes in Perturbed Periodic Fields", *Phys. Rev.* **97**, 869–883 (1955).
- [82] J. M. Luttinger, "Quantum Theory of Cyclotron Resonance in Semiconductors: General Theory", *Phys. Rev.* **102**, 1030–1041 (1956).
- [83] D. Norris, "Measurement and Assignment of the Size-Dependent Optical Spectrum in CdSe Quantum Dots", *Phys. Rev. B* **53**, 16338–16346 (1996).
- [84] R. Sauer, *Halbleiterphysik: Lehrbuch für Physiker und Ingenieure*. Oldenbourg Verlag, (2009).
- [85] U. Woggon, *Optical Properties of Semiconductor Quantum Dots*. Berlin, Heidelberg: Springer, 1 ed., (1997).
- [86] C. G. Van de Walle and J. Neugebauer, "Universal Alignment of Hydrogen Levels in Semiconductors, Insulators and Solutions", *Nature* **423**, 626–628 (2003).
- [87] S. Adachi, *Handbook on Physical Properties of Semiconductors*. Springer, (2004).
- [88] X. Peng, L. Manna, W. Yang, J. Wickham, E. Scher, A. Kadavanich, and A. P. Alivisatos, "Shape Control of CdSe Nanocrystals", *Nature* **404**, 59–61 (2000).
- [89] L. Manna, E. C. Scher, and A. P. Alivisatos, "Synthesis of Soluble and Processable Rod-, Arrow-, Teardrop-, and Tetrapod-Shaped CdSe Nanocrystals", *J. Am. Chem. Soc.* **122**, 12700–12706 (2000).
- [90] Z. A. Peng and X. Peng, "Nearly Monodisperse and Shape-Controlled CdSe Nanocrystals via Alternative Routes: Nucleation and Growth", *J. Am. Chem. Soc.* **124**, 3343–3353 (2002).
- [91] W. W. Yu, Y. A. Wang, and X. Peng, "Formation and Stability of Size-, Shape-, and Structure-Controlled CdTe Nanocrystals: Ligand Effects on Monomers and Nanocrystals", *Chem. Mater.* **15**, 4300–4308 (2003).
- [92] L. Manna, E. C. Scher, and A. P. Alivisatos, "Shape Control of Colloidal Semiconductor Nanocrystals", *J. Cluster Sci.* **13**, 521–532 (2002).
- [93] W. Wang, S. Banerjee, S. Jia, M. L. Steigerwald, and I. P. Herman, "Lig-

BIBLIOGRAPHY

- and Control of Growth, Morphology, and Capping Structure of Colloidal CdSe Nanorods*", Chem. Mater. **19**, 2573–2580 (2007).
- [94] Z. A. Peng and X. Peng, "Mechanisms of the Shape Evolution of CdSe Nanocrystals", J. Am. Chem. Soc. **123**, 1389–1395 (2001).
- [95] L. Manna, Wang, R. Cingolani, and A. P. Alivisatos, "First-Principles Modeling of Unpassivated and Surfactant-Passivated Bulk Facets of Wurtzite CdSe: A Model System for Studying the Anisotropic Growth of CdSe Nanocrystals", J. Phys. Chem. B **109**, 6183–6192 (2005).
- [96] A. Puzder, A. J. Williamson, N. Zaitseva, G. Galli, L. Manna, and A. P. Alivisatos, "The Effect of Organic Ligand Binding on the Growth of CdSe Nanoparticles Probed by Ab Initio Calculations", Nano Lett. **4**, 2361–2365 (2004).
- [97] J. Y. Rempel, B. L. Trout, M. G. Bawendi, and K. F. Jensen, "Properties of the CdSe(0001), (000 $\bar{1}$), and (11 $\bar{2}$ 0) Single Crystal Surfaces: Relaxation, Reconstruction, and Adatom and Admolecule Adsorption", J. Phys. Chem. B **109**, 19320–19328 (2005).
- [98] D. V. Talapin, I. Mekis, S. Götzinger, A. Kornowski, O. Benson, and H. Weller, "CdSe/CdS/ZnS and CdSe/ZnSe/ZnS Core-Shell-Shell Nanocrystals", J. Phys. Chem. B **108**, 18826–18831 (2004).
- [99] P. Reiss, S. Carayon, J. Bleuse, and A. Pron, "Low Polydispersity Core/Shell Nanocrystals of CdSe/ZnSe and CdSe/ZnSe/ZnS Type: Preparation and Optical Studies", Synth. Met. **139**, 649–652 (2003).
- [100] Y. Chen, J. Vela, H. Htoon, J. L. Casson, D. J. Werder, D. A. Bussian, V. I. Klimov, and J. A. Hollingsworth, "'Giant' Multishell CdSe Nanocrystal Quantum Dots with Suppressed Blinking", J. Am. Chem. Soc. **130**, 5026–5027 (2008).
- [101] W. K. Bae, L. A. Padilha, Y.-S. Park, H. McDaniel, I. Robel, J. M. Pietryga, and V. I. Klimov, "Controlled Alloying of the Core–Shell Interface in CdSe/CdS Quantum Dots for Suppression of Auger Recombination", ACS Nano **7**(4), 3411–3419 (2013).
- [102] J. E. B. Katari, V. L. Colvin, and A. P. Alivisatos, "X-ray Photoelectron Spectroscopy of CdSe Nanocrystals with Applications to Studies of the Nanocrystal Surface", J. Phys. Chem. **98**, 4109–4117 (1994).
- [103] J. Jasieniak and P. Mulvaney, "From Cd-Rich to Se-Rich - the Manipulation of CdSe Nanocrystal Surface Stoichiometry", J. Am. Chem. Soc. **129**, 2841–2848 (2007).
- [104] D. V. Talapin, A. L. Rogach, A. Kornowski, M. Haase, and H. Weller, "Highly Luminescent Monodisperse CdSe and CdSe/ZnS Nanocrystals Synthesized in

- a Hexadecylamine-Trioctylphosphine Oxide-Trioctylphosphine Mixture*”, *Nano Lett.* **1**, 207–211 (2001).
- [105] C. Bullen and P. Mulvaney, “*The Effects of Chemisorption on the Luminescence of CdSe Quantum Dots*”, *Langmuir* **22**, 3007–3013 (2006).
- [106] Z. Hens and J. C. Martins, “*A Solution NMR Toolbox for Characterizing the Surface Chemistry of Colloidal Nanocrystals*”, *Chem. Mater.* **25**, 1211–1221 (2013).
- [107] L. Hartmann, A. Kumar, M. Welker, A. Fiore, C. Julien-Rabant, M. Gromova, M. Bardet, P. Reiss, P. N. Baxter, F. Chandezon, and R. B. Pansu, “*Quenching Dynamics in CdSe Nanoparticles: Surface-Induced Defects upon Dilution.*”, *ACS Nano* **6**, 9033–9041 (2012).
- [108] S. Hohng and T. Ha, “*Near-Complete Suppression of Quantum Dot Blinking in Ambient Conditions*”, *J. Am. Chem. Soc.* **126**, 1324–1325 (2004).
- [109] T. Förster, “*Zwischenmolekulare Energiewanderung und Fluoreszenz*”, *Ann. Phys.* **437**, 55–75 (1948).
- [110] M. Jones, S. S. Lo, and G. D. Scholes, “*Quantitative Modeling of the Role of Surface Traps in CdSe/CdS/ZnS Nanocrystal Photoluminescence Decay Dynamics*”, *PNAS* **106**, 3011 (2009).
- [111] D. Chepic, A. Efros, A. Ekimov, M. Ivanov, V. Kharchenko, I. Kudriavtsev, and T. Yazeva, “*Auger Ionization of Semiconductor Quantum Drops in a Glass Matrix*”, *J. Lumin.* **47**, 113–127 (1990).
- [112] M. I. Dyakonov and V. Y. Kachorovskii, “*Nonthreshold Auger Recombination in Quantum Wells*”, *Phys. Rev. B* **49**, 17130–17138 (1994).
- [113] V. Kharchenko and M. Rosen, “*Auger Relaxation Processes in Semiconductor Nanocrystals and Quantum Wells*”, *J. Lumin.* **70**, 158–169 (1996).
- [114] A. L. Efros, V. Kharchenko, and M. Rosen, “*Breaking the Phonon Bottleneck in Nanometer Quantum Dots: Role of Auger-Like Processes*”, *Solid State Commun.* **93**, 281–284 (1995).
- [115] V. I. Klimov and D. W. McBranch, “*Femtosecond IP-to-IS Electron Relaxation in Strongly Confined Semiconductor Nanocrystals*”, *Phys. Rev. Lett.* **80**, 4028–4031 (1998).
- [116] P. Guyot-Sionnest, “*Intraband Relaxation in CdSe Quantum Dots*”, *Phys. Rev. B* **60**, R2181–R2184 (1999).
- [117] L.-W. Wang, M. Califano, A. Zunger, and A. Franceschetti, “*Pseudopotential Theory of Auger Processes in CdSe Quantum Dots*”, *Phys. Rev. Lett.* **91**, 056404 (2003).
- [118] V. I. Klimov, A. A. Mikhailovsky, D. W. McBranch, C. A. Leatherdale, and

BIBLIOGRAPHY

- M. G. Bawendi, “*Quantization of Multiparticle Auger Rates in Semiconductor Quantum Dots*”, *Science* **287**, 1011–1013 (2000).
- [119] G. E. Cragg and A. L. Efros, “*Suppression of Auger Processes in Confined Structures*”, *Nano Lett.* **10**, 313–317 (2010).
- [120] F. García-Santamaría, S. Brovelli, R. Viswanatha, J. A. Hollingsworth, H. Htoon, S. A. Crooker, and V. I. Klimov, “*Breakdown of Volume Scaling in Auger Recombination in CdSe/CdS Heteronanocrystals: The Role of the Core-Shell Interface*”, *Nano Lett.* **11**, 687–693 (2011).
- [121] H. J. Kimble, M. Dagenais, and L. Mandel, “*Photon Antibunching in Resonance Fluorescence*”, *Phys. Rev. Lett.* **39**, 691–695 (1977).
- [122] F. Diedrich and H. Walther, “*Nonclassical Radiation of a Single Stored Ion*”, *Phys. Rev. Lett.* **58**, 203–206 (1987).
- [123] T. Basché, W. E. Moerner, M. Orrit, and H. Talon, “*Photon Antibunching in the Fluorescence of a Single Dye Molecule Trapped in a Solid*”, *Phys. Rev. Lett.* **69**, 1516–1519 (1992).
- [124] Fleury, Segura, Zumofen, Hecht, and Wild, “*Nonclassical Photon Statistics in Single-Molecule Fluorescence at Room Temperature*”, *Phys. Rev. Lett.* **84**, 1148–1151 (2000).
- [125] Michler, Imamoglu, Mason, Carson, Strouse, and Buratto, “*Quantum Correlation Among Photons from a Single Quantum Dot at Room Temperature*”, *Nature* **406**, 968–970 (2000).
- [126] R. Hanbury Brown and R. Q. Twiss, “*A Test of a New Type of Stellar Interferometer on Sirius*”, *Nature* **178**, 1046–1048 (1956).
- [127] R. R. Chance, A. Prock, and R. Silbey, “*Molecular Fluorescence and Energy Transfer Near Interfaces*” in *Advances in Chemical Physics* (edited by I. Prigogine and S. A. Rice), vol. 37, 1–65, Hoboken, NJ, USA: John Wiley & Sons, Inc., (1978).
- [128] G. W. Ford and W. H. Weber, “*Electromagnetic Interactions of Molecules With Metal Surfaces*”, *Phys. Rep.* **113**, 195–287 (1984).
- [129] D. H. Waldeck, A. P. Alivisatos, and C. B. Harris, “*Nonradiative Damping of Molecular Electronic Excited States by Metal Surfaces*”, *Surf. Sci.* **158**, 103 – 125 (1985).
- [130] W. L. Barnes, “*Fluorescence Near Interfaces: The Role of Photonic Mode Density*”, *J. Mod. Opt.* **45**, 661–699 (1998).
- [131] J. P. Hoogenboom, J. Hernando, E. M. H. P. van Dijk, N. F. van Hulst, and M. F. García-Parajó, “*Power-Law Blinking in the Fluorescence of Single Organic Molecules*”, *ChemPhysChem* **8**, 823–833 (2007).

- [132] E. K. L. Yeow, S. M. Melnikov, T. D. M. Bell, F. C. De Schryver, and J. Hofkens, “*Characterizing the Fluorescence Intermittency and Photobleaching Kinetics of Dye Molecules Immobilized on a Glass Surface*”, *J. Phys. Chem. A* **110**, 1726–1734 (2006).
- [133] R. M. Dickson, A. B. Cubitt, R. Y. Tsien, and W. E. Moerner, “*On/Off Blinking and Switching Behaviour of Single Molecules of Green Fluorescent Protein*”, *Nature* **388**, 355–358 (1997).
- [134] M. Kuno, D. P. Fromm, H. F. Hamann, A. Gallagher, and D. J. Nesbitt, “*“On”/“Off” Fluorescence Intermittency of Single Semiconductor Quantum Dots*”, *J. Chem. Phys.* **115**, 1028–1040 (2001).
- [135] F. D. Stefani, W. Knoll, M. Kreiter, X. Zhong, and M. Y. Han, “*Quantification of Photoinduced and Spontaneous Quantum-Dot Luminescence Blinking*”, *Phys. Rev. B* **72**, 125304 (2005).
- [136] I. Chung and M. G. Bawendi, “*Relationship Between Single Quantum-Dot Intermittency and Fluorescence Intensity Decays from Collections of Dots*”, *Phys. Rev. B* **70**, 165304 (2004).
- [137] F. Cichos, J. Martin, and C. von Borczyskowski, “*Emission Intermittency in Silicon Nanocrystals*”, *Phys. Rev. B* **70**, 115314 (2004).
- [138] S. Wang, C. Querner, T. Emmons, M. Drndic, and C. H. Crouch, “*Fluorescence Blinking Statistics from CdSe Core and Core/Shell Nanorods*”, *J. Phys. Chem. B* **110**, 23221–23227 (2006).
- [139] J. J. Glennon, R. Tang, W. E. Buhro, and R. A. Loomis, “*Synchronous Photoluminescence Intermittency (Blinking) Along Whole Semiconductor Quantum Wires*”, *Nano Lett.* **7**, 3290–3295 (2007).
- [140] D. E. Gómez, M. Califano, and P. Mulvaney, “*Optical Properties of Single Semiconductor Nanocrystals*”, *Phys. Chem. Chem. Phys.* **8**, 4989–5011 (2006).
- [141] U. Banin, M. Bruchez, A. P. Alivisatos, T. Ha, S. Weiss, and D. S. Chemla, “*Evidence for a Thermal Contribution to Emission Intermittency in Single CdSe/CdS Core/Shell Nanocrystals*”, *J. Chem. Phys.* **110**, 1195–1201 (1999).
- [142] K. L. Knappenberger, D. B. Wong, W. Xu, A. M. Schwartzberg, A. Wolcott, J. Z. Zhang, and S. R. Leone, “*Excitation-Wavelength Dependence of Fluorescence Intermittency in CdSe Nanorods*”, *ACS Nano* **2**, 2143–2153 (2008).
- [143] J. J. Peterson and D. J. Nesbitt, “*Modified Power Law Behavior in Quantum Dot Blinking: A Novel Role for Biexcitons and Auger Ionization*”, *Nano Lett.* **9**, 338–345 (2009).
- [144] Y. Ito, K. Matsuda, and Y. Kanemitsu, “*Size-Dependent Photoluminescence Blinking Statistics of Single CdSe/ZnS Nanocrystals*”, *phys. stat. sol. (c)* **6**, 221–223 (2009).

- [145] D.-H. Lee, C.-T. Yuan, M. Tachiya, and J. Tang, “*Influence of Bin Time and Excitation Intensity on Fluorescence Lifetime Distribution and Blinking Statistics of Single Quantum Dots*”, *Appl. Phys. Lett.* **95**, 163101 (2009).
- [146] W. G. van Sark, P. L. T. M. Frederix, D. J. Van den Heuvel, H. C. Gerritsen, A. A. Bol, J. N. J. van Lingen, C. de Mello Donega, and A. Meijerink, “*Photooxidation and Photobleaching of Single CdSe/ZnS Quantum Dots Probed by Room-Temperature Time-Resolved Spectroscopy*”, *J. Phys. Chem. B* **105**, 8281–8284 (2001).
- [147] W. G. J. H. M. van Sark, P. L. T. M. Frederix, A. A. Bol, H. C. Gerritsen, and A. Meijerink, “*Blueing, Bleaching, and Blinking of Single CdSe/ZnS Quantum Dots*”, *ChemPhysChem* **3**, 871–879 (2002).
- [148] T. Krauss, S. O’Brien, and L. Brus, “*Charge and Photoionization Properties of Single Semiconductor Nanocrystals*”, *J. Phys. Chem. B* **105**, 1725–1733 (2001).
- [149] T. D. Krauss and L. E. Brus, “*Electronic Properties of Single Semiconductor Nanocrystals: Optical and Electrostatic Force Microscopy Measurements*”, *Mater. Sci. Eng. B* **69**, 289–294 (2000).
- [150] A. W. Cohn, A. M. Schimpf, C. E. Gunthardt, and D. R. Gamelin, “*Size-Dependent Trap-Assisted Auger Recombination in Semiconductor Nanocrystals*”, *Nano Lett.* **13**, 1810–1815 (2013).
- [151] E. Schrödinger, “*Zur Theorie der Fall- und Steigversuche an Teilchen mit Brownscher Bewegung*”, *Physik. Z.* **16**, 289–295 (1915).
- [152] J. Tang and R. A. Marcus, “*Mechanisms of Fluorescence Blinking in Semiconductor Nanocrystal Quantum Dots*”, *J. Chem. Phys.* **123**, 054704 (2005).
- [153] J. Tang and R. Marcus, “*Diffusion-Controlled Electron Transfer Processes and Power-Law Statistics of Fluorescence Intermittency of Nanoparticles*”, *Phys. Rev. Lett.* **95**, 107401 (2005).
- [154] J. Tang and R. A. Marcus, “*Single Particle Versus Ensemble Average: From Power-law Intermittency of a Single Quantum Dot to Quasistretched Exponential Fluorescence Decay of an Ensemble*”, *J. Chem. Phys.* **123**, 204511 (2005).
- [155] R. A. Marcus and N. Sutin, “*Electron Transfers in Chemistry and Biology*”, *Biochim. Biophys. Acta* **811**, 265–322 (1985).
- [156] M. Pelton, G. Smith, N. F. Scherer, and R. A. Marcus, “*Evidence for a Diffusion-Controlled Mechanism for Fluorescence Blinking of Colloidal Quantum Dots*”, *PNAS* **104**, 14249 (2007).
- [157] S. A. Empedocles and M. G. Bawendi, “*Influence of Spectral Diffusion on the Line Shapes of Single CdSe Nanocrystallite Quantum Dots*”, *J. Phys. Chem. B* **103**, 1826–1830 (1999).
- [158] P. Frantsuzov, “*Explanation of Quantum Dot Blinking Without the Long-Lived Trap Hypothesis*”, *Phys. Rev. B* **72**, 155321 (2005).

- [159] M. Kuno, D. Fromm, S. Johnson, A. Gallagher, and D. Nesbitt, “*Modeling Distributed Kinetics in Isolated Semiconductor Quantum Dots*”, *Phys. Rev. B* **67**, 125304 (2003).
- [160] J. L. Nadeau, L. Carlini, D. Suffern, O. Ivanova, and S. E. Bradforth, “*Effects of β -Mercaptoethanol on Quantum Dot Emission Evaluated from Photoluminescence Decays*”, *J. Phys. Chem. C* **116**, 2728–2739 (2012).
- [161] J. Antelman, Y. Ebenstein, T. Dertinger, X. Michalet, and S. Weiss, “*Suppression of Quantum Dot Blinking in DTT-Doped Polymer Films*”, *J. Phys. Chem. C* **113**, 11541–11545 (2009).
- [162] H. C. Ko, C. T. Yuan, S. H. Lin, and J. Tang, “*Blinking Suppression of Single Quantum Dots in Agarose Gel*”, *Appl. Phys. Lett.* **96**, 012104 (2010).
- [163] N. I. Hammer, K. T. Early, K. Sill, M. Y. Odoi, T. Emrick, and M. D. Barnes, “*Coverage-Mediated Suppression of Blinking in Solid State Quantum Dot Conjugated Organic Composite Nanostructures*”, *J. Phys. Chem. B* **110**, 14167–14171 (2006).
- [164] M. Hamada, S. Nakanishi, T. Itoh, M. Ishikawa, and V. Biju, “*Blinking Suppression in CdSe/ZnS Single Quantum Dots by TiO₂ Nanoparticles*”, *ACS Nano* **4**, 4445–4454 (2010).
- [165] K. Shimizu, W. Woo, B. Fisher, H. Eisler, and M. Bawendi, “*Surface-Enhanced Emission from Single Semiconductor Nanocrystals*”, *Phys. Rev. Lett.* **89**, 117401 (2002).
- [166] X. Ma, H. Tan, T. Kipp, and A. Mews, “*Fluorescence Enhancement, Blinking Suppression, and Gray States of Individual Semiconductor Nanocrystals Close to Gold Nanoparticles*”, *Nano Lett.* **10**, 4166–4174 (2010).
- [167] C. T. Yuan, P. Yu, and J. Tang, “*Blinking Suppression of Colloidal CdSe/ZnS Quantum Dots by Coupling to Silver Nanoprisms*”, *Appl. Phys. Lett.* **94**, 243108 (2009).
- [168] C. T. Yuan, P. Yu, H. C. Ko, J. Huang, and J. Tang, “*Antibunching Single-Photon Emission and Blinking Suppression of CdSe/ZnS Quantum Dots*”, *ACS Nano* **3**, 3051–3056 (2009).
- [169] B. Mahler, P. Spinicelli, S. Buil, X. Quelin, J. P. Hermier, and B. Dubertret, “*Towards Non-Blinking Colloidal Quantum Dots*”, *Nat. Mater.* **7**, 659–664 (2008).
- [170] G. Schlegel, J. Bohnenberger, I. Potapova, and A. Mews, “*Fluorescence Decay Time of Single Semiconductor Nanocrystals*”, *Phys. Rev. Lett.* **88**, 137401 (2002).
- [171] B. R. Fisher, H.-J. Eisler, N. E. Stott, and M. G. Bawendi, “*Emission Intensity Dependence and Single-Exponential Behavior In Single Colloidal Quantum Dot Fluorescence Lifetimes*”, *J. Phys. Chem. B* **108**, 143–148 (2004).

BIBLIOGRAPHY

- [172] K. Zhang, H. Chang, A. Fu, A. P. Alivisatos, and H. Yang, “*Continuous Distribution of Emission States from Single CdSe/ZnS Quantum Dots*”, *Nano Lett.* **6**, 843–847 (2006).
- [173] A. Biebricher, M. Sauer, and P. Tinnefeld, “*Radiative and Nonradiative Rate Fluctuations of Single Colloidal Semiconductor Nanocrystals*”, *J. Phys. Chem. B* **110**, 5174–5178 (2006).
- [174] D. Montiel and H. Yang, “*Observation of Correlated Emission Intensity and Polarization Fluctuations in Single CdSe/ZnS Quantum Dots*”, *J. Phys. Chem. A* **112**, 9352–9355 (2008).
- [175] S. A. Blanton, M. A. Hines, and P. Guyot-Sionnest, “*Photoluminescence Wandering in Single CdSe Nanocrystals*”, *Appl. Phys. Lett.* **69**, 3905–3907 (1996).
- [176] S. A. Empedocles, D. J. Norris, and M. G. Bawendi, “*Photoluminescence Spectroscopy of Single CdSe Nanocrystallite Quantum Dots*”, *Phys. Rev. Lett.* **77**, 3873–3876 (1996).
- [177] S. A. Empedocles and M. G. Bawendi, “*Quantum-Confined Stark Effect in Single CdSe Nanocrystallite Quantum Dots*”, *Science* **278**, 2114–2117 (1997).
- [178] R. G. Neuhauser, K. T. Shimizu, W. K. Woo, S. A. Empedocles, and M. G. Bawendi, “*Correlation between Fluorescence Intermittency and Spectral Diffusion in Single Semiconductor Quantum Dots*”, *Phys. Rev. Lett.* **85**, 3301–3304 (2000).
- [179] R. Memming, *Semiconductor Electrochemistry*. Weinheim ; New York: Wiley-VCH, (2000).
- [180] M. Grundmann, *The Physics of Semiconductors: An Introduction Including Nanophysics and Applications*. Berlin Heidelberg: Springer, 2 ed., (2010).
- [181] D. Meschede and C. Gerthsen, *Gerthsen Physik*. Berlin Heidelberg: Springer, 21 ed., (2001).
- [182] H. Lüth, *Surfaces and Interfaces of Solids*. Springer, (1993).
- [183] K. Tvrđy, P. A. Frantsuzov, and P. V. Kamat, “*Photoinduced Electron Transfer from Semiconductor Quantum Dots to MetalOxide Nanoparticles*”, *PNAS* **108**, 29–34 (2011).
- [184] T. Sakata, K. Hashimoto, and M. Hiramoto, “*New Aspects of Electron Transfer on Semiconductor Surface: Dye-Sensitization System*”, *J. Phys. Chem.* **94**, 3040–3045 (1990).
- [185] D. Vanmaekelbergh, “*Direct and Surface State Mediated Electron Transfer at Semiconductor/Electrolyte Junctions — I. A Comparison of Steady-State Results*”, *Electrochim. Acta* **42**, 1121–1134 (1997).
- [186] K. Rajeshwar, “*Fundamentals of Semiconductor Electrochemistry and Photoelectrochemistry*”, *Encyclopedia of electrochemistry* (2002).

- [187] S. N. Frank and A. J. Bard, “*Semiconductor Electrodes. II. Electrochemistry at N-Type Titanium Dioxide Electrodes in Acetonitrile Solutions*”, J. Am. Chem. Soc. **97**, 7427–7433 (1975).
- [188] R. Kubin and A. Fletcher, “*Fluorescence Quantum Yields of Some Rhodamine Dyes*”, J. Lumin. **27**, 455–462 (1982).
- [189] M. Grabolle, M. Spieles, V. Lesnyak, N. Gaponik, A. Eychmüller, and U. Resch-Genger, “*Determination of the Fluorescence Quantum Yield of Quantum Dots: Suitable Procedures and Achievable Uncertainties*”, Anal. Chem. **81**, 6285–6294 (2009).
- [190] W. W. Yu, L. Qu, W. Guo, and X. Peng, “*Experimental Determination of the Extinction Coefficient of CdTe, CdSe, and CdS Nanocrystals*”, Chem. Mater. **15**, 2854–2860 (2003).
- [191] B. O. Dabbousi, J. Rodriguez-Viejo, F. V. Mikulec, J. R. Heine, H. Mattoussi, R. Ober, K. F. Jensen, and M. G. Bawendi, “*(CdSe)ZnS Core-Shell Quantum Dots: Synthesis and Characterization of a Size Series of Highly Luminescent Nanocrystallites*”, J. Phys. Chem. B **101**, 9463–9475 (1997).
- [192] C. A. Leatherdale, W.-K. Woo, F. V. Mikulec, and M. G. Bawendi, “*On the Absorption Cross Section of CdSe Nanocrystal Quantum Dots*”, J. Phys. Chem. B **106**, 7619–7622 (2002).
- [193] E. Hecht and A. Zajac, *Optics*. Reading, Mass.: Addison-Wesley Pub. Co., 2 ed., (1987).
- [194] R. H. Webb, “*Confocal Optical Microscopy*”, Rep. Prog. Phys. **59**, 427–471 (1996).
- [195] E. Gileadi, *Physical Electrochemistry: Fundamentals, Techniques and Applications*. Weinheim: Wiley-VCH, (2011).
- [196] A. J. Bard and L. R. Faulkner, *Electrochemical Methods: Fundamentals and Applications*. New York: John Wiley & Sons, 2 ed., (2001).
- [197] C. H. Hamann and W. Vielstich, *Elektrochemie*. Weinheim: Wiley-VCH, (1998).
- [198] J. P. Hoogenboom, W. K. den Otter, and H. L. Offerhaus, “*Accurate and Unbiased Estimation of Power-Law Exponents from Single-Emitter Blinking Data*”, J. Chem. Phys. **125**, 204713 (2006).
- [199] S. Milojević, “*Power-law Distributions in Information Science - Making the Case for Logarithmic Binning*”, J. Am. Soc. Inf. Sci. Technol. **61**, 2417–2425 (2010).
- [200] M. L. Goldstein, S. A. Morris, and G. G. Yen, “*Problems with Fitting to the Power-Law Distribution*”, Eur. Phys. J. B **41**, 255–258 (2004).

- [201] A. Clauset, C. Shalizi, and M. Newman, “*Power-Law Distributions in Empirical Data*”, *SIAM Rev.* **51**, 661–703 (2009).
- [202] M. Pelton, D. G. Grier, and P. Guyot-Sionnest, “*Characterizing Quantum-Dot Blinking Using Noise Power Spectra*”, *Appl. Phys. Lett.* **85**, 819–821 (2004).
- [203] L. P. Watkins and H. Yang, “*Detection of Intensity Change Points in Time-Resolved Single-Molecule Measurements*”, *J. Phys. Chem. B* **109**, 617–628 (2005).
- [204] R. Schmidt, C. Krasselt, and C. von Borczyskowski, “*Change Point Analysis of Matrix Dependent Photoluminescence Intermittency of Single CdSe/ZnS Quantum Dots with Intermediate Intensity Levels*”, *Chem. Phys.* **406**, 9–14 (2012).
- [205] G. Margolin, V. Protasenko, M. Kuno, and E. Barkai, “*Power Law Blinking Quantum Dots: Stochastic and Physical Models*”, *Adv. Chem. Phys.* **133 A**, 327–356 (2006).
- [206] N. Amecke, A. Heber, and F. Cichos, “*Distortion of Power Law Blinking with Binning and Thresholding*”, *J. Chem. Phys.* **140**, 114306 (2014).
- [207] R. T. Sibatov and V. V. Uchaikin, “*Statistics of Photocounts of Blinking Fluorescence of Quantum Dots*”, *Opt. Spectrosc.* **108**, 761–767 (2010).
- [208] G. Margolin and E. Barkai, “*Nonergodicity of Blinking Nanocrystals and Other Lévy-Walk Processes*”, *Phys. Rev. Lett.* **94** (2005).
- [209] N. Amecke and F. Cichos, “*Intermediate Intensity Levels During the Emission Intermittency of Single CdSe/ZnS Quantum Dots*”, *J. Lumin.* **131**, 375–378 (2011).
- [210] D. Gómez, J. Van Embden, P. Mulvaney, M. Fernée, and H. Rubinsztein-Dunlop, “*Exciton-Trion Transitions in Single CdSe–CdS Core–Shell Nanocrystals*”, *ACS Nano* **3**, 2281–2287 (2009).
- [211] C. Krasselt, J. Schuster, and C. v. Borczyskowski, “*Photoinduced Hole Trapping in Single Semiconductor Quantum Dots at Specific Sites at Silicon Oxide Interfaces*”, *Phys. Chem. Chem. Phys.* **13**, 17084–17092 (2011).
- [212] R. Schmidt, C. Krasselt, C. Göhler, and C. von Borczyskowski, “*The Fluorescence Intermittency for Quantum Dots Is Not Power-Law Distributed: A Luminescence Intensity Resolved Approach*”, *ACS Nano* **8**, 3506–3521 (2014).
- [213] I. Gryczynski, J. Malicka, K. Nowaczyk, Z. Gryczynski, and J. R. Lakowicz, “*Effects of Sample Thickness on the Optical Properties of Surface Plasmon-Coupled Emission*”, *J. Phys. Chem. B* **108**, 12073–12083 (2004).
- [214] Y. S. Jung, “*Spectroscopic Ellipsometry Studies on the Optical Constants of Indium Tin Oxide Films Deposited Under Various Sputtering Conditions*”, *Thin Solid Films* **467**, 36–42 (2004).

- [215] V. Vaicikauskas, J. Bremer, O. Hunderi, R. Antanavicius, and R. Januskevicius, “*Optical Constants of Indium Tin Oxide Films as Determined by a Surface Plasmon Phase Method*”, *Thin Solid Films* **411**, 262 – 267 (2002).
- [216] Z.-H. Dai, R.-J. Zhang, J. Shao, Y.-M. Chen, Y.-X. Zheng, J.-D. Wu, and L.-Y. Chen, “*Optical Properties of Zinc-oxide Films Determined Using Spectroscopic Ellipsometry with Various Dispersion Models*”, *J. Korean Phys. Soc.* **55**, 1227–1232 (2009).
- [217] M.-S. Kim, K.-G. Yim, J.-S. Son, and J.-Y. Leem, “*Effects of Al Concentration on Structural and Optical Properties of Al-doped ZnO Thin Films*”, *Bull. Korean Chem. Soc.* **33**, 1235–1241 (2012).
- [218] N. G. Connelly and W. E. Geiger, “*Chemical Redox Agents for Organometallic Chemistry*”, *Chem. Rev.* **96**, 877–910 (1996).
- [219] K. Ellmer, A. Klein, and B. Rech, *Transparent Conductive Zinc Oxide: Basics and Applications in Thin Film Solar Cells*. Berlin: Springer, (2008).
- [220] T. C. Kaspar and T. C. Droubay, “*Variation in Band Offsets at ZnO/Sn:In₂O₃ Heterojunctions Measured by X-Ray Photoelectron Spectroscopy*”, *J. Vac. Sci. Technol. A* **30**, 04D112 (2012).
- [221] A. Walsh, J. Da Silva, S.-H. Wei, C. Körber, A. Klein, L. Piper, A. DeMasi, K. Smith, G. Panaccione, P. Torelli, D. Payne, A. Bourlange, and R. Egdell, “*Nature of the Band Gap of In₂O₃ Revealed by First-Principles Calculations and X-Ray Spectroscopy*”, *Phys. Rev. Lett.* **100**, 167402 (2008).
- [222] I. Hamberg, C. G. Granqvist, K.-F. Berggren, B. E. Sernelius, and L. Engström, “*Band-gap Widening in Heavily Sn-Doped In₂O₃*”, *Phys. Rev. B* **30**, 3240–3249 (1984).
- [223] Y. Park, V. Choong, Y. Gao, B. R. Hsieh, and C. W. Tang, “*Work Function of Indium Tin Oxide Transparent Conductor Measured by Photoelectron Spectroscopy*”, *Appl. Phys. Lett.* **68**, 2699–2701 (1996).
- [224] A. Klein, C. Körber, A. Wachau, F. Säuberlich, Y. Gassenbauer, S. P. Harvey, D. E. Proffit, and T. O. Mason, “*Transparent Conducting Oxides for Photovoltaics: Manipulation of Fermi Level, Work Function and Energy Band Alignment*”, *Materials* **3**, 4892–4914 (2010).
- [225] F.-L. Kuo, Y. Li, M. Solomon, J. Du, and N. D. Shepherd, “*Workfunction Tuning of Zinc Oxide Films by Argon Sputtering and Oxygen Plasma: An Experimental and Computational Study*”, *J. Phys. D* **45**, 065301 (2012).
- [226] V. Christou, M. Etchells, O. Renault, P. J. Dobson, O. V. Salata, G. Beamson, and R. G. Egdell, “*High Resolution X-Ray Photoemission Study of Plasma Oxidation of Indium–Tin–Oxide Thin Film Surfaces*”, *J. Appl. Phys.* **88**, 5180–5187 (2000).

- [227] D. J. Milliron, I. G. Hill, C. Shen, A. Kahn, and J. Schwartz, “*Surface Oxidation Activates Indium Tin Oxide for Hole Injection*”, *J. Appl. Phys.* **87**, 572 (2000).
- [228] K. Sugiyama, H. Ishii, Y. Ouchi, and K. Seki, “*Dependence of Indium–Tin–Oxide work Function on Surface Cleaning Method as Studied by Ultraviolet and X-Ray Photoemission Spectroscopies*”, *J. Appl. Phys.* **87**, 295 (2000).
- [229] J. Jasieniak, M. Califano, and S. E. Watkins, “*Size-Dependent Valence and Conduction Band-Edge Energies of Semiconductor Nanocrystals*”, *ACS Nano* **5**, 5888–5902 (2011).
- [230] S.-H. Wei and A. Zunger, “*Calculated Natural Band Offsets of All II–VI and III–V Semiconductors: Chemical Trends and the Role of Cation D Orbitals*”, *Appl. Phys. Lett.* **72**, 2011 (1998).
- [231] N. Y. Morgan, C. A. Leatherdale, M. Drndić, M. V. Jarosz, M. A. Kastner, and M. Bawendi, “*Electronic Transport in Films of Colloidal CdSe Nanocrystals*”, *Phys. Rev. B* **66**, 075339 (2002).
- [232] B. L. Wehrenberg and P. Guyot-Sionnest, “*Electron and Hole Injection in PbSe Quantum Dot Films*”, *J. Am. Chem. Soc.* **125**, 7806–7807 (2003).
- [233] J. D. Rinehart, A. L. Weaver, and D. R. Gamelin, “*Redox Brightening of Colloidal Semiconductor Nanocrystals Using Molecular Reductants*”, *J. Am. Chem. Soc.* **134**, 16175–16177 (2012).
- [234] T. Blaudeck, E. I. Zenkevich, F. Cichos, and C. von Borczyskowski, “*Probing Wave Functions at Semiconductor Quantum-Dot Surfaces by Non-FRET Photoluminescence Quenching*”, *J. Phys. Chem. C* **112**, 20251–20257 (2008).
- [235] D. Kowerko, S. Krause, N. Amecke, M. Abdel-Mottaleb, J. Schuster, and C. von Borczyskowski, “*Identification of Different Donor-Acceptor Structures via Förster Resonance Energy Transfer (FRET) in Quantum-Dot-Perylene Bisimide Assemblies*”, *International Journal of Molecular Sciences* **10**, 5239–5256 (2009).
- [236] D. Kowerko, J. Schuster, N. Amecke, M. Abdel-Mottaleb, R. Dobrawa, F. Würthner, and C. v. Borczyskowski, “*FRET and Ligand Related NON-FRET Processes in Single Quantum Dot-Perylene Bisimide Assemblies*”, *Phys. Chem. Chem. Phys.* **12**, 4112–4123 (2010).
- [237] E. Zenkevich, T. Blaudeck, D. Kowerko, A. Stupak, F. Cichos, and C. von Borczyskowski, “*Ligand Exchange Dynamics and Temperature Effects upon Formation of Nanocomposites Based on Semiconductor CdSe/ZnS Quantum Dots and Porphyrins: Ensemble and Single Object Measurements*”, *Macromolecules* **5**, 98–114 (2012).
- [238] P. Kukura, M. Celebrano, A. Renn, and V. Sandoghdar, “*Imaging a Single Quantum Dot When It Is Dark*”, *Nano Lett.* **9**, 926–929 (2009).

- [239] Y.-S. Park, W. K. Bae, J. M. Pietryga, and V. I. Klimov, “*Auger Recombination of Biexcitons and Negative and Positive Trions in Individual Quantum Dots*”, *ACS Nano* **8**, 7288–7296 (2014).
- [240] M. W. Holman, R. Liu, and D. M. Adams, “*Single-Molecule Spectroscopy of Interfacial Electron Transfer*”, *J. Am. Chem. Soc.* **125**, 12649–12654 (2003).
- [241] D. S. Ginger and N. C. Greenham, “*Charge Injection and Transport in Films of CdSe Nanocrystals*”, *J. Appl. Phys.* **87**, 1361–1368 (2000).
- [242] T. A. Baker, J. L. Rouge, and D. J. Nesbitt, “*Single Molecule Studies of Quantum Dot Fluorescence Intermittency: Evidence for Both Dark and Light-Assisted Blinking Dynamics*”, *Mol. Phys.* **107**, 1867–1878 (2009).
- [243] M. Jones, J. Nedeljkovic, R. J. Ellingson, A. J. Nozik, and G. Rumbles, “*Photoenhancement of Luminescence in Colloidal CdSe Quantum Dot Solutions*”, *The Journal of Physical Chemistry B* **107**, 11346–11352 (2003).
- [244] C. Bradac, T. Gaebel, N. Naidoo, M. J. Sellars, J. Twamley, L. J. Brown, A. S. Barnard, T. Plakhotnik, A. V. Zvyagin, and J. R. Rabeau, “*Observation and Control of Blinking Nitrogen-Vacancy Centres in Discrete Nanodiamonds*”, *Nature Nanotechnology* **5**, 345–349 (2010).
- [245] S. C. Boehme, H. Wang, L. D. Siebbeles, D. Vanmaekelbergh, and A. J. Houtepen, “*Electrochemical Charging of CdSe Quantum Dot Films: Dependence on Void Size and Counterion Proximity*”, *ACS Nano* **7**, 2500–2508 (2013).
- [246] G. Nienhuis and C. T. J. Alkemade, “*Atomic Radiative Transition Probabilities in a Continuous Medium*”, *Physica B+C* **81**, 181–188 (1976).
- [247] X. Brokmann, L. Coolen, J. Hermier, and M. Dahan, “*Emission Properties of Single CdSe/ZnS Quantum Dots Close to a Dielectric Interface*”, *Chem. Phys.* **318**, 91–98 (2005).
- [248] W. Lukosz and R. E. Kunz, “*Light Emission by Magnetic and Electric Dipoles Close to a Plane Interface. I. Total Radiated Power*”, *J. Opt. Soc. Am.* **67**, 1607–1615 (1977).
- [249] J. Liu, W. Yang, Y. Li, L. Fan, and Y. Li, “*Electrochemical Studies of the Effects of the Size, Ligand and Composition on the Band Structures of CdSe, CdTe and Their Alloy Nanocrystals*”, *Phys. Chem. Chem. Phys.* **16**, 4778–4788 (2014).

Publications

Journal Publications

- N. Amecke, A. Heber, and F. Cichos: “*Distortion of Power Law Blinking with Binning and Thresholding*”, J. Chem. Phys. **140**, 114306 (2014)
- N. Amecke, and F. Cichos: “*Intermediate Intensity Levels During the Emission Intermittency*”, J. Lumin. **131**, 375-378 (2011)
- D. Kowerko, J. Schuster, N. Amecke, M. Abdel-Mottaleb, R. Dobrawa, F. Würthner, and C. v. Borczyskowski: “*FRET and Ligand Related NON-FRET Processes in Single Quantum Dot-Perylene Bisimide Assemblies*”, Phys. Chem. Chem. Phys. **12**, 4112-4123 (2010)
- D. Kowerko, S. Krause, N. Amecke, M. Abdel-Mottaleb, J. Schuster, and C. v. Borczyskowski: “*FRET and Ligand Related NON-FRET Processes in Single Quantum Dot-Perylene Bisimide Assemblies*”, Phys. Chem. Chem. Phys. **12**, 4112-4123 (2010)

Talks

- N. Amecke, D. Plotzki and F. Cichos: “*Electrochemical Manipulation of Single CdSe/ZnS Quantum Dots*”, DPG spring meeting, Regensburg (March 2013)
- N. Amecke and F. Cichos: “*Fluorescence and Migration of Charged Quantum Dots Dispersed in Toluene*”, Optical Spectroscopy and Molecular Physics group seminar, Chemnitz (June 2010) – **invited**
- N. Amecke and F. Cichos: “*Net Charge on Colloidal CdSe/ZnS Evidots in Non-polar Solvents*”, DPG spring meeting, Regensburg (March 2010)
- N. Amecke, A. Topalov and F. Cichos: “*Optically Detected Cyclic Voltammetry on Single Semiconductor Quantum Dots*”, Bunsentagung, Köln (May 2009)
- N. Amecke and F. Cichos: “*Investigations to the Influences of Charges on the Fluorescence of Single CdSe/ZnS Quantum Dots Dependent on Crystal Size*”, DPG spring meeting, Dresden (March 2009)
- N. Amecke and F. Cichos: “*Fluorescence Correlation Spectroscopy and Blinking of Single CdSe/ZnS Nanocrystals with Different Sizes*”, Workshop for German and Korean Junior Scientists, Seoul (Korea) (October 2008)

Poster Presentations

- N. Amecke and F. Cichos: “*Fluorescence of Surface-Charged CdSe/ZnS Quantum Dots in Apolar Solvents*”, Nanoscience with Nanocrystals 5 conference, Fuengirola (Spain) (May 2012)
- N. Amecke and F. Cichos: “*Surface Charges on CdSe/ZnS Quantum Dots in Apolar Solvents*”, DPG spring meeting, Berlin (March 2012)
- N. Amecke and F. Cichos: “*Optical Detection of a Surface Charge on CdSe/ZnS Quantum Dots in Apolar Solvents*”, 488. WE Heraeus Seminar, Chemnitz (July 2011)
- N. Amecke and F. Cichos: “*Detection of a surface charge on fluorescent CdSe/ZnS Quantum Dots in Toluene*”, DPG spring meeting, Dresden (March 2011)
- N. Amecke and F. Cichos: “*Positively Charged CdSe/ZnS Quantum Dots in Nonpolar Solvents*”, Nanoscience with Nanocrystals 4 conference, München-Tutzing (April 2010)
- N. Amecke and F. Cichos: “*Investigations of Single Quantum Dot Blinking via Fluorescence Correlation Spectroscopy*”, DPG spring meeting, Berlin (February 2008)

Acknowledgements

At this point I would like to thank everybody who made the finishing of this work not only possible but also a mostly pleasant experience.

First of all I thank Prof. Dr. Frank Cichos for giving me the opportunity to work in the MONA-Lab and study the crazy world of semiconductor quantum dots. Our discussions have always been inspiring and motivating. I am especially grateful for his constant support and help with any arising challenges. Also the manuscript itself profited by his comments, ideas and constructive criticism.

Special thanks also go to David Plotzki who as a master student during the last years of research performed and accompanied several of the final measurements. He has always been very motivated and diligent and I enjoyed very much working with him. He also helped a lot with proofreading of the manuscript.

I further thank André Heber, Zachar Krumer, Angel Topalov and Momchil Ivanov who as bachelor and master students were involved in the earlier experiments on blinking statistics and fluorescence electrochemistry.

I am also thankful to Uwe Weber of our group who built the potentiostat, Holger Hochmuth of the semiconductor physics group who deposited the ZnO on the ITO substrates, Dr. Johannes Schwarz from the Kurt-Schwabe-Institut in Meinsberg who provided the commercial potentiostat for reference measurements and Martin Treß of the molecular physics group who took the AFM images.

A big “Thank you!” goes to the MONA group, who supplied many cakes and entertaining lunch breaks, which made work feel a lot less like work. I especially thank Rebecca Wagner and Romy Schachoff with whom I started this MONA-experience and whose company I always enjoyed very much. With Rebecca Wagner I particularly enjoyed some good lab- and pizza-times on our long journey together and am thankful for her proofreading of parts of the manuscript. I also very much appreciated some helpful comments on the related summary pages by Dr. Markus Selmke.

For proofreading I further thank Annika Klüh and Anne Blankenburg who made it through many pages despite their content.

Last but not least I thank my family for their constant support, patience and being the way they are. Special thanks go to my brothers Christoph and Stephan who helped with the literature data base and some \LaTeX tricks.

Declaration

I hereby certify that this thesis was written by the author herself and that no means of help were used other than those mentioned in the text. All work and thoughts from other authors and sources have been duly acknowledged and clearly marked as such in the thesis.

I hereby name Prof. Dr. Frank Cichos, David Plotzki, Rebecca Wagner, Annika Klüh and Anne Blankenburg as the only persons who assisted the author during the compilation of this manuscript by careful proofreading and helpful comments.

I further name David Plotzki, who as a master student recorded some of the measurements on ZnO/ITO.

Apart from the above mentioned individuals, no other person has been involved in the process of the compilation and work on the present thesis. Especially, no attempt has been made to make use of doctoral consulting. No other individuals have received payment of any kind by the author, neither direct nor indirect, for work which is connected with the contents of this thesis.

I further certify that neither this thesis nor any derivative thereof has been submitted or presented to any other examination department for the purpose of achieving a PhD. Neither has it been presented to any other examination office and has not yet been published in its full form.

No earlier attempts to achieve a PhD degree have been made.

I acknowledge the doctoral regulations of the faculty of physics and geosciences (Promotionsordnung der Fakultät für Physik und Geowissenschaften) dated 23rd March 2010 in their full sense.

(Nicole Amecke-Mönnihoff)